

Institute of Experimental Pharmacology and Toxicology
Centre for Experimental Medicine
University Medical Centre Hamburg-Eppendorf

**Role of the nebulin related anchoring protein – NRAP in
the development of heart disease**

Dissertation

Submitted to the Department of Chemistry
Faculty of Mathematics, Informatics and Natural Sciences
University of Hamburg

for the degree of
Doctor of Natural Sciences
(Dr. rer. nat)

by
Janice Raabe
From Delmenhorst

Hamburg 2023

First referee: Prof. Dr. Wolfram Brune

Second referee: Prof. Dr. Friederike Cuello

Disputation committee:

Prof. Dr. Thomas Eschenhagen

Prof. Dr. Wolfram Brune

Prof. Dr. Ralph Holl

Date of disputation: 01.09.2023

Approved for printing: 21.09.2023

This thesis was carried out at the Institute of Experimental Pharmacology and Toxicology (IEPT) from May 2020 to June 2023 under the supervision of Prof. Dr. Friederike Cuello and Prof. Dr. Wolfram Brune

I. Publications

Raabe J, Wittig I, Laurette P, Yang J, Meisterknecht J, Heidler J, Shibamiya A, Laufer S.D, Klampe B, Schulze T, Fuchs S, Stathopoulou K, Piasecki A, Reinsch M, Hansen A, Lukowski R, Gilsbach R, Eschenhagen T, Ulmer B. M, Cuello F (2023) Mitochondrial and metabolic alterations contribute to normoxia-induced senescence in human induced pluripotent stem cells. *In preparation*.

Billing A, Kim Y. C, Gulakson S, Schrage B, **Raabe J**, Hutzfeldt A, Demir F, Klampe B, Lassé M, Li Q, Kravtsova O, Palermo A, Hoxha E, Blankenberg S, Kirchhof P, Huber T. B, Laugesen E, Zeller T, Chrysopolou M, Probul N, Almeida M, Magnussen C, Eschenhagen T, Staruschenko A, Siuzdak G, Poulsen P. L, Schwab C, Cuello F, Vallon V, Rinschen M. M (2023) Multi-omic analysis reveals metabolic organ communication by SGLT2 inhibition. *In revision*.

Stathopoulou K, Schnittger J, **Raabe J**, Fleischer F, Mangels N, Piasecki A, Findlay J, Hartmann K, Krasemann S, Schlossarek S, Uebeler J, Wixler V, Blake D.J, Baillie G.S, Carrier L, Ehler E, Cuello F (2022) CMYA5 is a novel interaction partner of FHL2 in cardiac myocytes. *FEBS J*, 289: 4622-4645. <https://doi.org/10.1111/febs.16402>.

Cuello F, Knaust A. E, Saleem U, Loos M, **Raabe J**, Mosqueira D, Laufer S, Schweizer M, van der Kraak P, Flenner F, Ulmer B. M, Braren I, Yin X, Theofilatos K, Ruiz-Orera J, Patone G, Klampe B, Schulze T, Piasecki A, Pinto Y, Vink A, Hübner N, Harding S, Mayr M, Denning C, Eschenhagen T, Hansen A (2021) Impairment of the ER/mitochondria compartment in human cardiomyocytes with PLN p.Arg14del mutation. *EMBO molecular medicine*, 13(6), e13074. <https://doi.org/10.15252/emmm.202013074>.

Rhoden A, Friedrich F. W, Brandt T, **Raabe J**, Schweizer M, Meisterknecht J, Wittig I, Ulmer B. M, Klampe B, Uebeler J, Piasecki A, Lorenz K, Eschenhagen T, Hansen A, Cuello F (2021) Sulforaphane exposure impairs contractility and mitochondrial function in three-dimensional engineered heart tissue. *Redox biology*, 41, 101951. <https://doi.org/10.1016/j.redox.2021.101951>

Diering S, Stathopoulou K, Goetz M, Rathjens L, Harder S, Piasecki A, **Raabe J**, Schulz S, Brandt M, Pflaumenbaum J, Fuchs U, Donzelli S, Sadayappan S, Nikolaev V. O, Flenner F, Ehler E, Cuello F (2020) Receptor-independent modulation of cAMP-dependent protein kinase and protein phosphatase signaling in cardiac myocytes by oxidizing agents. *The Journal of biological chemistry*, 295(45), 15342–15365. <https://doi.org/10.1074/jbc.RA120.014467>.

II. Conference participation

Basic Cardiovascular Sciences Scientific Sessions, Boston (USA; 2023)

- Poster presentation: “Alteration in intercalated disc composition impacts cardiac disease progression”

Dutch-German Joint Meeting, Würzburg (2023)

- Poster presentation: “Human p.G592R PRKD1 mutation attenuates kinase activity and impacts cardiomyocyte function”

9th DZHK Retreat & 8th Young DZHK Retreat, Potsdam (2022)

- Oral presentation: “PKD regulates myofibrillogenesis and intercalated disc composition”

NCCR summer retreat, virtual (2022)

- Oral presentation: “The PKD-HDAC-MEF2-TFEB signaling axis orchestrates dynamic intercalated disc assembly and myofibrillogenesis in health and disease”

International Society for Heart Research (ISHR), Berlin – world congress (2022)

- Poster presentation: “Protein kinase D regulates myofibrillogenesis and intercalated disc composition”

Myofilament Meeting, Madison (USA; 2022)

- Oral presentation: “Protein kinase D-mediated regulation of myofilament function in cardiac health and disease”
- Poster presentation: “Protein kinase D regulates myofibrillogenesis and intercalated disc composition”

Society for Redox Biology and Medicine (SfRBM), virtual (2021)

- Poster presentation: “Comparison of Human Induced Pluripotent Stem Cells Cultured at Different Oxygen Concentrations by Proteomic Analysis Suggests Normoxia-induced Cellular Senescence”

International Society for Heart Research (ISHR), virtual – European section (2021)

- Poster presentation: “Analysis of intercalated disc composition in hypertrophic cardiomyopathy revealed enhanced expression and mislocalisation of nebulin-related anchoring protein”

III. Scientific achievements

2023 Poster Award (Dutch German Joint Meeting, Würzburg)

2021 Poster Award (International Society for Heart Research Annual Meeting of the European Section)

2021 Paper of the month (German Centre for Cardiovascular Research) (*Deutsches Zentrum für Herz-Kreislauf-Forschung*)

doi: 10.15252/emmm.202013074.

IV. Grants and stipends

- 11/2023-05/2025** **Postdoctoral Researchers International Mobility Experience (PRIME)** from the German Academic Exchange Service (DAAD) (*Deutscher Akademischer Austauschdienst*)
- 04/2023-04/2024** **Project funding from the German Centre for Cardiovascular Research** (*Deutsches Zentrum für Herz-Kreislauf-Forschung*)
Shared expertise with the University of Greifswald
- 04/2022-04/2024** **Grant of the German Heart Foundation** (*Deutsche Herzstiftung*)
Project number: F/21/21
- 12/2021** **Research funding from the University-Medical Centre Hamburg-Eppendorf** (*Universitätsklinikum Hamburg-Eppendorf*)
Project title: “How to break a heart – *Wenn Herzmuskelzellen reißen..*”.
- 05/2020-03/2023** **German Academic Scholarship Foundation** (*Studienstiftung des Deutschen Volkes*)
Doctoral scholarship

V. List of abbreviations

Unit prefixes

k-	Kilo- (10^3)
m-	Milli (10^{-3})
μ -	Micro (10^{-6})
n-	Nano (10^{-9})

Nucleic acids

A	Adenine
C	Cytosine
G	Guanine
T	Thymine

Units

%	Percent
$^{\circ}\text{C}$	Degree Celsius
A	Ampere
b	Base
bp	Base pair
d	Day
Da	Dalton
g	Gram or relative centrifuge force
h	Hour
L	Litre
m	Metre
M	Molar
min	Minute
Mio	Million
N	Newton
s	Second
Hz	Hertz
V	Volt
v/v	Volume/volume percentage
w/v	Weight per volume

A

α -cat	Alpha-catenin
A-band	Anisotropic band
AAV	Adeno-associated virus
AAVS1	Adeno-associated virus integration site 1
ACTC1	Gene encoding for actin alpha cardiac muscle 1
ADP	Adenosine diphosphate
ANOVA	Analysis of variance
APD	Action potential duration
APS	Ammonium persulfate
Arcn1	Archain 1
ARVC	Arrhythmogenic right ventricular cardiomyopathy
ATAC	Assay for transposase-accessible chromatin
ATP	Adenosine triphosphate
ATP2A3	ATPase sarcoplasmic/endoplasmic reticulum Ca ²⁺ transporting 3
AV	Atrioventricular

B

β -cat	Beta-catenin
BafA1	Bafilomycin A1
BAG3	BAG family molecular chaperone regulator 3
BDM	Butanedione monoxime
BIC	Bicarbonate buffer
BMP4	Bone morphogenetic protein 4
BPKDi	Bipyridyl protein kinase D inhibitor
BPM	Beats per minute
BSA	Bovine serum albumin
BTS	N-benzyl-p-toluenesulfonamide

C

c-Myc	Cellular myelocytomatosis oncogene
C-terminus	Carboxyl-terminus
CaCl ₂	Calcium chloride
CaMK	Ca ²⁺ /Calmodulin-dependent kinase
Cas9	CRISPR-associated protein 9
Cat.	Catalogue number
CBFHH	Calcium and bicarbonate-free Hanks buffer with HEPES
Cbx	Chromobox Protein Homolog 1
cDNA	Complementary deoxyribonucleic acid
cMyBP-C	Cardiac myosin-binding protein C
Cnn1	Calponin-1
CO ₂	Carbon dioxide
CON	Control
COPII	Coat protein complex II
COPS3	COP9 signalosome subunit 3
CRISPR	Clustered regularly interspaced short palindromic repeats
crRNA	CRISPR RNA
Csnk1d	Stress-induced protein kinase CK1 delta

CT	Cycle threshold
cTNI	Cardiac troponin I
cTnT	Cardiac troponin T
D	
Δ CT	Difference of cycle thresholds
DAG	Diacylglycerol
DAPI	4',6-diamidino-2-phenylindole
DCM	Dilated cardiomyopathy
ddH ₂ O	Double distilled water
DLP1	Dynamin-like protein 1
DMEM	Dulbecco's Modified Eagle's Medium
DMSO	Dimethyl sulfoxide
DNA	Deoxyribonucleic acid
dNTP	Deoxynucleoside triphosphate
DSC	Desmocollin
DSG	Desmoglein
DSP	Desmoplakin
DTT	Dithiothreitol
DYSF	Dysferlin
E	
E.g.	Exempli gratia (for example)
ECL	Enhanced chemiluminescence
EDTA	Ethylene diamine tetraacetic acid
EGTA	Ethylene glycol tetraacetic acid
EHT	Engineered heart tissue
ELISA	Enzyme-linked immunosorbent assay
ER	Endoplasmic reticulum
ERCIC	ER-Golgi intermediate compartment
ERO1L	Endoplasmic reticulum oxidoreductin-1-like
ES cell	Embryonic stem cell
Et al.	Et alii (and others)
ET1	Endothelin-1
EtOH	Ethanol
F	
F-actin	Filamentous actin
FACS	Fluorescence-activated cell sorting
FBS	Fetal bovine serum
FDR	False discovery rate
FGF	Fibroblast growth factor
FITC	Fluorescein isothiocyanate
FLNC	Gene encoding for filamin C
FOR	5'-3', forward
FTDA	FGF, TGF β , dorsomorphin, activin a based hiPSC culture medium

G

GAPDH	Glyceraldehyde-3-phosphate-dehydrogenase
gDNA	Genomic DNA
GFP	Green fluorescent protein
GimC	Prefoldin
GPCR	G protein-coupled receptors
GPX4	Glutathione peroxidase 4
GRB2	Growth factor receptor bound protein 2
gRNA	Guide ribonucleic acid
GusB	β -Glucuronidase
GYG1	Glycogenin 1

H

HA-L	Left homology arm
HA-R	Right homology arm
HBSS	Hank's Balanced Salt Solution
HCl	Hydrochloric acid
HCM	Hypertrophic cardiomyopathy
HDAC	Histone deacetylases
HDR	Homology-directed repair
HEK cells	Human embryonic kidney cells
HEPES	4-(2-hydroxyethyl)-1-piperazineethanesulfonic acid
hES	Human embryonic stem cells
Het	Heterozygous
HF	Heart failure
HIF1a	Hypoxia inducible factor 1a
hiPSC	Human induced pluripotent stem cell
hiPSC-CMs	Human-induced pluripotent stem cell derived cardiac myocytes
Hom	Homozygous
HRP	Horseradish peroxidase
HSA	Human serum albumin

I

I-band	Isotropic band
IB	Immunoblot
ICM	Ischemic cardiomyopathy
IDH3G	Isocitrate dehydrogenase 3 non-catalytic subunit gamma
IEPT	Institute of Experimental Pharmacology and Toxicology
I_{K1}	Inward rectifier potassium current
I_{Na}	Sodium current
Indel	Insertion/deletion
iPSC	Induced pluripotent stem cells
ISO	Isoprenaline

K

K ⁺	Potassium ions
KCl	Potassium chloride

KD	Knock-down
KEGG	Kyoto encyclopedia of genes and genomes
KI	Knock-in
KLF4	Kruppel-like factor 4
KLHL41	Kelch-like protein 41
KO	Knock-out
KY02111	N(6-chloro-2-benzothiazolyl)-3,4-dimethoxybenzenepropanamide

L

LB	Lysogeny broth
LC-MS	Liquid chromatography–mass spectrometry
LDB3	LIM domain binding 3
LIM	Lin-11, Isl-1, and Mec-3

M

MDH1	Malate dehydrogenase 1
MDP	Maximal diastolic potential
MEF	Mouse embryonic fibroblasts
MEF2	Myocyte enhancer factor 2
MG132	Carbobenzoxyl-L-leucyl-L-leucyl-L-leucine, Proteasome inhibitor
MHC	Myosin heavy chain
MLP	Cysteine and glycine-rich protein 3/Muscle LIM protein
MM	Maintenance medium
MOI	Multiplicity of infection
mRNA	Messenger ribonucleic acid
MRPS5	Mitochondrial ribosomal protein S5
MS	Mass spectrometry
MuRF	Muscle RING finger protein
MW	Molecular weight
MYC-tag	Polypeptide tag derived from <i>c-MYC</i> gene
MYH	Myosin heavy chain
MYL	Myosin light chain

N

n	Number of biological replicates
N-cad	N-cadherin
N-terminus	Amino-terminus
Na ²⁺	Sodium ions
NaCl	Sodium chloride
NC	Nitrocellulose
NCBI	National Centre for Biotechnology Information
NDUFA4	NADH dehydrogenase 1 alpha subcomplex subunit 4
NDUFA4L2	NADH-dehydrogenase 1 alpha-subkomplex, 4-like 2
NDUFB7	NADH dehydrogenase 1 beta subcomplex subunit 7
NF	Non-failing
NGS	Normal goat serum
NHEJ	Non-homologous end joining

NKM	Non-cardiac myocyte medium
NRAP	Nebulin-related anchoring protein
NRVMs	Neonatal rat ventricular myocytes
nt	Nucleotides
O	
O ₂	Oxygen
Oct4	Oktamer-binding transcription factor 4
OE	Overexpression
P	
p	P value, indicator for significance
PAGE	Polyacrylamide gel electrophoresis
PAM	Protospacer adjacent motif
PBS	Phosphate buffered saline
PCA	Principal component analysis
PCBP4	Poly(RC) binding protein 4
PCR	Polymerase chain reaction
PDMS	Polydimethylsiloxane
PDVF	Polyvinylidene difluoride
PE	Phenyephrine
Pen/Strep	Penicillin/streptomycin
PFA	Paraformaldehyde
PKA	Protein kinase A
PKC	Protein kinase C
PKD	Protein kinase D
PKG	Plakoglobin
PKP-2	Plakophilin-2
PLEKHA7	Pleckstrin homology domain containing A7
PM	Plating medium
PMCA	Plasma membrane-associated ATPase
PPP1R12C	Protein phosphatase 1 regulatory subunit 12C
PRMT1	Protein arginine methyltransferase 1
PTFE	Polytetrafluorethylene
PVDF	Polyvinylidene fluoride
PYGM	Glycogen phosphorylase
R	
Ral-A	Ras-related protein A
RAN	Ras-related nuclear protein
RBL2	RB transcriptional corepressor like 2
RCM	Restrictive cardiomyopathy
REV	3'–5', reverse
rH	Relative humidity
RIPA buffer	Radioimmunoprecipitation assay buffer
RMP	Resting membrane potential
RNA	Ribonucleic acid
RNP	Ribonucleoprotein

ROS	Reactive oxygen species
ROX	Passive reference dye for qPCR amplification
Rpm	Rounds per minute
RPMI	Roswell Park Memorial Institute
RT	Room temperature
RT (80%)	Relaxation time at 80% relaxation
RT-qPCR	Real-time quantitative PCR
RTN3	Reticulon-3
RYR2	Ryanodine receptor 2
S	
SA	Sinoatrial
SD	Standard deviation
SDS	Sodium-dodecyl sulfate
SEM	Standard error of the mean
SERCA	Sarco(endo)plasmic reticulum calcium-ATPase
SFXN1	Sideroflexin 1
sgRNA	Single guide RNA SOP
SH3	SRC homology 3
SH3BGRL	SH3 domain binding glutamate rich protein like
SILAC	Stable isotope labeling by/with amino acids in cell culture
SNX5	Sorting nexin 5
Sox2	SYR (sex determining region Y)-box transcription factor 2
Sp1	Specificity protein
SR	Sarcoplasmic reticulum
Sra1	Signal-retaining autophagy indicator
SSEA3	Stage-specific embryonic antigen 3
ssODN	Single-stranded oligodeoxynucleotide
SYBR	Fluorescent dye binding double-stranded DNA
T	
T-tubule	Transverse tubulus
TAE	Tris acetate EDTA
TBS	Tris buffered saline
TBS-T	Tris buffered saline with tween-20
TCAP	Telethonin
TCEP	Tris(2-chlorehyl)phosphate
TEMED	Tetramethylethylenediamine
TFEB	Transcription factor EB
T _m	Melting temperature
TNNI	Gene encoding for troponin I
TNPO1	Transportin 1
TNRC6B	Trinucleotide repeat containing adaptor 6B
TOT	Tropomodulin-overexpressing transgenic
TPM1	Tropomyosin 1
TracrRNA	Trans-activating CRISPR RNA
TRiC	TCP-1 ring complex

Tris	Tris-(hydroxymethyl)-aminoethane
TTP	Time to peak
U	
UKE	University Medical Centre Hamburg-Eppendorf
UPS	Ubiquitine-proteasome system
V	
VIN	Vinculin
W	
WGA	Wheat germ agglutinin
Wnt	Wingless-related integration site
WT	Wildtype
X	
X-gal	5-Bromo-4-chloro-3-indoxyl- β -D-galactopyranoside
XAV939	3,5,7,8-tetrahydro-2-[4-(trifluoromethyl)phenyl]-4H-thiopyrano [4,3d]pyrimidin-4-one
Y	
Y-27632	ROCK inhibitor
YWHAE	Tyrosine 3-monooxygenase/tryptophan 5-monooxygenase activation protein epsilon
Z	
ZASP	Z-band alternatively spliced PDZ-motif

Table of contents

I. Publications	I
II. Conference participation	II
III. Scientific achievements	III
IV. Grants and stipends	IV
V. List of abbreviations	V
1. Zusammenfassung	1
2. Abstract	3
3. Introduction	5
3.1 Mechanisms of cardiac contraction and relaxation	5
3.1.1 Cardiac myocytes	5
3.1.2 Myofibrils	5
3.1.2.1 Actin and myosin interaction	7
3.1.2.2 Myofibrillogenesis	7
3.1.2.3 Myofibril maintenance and turnover	9
3.1.3 Intercalated discs.....	10
3.1.3.1 Gap junctions.....	12
3.1.3.2 Adherens junctions	12
3.1.3.3 Desmosomes.....	13
3.1.4 Transitional junctions	13
3.1.5 Nebulin-related anchoring protein	14
3.1.6 Mechanotransduction.....	14
3.2 Cardiac disease	15
3.2.1 Cardiomyopathies.....	15
3.2.1.1 Hypertrophic cardiomyopathy	15
3.2.1.2 Dilated cardiomyopathy	16
3.2.1.3 Arrhythmogenic right ventricular cardiomyopathy.....	17
3.2.1.4 Restrictive cardiomyopathy	17
3.2.2 Intercalated discs in disease	17
3.2.3 Nebulin-related anchoring protein in heart disease	20
3.3 Disease modelling	21
3.3.1 Human-induced pluripotent stem cells	21
3.3.2 CRISPR-based genome editing	23
3.3.3 Differentiation to cardiac myocytes	24
3.3.4 Engineered heart tissues	26
4. Aims	27
5. Materials and Methods	28
5.1 Animal models	28

5.1.1	<i>Mybpc3</i> -targeted knock-in mouse model	28
5.1.2	Neonatal rat ventricular cardiac myocytes	28
5.1.2.1	Isolation of NRVMs.....	28
5.1.2.2	Culture of neonatal rat ventricular cardiac myocytes	29
5.1.2.3	Treatments of NRVMs	30
5.1.2.4	Immunoprecipitation	30
5.1.2.5	Stable isotope labeling by/with amino acids in cell culture (SILAC)	31
5.1.2.6	Mass spectrometry	31
5.2	Human models	32
5.2.1	Heart samples from patients.....	32
5.2.2	Human-induced pluripotent stem cells.....	32
5.2.2.1	Reprogramming of human fibroblasts into hiPSC	32
5.2.2.2	Thawing and culture of human-induced pluripotent stem cells.....	33
5.2.2.3	Freezing of human-induced pluripotent stem cells.....	34
5.2.2.4	Karyotyping analysis by Giemsa staining	34
5.2.2.5	Senescence-associated beta-galactosidase activity assay.....	35
5.2.2.6	RNA- and ATAC-sequencing	36
5.2.2.7	Blue-native PAGE.....	37
5.2.2.8	Complexome analysis	37
5.3	Gene editing by CRISPR-Cas9	38
5.3.1	AAVS1-cTnT-NRAP/MYC and -NRAP/GFP plasmid validation.....	38
5.3.2	Culture and nucleofection.....	39
5.3.3	Single cell seeding	40
5.3.4	Validation of successful edited CRISPR clones	40
5.3.4.1	Genomic DNA isolation.....	40
5.3.4.2	Polymerase chain reaction	41
5.3.4.3	Agarose gel electrophoresis	42
5.3.4.4	PCR purification and sequencing	42
5.3.5	Production of master and working cell banks.....	43
5.3.5.1	Mycoplasma testing.....	43
5.3.5.2	Stage-specific embryonic antigen 3 detection by flow cytometry	44
5.3.5.3	Karyotype analysis	44
5.3.5.4	Off-target analysis	45
5.4	Human-induced pluripotent stem cell derived cardiac myocytes	46
5.4.1	Cardiac monolayer differentiation	46
5.4.2	Dissociation of hiPSC-CMs from monolayer differentiation	47
5.4.3	Flow cytometry	47
5.4.4	Freezing and thawing of cardiac myocytes.....	48
5.4.5	Culture of cardiac myocytes	48
5.5	Engineered heart tissues.....	49
5.5.1	Generation and culture of engineered heart tissues	49
5.5.2	Treatment of NRVMs-derived engineered heart tissues.....	49
5.5.3	Video-optical contraction analysis.....	49

5.5.4	Electrical synchronisation	51
5.5.5	Action potential measurements	51
5.5.6	Frank-Starling measurements	51
5.5.7	Transmission electron microscopy	52
5.5.8	Dissociation of engineered heart tissues.....	52
5.5.9	Proteomics.....	52
5.6	Molecular analyses.....	53
5.6.1	RNA isolation	53
5.6.2	cDNA synthesis.....	54
5.6.3	Realtime quantitative polymerase chain reaction (RT-qPCR).....	54
5.7	NRAP antibody development and validation.....	55
5.8	Protein analysis.....	56
5.8.1	Sample preparation and SDS-PAGE.....	56
5.8.2	Western immunoblot analysis	56
5.9	Immunofluorescence	57
5.9.1	Preparation and immunofluorescent staining of heart sections	57
5.9.2	Preparation and staining of engineered heart tissue sections	57
5.9.3	Immunofluorescence staining of cardiac myocytes	58
5.9.4	Confocal microscopy.....	58
5.10	Data analysis	59
5.10.1	Softwares.....	59
5.10.2	Statistical analysis	59
6.	Results.....	60
6.1	Impact of different culture conditions on hiPSC characteristics	60
6.2	NRAP antibody development and validation.....	64
6.2.1	Western immunoblot analysis	64
6.2.2	Immunofluorescence.....	67
6.3	Development of NRAP-OE and -KD hiPSC lines	70
6.3.1	Generation of a NRAP/MYC-OE hiPSC line.....	70
6.3.2	Generation of a NRAP/GFP-OE hiPSC line	77
6.3.3	Generation of a NRAP-KD hiPSC line.....	82
6.4	NRAP/MYC-OE and NRAP-KD hiPSC-derived cardiac myocytes.....	86
6.4.1	Cardiac differentiation of NRAP/MYC-OE and NRAP-KD hiPSC.....	86
6.4.2	NRAP RNA and protein levels.....	90
6.4.3	Myofilament structure.....	91
6.5	Impact of NRAP gain- and loss-of-function in EHTs	93
6.5.1	Contractile function	93
6.5.2	Mechanical stretch.....	99
6.5.3	Proteome.....	100
6.6	Impact of protein kinase D inhibition on NRAP.....	104
6.6.1	NRAP localisation and protein levels	105
6.6.2	Contractile function	109
6.6.3	Structural impact.....	112

6.6.3.1	Sarcomeres.....	112
6.6.3.2	Mitochondria and lateral width of intercalated discs.....	115
6.6.4	Impact on protein expression.....	117
6.6.5	Regulation of degradational pathways by protein kinase D.....	122
6.6.6	Immunoprecipitation of NRAP	123
7.	Discussion.....	126
7.1	Normoxic oxygen tensions impact on hiPSC characteristics.....	126
7.2	Successful generation and validation of a human NRAP antibody.....	127
7.3	Impact of NRAP modulation on hiPSC-derived cardiac myocytes	129
7.3.1	<i>NRAP</i> -OE.....	130
7.3.2	<i>NRAP</i> -KD	131
7.3.3	Differentiation into hiPSC-derived cardiac myocytes	132
7.3.4	<i>NRAP</i> mRNA and protein expression	133
7.3.5	Modulation of <i>NRAP</i> lead to structural alterations in cardiac myocytes.....	133
7.3.6	Gain- and loss-of-function of <i>NRAP</i> impacts contractile parameters.....	134
7.3.7	<i>NRAP</i> impacts mechanical stiffness	135
7.3.8	<i>NRAP/MYC</i> -OE and -KD enhance cardiomyopathy-related proteins	136
7.4	PKD-mediated regulation in the developing and diseased heart	137
7.4.1	Impact of PKD inhibition on <i>NRAP</i> expression and phosphorylation.....	137
7.4.2	<i>NRAP</i> translocation in response to modulation of PKD protein level.....	138
7.4.3	PKD negatively impacts contractile force.....	140
7.4.4	Involvement of PKD1 in degradational pathways.....	141
8.	Conclusion	144
9.	Further perspectives	145
10.	References	147
11.	Supplements	167
11.1	Figures and tables	167
11.2	Materials	175
11.2.1	Buffer and cell culture medium compositions.....	175
11.2.2	Antibodies, kits and enzymes	179
11.2.3	Primer	181
11.2.4	Devices, consumables and programmes.....	183
11.2.5	Chemical compounds including H- and P-statements.....	186
11.3	Financial support	190
11.4	Declaration of contribution	190
12.	Acknowledgements	191
13.	Declaration of academic honesty - Eidesstaatliche Erklärung.....	193

1. Zusammenfassung

Kardiomyopathien stellen eine der häufigsten Todesursachen weltweit dar. Unter anderem werden dysfunktionale Glanzstreifen als eine Krankheitsursache diskutiert, welche die elektromechanische Verbindung benachbarter Herzmuskelzellen (HM) sicherstellen. Sowohl in experimentellen murinen Kardiomyopathiemodellen als auch bei dem humanen Krankheitsbild wurde sowohl eine vermehrte als auch eine verminderte Expression des Glanzstreifen-assoziierten *Nebulin-Related Anchoring Proteins* (NRAP) berichtet. NRAP spielt eine wichtige Rolle bei der *de novo* Synthese der Myofibrillen in der Herzentwicklung und in der Mechanotransduktion im adulten Herzen. Da die genaue Funktion von NRAP unbekannt ist, bestand das übergeordnete Ziel dieser Arbeit darin zu untersuchen, ob eine Veränderung der NRAP Expression zur Progression von Kardiomyopathien beiträgt und durch welche Mechanismen diese reguliert wird.

Um den Einfluss der NRAP-Proteinmenge auf die Funktion von HM zu untersuchen, wurden humane induzierte *NRAP*-überexprimierende (OE) und *-knock-down* (KD) Stammzelllinien (hiPSC) mittels *Clustered Regularly Interspaced Short Palindromic Repeats and CRISPR-associated protein 9* (CRISPR-Cas9)-Genomeditierung generiert. Nach erfolgreicher Validierung der hiPSC, wurden diese zu HM differenziert und zusätzlich in 3D künstlichen Herzgeweben (*Engineered Heart Tissues*, EHTs) charakterisiert. Die Untersuchung der *NRAP*-OE HM zeigte im 2D-Modell eine vermehrte Translokation von NRAP zu den lateralen Zellenden, während in *NRAP*-KD HM, ähnlich zur Kontrolle, NRAP an den Z-Scheiben lokalisiert war. Die Analyse der kontraktiven Eigenschaften im 3D-EHT-Format ergab eine geringere Kraftentwicklung und beschleunigte Relaxationszeit in *NRAP*-OE und -KD EHTs im Vergleich zur Kontrollgruppe. *NRAP*-KD EHTs reagierten auf eine mechanische Dehnung mit einem Anstieg der Kontraktionskraft, während bei *NRAP*-OE EHTs ein arrhythmisches Schlagverhalten bei Dehnung zu beobachten war. *NRAP*-OE EHTs zeigten ein weniger negatives *Take-Off Potential* (TOP) und Maximal Diastolisches Potential (MDP). Die Proteomanalyse ergab insbesondere für die *NRAP*-OE EHTs eine Überrepräsentation Kardiomyopathie-assoziiierter Signalwege.

Auch wurde untersucht wie die NRAP-Expression reguliert wird. Protein Kinase D1 (PKD1) reguliert die Transkription fetaler und pro-hypertropher Gene über die Aktivierung des *Myocyte Enhancer Factors 2* (MEF2) und wurde zuvor als potentieller NRAP-Interaktionspartner identifiziert. Da angenommen wird, dass die NRAP-Expression durch MEF2 reguliert wird, wurden ventrikuläre HM neonataler Ratten (NRVMs) mit einem selektiven pharmakologischen PKD1-Inhibitor BPKDi und/oder dem pro-hypertrophen

Stimulus Phenylephrin (PE) behandelt. Die Quantifikation *de novo* translaterter Proteine mittels *Stable Isotope labeling by/with Amino Acids* nach Exposition mit BPKDi ergab eine verminderte NRAP-Expression und eine höhere Abundanz von Proteinen, die an proteasomalen, lysosomalen und spliceosomalen Signalwegen beteiligt sind. Zusätzlich konnte mittels Immunfluoreszenz gezeigt werden, dass BPKDi zu einer perinukleären, löchrigen NRAP-Mislokalisierung führte. Die zusätzliche PE-Stimulation führte zu einem Zerreißen der Myofilamente und einer NRAP-Akkumulation in diesen Bereichen sowie an den lateralen Zell-Zellverbindungen.

Insgesamt konnten zwei krankheitsrelevante humane Zellmodelle generiert werden, die die Untersuchung der phänotypischen und funktionellen Konsequenzen einer höheren oder geringeren NRAP-Proteinmenge erlaubten. Die Charakterisierung zeigte, dass sowohl eine höhere als auch eine reduzierte NRAP-Proteinmenge pathophysiologische Auswirkungen hat, eine Beobachtung, die durch die Proteomanalyse bestätigt wurde. Dabei zeigte insbesondere die NRAP-Überexpression einen ausgeprägteren pathophysiologischen Phänotyp, vor allem unter Zuständen mechanischer Überdehnung. Auf Expressions- und Lokalisationsebene konnte eine Regulation von NRAP durch PKD1 gezeigt werden, die Details der NRAP Regulation in Herzerkrankungen ist Thema momentaner Untersuchungen.

2. Abstract

Cardiomyopathies are one of the major causes of death worldwide. They have been linked to improper functioning of intercalated discs, a lateral microdomain, which connects cardiac myocytes electromechanically ascertaining unperturbed contractility. In experimental murine models of cardiomyopathy as well as in human disease, the intercalated disc-associated nebulin-related anchoring protein (NRAP) was shown to be up- or down-regulated. NRAP plays a crucial role during heart development, in *de novo* myofibril assembly and in mechanotransduction in the adult heart although its specific functions and mechanisms that regulate its expression remain unknown to date. Therefore, the aim was to investigate whether altered NRAP protein levels contribute to cardiac disease development and to analyse the underlying regulatory mechanisms.

NRAP-overexpressing (OE) and -knock-down (KD) human induced pluripotent stem cells (hiPSC) were generated by clustered regularly interspaced short palindromic repeats and CRISPR-associated protein 9 (CRISPR-Cas9) genome editing. To investigate the impact of NRAP gain- and loss-of-function, hiPSC were differentiated into cardiac myocytes and function assessed in 3D engineered heart tissues (EHTs). Characterisation of *NRAP*-OE in 2D cardiac myocytes resulted in enhanced NRAP translocation towards the lateral cell borders. In *NRAP*-KD cardiac myocytes, NRAP localised to the Z-discs similarly as in control cardiac myocytes. Assessment of contractile parameters in 3D-EHTs revealed lower force development and faster relaxation time in *NRAP*-KD and *NRAP*-OE EHTs compared to control EHTs. Upon increase of mechanical tension, *NRAP*-KD EHTs responded with higher force development. In contrast, *NRAP*-OE EHTs developed an arrhythmic beating behaviour during increasing stretch. *NRAP*-OE EHTs had a less negative take-off potential (TOP) and maximal diastolic potential (MDP) compared to control and *NRAP*-KD EHTs. Proteome analysis revealed especially for *NRAP*-OE EHTs enhanced representation of cardiomyopathy-related signaling pathways.

Additionally, underlying regulatory mechanisms of NRAP expression were investigated. Protein kinase D1 (PKD1) regulates myocyte enhancer factor 2 (MEF2)-mediated fetal and pro-hypertrophic gene expression and was identified as an interaction partner of NRAP. Since it has been assumed that NRAP expression is regulated by MEF2, neonatal rat ventricular myocytes (NRVMs) were exposed to the selective pharmacological PKD1 inhibitor BPKDi and/or the pro-hypertrophic stimulus phenylephrine (PE). Quantification of *de novo* translated proteins by stable isotope labeling by/with amino acids coupled mass spectrometry after exposure to BPKDi revealed decreased NRAP expression and

enhanced abundance of proteins involved in proteasomal, spliceosomal and lysosomal pathways. Further, immunofluorescence of NRVMs showed a perinuclear, punctate-appearing NRAP mislocalisation. Additional exposure to PE led to NRAP translocation to the lateral cell-cell borders. Combined exposure to BPKDi and PE prevented intercalated disc localisation of NRAP and instead induced a sarcomeric redistribution with disrupted sarcomeric structure.

Taken together, two hiPSC lines were developed that allowed to study the phenotypical and functional consequences of NRAP gain- and loss-of-function. Both, higher and lower NRAP protein levels resulted in a pathophysiological phenotype. This observation was confirmed by proteome analysis. In this context, especially *NRAP*-OE developed a more severe pathophysiological phenotype during conditions of enhanced mechanical stretch. NRAP expression and localisation was shown to be regulated by PKD1, however, the precise mechanisms of how NRAP expression is regulated in cardiac disease development is subject of ongoing investigations.

3. Introduction

Cardiovascular diseases are the most prevalent cause of mortality worldwide (Mathers et al. 2009; Rana et al. 2021). Among those diseases, heart failure is one of the predominant reasons for death. This disease is associated with impaired cardiac inotropic and lusitropic function and might ultimately lead to sudden cardiac death if the heart fails to ensure the appropriate equilibrium between sufficient cardiac output and nutrient and oxygen supply of the periphery (McNally et al. 2015).

3.1 Mechanisms of cardiac contraction and relaxation

The heart consists of different cell types including 30% cardiac myocytes and 70% non-cardiac myocytes (Nag 1980; Pinto et al. 2016a). The non-cardiac myocytes mainly include endothelial cells, fibroblasts, smooth muscle cells, macrophages and other leukocytes (Pinto et al. 2016a; Zaman et al. 2021; Zhou and Pu 2016). The cardiac myocytes ensure proper functioning during the contraction-relaxation cycle (Pinto et al. 2016a).

3.1.1 Cardiac myocytes

In the left murine ventricle, only 15% of cells were identified as cardiac myocytes forming 90% of the muscular mass in the left ventricle (Reiss et al. 1996; Soonpaa et al. 1996). Immature neonatal cardiac myocytes are still able to divide, however adult cardiac myocytes have only a limited capacity of approximately 1% regeneration per year (Bergmann et al. 2009). In the adult heart, cardiac myocytes are organised in a parallel manner with a complex cytoarchitecture to form a functional syncytium and ensure the contractility of the heart tissue (Ehler 2016). However, in case of cardiac damage, the necrotic tissue is replaced by fibrotic tissue which might impact cardiac function. Cardiac myocytes mainly consist of mitochondria to comply with the high energy demand and parallel aligned myofibrils that constitute the contractile machinery and utilise the produced energy for proper contraction-relaxation cycles (Barth et al. 1992; Ehler 2016).

3.1.2 Myofibrils

Myofibrils are highly organised structures formed by many repeating, contractile subunits that are termed sarcomeres (**Figure 1**). Sarcomeres are defined as the area between Z-discs and mainly consist of filamentous actin (F-actin), tropomyosin, a troponin complex, titin and thick myosin filaments (Ahmed et al. 2022). The Z-disc crosslinks the F-actin by α -actinin (Luther 2009; Takahashi and Hattori 1989). Within the anisotropic (A)-band region of the sarcomere, the thin actin filaments interact with the thick myosin filaments

that are anchored to a structure in the centre of the sarcomere termed M-band (**Figure 1**) (Lange et al. 2020). At this structure, thick filaments are linked to the elastic filament system composed of titin that stretches from the M-band to Z-discs and is crucial for the development of myofibrils (Lange et al. 2020; Trinick et al. 1984). The area close to the Z-discs, which contains only F-actin but not myosin, is defined as the isotropic (I)-band. The thin actin filaments reach from Z-discs to M-bands (Pappas et al. 2010; Wang and Williamson 1980). For stabilisation purposes, parallel arranged Z-discs are connected by the intermediate filament desmin to costameres at the muscle membrane (Frank and Frey 2011).

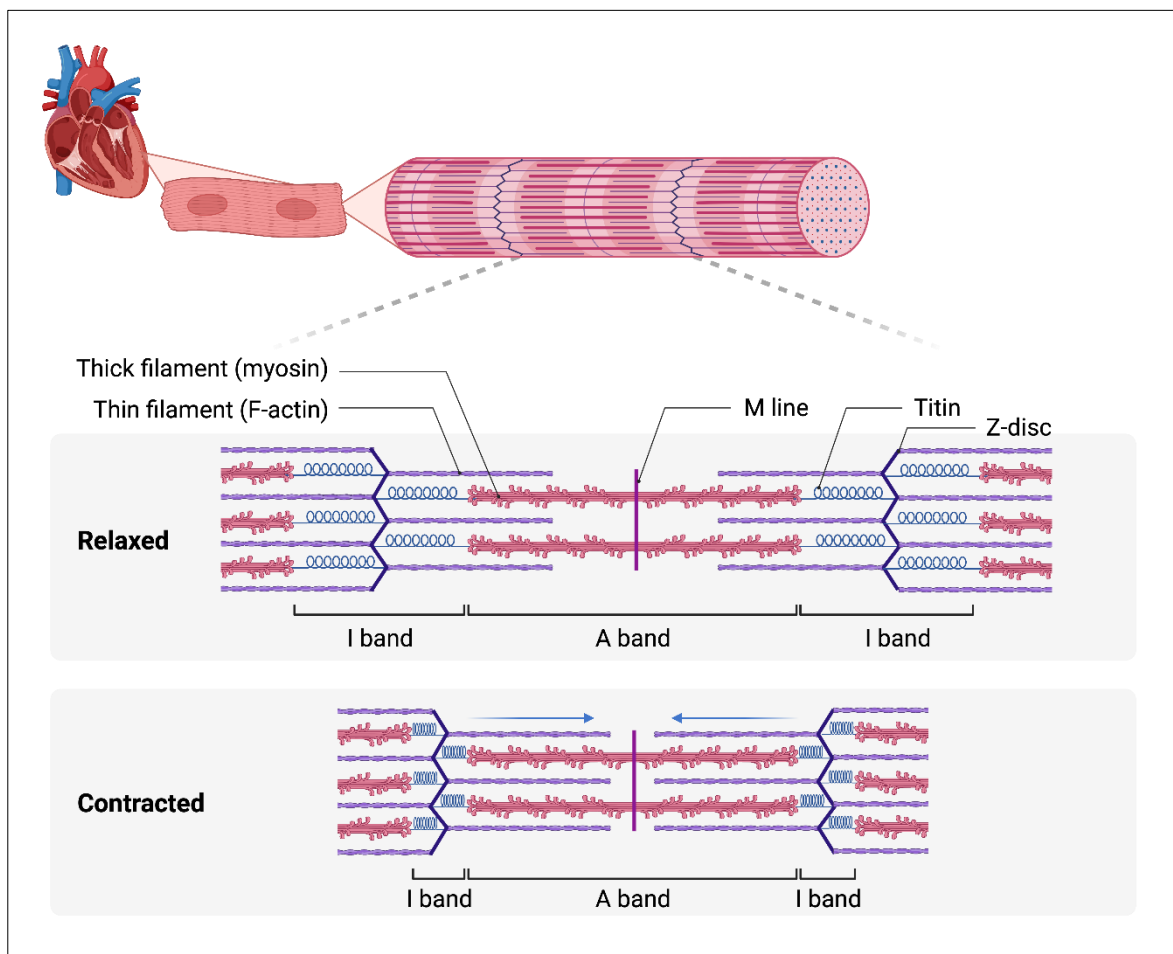


Figure 1: Contractile machinery of cardiac cells. Schematic overview of hierarchical structures in cardiac myocytes. Contractile elements of cardiac myocytes consist of myofibrils, which in turn are subdivided into sarcomeres that are bordered laterally by Z-discs. Sarcomeres enable the contraction and relaxation of cardiac myocytes by ATP-dependent interaction between the thick filament (myosin) and the thin filament (F-actin). Myosin is anchored at the M-band by myomesin, while F-actin is cross-linked at Z-discs with the main Z-disc component α -actinin. Titin stretches from the M-band to the Z-discs. The A-band corresponds to the overlap between thin and thick filaments and the I-band corresponds to the area with only thin filaments. The illustration was generated with BioRender and modified from (Ahmed et al. 2022).

3.1.2.1 Actin and myosin interaction

For the contraction of cardiac myocytes, the thin actin filament interacts with the thick myosin filaments (Huxley and Niedergerke 1954; Huxley and Hanson 1954). Upon release of an action potential from pacemaker cells in the sinoatrial (SA) node, the depolarisation wave is transmitted via the atrioventricular (AV) node to the ventricles. The signal is conducted to transverse (T)-tubules where voltage-operated L-type calcium channels release calcium into the cytosol of cardiac myocytes (Donald and Lakatta 2023; Mackrill 2022). The increase in cytosolic calcium induces calcium binding to ryanodine receptors at the sarcoplasmic reticulum which then induces a calcium-induced calcium release into the cytosol. This induces the binding of calcium to the cardiac troponin C-tropomyosin complex, thus leading to the removal of tropomyosin from the actin binding site and initiating the binding of myosin heads to actin (Fabiato and Fabiato 1978; Wang and Raunser 2023). ATP binds to myosin and is hydrolysed into ADP and phosphate which cause the formation of a cross-bridge with binding of myosin heads to a new position on F-actin. By release of the hydrolysed phosphate, myosin heads change their conformation to perform a power stroke and induce contraction by moving actin filaments closer to the M-band of the sarcomere (Squire 2019). For relaxation, ADP is released and ATP binds to the myosin head leading to the detachment of myosin heads from actin filaments (Wang and Raunser 2023). The removal of cytosolic calcium occurs by reuptake into the sarcoplasmic reticulum (SR) via the sarco(endo)plasmic reticulum calcium-ATPase (SERCA), or the plasma membrane-associated ATPase (PMCA) pump or the sodium-calcium exchanger (NCX; Kuo and Ehrlich 2015). The reduction of calcium concentration leads to blocking of the actin binding site by tropomyosin, thus preventing further binding of myosin and inducing relaxation of myofibrils (Wang and Raunser 2023).

3.1.2.2 Myofibrillogenesis

Embryonic and postnatal myofibrils are assembled in a process termed myofibrillogenesis. This process is still not completely understood but it was previously postulated to occur in a premyofibril model starting initially with the formation of premyofibrils, followed by progression to nascent myofibrils until finally mature myofibrils are formed (**Figure 2**; Rhee et al. 1994). The development of Z-discs starts as Z-bodies, composed of α -actinin and actin, in close proximity to the sarcolemma (Firket 1967; Rhee et al. 1994; Sanger et al. 2017). The proteins integrin, talin and vinculin are incorporated into the membrane, forming protocostameres (**Figure 2 A**; Humphries et al. 2007; Tokuyasu 1989; Volk et al. 1990).

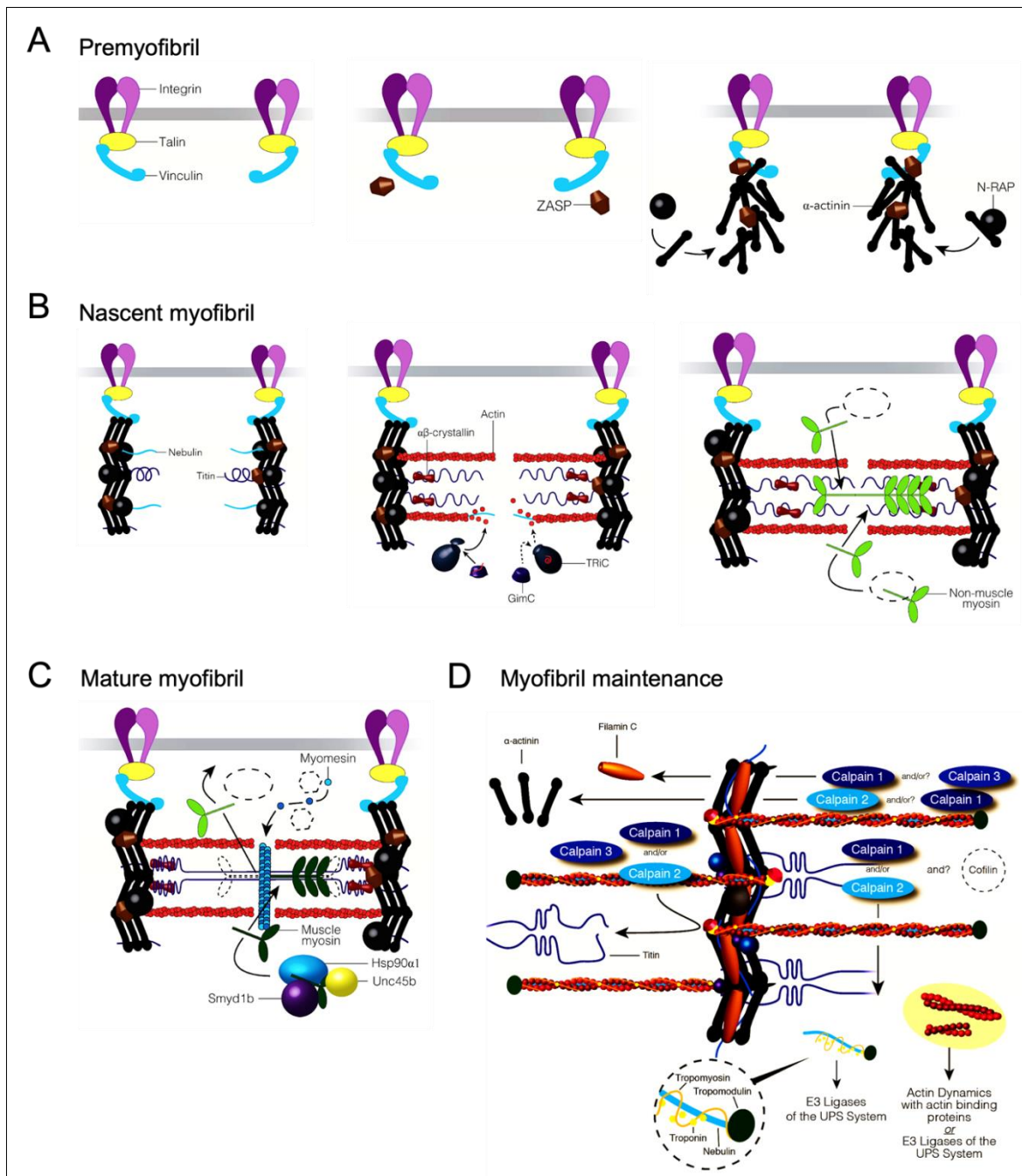


Figure 2: Myofibril assembly and maintenance. **A-C)** Premyofibril model, distinguished between **A)** premyofibrils, **B)** nascent myofibrils and **C)** mature myofibrils. **A)** Talin and vinculin are recruited to the membrane to form protocostameres. The Z-disc alternatively spliced PDZ-motif protein (ZASP) recruits α -actinin and the nebulin-related anchoring protein (NRAP) for folding of actin. **B)** Nebulin and titin are recruited to Z-discs and extend to the centre of sarcomeres, thus increasing the sarcomere length. The folding of actin is mediated by prefoldin (GimC) and TCP-1 ring complex (TRiC). In nascent myofibrils non-muscle myosin is incorporated. **C)** Formation of thick filaments by replacement of the non-muscle myosin by muscle myosin II. The M-band assembles by incorporation of myomesin and myosin heavy chain. **D)** Calpain-mediated clearance and ubiquitin turnover of dysfunctional proteins from myofibrils. Proteins are released from the sarcomeres by calpain 1, 2 and 3 and targeted by the ubiquitin system for proteasomal degradation by the muscle RING finger protein (MuRF) 1, 2 or 3. The image was modified from (Carlisle et al. 2017; Prill and Dawson 2020).

Z-disc alternatively spliced PDZ-motif protein (ZASP) localises to this structure to recruit filamin and α -actinin through its chaperone, the nebulin-related anchoring protein (NRAP), which is suggested to act as a scaffolding protein for actin filament assembly (Carroll et al. 2004; Jani and Schöck 2007; Lu and Horowitz 2008; Manisastri et al. 2009). Non-muscle myosin II is incorporated in premyofibrils that is thought to support protein folding. During maturation to nascent myofibrils, muscle myosin II, titin and nebulin are recruited to the premyofibrils (**Figure 2 B**; Wang et al. 2022). At this stage, nebulin and CapZ form an initial pro-I-band and link to Z-discs (Chu et al. 2016; Moncman and Wang 1996; Schafer et al. 1995). In the heart, it is discussed whether nebulin is generally replaced by the shorter cardiac-specific homologue nebulette. Similar to nebulin, nebulette contains a C-terminal SH3 domain with localisation at the ends of thin filaments at the Z-discs where it interacts with actin, α -actinin 2 and tropomyosin (Moncman and Wang 1999). For the formation of thin filaments, prefoldin (GimC) and TCP-1 ring complex (TRiC) support actin folding and orientation along the nebulin scaffold (Berger et al. 2018). The elongation of actin filaments occurs by leiomodin 2 (Chereau et al. 2008). In the last step towards mature myofibrils, muscle myosin II aligns into A-bands and the protein myomesin cross-link and stabilise thick filaments at the M-band (**Figure 2 C**; Carlisle et al. 2017). Indeed, degradation of non-muscle myosin and replacement by muscle myosin II is a prerequisite to form mature myofibrils.

During maturation of cardiac myocytes, transcriptional, structural and metabolic alterations occur. While myofibrils mature, sarcomeres are added laterally and longitudinally to existing myofibrils and some sarcomere proteins undergo a switch from fetal to adult isoforms (Beisaw and Wu 2022). For example, the predominant troponin isoform in fetal murine and human hearts is the skeletal troponin I isoform and it has been shown to switch to cardiac troponin I in the adult heart (Sasse et al. 1993; Siedner et al. 2003). In addition, titin has been identified to be subject of alternative splicing, resulting in different isoforms that switch during the maturation process from the postnatal to the adult heart (Granzier and Labeit 2004; Lahmers et al. 2004). The switch in the titin isoform from N2BA to the shorter isoform N2B leads to increased stiffness, suggesting a balance between the isoforms to be involved in passive tension regulation in the sarcomere (Opitz et al. 2004).

3.1.2.3 Myofibril maintenance and turnover

In order to maintain the functional integrity of myofibrils, specific factors (e.g. chaperones, structural proteins) and mechanisms that degrade non-functional proteins are necessary (**Figure 2 D**; Carlisle et al. 2017). Degradation of proteins for the maintenance of the thin actin filament occur via two pathways, the autophagy or the ubiquitine-proteasome system

(UPS). The major pathway in myofilament maintenance and turnover is UPS-mediated degradation which first requires isolation of targeted proteins from the myofibrils by calpains (**Figure 2 D**; Ono and Sorimachi 2012; Portbury et al. 2011). It has been shown that calpains 1 and 2 target F-actin by cleavage of troponin T, troponin I and tropomodulin (Di Lisa et al. 1995; Gokhin et al. 2014). However, this cleavage can be regulated by protein phosphorylations. For example, phosphorylation of troponin I by cyclic AMP-dependent protein kinase A (PKA) decreases troponin I cleavage by calpain 1. In contrast, phosphorylation by protein kinase C (PKC) increases troponin I cleavage at the myofilaments (Di Lisa et al. 1995).

Subsequently, degradation of the cleaved non-functional proteins from the sarcomeres is mediated by the UPS or autophagy pathways. The UPS system consists of three ubiquitin ligases, E1, E2 and E3. Non-functional proteins are first detected by E3 ubiquitin ligases (MuRFs), they are then ubiquitinated by E1 and E2 ligases and this is followed by proteasomal degradation (Carlisle et al. 2017; Wang et al. 2020). Myofilament-associated proteins such as nebulin, troponin T and I, titin, myotilin, myosin light chain 2, telethonin and NRAP have been identified as ubiquitination targets of MuRF1 and MuRF2 (Witt et al. 2005). If refolding of misfolded proteins or proteasomal degradation is not possible, protein aggregates are formed. These protein aggregates are targeted and incorporated by the autophagy-lysosomal pathway into autophagosomes from membrane-enclosed vesicles (Henning and Brundel 2017). Proteins and protein aggregates that are targeted for autophagy contain a K63- or K48-ubiquitination tag which is recognised by adapter proteins that enable the transfer to the autophagosome (Johansen and Lamark 2011; Willis et al. 2010). Moreover, protein aggregates can be linked to ubiquitinated proteins or autophagosomal marker proteins, such as BAG3, that only mediate autophagosomal degradation without being self-degraded (Carra et al. 2008; Gamerding et al. 2009). Lysosome hydrolases recycle protein aggregates after fusion of the autophagosome to lysosomes.

Once the sarcomeres are assembled, they are continuously exposed to mechanical and oxidative stress. To avoid proteotoxicity and ensure proper maturation, the degradation of misfolded proteins or protein aggregates is required for the maturation and functional maintenance of myofibrils (Martin and Kirk 2020).

3.1.3 Intercalated discs

During cardiac myocyte maturation, cell-cell junctions relocate to the lateral borders and anchor myofibrils at the lateral ends of cardiac myocytes (Carroll and Horowitz 2000). These cell-cell junctions are termed intercalated discs. Intercalated discs are micro-

domains at the lateral borders between neighbouring cardiac myocytes ensuring the electromechanical coupling for proper heart functioning as a functional syncytium (**Figure 3**; Ehler 2016; Saphir and Karsner 1924).

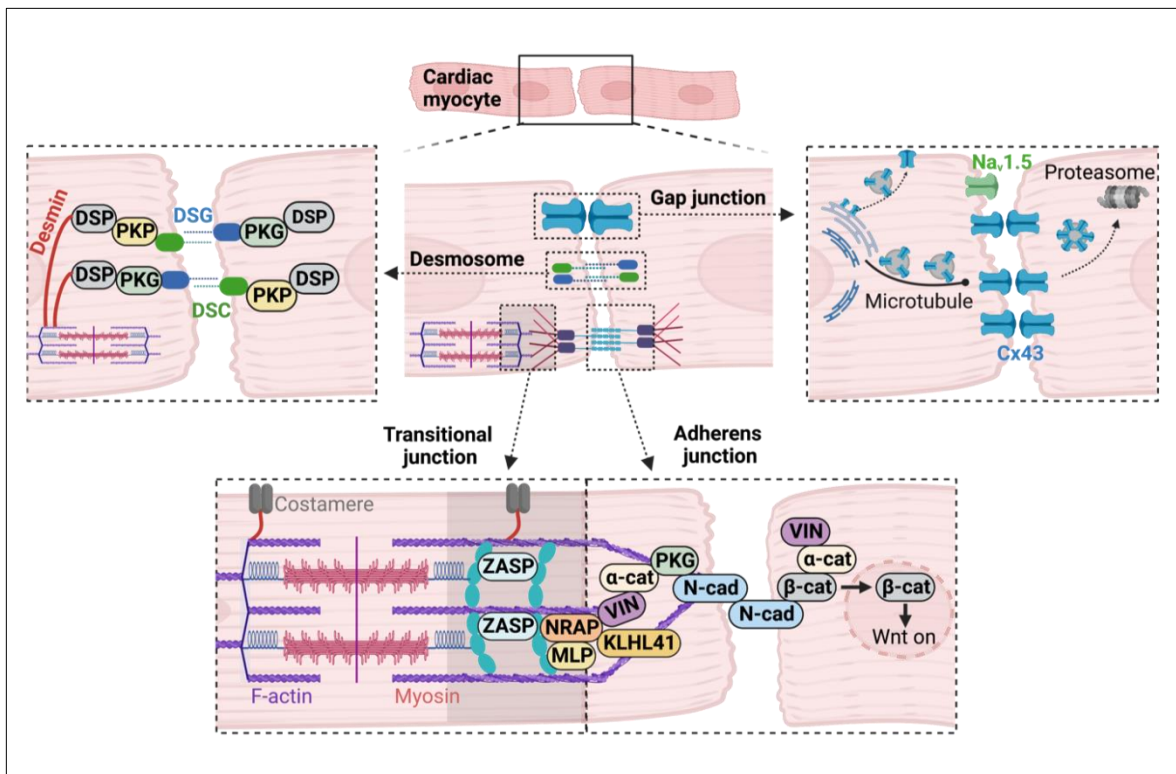


Figure 3: Intercalated disc microdomain. Schematic representation of cell-cell connection mainly composed of gap junctions, desmosomes and adherens junctions. In addition, the transitional junction involved in mechanotransduction, is depicted. Gap junctions consist of two hemichannels from adjacent cardiac myocytes. Hemichannels in the left ventricle are mainly formed by connexin 43 (Cx43). Cx43 is transported in vesicles from the trans-Golgi network to the sarcolemma by microtubules. The degradation of gap junctions occurs by the proteasome system. Desmosomes connect cells via the cadherin system of desmoglein (DSG) and desmocollin (DSC). Plakoglobin (PKG) and desmoplakin (DSP) are bounded to the desmosomal cadherin system. In addition, the intermediate filament desmin connects the filamentous (F-) actin to desmosomes. Adherens junctions connect cells via N-cadherin (N-cad) that binds to PKG and β-catenin (β-cat). β-cat shuttles into the nucleus to activate the wiggless-related integration site (Wnt) canonical pathway and further binds to α-catenin (α-cat) and vinculin (VIN). In close proximity to the intercalated disc, the transitional junction is located that replaces the last Z-discs of the sarcomere and connects it to costameres and adherens junctions. This complex is characterised by the presence of the Z-disc alternatively spliced PDZ-motif protein (ZASP), α-actinin (turquoise) and the nebulin-related anchoring protein (NRAP). NRAP binds to the muscle Lin-11, Isl-1, and Mec-3 (LIM) protein (MLP) and the kelch-like protein 41 (KLHL41). The illustration was generated with BioRender and modified from (Bennett et al. 2006; Lyon et al. 2015; Nielsen et al. 2023).

This compartment ensures the propagation of electrical signals between neighbouring cardiac myocytes for appropriate contraction of the myocardium and maintains the structural integrity of cardiac myocytes during exposure to tremendous mechanical forces during heart contraction (Ehler 2016). The intercalated disc is distinguished by three main

complexes: Gap junctions, desmosomes and adherens junctions. In addition, ion channels in close proximity to the intercalated disc as well as transitional junctions that are not directly involved in the intercellular connection between adjacent cardiac myocytes are considered to contribute to the intercalated disc function (Bennett et al. 2006; Delmar and McKenna 2010).

3.1.3.1 Gap junctions

Gap junctions ensure the intercellular ion transfer for unperturbed synchronisation of contraction (Epifantseva and Shaw 2018). This occurs by passive diffusion of molecules that are smaller than 1 kDa, for example metabolites, ions or microRNAs (Elfgang et al. 1995; Zong et al. 2016). Gap junctions consist of 12 connexins, mainly connexin 43 in ventricular cardiac myocytes, which form two hemichannels/connexons (Makowski et al. 1977; Vozzi et al. 1999). The hemichannels are located in the plasma membrane of neighbouring cardiac myocytes and are intercellularly anchored to ensure the transmission of electrical and metabolic signals between adjacent cells (**Figure 3**). Since gap junctions are transient structures with a half-life of approximately 2 h (Rhett et al. 2011), vesicles from the Golgi network transport connexin 43 to the intercalated disc via microtubules that are concomitantly anchored to adherens junctions. Moreover, different proteins that are involved in electrochemical conduction between cells, such as the voltage-gated Na⁺ channel, Nav1.5, are localised at the intercalated disc (Maier et al. 2004; Veeraraghavan et al. 2015).

3.1.3.2 Adherens junctions

Adherens junctions and desmosomes are both connected to the cytoskeleton and thus involved in mechanical stabilisation. Previously, it has been shown that these structures crosstalk with each other and form a mixed-type junctional complex known as *area composita* (Borrmann et al. 2006). Both adherens junctions and desmosomes share common proteins such as plakoglobin (PKG), p120 and plakophilin-2 (PKP-2; Borrmann et al. 2006). PKG has been shown to have a higher affinity to desmosomes, suggesting it is mainly a component of the desmosomal junction (Choi et al. 2009).

Adherens junctions ensure cardiac myocytes strength upon exposure to mechanical stress during contraction. For this reason, their main function includes anchoring myofibrils and connecting actin filaments of neighbouring cardiac myocytes (Bays et al. 2014). The main component of adherens junctions is the transmembrane protein N-cadherin that interacts with the same cadherins from neighbouring cardiac myocytes to form homodimers (**Figure 3**; Volk and Geiger 1984). The cytosolic C-terminus of N-cadherin interacts with β -catenin that connects the adherens junctions with actin filaments

through vinculin and α -catenin (Vermij et al. 2017). Moreover, β -catenin is involved in cadherin-mediated signalling by shuttling into the nucleus and activating the wingless-related integration site (Wnt) canonical pathway. The latter plays a role in cardiac development and cardiac disease development (Vermij et al. 2017). Alternatively to β -catenin, PKG and α -actinin or p120 catenin can link actin filaments to N-cadherin (Nielsen et al. 2023). The p120 catenin links the adherens junctions, by binding to the two proteins PLEKHA7 and Nezha, to the minus end of microtubules (Nielsen et al. 2023; Shaw et al. 2007).

3.1.3.3 Desmosomes

Desmosomes ensure the mechanical stability of cardiac myocytes by integrating resilient intermediate filaments into the intercalated disc (Green et al. 2019). Between adjacent cardiac myocytes, the cadherins desmoglein-2 (DSG) and desmocollin-2 (DSC) form the intercellular connection (**Figure 3**; Zhao et al. 2019). Intracellularly, these cadherins are linked to the intermediate filament desmin by the adapter proteins PKG, PKP-2 and desmoplakin. The N-terminal region of desmoplakin binds to PKG and PKP-2 ensuring the connection to the desmosome while its C-terminal region links the desmosome to desmin (Zhao et al. 2019). PKP-2 interacts with the sodium channel-anchoring protein ankyrin-G and connexin 43, linking desmosomal proteins to gap junctions (Sato et al. 2011).

3.1.4 Transitional junctions

The structure that enables the connection between myofibrils and intercalated disc is termed transitional junctions (**Figure 3**). The transitional junction replaces the last Z-disc of the sarcomere in the closest proximity to the intercalated disc (Bennett et al. 2006). The actin filaments integrate in this structure and reach out further to adherens junctions for anchorage and transmission of force. This compartment is characterised by folded membranes that contain high amounts of spectrin and vesicles of the sarcoplasmic reticulum (Bennett et al. 2016). The transitional junction harbours only a few proteins that are concomitantly involved in Z-disc composition such as titin, α -actinin and ZASP (Vermij et al. 2017). Titin ensures sarcomeric integrity and stabilisation, suggesting that the transitional junction serves as a site for sarcomere assembly and Z-disc/SR/T-tubule complex (Bennett 2012). In addition, the non-myofibrillar protein NRAP, which was identified to be distributed throughout the intercalated disc in adult cardiac myocytes (Lu et al. 2005), mainly accumulates at transitional junctions in combination with α -actinin (Bennett et al. 2006).

3.1.5 Nebulin-related anchoring protein

NRAP is a multidomain protein expressed at myotendinous junctions in skeletal muscle or intercalated discs in the heart (Lu et al. 2008; Luo et al. 1997). The *NRAP* gene is located on chromosome 10q25.3 of the human genome and encodes for 1731 amino acids from 42 exons. There are four known NRAP isoforms that differ in missing exon 12 in isoform 1 and missing exon 23 in isoform 4, while isoform 3 contains one additional amino acid encoded from exon 42 (Gehmlich et al. 2004; Mohiddin et al. 2003). Therefore, the molecular weight for NRAP isoforms ranges between 192.9 and 197.1 kDa.

The N-terminus of *NRAP* contains a Lin-11, Isl-1, and Mec-3 (LIM) domain (Mohiddin et al. 2003). The LIM domain covers the first two exons and the first codon of exon 3. The remaining parts of exon 3 include a linker region. This is followed by 11 simple repeats in exon 4-14 and five super repeats, each consisting of seven repeats in exon 15-41. The repeats deriving from exon 4-41 are approximately 40% homologous to those of nebulin (Mohiddin et al. 2003).

Although the function of NRAP is still not completely unravelled, it has been shown that NRAP plays a crucial role in myofibrillogenesis as it is one of the earliest appearing proteins involved in newly formed sarcomeres (Manisastry et al. 2009; Pervolaraki et al. 2018). In addition, an emerging role of NRAP in mechanotransduction was suggested since NRAP was co-purified both with adherens junction and myofilament fractions (Zhang et al. 2001). Moreover, NRAP contains a C-terminal actin binding domain and its LIM domain has recently been shown to impact mechanotransduction (Anderson et al. 2021; Zhang et al. 2001). Previous studies showed the interaction of NRAP with different proteins involved both in intercalated disc signaling and myofibril stability. Regarding the LIM domain and single repeat domain of NRAP, binding sites of the Z-disc protein α -actinin, talin and the muscle LIM protein (MLP) were identified (Ehler et al. 2001; Lu et al. 2003; Luo et al. 1999). In the single repeat and super repeat domains of NRAP, the binding of sarcosin was detected (Lu et al. 2003). Moreover, filamin, KLHL41 and vinculin bind to the super repeat domain of NRAP (Jirka et al. 2019; Lu et al. 2003; Luo et al. 1999). Due to this interaction with both intercalated disc proteins and Z-disc proteins, NRAP was associated with cardiac muscle mechanotransduction.

3.1.6 Mechanotransduction

During the contraction and relaxation of cardiac myocytes, it is required that cells sense and respond to high and varying mechanical forces as a compensatory mechanism in a process termed mechanotransduction (Lyon et al. 2015). During this process, the

mechanical load is transduced into electrochemical signals that activate a plethora of biological signalling pathways (Wang et al. 2009).

Costameres serve as anchoring sites for the Z-discs in the sarcolemma and transduce mechanical tensions from myofibrils to the extracellular matrix (Ahmed et al. 2022). This submembranous structure consists of a dystrophin-glycoprotein complex and a vinculin-talin-integrin complex localised in the I-band region of sarcomeres (Anastasi et al. 2009). Mechanical force transmission mainly occurs via the intermediate filament desmin (Ahmed et al. 2022; Paulin and Li 2004). In addition, desmin links Z-discs to other subcellular compartments such as mitochondria and the nucleus (Milner et al. 2000).

Previous studies showed that LIM proteins are involved in mechanotransduction pathways and mediate the assembly of stress fibres (Kadrmaz and Beckerle 2004; Smith et al. 2014). LIM proteins mediate protein-protein or protein-DNA interactions by representing a dual zinc-finger motif functioning as a protein-binding interface (Feuerstein et al. 1994; Schmeichel and Beckerle 1994). Most of the LIM proteins were thought to either participate in biological processes related to the cytoskeletal function or in the control of gene expression. However, increasing numbers of LIM proteins have been identified shuttling between the cytoplasm and the nucleus (Wang et al. 2009).

Conclusively, dysfunctional mechanotransduction mediated by sarcomeres, intercalated discs and the sarcolemma can result in pathophysiological conditions and thus in the transition to heart failure (Lyon et al. 2015).

3.2 Cardiac disease

3.2.1 Cardiomyopathies

Heart failure is often preceded by sporadic or inherited heart muscle diseases that are termed cardiomyopathies (Ommen et al. 2020). Cardiomyopathies are characterised by impairment of mechanical or electrical properties of the heart (Maron et al. 2006). The mechanical properties include dysfunctional systole and diastole while the electrical properties refer to arrhythmogenesis (Maron et al. 2006). The most common types of cardiomyopathies are hypertrophic (HCM), dilated (DCM), arrhythmogenic right ventricular (ARVC) and restrictive (RCM) cardiomyopathies.

3.2.1.1 Hypertrophic cardiomyopathy

The most common type of cardiomyopathy is HCM with an estimated clinical prevalence of 1:200-1:500 worldwide. This includes a wide range of different countries, ages and both genders with a large genetic diversity and characteristic clinical phenotypes (Maron 2018).

HCM is frequently inherited and in 40-60% of the cases it is caused by dominant variants of genes (*ACTC1*, *MYBPC3*, *MYH7*, *MYL2*, *MYL3*, *TNNI3*, *TNNT2*, and *TPM1*) that encode for pathogenic sarcomeric proteins with highest prevalence of pathogenic variants in *MYBPC3* and *MYH7* (Alfares et al. 2015; Elliott et al. 2014; Maron et al. 2022).

Clinical phenotypes of HCM are heterogeneous, ranging from asymptomatic to different severities in symptomatic patients (Braunwald et al. 1960; Wigle et al. 1962). The major pathophysiological symptoms include dysfunctional systole or diastole, cardiac arrhythmias and insufficient balance between oxygen supply and demand of the periphery (Ciarambino et al. 2021; Marian and Braunwald 2017; Wigle et al. 1962). On the physiological level, HCM is characterised by left ventricular hypertrophy with left ventricular wall thickness defined as >15 mm in adults and thickening of the interstitial septum (Elliott et al. 2014). On a histological level, the disease is identified by enlarged cardiac myocytes with a loss of parallel alignment, myofibrillar disarray and fibrosis of the myocardium (Marian and Braunwald 2017).

3.2.1.2 Dilated cardiomyopathy

In contrast to HCM, DCM affects all four heart chambers, frequently starting in the left ventricle. The ventricles are characterised by enlargement and decrease in ventricular wall thickness referring to the term dilation. This alteration leads to a decrease of the left ventricular ejection fraction between 45% and 50% and thereby consequently to systolic dysfunction without any other explanation for abnormal loading such as hypertension (Pinto et al. 2016b). On the cellular level, cardiac myocytes are arranged in parallel, but areas of necrosis and fibrosis can be observed (Pluess et al. 2015).

The estimated prevalence for DCM is 1:2500 but DCM accounts for the third most common reason for heart failure and is a leading cause of heart transplantation (Maron et al. 2006). However, compared to HCM, DCM is not predominantly caused by genetic mutations. Only 35% of cases involve mutations in genes encoding for sarcomere, cytoskeletal or nuclear envelope proteins (Weintraub et al. 2017). While the underlying genetic mutations mostly derive from only a few genes, genetic mutations in DCM are more heterogeneous involving more than 50 related genes (McNally et al. 2015). However, it was shown that 25% of idiopathic DCM cases and 18% of sporadic DCM cases are caused by mutations in the gene encoding for titin (Herman et al. 2012). Other reasons are bacterial or viral infection resulting in myocarditis, autoimmune diseases, exposure to drugs and toxins or diseases related to metabolic impairment (Weintraub et al. 2017).

3.2.1.3 Arrhythmogenic right ventricular cardiomyopathy

ARVC predominantly affects the right ventricle and is characterised by the loss of cardiac myocytes accompanied by replacement with fatty and fibrofatty tissue (Basso et al. 1996). In 75% of patients affected by ARVC, additional fibrofatty replacement in the left ventricle, chamber enlargement and myocarditis have been reported (Maron et al. 2006). Clinical phenotypes are characterised by ventricular tachyarrhythmias (Marrone et al. 2019). ARVC is often autosomal-dominant inherited with mutations in genes encoding proteins for the desmosomal compartment such as DSP, PKG, DSC2, DSG2 or PKP (Ciarambino et al. 2021).

3.2.1.4 Restrictive cardiomyopathy

Regarding the major types of cardiomyopathies, RCM is rather a scarce form accounting for 2-5% of cardiomyopathies (Ciarambino et al. 2021). The disease has heterogeneous origins of sporadic or inherited predispositions including cardiac amyloidosis, storage diseases and endomyocardial diseases (Bang et al. 2022). Associated RCM mutations are autosomal-dominant inherited and affect genes encoding the sarcomere proteins cTnT, troponin I (cTnI), α -actin, and β -MHC (Muchtar et al. 2017). The RCM disease phenotype is characterised by decreased ability of the ventricular chamber, without impairment of left ventricular wall thickness or systolic function and enlarged atria (Maron et al. 2006). Pathophysiologically, RCM is characterised by myocardial stiffness accompanied by dysfunctional diastole, arrhythmias and altered conduction (Ciarambino et al. 2021).

3.2.2 Intercalated discs in disease

The contraction of the heart requires a functional electromechanical coupling between adjacent cardiac myocytes to conduct electrochemical signals and synchronous contraction. As the propagation of electrochemical stimuli throughout the heart occurs via the intercalated discs, mutations or dysfunction of intercalated disc proteins cause a variety of heart diseases (Zhao et al. 2019).

Recent reports identified that approximately 30-50% of ARVC patients carry a mutation in desmosomal proteins (Marcus et al. 2013). These mainly originate from mutations in five different genes encoding the desmosomal proteins PKP-2, DSG-2, DSC-2, DSP and junctional PKG (Broussard et al. 2015; Calore et al. 2015; Rampazzo et al. 2014). Mutations in PKP-2 were shown to impair protein stability leading to calpain-dependent degradation and causing decreased PKP-2 protein levels (Kirchner et al. 2012; Rasmussen et al. 2014). Mutations in the cadherin protein DSG-2 impaired dimerisation at the intercalated disc, altered its own posttranslational modifications or the phosphorylation of the gap

junctional protein connexin 43 (Chen et al. 2012; Gehmlich et al. 2010; Gehmlich et al. 2012). In addition, a 2 bp deletion in PKG (2157-2158del GT) was shown to interrupt binding to other desmosomal proteins and, similarly to other desmosomal mutations, results in loss of connexin 43, thus impairing electrical coupling (Kaplan et al. 2004). This might be responsible for the arrhythmic phenotype observed in patients.

In addition, in left ventricular heart samples of DCM patients, different proteins of the intercalated disc and costameres were affected, indicating an important role of the intercalated disc in proper electromechanical functioning of the heart (Ortega et al. 2017). Recently, disorganised intercalated discs with reduced staining of the adherens junction protein N-cadherin were observed in heart biopsies of DCM patients (Ito et al. 2021). However, in two DCM mouse models, the *MLP*-knock-out (KO) and the tropomodulin-overexpressing transgenic (TOT) mouse, increased protein expression of proteins related to adherens junctions or the anchorage of myofilaments was detected (Ehler et al. 2001). This included upregulation of N-cad, α - and β -cat, PKG, VIN and NRAP.

Moreover, in the *MLP*-KO mouse model, as well as in DCM patients with reduced MLP protein levels, protein kinase C α (PKC α) accumulated at the intercalated discs (Lange et al. 2016). Increased MLP protein levels were associated with decreased PKC α autophosphorylation while MLP phosphorylation by PKC α was decreased in HCM and increased in DCM revealing MLP simultaneously as an inhibitor and substrate of PKC α (Lange et al. 2016). This suggests a potential regulatory role of protein kinases at the intercalated discs in the progression of cardiomyopathies.

A downstream kinase of PKC that has been associated with hypertrophic conditions, is the serine/threonine protein kinase D (PKD) which was shown to regulate gene expression, intracellular trafficking, cardiac contraction and phosphorylation of proteins (**Figure 4**; Avkiran et al. 2008; Bossuyt et al. 2011; Rozengurt 2011). Although PKD comprises three isoforms with high homology in the regulatory and catalytic domain, the major isoform in the heart is PKD1 (Simsek Papur et al. 2018). In heart failure, PKD1 is upregulated and involved in hypertrophy signalling, while cardiac-specific inhibition of PKD1 in mice resulted in cardiac improvement accompanied by reduction of hypertrophy and arrhythmias (Bossuyt et al. 2022; Fielitz et al. 2008).

Upon (patho)physiological stimulation, PKD1 is activated via G-protein coupled receptor stimulation (Rey et al. 2001b). Cytosolic PKD1 binds to diacylglycerol (DAG) which induces PKD1 translocation to the plasma membrane (**Figure 4**; Rey et al. 2001b; Zugaza et al. 1996). At the plasma membrane, PKD1 is phosphorylated by PKC isoforms at

Ser744/748 in rodents or at Ser738/742 in humans, followed by autophosphorylation at Ser916 in rodents and Ser910 in humans (Iglesias et al. 1998; Rybin et al. 2009; Simsek Papur et al. 2018; Waldron et al. 2001). Consequently, this leads to full kinase activation and redistribution into the cytosol and the nucleus (Rey et al. 2001a). In the nucleus, PKD1 phosphorylates class II histone deacetylases (HDAC) resulting in their export into the cytosol and a derepression of the HDAC-mediated myocyte enhancer factor 2 (MEF2)-dependent fetal and pro-hypertrophic gene transcription (**Figure 4**; McKinsey et al. 2002; Vega et al. 2004; Zhang et al. 2002).

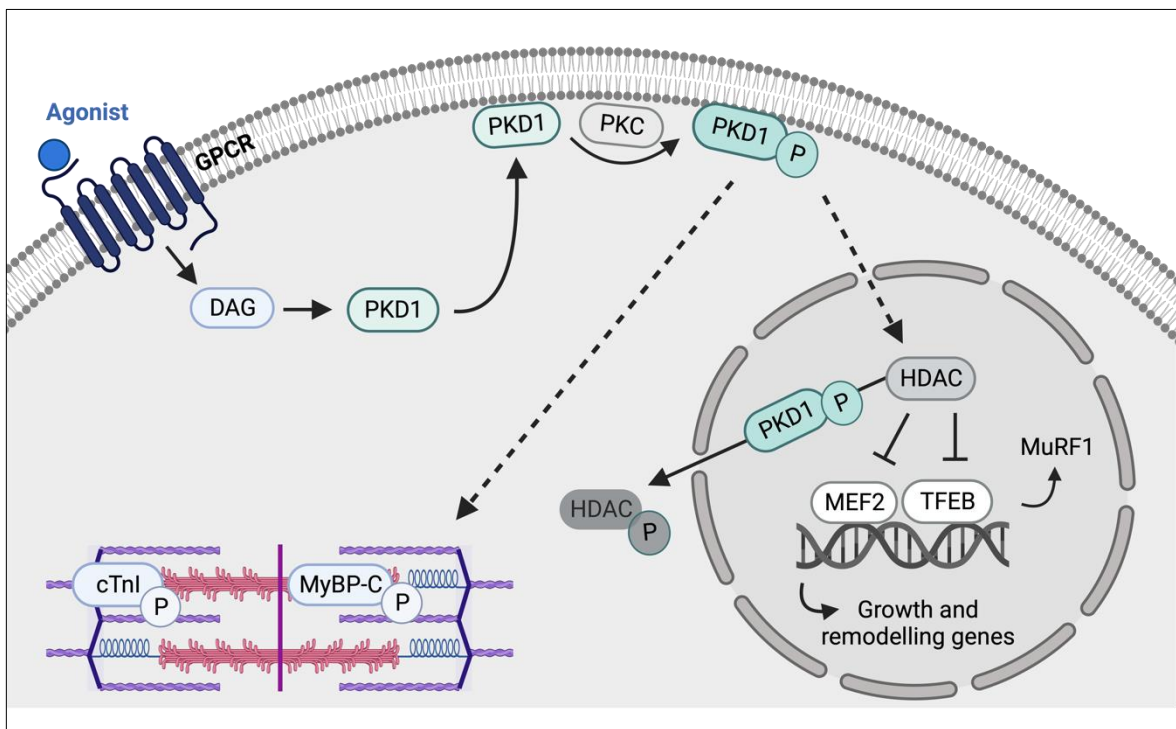


Figure 4: Protein kinase D1 signalling in cardiac myocytes. Upon (patho)physiological stimulation of G protein-coupled receptors (GPCR), diacylglycerol (DAG) increases. DAG binds to PKD1 and leads translocation of PKD1 to the sarcolemma where it is phosphorylated at serine 744/748 by PKC. This is followed by autophosphorylation at serine 916 resulting in full kinase activation. Active PKD1 translocates either to the cytosol or into the nucleus. In the cytosol, PKD1 impacts on contractile function by phosphorylating different myofibril-associated proteins, e.g cardiac troponin I (cTnI) or myosin-binding protein C (MyBP-C). In the nucleus, PKD1 phosphorylates histone deacetylases (HDAC) leading to their export into the cytosol and a derepression of the myocyte enhancer factor 2 (MEF2) or the transcription factor EB (TFEB). MEF2 activates the fetal and pro-hypertrophic gene expression, whereas TFEB is responsible for expression of the proteasome-associated muscle-RING-finger protein 1 (MuRF1). This illustration was generated with BioRender and modified from (Simsek Papur et al. 2018).

Moreover, PKD1-mediated export of HDAC5 results in derepression of the transcription factor EB (TFEB) that drives MuRF1 expression which has been involved in the UPS degradational system (Pablo Tortola et al. 2020). In addition to the role in remodelling by impacting gene transcription, implications of PKD1 in acute contractile function were

reported (**Figure 4**; Cuello et al. 2007). A yeast two-hybrid screen of a human cardiac library for the catalytic domain of PKD1 was used to identify interaction partners of PKD1. Investigation of myofibrillar preparation revealed phosphorylation of cTnI and numerous other myofilament proteins such as MyBP-C, myomesin and telethonin as well as NRAP as putative PKD substrate (Haworth et al. 2004).

3.2.3 Nebulin-related anchoring protein in heart disease

Recently, increasing evidence suggests an involvement of NRAP in the development of skeletal and cardiac disease, although its specific function remains elusive. NRAP has been involved in myofibrillar myopathies such as filaminopathy caused by mutations in *FLNC* encoding for filamin C. Patient biopsies of skeletal muscles fibres revealed that NRAP accumulated in aggregates (Kley et al. 2013). Moreover, a similar NRAP phenotype was identified in another myofibrillar myopathy, the nemaline myopathy that results in hypotonia and muscle weakness. Patients with a deficiency in the kelch-like protein KLHL41, which is involved in protein turnover of NRAP by the UPS system during the premyofibril-myofibril transition when skeletal muscle develops and forms mature myofibrils, showed massive accumulation of NRAP (Jirka et al. 2019). Interestingly, the reduction of NRAP protein levels in KLHL41-deficient zebrafish reversed the observed phenotype. Moreover, *NRAP* overexpression alone in zebrafish resulted in a myopathic phenotype without representation of mature myofibrils (Jirka et al. 2019). Another study recently showed that reduction of NRAP in nemaline myopathy caused by nebulin deficiency rescued the disease phenotype by reversing sarcomeric disorganisation, lowering the amount of protein aggregates and positively impacting skeletal muscle function (Casey et al. 2023). Nevertheless, not only NRAP protein levels were altered in myofibrillar myopathies. A recent study showed in patients with BAG3 myofibrillar myopathy, simultaneous occurrence of three different *NRAP* variants (c.3674G > A, c.1556T > A, c.844C > T; D'Avila et al. 2016).

In addition the skeletal muscle diseases, NRAP has been involved in the development of cardiomyopathies. A recent publication by Koskenvuo et al. showed in a gnomAD reference population that biallelic *NRAP* variants occur in 0.26-2.46% of all DCM cases, while other studies even suggested NRAP as an early DCM biomarker (Ehler et al. 2001; Koskenvuo et al. 2021).

In a 26-year-old male patient, a homozygous loss-of-function mutation in NRAP (Arg1502*) resulted in the development of a DCM phenotype with biventricular heart failure and ventricular tachycardia post-viral illness (Truszkowska et al. 2017). Another homozygous frameshift mutation in NRAP (c.259delC), resulting in a loss-of-function

phenotype, was observed in a patient with left ventricular non-compaction, a rare form of cardiomyopathy characterised by increased trabecular meshwork in the left ventricular wall (Zhang et al. 2023). Recently, different missense or frameshift variants of NRAP in unrelated patients were associated with the development of either HCM or DCM (Maurer et al. 2023). Moreover, two different DCM mouse models, the *MLP-KO* and the *TOT*-mouse, showed increased NRAP protein levels and NRAP accumulation at the intercalated disc (Ehler et al. 2001). However, overexpression of *Nrap* in a mouse model led to the development of right ventricular cardiomyopathy with minor effects on the left ventricle and the intercalated discs (Lu et al. 2011).

As indicated in this chapter, many studies based on different murine, zebrafish or human models showed evidence that NRAP might be involved in skeletal muscle-associated myofibrillar myopathies as well as in different kinds of cardiomyopathies (Prill and Dawson 2020). However, it remains elusive how NRAP is regulated and how NRAP contributes to these disease phenotypes.

3.3 Disease modelling

In recent years, improved therapies have been developed to treat cardiomyopathies but are not always efficient enough in preventing heart failure (Ponikowski et al. 2014). For the development of novel therapies, it is required to study the underlying pathomechanisms of cardiomyopathies and their progression towards heart failure. Since the availability of human heart tissue is limited, animal models are widely used. However, animal models differ in their cardiac physiology from human physiology, allowing only a restricted translation of results from animal models to human disease phenotypes and therapies (Flenner et al. 2021; Houser et al. 2012).

3.3.1 Human-induced pluripotent stem cells

To address this issue, Yamanaka and colleagues used mouse embryonic and adult fibroblasts for reprogramming into induced pluripotent stem cells (iPSC). This was achieved by retroviral transduction with the four pluripotency factors Oct 3/4, Sox 2, c-Myc, and Klf 4 resulting in murine iPSC with the similar properties regarding morphology, gene expression and pluripotency as embryonic stem cells (Guenther et al. 2010; Takahashi and Yamanaka 2006). In 2007, for the first time, human somatic cells were reprogrammed into human iPSC (hiPSC) that could be differentiated into all three germ layers (**Figure 5**; Takahashi et al. 2007). In the following years, this procedure was further optimised allowing in addition to reprogramming blood cells, keratinocytes and hepatocytes into iPSCs (Aasen et al. 2008; Aoi et al. 2008; Loh et al. 2009). Since retroviruses integrate into the host genome, the delivery of the four pluripotency factors

was further improved by using Sendai virus that functions only transiently, thus enhancing the safety for prospective clinical applications (Fusaki et al. 2009; Schlaeger et al. 2015).

The culture of hiPSC was initially performed at ambient air conditions but was changed to the cultivation of hiPSC at 5% oxygen as their physiological niche *in vivo* was suggested to range between 1% and 6% of oxygen concentration (Eliasson and Jönsson 2010; Shooter and Gey 1952). Increased oxygen tensions were correlated with mutations, loss of pluripotency and associated with an ageing process termed senescence (Busuttill et al. 2003; Kwon et al. 2017). Senescence describes a state in which cells are in a cell cycle arrest (Hernandez-Segura et al. 2018). However, it is still not completely unravelled how differences in oxygen tension impact the genome.

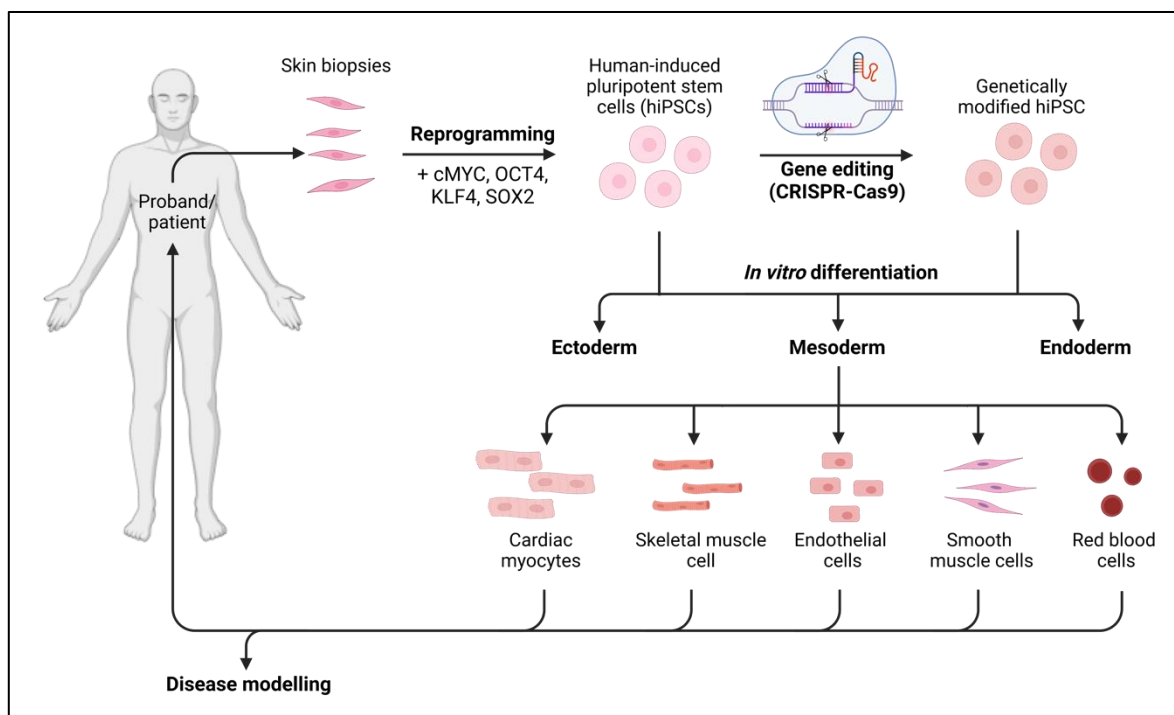


Figure 5: Schematic overview of reprogramming human fibroblasts into hiPSC and differentiation into different cell types. Fibroblasts are reprogrammed into human-induced pluripotent stem cells (hiPSC) using pluripotency factors (cMYC, OCT4, KLF4, SOX2). HiPSC can be genetically modified via the CRISPR-Cas9 gene editing system or directly differentiated into various cell types of ecto-, endo- or mesoderm. The mesoderm can be differentiated into cardiac myocytes, skeletal muscle cells, endothelial cells, smooth muscle cells or red blood cells, that can be enrolled for disease modelling or treatment of patients. The figure was illustrated using BioRender.

Due to their pluripotent characteristics and absence of ethical issues, hiPSC have become an invaluable tool for *in vitro* cardiac disease modelling, drug testing and patient-specific gene therapies (Musunuru et al. 2018). Concomitantly, different strategies have been developed for gene editing approaches, allowing to genetically modify specific genes, model human disease-related mutations, generate KO cell lines and knock-in (KI) specific

mRNAs or reporter proteins. To this end, the development of the clustered regularly interspaced short palindromic repeats (CRISPR)-based genome editing technology promoted the precise editing of the human genome and investigation of disease models (**Figure 5**; De Masi et al. 2020).

3.3.2 CRISPR-based genome editing

The CRISPR/CRISPR-associated protein 9 (Cas9) technology was initially discovered as an adaptive immune response in bacteria and archaea in response to viruses (Barrangou et al. 2007; Horvath and Barrangou 2010). When these prokaryotes get infected by viruses, the viral DNA is cleaved and integrated as 20 bp long protospacers into the host genome (**Figure 6 A**; Pourcel et al. 2005; Rath et al. 2015). Upon transcription of endogenous DNA, CRISPR RNAs (crRNAs) are expressed targeting the invasive viral DNA by the Cas protein complex (Horvath and Barrangou 2010). The complex consists of the Cas9 protein and a trans-activating crRNA (tracrRNA) that bind to the crRNA and thereby form a guide RNA (gRNA). This activates the endonuclease activity of the Cas9 complex that initiates DNA double-strand breaks upstream of the recognition signal, the protospacer-adjacent motif (PAM), at the 3'-site of the viral protospacer region (**Figure 6 A**; Gasiunas et al. 2012). Since the Cas protein complex only recognises the PAM sites upstream of the protospacer, induction of double-strand breaks of the host genome is prevented. The PAM sequence is dependent on the appropriate Cas protein and is 5'-NGG-3' in the case of the Cas9 with the *N* representing any nucleotide (Jinek et al. 2012).

This bacterial system was transferred and modified for gene-editing approaches to the human genome (Doudna 2020). For simplification, the tracrRNA and crRNA were combined to a gRNA in advance to transfection. The gene-editing approach by CRISPR/Cas9 can be achieved by different delivery methods into mammalian cells including chemical or physical transfection or viral delivery (Ran et al. 2013). The expression systems can either be delivered by plasmids expressing the Cas9 and gRNAs or by Cas9 mRNA and gRNAs directly or beforehand assembled RNP complexes. This system induces a double-strand break in mammalian cells directed by the gene-specific designed gRNAs. This is followed by an intrinsic mammalian repair mechanism that can either take place in a process termed homology-directed repair (HDR) or a process termed non-homologous end joining (NHEJ) (**Figure 6 B**; Weterings and Chen 2008).

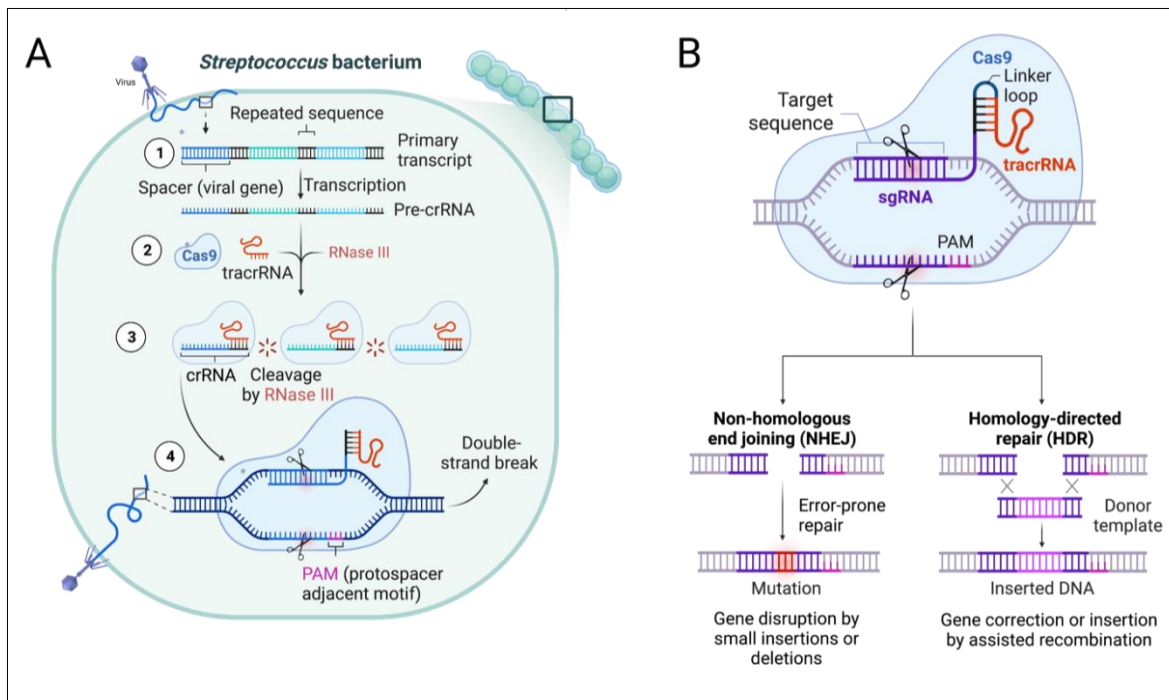


Figure 6: CRISPR-Cas9 technology for gene editing approaches. A) Adaptive immune response of *Streptococcus bacterium*. Invasive viral DNA is inserted into the host's DNA as small spacers. The regions are transcribed to crRNAs that interact with tracrRNAs and the Cas9 protein to induce double-strand breaks upon repeated viral invasion. **B)** Cellular, intrinsic repair mechanisms in response to double-strand breaks by homology-directed repair (HDR) or non-homologous end joining (NHEJ). This illustration was modified from BioRender.

During NHEJ, the disrupted DNA ends are re-ligated in an error-prone process as small insertions/deletions (Indels) might result. This alteration can further lead to frameshift mutations and premature stop codons. However, if the gene-editing by CRISPR-Cas9 is performed in the presence of a DNA template in the form of a plasmid or single-stranded oligodeoxynucleotide (ssODN), the intrinsic cellular repair machine is able to precisely re-ligate and integrate the DNA template via HDR (Ran et al. 2013). For HDR-mediated approaches in hiPSC, CRISPR efficiencies of 2-4% have been reported (Mali et al. 2013). This efficiency can further be increased by performing a cold shock at 32 °C for 24-48 h post-transfection into hiPSC (Guo et al. 2018).

3.3.3 Differentiation to cardiac myocytes

As hiPSC represent a human model that can be genetically modified with the CRISPR/Cas9-based approach to generate pluripotent disease cell lines with unlimited ability for self-renewal, they serve as an eligible tool to study cell types with low regenerative potential such as cardiac myocytes. During the differentiation of hiPSC to cardiac myocytes signalling pathways of mammalian embryonic development are imitated (**Figure 7**; Calderon et al. 2016). For cardiac monolayer differentiation, efficiencies of >90% cardiac myocytes can be achieved depending on the cell density (Palpant et al. 2017).

The successful differentiation from hiPSC to cardiac myocytes was shown to depend on the exposure at specific time points of specific growth factors and inhibitors of signalling pathways at specific time points (**Figure 7**; Burridge et al. 2012).

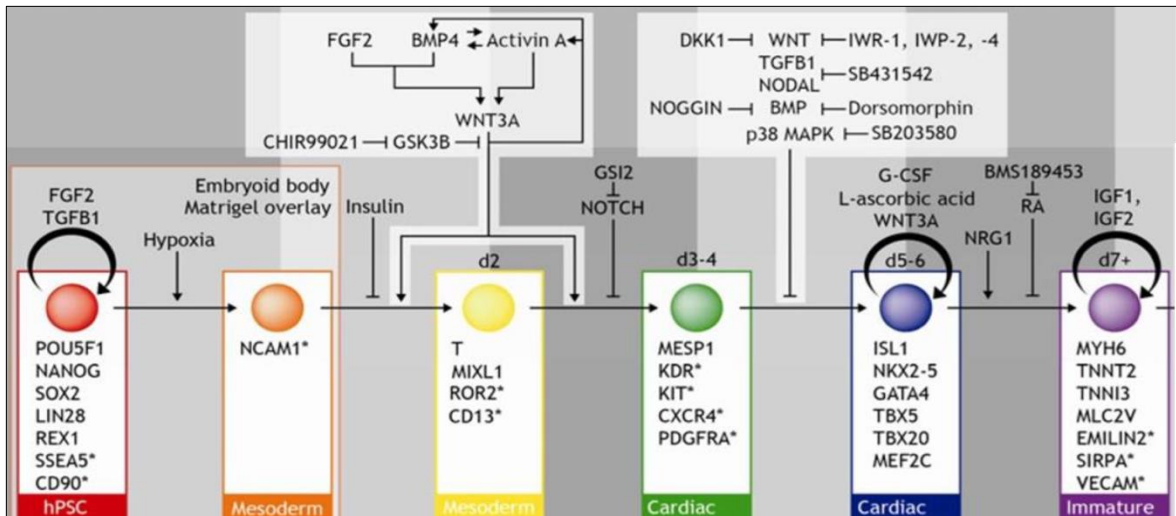


Figure 7: Schematic overview of factors involved in cardiac myocyte differentiation. Depicted are factors and genes that are associated with the appropriate differentiation steps. The asterisks indicate surface markers. HiPSC undergo an epithelial-to-mesenchymal transition, differentiation to mesoderm, followed by cardiac mesoderm specification, differentiation to cardiac progenitor cells and finally to immature cardiac myocytes that can be further matured. Adapted from (Burridge et al. 2012).

The major pathways involved in cardiac differentiation include the BMP, TGFβ/activin/NODAL, WNT, and FGF signalling pathways (Burridge et al. 2012; Kattman et al. 2011). In order to mimic the epithelial-to-mesenchymal transition during gastrulation in somatic cells, activin A, BMP4, high-growth factor matrigel and B27 without insulin are commonly used to induce WNT3 expression (**Figure 7**; Calderon et al. 2016; Palpant et al. 2017; Zhang et al. 2012). Subsequently, the WNT pathway is inhibited by XAV-939, a step required for induction of cardiac differentiation (Lian et al. 2012; Willems et al. 2011). However, investigations of hiPSC-derived cardiac myocytes revealed a fetal, immature phenotype differing from adult cardiac myocytes (Mummery 2018; Ulmer and Eschenhagen 2020). In the human fetal heart, growth of the heart mainly occurs by cell division, a process termed hyperplasia, while postnatal hearts are characterised by cardiac myocyte growth, a process termed hypertrophy (Hirschy et al. 2006). During this process many metabolic alterations occur that affect the gene and protein expression of mitochondria, the tricarboxylic acid cycle (TCA) cycle and the fatty acid metabolism (Ulmer and Eschenhagen 2020).

3.3.4 Engineered heart tissues

In order to overcome the issue of the immaturity of hiPSC-derived cardiac myocytes, the cells are embedded in a hydrogel-based engineered heart tissue (EHT) format with elastic silicone posts ensuring physiological contractile properties (Hansen et al. 2010; Weinberger et al. 2017). The physiological contraction of EHTs against a mechanical load is termed auxotonic contraction (Ulmer and Eschenhagen 2020). Indeed, cultivation of hiPSC-derived EHTs revealed metabolic maturation in comparison to two-dimensional cultured hiPSC-derived cardiac myocytes as indicated by a higher abundance of mitochondrial proteins and a switch of metabolic pathways towards less fatty acid metabolism and to a minor extent anaerobic glycolysis (Ulmer et al. 2018). In addition to human EHTs, cardiac cells of various other species have been successfully used for the generation of EHTs including neonatal mouse cardiac cells and neonatal rat ventricular myocytes (NRVMs) (Stöhr et al. 2013; Zimmermann et al. 2000). The generation of EHTs provided many advances in cardiac *in vitro* drug testing, transplantation in regenerative medicine and disease modelling to study their direct impact on cardiac contractile properties (Mannhardt et al. 2020; Saleem et al. 2020).

4. Aims

An important role of intercalated discs is to regulate cardiac myocytes contractility in a functional syncytium. Dysfunction of intercalated discs contributes to the development of different forms of cardiomyopathies, such as HCM and DCM. In these cardiomyopathies, increased NRAP protein levels and accumulation of NRAP at the intercalated disc leaking into the myofilaments have been detected. Moreover, recent observations in a growing number of patients showed that dysfunction of NRAP resulted in the development of DCM with a prevalence of approximately 2% of screened cardiomyopathy patients (Koskenvuo et al. 2021).

Even though NRAP seems to play a crucial role in different forms of cardiomyopathies as well as in early myofibrillogenesis, not much is known about the causal impact of NRAP in heart disease development and progression and the underlying molecular pathomechanisms. The contribution of altered NRAP expression and localisation and how this might be regulated and impact cardiomyopathies remains elusive. Therefore, the main question of this thesis was to investigate whether NRAP has a protective function during the development of cardiomyopathies or whether it causally contributes to the development of heart disease.

Our hypothesis was that NRAP as a mechanosensing protein contributes to the pathophysiology of cardiomyopathies.

In order to enhance the understanding of the impact of NRAP on cardiac myocytes on myofibrillogenesis and the development of heart disease, we aimed to:

- (1) Generate and validate a functional *NRAP*-overexpressing (OE) and -knock-out (KO) hiPSC line by CRISPR-Cas9 gene editing.
- (2) Generate a *NRAP/green fluorescent protein (GFP)*-OE hiPSC line to study the specific roles of NRAP during myofibrillogenesis.
- (3) Investigate the loss- and gain-of-function of NRAP in a gene-dose-dependent manner on myofilament structure in two-dimensional hiPSC-derived cardiac myocytes.
- (4) Characterise the loss- and gain-of-function of NRAP in a gene-dose-dependent manner on cardiac function in a three-dimensional EHT model.
- (5) Investigate the importance of posttranslational modifications in the regulation of NRAP functions.

5. Materials and Methods

All materials, media and buffer compositions as well as detailed information about sequences that have been used in this project, are listed in materials section 11.2.

5.1 Animal models

5.1.1 *Mybpc3*-targeted knock-in mouse model

The cardiac myosin-binding protein C Knock-in (KI) mouse model (*Mybpc3*-KI) on a C57 BL/6J genetic background had previously been developed by using the Cre/lox system by a G>A transition in the last nucleotide of exon 6 and was kindly provided by Prof. Dr. Lucie Carrier and Dr. Saskia Schlossarek (Vignier et al. 2009). The mouse model carries a mutation that has been associated with a severe HCM phenotype in patients and was accompanied by a *Mybpc3* mRNA reduction by 50% in heterozygous and 80% in homozygous *Mybpc3*-KI mice (Vignier et al. 2009). In this mouse model, three different mutant mRNAs were discovered, ultimately resulting in 21% decreased protein levels of cMyBP-C in heterozygous and 90% in homozygous mutant mice. Compared to WT mice, the *Mybpc3*-KI mouse phenotype in homozygous mutant mice was characterised by left ventricular hypertrophy, reduced fractional shortening, increased heart weight to tibia length ratio, interstitial cardiac fibrosis and cardiac myocyte disarray. For the experiments, WT mice at the age of 24-46 weeks and *Mybpc3*-KI mice at the age of 25-47 weeks were enrolled. The mouse hearts and other organs such as liver and skeletal muscle were isolated with the help of Angelika Piasecki.

5.1.2 Neonatal rat ventricular cardiac myocytes

Experimental animal procedures were performed according to the guidelines for the care and use of laboratory animals as issued by the National Institutes of Health (Publication no. 85-23, revised 1985) and the German law for the protection of animals. Wistar rats were kept in a 12 h light/dark cycle at room temperature (RT) with water and food supply *ad libitum*.

5.1.2.1 Isolation of NRVMs

Neonatal rat ventricular myocytes (NRVMs) were isolated according to the standard operating procedures that are established within the Institute of Experimental Pharmacology and Toxicology (IEPT) of the University Medical Centre Hamburg-Eppendorf (UKE). Therefore, 0-3 day-old Wistar rats (P0-3) were decapitated, hearts were isolated and atria were removed. The isolation of the hearts was kindly prepared by Prof. Dr. Friederike Cuello and Dr. Konstantina Stathopoulou. All subsequent isolation steps were

performed on ice if not indicated otherwise. After three washing steps in calcium and bicarbonate-free Hanks buffer with HEPES (CBFHH), hearts were homogenised with scissors. The homogenate was transferred to a 50 mL falcon tube. After sedimentation, the supernatant was aspirated and for each 30 hearts 3.9 mL trypsin-working solution was added to the tissue. After 10 min incubation at RT, the supernatant was discarded, and the digestion step was repeated, followed by the addition of 3.4 mL DNase-working solution to block digestion. The amount of trypsin- and DNase-working solutions was adjusted to the amount of rat hearts. After each digestion, DNase-working solution was added, and the suspension was mixed by careful trituration and then incubated for sedimentation of cells.

After sedimentation, the supernatant was transferred to collection tubes. The procedure was repeated approximately 10-15 times with 2-5 min digestion and subsequent neutralising steps at RT until only white fibres remained in the heart homogenate. The collection tubes, containing the cardiac myocytes, were centrifuged for 15 min at 60 g at 4 °C. After aspiration of the supernatant, 5 mL non-cardiac myocyte medium (NCM) was added, followed by another centrifugation step. The supernatant was filtered with a sterile falcon filter (100 µm) into a sterile falcon tube. Cells were counted using a Neubauer chamber and calculated per mL. For each NRVM isolation, a yield of approximately 1.4-3 Mio cells/heart was achieved.

5.1.2.2 Culture of neonatal rat ventricular cardiac myocytes

In order to remove adherent non-myocytes and fibroblasts, 10 Mio NRVMs in 5 mL pre-plating medium (PPM) were incubated for 60-90 min in the incubator in a 60 mm culture dish. All 2-dimensional-cultured NRVMs were maintained in an incubator set to 37 °C in a humidified atmosphere of 5% CO₂ and ambient air oxygen concentrations. Meanwhile, 35 mm dishes were coated with 1 mL of 1% (w/v) gelatine in PBS for 1 h at RT. After completion of pre-plating, the cardiac myocytes-containing suspension was transferred from the 60 mm dish to a 50 mL falcon tube. To increase the yield of NRVMs in the falcon tube, the 60 mm culture dish was washed twice with plating medium (PM) to remove as many cardiac myocytes as possible from the dish.

For counting of cells, 30 µL cell suspension was mixed with 30 µL trypan blue followed by counting of eight squares of a Neubauer chamber. Cells per mL were calculated by multiplication of the average cell number per square with the dilution factor 20.000. Prior to plating of cells, 1% gelatine-coated 35 mm dishes were washed with PBS and either 400.000 cells for immunofluorescent stainings or 1 Mio cells for RNA/protein analyses per 35 mm dish were plated in PM.

5.1.2.3 Treatments of NRVMs

After incubation for two days in the incubator, the medium was exchanged to serum-free maintenance medium (MM) and cardiac myocytes were incubated for another day in the incubator prior to the start of any experiments. On the next day, NRVMs were stimulated with either 3 μ M of the pharmacological bipyridyl PKD inhibitor (BPKDi) or for the respective control group with DMSO in the absence or presence of exposure of cells to 10 μ M of the pro-hypertrophic stimulus phenylephrine (PE) or 10 nM isoprenaline (ISO) in MM. Cells were treated daily for up to 96 h in serum-free conditions prior to downstream experiments. At the treatment start, 24 h, 48 h, 72 h and 96 h of incubation, samples for different purposes such as immunofluorescence and western immunoblotting were collected. To inhibit autophagy, 50 nM bafilomycin A1 (BafA1) in water was added once to the respective culture wells 3 h prior to sample collection. For inhibition of the ubiquitin-proteasome system (UPS), 1 μ M MG132 in DMSO or DMSO for control were added to culture wells 24 h prior to sample collection.

5.1.2.4 Immunoprecipitation

To investigate if NRAP can successfully be immunoprecipitated, NRVMs were treated as described above for 72 h with DMSO or BPKDi in the presence or absence of PE. The 6-well plates were washed twice with ice-cold PBS and frozen on liquid nitrogen. For that purpose, plates were thawed on ice and samples were harvested in 500 μ L radioimmuno-precipitation assay buffer (RIPA). Two wells of the same treatment were combined into Eppendorf tubes and incubated on ice for 30 min with intermittent vortexing every 2-3 min. During the immunoprecipitation process, different samples were taken to allow the validation of successful NRAP immunoprecipitation by western immunoblotting.

A sample of the crude lysate was taken and the remainder was centrifuged at 14.000 g for 10 min at 4 °C. After centrifugation, an input sample from each treatment group was taken and the pellet was kept as well as a sample. From the supernatant, 400 μ L of each treatment sample were incubated with 2 μ L anti-NRAP (Davids Biotechnology) overnight at 4 °C under constant rotation. On the following day, samples were quickly spun down and incubated with 40 μ L protein A/G agarose beads for 4 h at 4 °C under constant rotation. After that, samples were centrifuged at 2.000 g for 1 min at 4 °C. From the supernatant, 370 μ L were kept as a sample and the beads were washed four times with 500 μ L RIPA buffer each with intermittent centrifugation at 2.000 g for 1 min at 4 °C. The proteins of the beads/pellet fraction were extracted with 100 μ L reducing sample buffer to generate SDS samples. To all other samples, that were taken during the experiment, 3x reducing sample buffer was added.

For denaturation of proteins, sodium dodecyl sulfate (SDS) samples were boiled at 75 °C for 5 min prior to SDS-polyacrylamid gel electrophoresis (PAGE) and western immunoblotting. The immunoblotting was performed as described in section 5.8.2 with the NRAP antibody to investigate if NRAP was immunoprecipitated. The immunoprecipitation procedure was kindly performed once by Dr. Konstantina Stathopoulou.

5.1.2.5 Stable isotope labeling by/with amino acids in cell culture (SILAC)

After culture for one day in plating medium, medium was removed and cells were washed once with SILAC medium and then incubated in 1.5 mL SILAC light medium per 6-well overnight at 37 °C, 5% CO₂ (**Figure 8**). On the next day, the procedure was repeated. After 48 h incubation in SILAC light medium, cells were incubated in SILAC heavy medium containing the heavily labelled amino acids lysine and arginine, allowing to distinguish newly synthesised proteins. Concomitantly, cells were treated with 3 μM BPKDi or equivalent amounts of DMSO for the respective control group. After 30 min incubation at 37 °C and 5% CO₂, 10 μM PE or 10 μM ISO were added to induce prohypertrophic stimulation. These treatments were repeated daily with a daily medium exchange of SILAC heavy medium until 72 h of treatment.

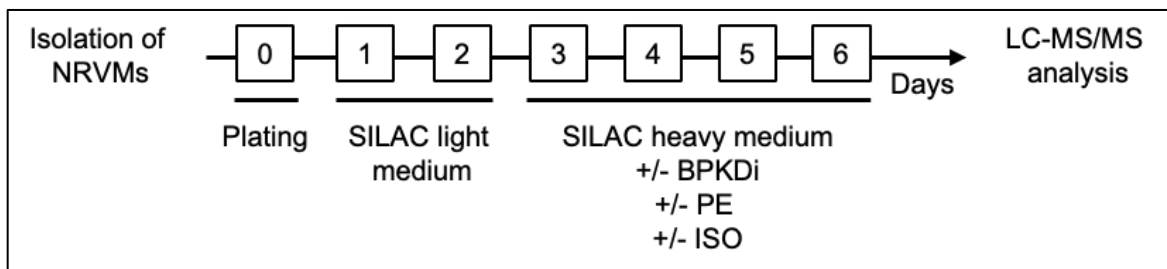


Figure 8: Stable isotope labelling by/with amino acids in cell culture (SILAC) setup. Neonatal rat ventricular myocytes (NRVMs) were isolated and incubated in SILAC light medium for 48 h prior to incubation for 72 h in SILAC heavy medium. Concomitantly with incubation in SILAC heavy medium, cells were treated with or without 3 μM BPKDi in the presence or absence of 10 μM phenylephrine (PE) and/or 10 nM isoprenaline (ISO). Afterwards, samples were analysed by liquid chromatography-mass spectrometry (LC-MS/MS analysis).

For sample collection, the medium was removed, and wells were washed once with PBS. Then 0.5 mL PBS per 6-well was added and cells were scraped and transferred to Eppendorf tubes. To increase the amount of cells, the wells were washed again with PBS and transferred to the same respective tube. The tubes were centrifuged at 16.000 rpm for 5 min and pellets were dry frozen at -80 °C until analysis by mass spectrometry.

5.1.2.6 Mass spectrometry

For mass spectrometric analysis, the pellets were supplemented with 20 μL 6 M guanidinium chloride, 50 mM Tris(hydroxymethyl)aminomethan (Tris)/ hydrogen chloride (HCL)

and 10 mM Tris(2-chlorehyl)phosphat (TCEP) and incubated at 95 °C for 5 min. Afterwards, the reduced thiols were alkylated with 40 mM chloroacetamid and in order to obtain a final guanidinium chloride concentration of 0.6 M, samples were diluted with 25 mM Tris/HCl, pH 8.5 and 10% acetonitrile. After sonification of samples, protein content was determined and 50 µg of samples were used for protein digestion with 1 µg trypsin overnight at 37 °C under gentle agitation. Digestion was interrupted by the addition of trifluoroacetic acid to a final concentration of 0.5%. The peptides were loaded on multi-stop-and-go tip (StageTip) containing three C18-pdisks and 3 SCX-disks. The purification and elution of peptides were performed as previously described (Rappsilber et al. 2007). Finally, the peptides were eluted in a microtiter plate, dried, and resolved in 1% acetonitrile, supplied with 0.1% formic acid. The mass spectrometric analysis was performed by Dr. Ilka Wittig with Peaks 7.0 and MaxQuant 1.3.0.5. The initial data analysis was performed with the help of Dr. Steven Schulz.

5.2 Human models

5.2.1 Heart samples from patients

For the validation of the custom-made NRAP antibody produced by the company Davids Biotechnology, human heart tissue from the left ventricle of a patient with DCM was used for immunofluorescence. For western immunoblot analysis additionally heart tissue from non-failing, HCM and ischemic cardiomyopathy (ICM) patients was enrolled.

5.2.2 Human-induced pluripotent stem cells

The established in-house control hiPSC line (UKEi001-A/ERC001) from a healthy proband was used for the genetical engineering of stem cells and was registered at the European Human Stem Cell Registry (hPSCreg). Additionally, the utilisation of the hiPSC line was approved by the ethical committee of the UKE (Az. PV4798, 28.10.2014). It had been generated from dermal fibroblasts of punch skin biopsies as previously described (Takahashi et al. 2007).

5.2.2.1 Reprogramming of human fibroblasts into hiPSC

Punch skin biopsies (3 mm diameter) from human donors were taken under local anaesthesia. Skin biopsies were collected in MACS tissue storage solution and dissociated by digestion with collagenase type 2. Dissociated tissue was collected into a T25 TC flask containing fibroblast medium, L-glutamine, penicillin and streptomycin. Outgrowing dermal fibroblasts were expanded in the T75 tissue culture flask, passaged with trypsin or cryopreserved (passage number 1-5) in FBS with 10% DMSO, and used for subsequent reprogramming until passage number 5. For reprogramming, human dermal fibroblasts

were thawed and cultured in fibroblast medium, transduced by Sendai virus vectors containing four different Yamanaka reprogramming factors (hOct3/4, hSox2, hKlf4, hc-Myc) according to the manufacturer's instructions at multiplicity of infection (MOI) 6 (CytoTune-iPS Sendai Reprogramming Kit).

At day 7 post-transduction, Sendai virus-transduced fibroblasts were trypsinised and re-seeded in three different densities (1.6×10^4 , 3.2×10^4 , 6.4×10^4 per 6 well) on feeder cells (primary mouse embryonic fibroblasts (MEF) from CF-1 mice), mitotically inactivated with $10 \mu\text{g/mL}$ mitomycin C (SERVA), MMC-MEF density 2.5×10^5 per 10 cm^2 , and cultured with human embryonic stem cell (hES) medium supplemented with 30 ng/mL fibroblast growth factor (FGF), with daily medium change. 30-40 days after transduction, the reprogrammed hiPSC colonies were picked with an inverted EVOS microscope and transferred under sterile conditions. Every single individual clone was further expanded and cryopreserved. For the initial passages after picking, the lines were cultured with CF-1 MEF-conditioned hES medium supplemented with FGF on plates coated with growth factor reduced matrigel and for passaging dissociated with $0,75 \text{ mM}$ EDTA. At later passages (passage number 5-10), culture conditions were adapted gradually to the ones described in the following section. This method was performed by Dr. Sandra Laufer and Dr. Aya Shibamiya and has been adopted from the manuscript Raabe et al. (*in preparation*).

5.2.2.2 Thawing and culture of human-induced pluripotent stem cells

Cryopreserved hiPSC from working cell banks were thawed for 2-3 min at $37 \text{ }^\circ\text{C}$ and then drawn up into a 5 mL FTDA-containing pipette supplied by the ROCK-Inhibitor Y-27632 ($10 \mu\text{M}$). When hiPSC were thawed for gene editing approaches, mTESR⁺ medium was used instead of FTDA. The cell suspension was transferred to a 15 mL falcon tube and centrifuged for 3 min at 800 rpm. After centrifugation, the supernatant was removed and the pellet resuspended in FTDA, supplemented with 30 ng/mL FGF and $10 \mu\text{M}$ Y-27632. These concentrations of FGF and Y-27632 were used in all following applications in which those compounds were used. For the plating of cells, 1 Mio hiPSC per 6-well culture well were cultured on geltrex-coated plates (1:100 in ice-cold RPMI 1640). The standard culture conditions of hiPSC were $37 \text{ }^\circ\text{C}$, 5% CO_2 and 5% O_2 with daily medium exchange (FTDA, supplied with FGF). For experiments to test oxygen concentrations, hiPSC were cultured at hypoxic or normoxic conditions. In this thesis, hypoxia refers to hiPSCs culture at 5% O_2 , $37 \text{ }^\circ\text{C}$, 5% CO_2 and normoxic culture refers to 20% O_2 , $37 \text{ }^\circ\text{C}$, 5% CO_2 .

When the cell layer reached >90% confluence, cells were passaged. For that purpose, the cells were washed once with PBS and then detached with accutase solution, supplemented with Y-27632 for 5-10 min at $37 \text{ }^\circ\text{C}$. With a $1000 \mu\text{L}$ pipette, cells were detached

and transferred to a falcon tube. To remove as many cells as possible, all wells were washed with pre-warmed FTDA, supplemented with FGF and Y-27632, and added to the falcon tube. This was followed by centrifugation at 800 rpm for 3 min. The supernatant was removed and cells were resuspended in FTDA with FGF and Y-27632. After counting of cells with trypan blue, densities of 50.000-70.000 cells/cm², i.e. 500.000-700.000 cells per 6-well or 4.5-6.5 Mio cells per T75 flask were plated. Prior to enrolling cells into experiments, hiPSC were passaged at least three times.

5.2.2.3 Freezing of human-induced pluripotent stem cells

For freezing of cells, hiPSC were washed once with PBS and then incubated with accutase solution, supplemented with Y-27632, for 5-10 min at 37 °C, 5% CO₂ and 5% O₂. Cells were detached with a 1000 µL pipette and wells were washed once with FTDA (+ Y-27632). After centrifugation at 800 rpm for 3 min, supernatant was removed and cells were resuspended in FTDA (+Y-27632, + FGF) for counting as previously described. As an appropriate amounts of cells per aliquot, usually 1 Mio cells per cryotube were calculated, centrifuged again at 800 rpm for 3 min. Cells were resuspended in FBS and transferred to cryotubes. After addition of 20% dimethyl sulfoxide (DMSO), cryotubes were inverted and stepwise frozen with a Mr. Frosty at -80 °C. On the next day, frozen cells were transferred to -150 °C for storage and to liquid nitrogen tanks for long-term storage.

5.2.2.4 Karyotyping analysis by Giemsa staining

Karyotype analysis was performed as previously described (Breckwoldt et al. 2017). In brief, to ensure an appropriate proportion of cells during metaphases, at least 400.000 hiPSC were used for karyotyping. Before harvesting, 40 µL colcemid was added to each well and incubated for 5 h at 37 °C and 5% CO₂. After two intermittent washing steps with PBS, hiPSC were incubated with 0.5 mM EDTA at RT. Afterwards, cells were detached with 2 mL F10 complete medium and four times triturated with a 10 mL pipette. The cells were then centrifuged for 10 min at 250 g at RT. After removal of the supernatant, 7 mL of 75 mM KCl solution was dropwise added under swirling and incubated for 15 min at 37 °C. Subsequently, 13 drops of the fixative solution were added to the suspension and then centrifuged at 250 g for 10 min at RT. Almost the entire supernatant was removed, except 1 mL, vortexed and 6 mL of ice-cold fixative were dropwise added. The centrifugation and fixative steps were repeated twice before the fixative was removed. The cell suspension was then used for slide generation.

First, the slides were rinsed with the detergent solution Mucasol in hot water and covered overnight at RT. The slides were washed once with water for 15 min, followed by rinsing twice with purified water. For the generation of slides, 80-100 µL of hiPSC were placed

onto a slide and transferred into a beaker containing dH₂O that had been pre-warmed to 80 °C until the fixative had evaporated. Cell density and metaphase spreading were monitored by phase-contrast microscopy. Afterwards, slides were incubated at 95 °C for 15 min. For trypsin Giemsa-banding, slides were placed for 1-5 s to 0.25% (v/v) trypsin in Hank's Balanced Salt Solution (HBSS), followed by a short incubation in PBS and subsequent incubation for 6 min in 10% (v/v) Giemsa stain in Titrisol (pH 7.2). Slides were rinsed with cold water and then air-dried for a few minutes. For chromosome analysis, slides were covered with a coverslip and Cytoseal 60 and for each sample 15 metaphases were analysed under a light microscope using a 1000x magnification. This method was kindly performed by Dr. Sigrid Fuchs and has been adopted from the manuscript Raabe et al. (*in preparation*).

5.2.2.5 Senescence-associated beta-galactosidase activity assay

To investigate cellular senescence as well as the induction of senescence by paracrine actions of pro-senescent factors in cells cultured under normoxic or hypoxic conditions, hiPSC of the master cell bank were thawed and cultured for three passages at 5% O₂ (5% CO₂; 37 °C) or 20% O₂ (5% CO₂, 37 °C). At the starting point of the experiment, media (FTDA supplemented with FGF) of cells from both culture conditions was exchanged. After 12 h incubation at the respective oxygen concentration, the hypoxic and normoxic medium were exchanged to the respective other hiPSC cell culture dish, meaning that hypoxic-cultured cells received media from cells that were cultured at normoxia in the first 12 h of the experiment and vice versa. After additional 24 h incubation, the media from all wells was removed and replaced with new medium before the crossover exchange procedure was repeated.

To investigate directly if media exchange from hypoxic to normoxic medium led to senescence of the cells, a senescence-associated beta-galactosidase (SA-β-gal) activity assay was performed according to the manufacturer's instructions (β-galactosidase staining kit). All used solutions were included in this kit. In brief, media was removed and hiPSC were washed once with 2 mL PBS, followed by incubation in 1x fixative solution for 10-15 min at RT. The plate was then washed twice with 2 mL PBS and incubated with 1 mL of the β-galactosidase staining solution. Plates were sealed with parafilm, covered for light protection and then incubated overnight in a dry incubator at 37 °C without additional CO₂. On the next day, the staining solution was replaced by 70% glycerol and analysed by light microscopy on a Nikon Eclipse TS2 microscope using 200x magnification. As a positive control, hiPSC were treated twice for 2 h with 75 μM H₂O₂ before media collection.

For analysis and quantification of the blue signals representing the SA- β -gal activity, three to five different areas per well were randomly chosen and imaged. In order to remove the background similarly in all images, images were opened in ImageJ and the colour threshold was changed for all images according to the following settings: Hue 68-198, saturation 53-255, brightness 110-255 and colour space HSB. After application of those values, the appropriate areas were selected and measured. Subsequently, the selection was inverted and the non-stained areas were measured. By the addition of those values, the total area could be calculated. The stained area was then calculated as the percentage of the total area. This method has been adopted from the manuscript Raabe et al. (*in preparation*).

5.2.2.6 RNA- and ATAC-sequencing

For RNA sequencing, RNA was isolated with the RNeasy Micro Kit (Qiagen) including on-column DNase digestion. Library preparation was then performed on 10 ng RNA input with the SMARTer Stranded Total RNA-Seq Kit v3 following the manufacturer's instructions. Libraries were sequenced on an Illumina Nextseq2000 in 50 bp paired-end mode (25×10^6 reads per sample). Sequencing data analysis was performed with bioinformatics tools integrated in the Galaxy platform. Quality and adapter trimming of sequencing reads were performed prior to mapping to remove low-quality reads and adapter contaminations. RNA-sequencing data was mapped to the human genome (hg19) using RNA STAR 2.6.0b-2 (Dobin et al. 2013). PCR duplicates were removed using SAMtools (Li et al. 2009). HTSeq-count (Anders et al. 2015) and DESeq2 (Love et al. 2014) were used for the read count and differential gene expression analysis.

The assay for transposase-accessible chromatin with sequencing (ATAC-sequencing) was performed according to Buenrostro et al. (2013) with minor modifications from the Kaestner laboratory (dx.doi.org/10.17504/protocols.io.bv9mn946; Buenrostro et al. 2013). For the transposition reaction, 2.5 μ L Tagment DNA enzyme 1 were used per 50000 freshly collected cells ($n = 3$ per condition). After the addition of EvaGreen, samples were amplified with fluorescence monitoring until the fluorescent signal reached the inflection point. The libraries were then subjected to double-sided purification using Ampure XP beads and sequenced on an Illumina Nextseq2000 in 50 bp paired-end mode (15×10^6 reads per sample). The analysis of sequencing data was performed with bioinformatics tools that were integrated into the Galaxy platform. Quality control and adapter trimming of reads were performed with Trim Galore to exclude low-quality reads and adapter contaminations. Reads were then mapped to the hg19 using Bowtie2 v2.5.0 (-X 700) and PCR duplicates were removed using SAMtools. Triplicates were merged for visualisation.

The initial sample preparation was performed by me and the two methods were performed by Dr. Patrick Laurette. This method has been adopted from the manuscript Raabe et al. (*in preparation*).

5.2.2.7 Blue-native PAGE

HiPSC from hypoxic or normoxic culture conditions were pelleted and dry-frozen in liquid nitrogen. Pellets were homogenised in a pre-chilled motor-driven glass/teflon Potter-Elvehjem homogeniser at 2000 rpm and 40 strokes. Homogenates were then centrifuged for 15 min at 600 g to remove nuclei, cell debris, and intact cells. Mitochondrial membranes were sedimented by centrifugation for 15 min at 22.000 g. Mitochondrial-enriched pellets from 20 mg cells were resuspended in 35 µL solubilisation buffer and solubilised with 10 µL 20% (w/v) digitonin. Samples were supplemented with 2.5 µL 5% Coomassie G250 in 500 mM aminocaproic acid and 5 µL 0.1% Ponceau S in 50% glycerol. Equal protein amounts of samples were loaded on top of a 3–18% acrylamide gradient gel (dimension 14 × 14 cm). After native electrophoresis in a cold chamber, blue-native gels were fixed in 50% (v/v) methanol, 10% (v/v) acetic acid, 10 mM ammonium acetate for 30 min and stained with Coomassie stain (0.025% Serva Blue G, 10% (v/v) acetic acid). Densitometry was performed using the GelQuantNET software. This method was performed by Dr. Ilka Wittig and has been adopted from the manuscript Raabe et al. (*in preparation*).

5.2.2.8 Complexome analysis

The complexome analysis, mass spectrometry raw data, identification/quantification of proteins and a detailed description of the procedure have been deposited to the ProteomeXchange Consortium via PRoteomics IDentification Database (PRIDE) repository Perez-Riverol et al. (2019) (Perez-Riverol et al. 2019). In addition, data were loaded to Perseus proteomics software PMID 29344888. The blue-native analysis was performed by Dr. Ilka Wittig similarly to what was published in Heidler et al. (2013). These methods were adopted from the manuscript Raabe et al. (*in preparation*) (Heidler et al. 2013).

5.3 Gene editing by CRISPR-Cas9

5.3.1 AAVS1-cTnT-NRAP/MYC and -NRAP/GFP plasmid validation

The *AAVS1-cTnT-NRAP/MYC* and *AAVS1-cTnT-NRAP/GFP* plasmids were self-designed, followed by production by the company VectorBuilder. After delivery of *Escherichia coli*, containing the respective plasmids, bacteria were incubated in 8 mL lysogeny broth (LB) medium supplemented with 100 µg ampicillin/mL on a shaker (150 rpm) for 16 h at 37 °C.

After incubation, plasmid DNA was isolated from bacteria cultures using the Qiagen high-copy plasmid DNA isolation kit with miniprep columns as described in the manufacturer's instructions. In brief, 8 mL bacteria suspension was stepwise centrifuged for 30 s at 11.000 g in 2 mL reaction tubes. For cell lysis, cell pellets were resuspended in 250 µL buffer A1, followed by the addition of 250 µL buffer A2. After inverting the reaction tubes 6-8 times and 5 min incubation at RT, 300 µL buffer A3 was added and tubes were again inverted 6-8 times. Another centrifugation step for 10 min at 11.000 g and RT was performed. The supernatant was then transferred for binding to NucleoSpin plasmid columns and centrifuged at 11.000 g for 1 min. The silica membrane was washed once with 500 µL buffer AW to increase DNA yield, centrifuged again for 1 min and 600 µL buffer A4 was added prior to another centrifugation step for 1 min. Afterwards, the silica membrane was dried for 2 min at 11.000 g centrifugation, followed by DNA elution with 30 µL aqua destillata at 11.000 g for 1 min. To increase plasmid DNA yield, this last centrifugation step was repeated by applying the eluted fraction once more to the NucleoSpin plasmid column. Subsequently to plasmid DNA isolation, DNA concentration was measured with the Nanodrop spectrometer and plasmids were validated by digestion with restriction enzymes.

For restriction digestion of plasmids, 2 µL 10x fast digest buffer, 1 µg plasmid DNA and 1 µL fast digest enzyme BamHI or BglII were combined in 20 µL reactions. The reactions were mixed, briefly centrifuged and incubated in a heat block at 37 °C for 30 min. Subsequently, samples were loaded on 1% agarose gels as described in section 5.3.4.3. For digestion of the *AAVS1-cTnT-NRAP/MYC* plasmid with BamHI products of the sizes 3735 bp, 2956 bp, 1791 bp, 1682 bp and 474 bp were expected and for digestion with BglII, product sizes of 4804 bp, 3248 bp and 2586 bp were expected. For digestion of the *AAVS1-cTnT-NRAP/GFP* plasmid with BamHI product sizes of 3735 bp, 2956 bp, 2369 bp, 1791 bp and 474 bp were expected and for digestion with BglII sizes of 5491 bp, 3248 bp and 2586 bp were expected. Subsequently, the whole *AAVS1-cTnT-NRAP/MYC*

plasmid was sequenced by Sanger sequencing using different primer that can be found in material section 11.2. After the exchange of the *MYC*-tag by a *GFP*, this area was sequenced again.

5.3.2 Culture and nucleofection

In order to generate genetically modified *NRAP*-overexpressing (*NRAP*-OE) and *NRAP*-knock-out (*NRAP*-KO) hiPSC lines, the in-house cell line of a healthy proband (ERC001) was used. This cell line had previously been characterised and used by many groups within the IEPT for CRISPR-Cas9 mediated genome editing approaches. In advance to genome editing, gDNA was prepared by combining 100 μ M crRNA and 100 μ M tracrRNA in a 1:1 ratio, followed by incubation for 5 min at 95 °C and incubation at RT for 5 min, resulting in 50 μ M gDNA. The gDNA was used directly or stored at -20 °C.

For the CRISPR-Cas9 genome editing approach, hiPSC with a low passage number (p26 for *NRAP*/*MYC*-OE, p24 for *NRAP*/*GFP*-OE and p24 *NRAP*-KO) were thawed as described in chapter 5.2.2.2. Therefore, 1 Mio hiPSC were plated in mTESR⁺ on a 6-well culture well plate that had been coated with reduced-growth factor matrigel (1:60 in RPMI 1640) for >1 h at RT. Cells were cultured at 37 °C, 5% CO₂ and 5% O₂ and passaged two times prior to genome editing. All steps for this approach were performed using mTESR⁺ medium and reduced-growth factor matrigel until producing master cell banks.

When the cell layer was still <80% confluent, mTESR⁺ was changed 1-2 h prior to nucleofection to mTESR⁺ supplemented with Y-27632. In between, a 12-well plate was coated with reduced-growth factor matrigel (1:60 in RPMI 1640) for >1 h at RT. Just before cells were detached with accutase, supplemented with Y-27632, ribonucleoprotein (RNP) complex assembly was performed by combining 2 μ L of the respective gDNA (50 μ M) with 1.6 μ L Cas9 (62 μ M) and incubated for at least 10 min up to 1 h at RT. Detached cells were centrifuged at 800 rpm for 3 min resuspended in mTESR⁺ (+ Y-27632) and counted using trypan blue and a Neubauer counting chamber. A total volume of 800.000 cells was transferred to a 1.5 mL tube and again centrifuged for 3 min at 800 rpm. After centrifugation, hiPSC were resuspended in 100 μ L nucleofection solution (82 μ L P3 and 18 μ L supplement of the Amaxa nucleofection kit). For *NRAP*-OE cell lines, 4 μ g of the respective *AAVS1-cTnT-NRAP/MYC* or *AAVS1-cTnT-NRAP/GFP* plasmid were added. After addition of 1 μ L electroporation enhancer (100 μ M), the cell mix was transferred to the prepared RNP complex, mixed and transferred into a nucleofection cuvette.

For nucleofection, the program CA137 on the Amaxa 4D nucleofector was used. Afterwards, the cuvette was incubated for 10 min at 37 °C, 5% O₂ and 5% CO₂. The matrigel

from the coated plates was then removed and nucleofected cells were plated on a 12-well in mTESR⁺ supplemented with cloneR (1:10). For control, 250.000 untreated hiPSC from the pool were plated on one 12-well. For the generation of *NRAP*-OE cell lines, a second control with 250.000 unedited cells were plated on a 12-well. 3-5 days after nucleofection, the unedited cells as well as the edited cells by CRISPR-Cas9 were treated daily for 3 days with 0.5 µg/mL puromycin to ensure that all unedited cells were removed. During the following days after nucleofection, pictures of each well were taken for documentation using the EVOS microscope. The medium of cells was daily exchanged by mTESR⁺, supplemented with cloneR for CRISPR cells or only mTESR⁺ for control cells.

5.3.3 Single cell seeding

After puromycin selection for the *NRAP*-OE cell lines or 3-5 days post-nucleofection for the *NRAP*-KO cell line, hiPSC were passaged in low densities of 100, 200, 400, 600 and 800 cells per 6-well culture well plate. In the following days a particular objective, containing an integrated marker, was used to mark single cells on the plate. The medium of the low-density seeded cells was replaced every second day by mTESR⁺ with cloneR until the marked circles were almost full of divided cells from one single cell. These clones were picked with a 100 µL pipette under sterile conditions using the 2x magnification of the EVOS microscope and transferred to a matrigel-coated 48-well plate. Each clone was transferred into a single well of a 48-well plate with mTESR⁺ with cloneR on a pre-warmed metal plate. The medium of single clones was exchanged every second day until confluency. This was followed by another splitting step to two 48-wells for each clone. As soon as these 48-wells reached a confluence, one well of each clone was frozen as above described in section 5.2.2.3.

The other well of the same clone was used to isolate gDNA for validation of successful genome editing. Therefore, cells were detached with accutase (+Y-27632), combined with the same amount of medium and centrifuged at 800 rpm for 3 min. The supernatant was aspirated and pellets were dry frozen at -20 °C until further gDNA isolation procedure was performed. The generation of *NRAP*-KO single-cell clones as well as parts of the validation process of successfully edited *NRAP*-KD clones were performed by Vanessa Lewandowski as part of her Master thesis under my supervision.

5.3.4 Validation of successful edited CRISPR clones

5.3.4.1 Genomic DNA isolation

In order to validate CRISPR clones and to perform quality controls for the edited hiPSC lines, genomic DNA (gDNA) was isolated following the manufacturer's instruction of the

DNeasy Blood & Tissue kit Quick-Start protocol from Qiagen. In brief, one 48-well for clones or 1 Mio hiPSC were centrifuged for 3 min at 800 rpm and pellets were dry frozen. The cells were then resuspended in 200 μ L PBS and 20 μ L protein kinase K were added, followed by addition of 200 μ L buffer AL, mixing and incubation for 10 min in a heat block at 56 °C. Thereafter, samples were mixed with 200 μ L ethanol (99%) and applied to DNeasy mini spin columns and centrifuged for 1 min at 8000 rpm. This was followed by one washing step with 500 μ L buffer AW1 and one washing step with 500 μ L AW2 and centrifugation for each step at 8000 rpm for 1 min. The spin column was transferred to a new 1.5 mL microcentrifuge tube and DNA was eluted by addition of 30 μ L aqua destillata, incubation for 1 min at RT and centrifugation at 8000 rpm for 1 min. The 30 μ L elution fraction was again added to the column and again centrifuged to maximise the DNA yield. The DNA yield was measured using the Nanodrop.

5.3.4.2 Polymerase chain reaction

For validation of successful hiPSC gene editing by CRISPR-Cas9, a polymerase chain reaction (PCR) was performed. To validate the integration of the *AAVS1-cTnT-NRAP/MYC*- or *AAVS1-cTnT-NRAP/GFP-OE* plasmids, gDNA was isolated as above-described in section 5.3.4.1. Using a forward primer in the left homology arm (HA-L For) and a reverse primer in the right homology arm (HA-R Rev) allowed distinguishing between WT, hetero- or homozygous clones. In WT clones, one band at ~870 bp and in the homozygous clones, a band at 7787 bp for the *NRAP/MYC*-OE cell line or 8474 bp for the *NRAP/GFP*-OE cell line was expected. Conclusively, heterozygous clones could be distinguished as these clones represented the WT as well as the respective homozygous band. However, in homozygous clones, only one band at 7787 bp or 8474 bp could be detected. In order to perform a long-range PCR, the LongAmp PCR kit from New England Biolabs (NEB) was used. Therefore, according to instructions of the manufacturer, the 5x LongAmp buffer, 300 μ M dNTPs, 0.4 μ M the forward and reverse primer, 200 ng gDNA or 1 ng plasmid DNA were combined with 5 units LongAmp polymerase per each 50 μ L PCR reaction. The cycling conditions were as follows: Initial denaturation for 2 min at 94 °C, 35 cycles of 30 s at 94 °C followed by 7 min at 65 °C. The final extension was performed at 65 °C for 10 min.

Similar to this validation setup, the successful generation of a *NRAP*-KO hiPSC line was validated by performing PCR amplifications with the LongAmp PCR kit from upstream of the 5' PAM site in the promotor-flanking region (KO FOR1) and downstream of the 3' PAM site (KO REV2) in the promotor region. The *NRAP* WT band in the control cell is 5805 bp while the successful generation of a KO would approximately result in a 477 bp PCR

product. Due to a smaller PCR product, the extension time during the 35 cycles was lowered to 5 min instead of 7 min for the *NRAP*-OE cell line validation.

For validation of smaller regions, the Dreamtaq polymerase was used. Therefore, 10x Dreamtaq buffer, 2.5 mM of each dNTP, 0.25 μ M of the forward and reverse primer, 200 ng of the respective gDNA were combined with 1.25 U Dreamtaq polymerase. The PCR cycling conditions were as follows: Denaturation at 95 °C for 3 min, followed by 35 cycles at 95 °C for 30 s, 30 s at the appropriate T_m and 1 min at 72 °C. The final extension was performed at 72 °C for 10 min, followed by storage at 4 °C until further processing. Since no homozygous *NRAP*-KO was found, but instead a compound heterozygous *NRAP*-KO, this hiPSC line was termed *NRAP*-knock-down (KD).

5.3.4.3 Agarose gel electrophoresis

For agarose gel electrophoresis, 1-1.5% agarose gels in 1x Tris-acetate-EDTA buffer (TAE) containing 2.3 μ L Midori Green per each 50 mL buffer were prepared. Therefore, the agarose solution was shortly boiled in a microwave until the agarose was dissolved. The solution was then cooled down to approximately 60 °C before the DNA-intercalating substance Midori green was added. The agarose solution was then transferred to the chamber containing a 20-well comb. After solidification of the agarose gel, it was transferred into a gel electrophoresis chamber filled with 1x TAE buffer. On each gel, 5 μ L of a 100 bp or 1 kb DNA marker and 10-50 μ L of samples that had been premixed with 6x loading dye were loaded. The gel was run at 120 V for approximately 45 min and then documented with the Chemidoc system.

5.3.4.4 PCR purification and sequencing

PCR products were purified with the high-pure PCR product purification kit from Roche according to the manufacturer's instructions. In brief, when PCR products were directly purified after PCR amplification, the amount of PCR product was added to water to 100 μ L total volume. To each PCR reaction, 500 μ L binding buffer was added, mixed and applied onto a high pure filter column. After centrifugation for 60 s at 13.000 g, two washing steps with 500 μ L and 200 μ L washing buffer with intermittent centrifugation steps followed. Subsequently, the PCR products were eluted in 30 μ L water from the columns into new 1.5 mL reaction tubes by centrifugation for 60 s at 13.000 g.

If PCR products were purified from agarose gels, 1-2% agarose gels were loaded with PCR products for approximately 45 min at 120 V. The appropriate band was cut out and transferred to a 1.5 mL reaction tube. Per each 100 mg gel slice, 300 μ L binding buffer was added, followed by incubation at 56 °C for 10 min with intermittent vortexing every 2-3

min. Afterwards, 150 μ L isopropanol for each 100 mg agarose slice were added to the mixture and applied to a high pure filter column. The washing and elution steps were performed as above described for the PCR product purification directly from PCR reactions. Subsequently to PCR product purification, the DNA amount was estimated by measuring the light absorbance at a wavelength of 260 nm using the Nanodrop.

For sequencing of purified PCR products, 150 ng of PCR product in water was added to 2 μ L of the appropriate forward or reverse primer to a total volume of 17 μ L in 1.5 mL Eppendorf tubes and sent to Eurofins for Sanger sequencing.

5.3.5 Production of master and working cell banks

As soon as heterozygous or homozygous CRISPR clones had been successfully identified and validated, clones were thawed as mentioned in section 5.2.2.2. However, CRISPR clones were thawed on a reduced-growth factor matrigel-coated (1:60 diluted in RPMI 1640) 48-well culture well plates, that had been pre-incubated for at least one hour at RT for coating. For CRISPR clones, mTESR⁺ without FGF was used instead of FTDA.

When the cell layer reached >90% confluence, cells were passaged to a 24-well culture well plate, then to a 12-well culture well plate and then to a 6-well culture well plate until approximately an amount of 4.5 Mio cells could be passaged into a T75 flask. During this procedure, coating was changed from reduced-growth factor matrigel to geltrex (1:100 in RPMI) and hiPSC were adjusted in 25% increments per day from mTESR⁺ media to FTDA supplemented with 0.3 μ L FGF per mL. After these adjustments, hiPSC were kept for at least one week at these conditions before freezing for a master cell bank. For producing a master cell bank, morphological images were taken using the EVOS microscope. The cells were counted both, manually and by CASY counter, and frozen as mentioned in section 5.2.2.3 for a master cell bank when the CASY values were: AGG>1.5 and viability >80%. The passage number for the production of master cell banks were p44 for the *NRAP/MYC*-OE hiPSC line, p35 for the *NRAP/GFP*-OE hiPSC line and p36 for the *NRAP*-KD hiPSC line. One part of the cells were kept in culture for 2-3 passages to freeze a working cell bank similarly to a master cell bank.

5.3.5.1 Mycoplasma testing

To ensure that the master cell bank, working cell bank and cell lines in culture are not contaminated with mycoplasma, mycoplasma testing was kindly performed by Anna Steenpaß and Ellen Orthey. In brief, 250 μ L media supernatant after at least one day of culture was mixed with 750 μ L aqua destillata and incubated for 10 min at 100 °C. The samples were briefly centrifuged and the supernatant transferred to a new microcentrifuge

tube. Per each sample 2 μL of the DNA sample were mixed with 48 μL master mix, consisting of 26.75 μL aqua destillata, 5 μL 10x buffer, 10 μL Q-solution, 4 μL of 25 mM MgCl_2 , 1 μL of the 10 pM primer pool, 1 μL dNTPs and 0.25 μL polymerase. For the PCR cycler program, the following settings were used: 15 min initiation phase at 95 °C, 40 cycles 30 s at 94 °C, 30 s at 56 °C and 1 min at 72 °C and a final extension for 10 min at 72 °C. Water served as negative control while contaminated medium supernatant was used as positive control. Afterwards, the PCR samples were loaded on a 1% (w/v) agarose gel in 1x TAE buffer for agarose gel electrophoresis which was performed at 120 V for approximately 45 min. The DNA bands were visualised with the Chemidoc and the Image Lab software.

5.3.5.2 Stage-specific embryonic antigen 3 detection by flow cytometry

Intending to investigate the pluripotency of cells from the master cell bank and working cell bank, immunofluorescence staining with the pluripotency marker stage-specific embryonic antigen 3 (SSEA3) was performed. During freezing of the master cell bank, 0.5 Mio cells were resuspended in FBS for blocking of unspecific antibody binding sites and incubated for >24 h at 4 °C. After this, cells were splitted into two flow cytometry tubes, centrifuged for 2 min at 800 rpm and 4 °C. These centrifugation settings apply for subsequent centrifugation steps. Ensuing, supernatant was removed, and cells were resuspended in 100 μL flow cytometry buffer with the appropriate antibody (1:50). For each sample, a staining with an isotype control, for adjustment of the proper settings at the NovoCyte Quanteon flow cytometer, and a staining with the SSEA3 antibody was performed. Cells were vortexed and incubated light-protected for 30 min in antibody solution at 4 °C. For removal of staining solution, 2 mL flow cytometry buffer was added to flow cytometry tubes followed by centrifugation. This procedure was repeated once before 500 μL PBS was applied to the isotype control tube and 250 μL to the respective SSEA3 sample. The samples were vortexed and immediately analysed at the NovoCyte Quanteon flow cytometer or BD Canto II. The isotype control was used for adjustments such as the removal of dead cells and cell clumps and then transferred to the SSEA3 sample. The data was analysed with the FlowJo software.

5.3.5.3 Karyotype analysis

Karyotyping was performed for quality control of hiPSC lines to exclude chromosomal abnormalities induced by CRISPR-Cas9 mediated genome editing. For this purpose, hiPSC from the respective CRISPR master cell bank were used when the cell layer was 80-90% confluent to isolate gDNA as described above.

The karyotyping procedure has kindly been performed by Elisabeth Krämer (IEPT, UKE) using the nCounter human karyotype panel from Nanostring. In brief, 1 µg gDNA was used for fragmentation through enzymatic digestion by the endonuclease AluI for 1-2 h at 37 °C in a thermal cycler. Successful digestion was validated by agarose gel electrophoresis. This was followed by the denaturation of samples at 95 °C for 5 min and subsequent incubation on ice for 2 min. For hybridisation, up to 10 µL of each DNA sample were mixed with a master mix containing 3 µL of reporter CodeSet and 5 µL of hybridisation buffer. Immediately before incubation at 65 °C for 16 h, 2 µL of capture probeSet were added to each sample. After hybridisation was completed, hybridised DNA was transferred from the nCounter cartridge (Nanostring) to the nCounter digital analyser (Nanostring) to start the 6 h analysis program. For the analysis of data, the nCounter CNV collector tool software was used by Elisabeth Krämer and Niels Pietsch (IEPT, UKE).

5.3.5.4 Off-target analysis

Since not only on-targets but also off-targets are predicted when designing gRNAs, the top ten predicted off-targets by the CRISPOR website tool were investigated for each cell line to exclude chromosomal abnormalities (**Table 1**). Therefore, unique primer for the specific gene region were designed using NCBI primer blast. As the same gRNA was used for the generation of the *NRAP/MYC-OE* and *NRAP/GFP-OE*, the same off-targets were validated for the *NRAP-OE* cell lines. Off-target analysis of the *NRAP-KD* hiPSC line was performed partly by Vanessa Lewandowski and partly by me.

Table 1: Predicted off-targets for the gRNAs of the *NRAP/MYC-OE*, *NRAP/GFP-OE* and *NRAP-KD* cell lines. The potentially affected genes are represented, the melting temperature (T_m) and the expected PCR product size [bp].

<i>NRAP/MYC</i> and <i>NRAP/GFP-OE</i>			<i>NRAP-KD</i> gRNA 1			<i>NRAP-KD</i> gRNA 2		
Off-target	T_m [°C]	PCR product [bp]	Off-target	T_m [°C]	PCR product [bp]	Off-target	T_m [°C]	PCR product [bp]
<i>APPL2</i>	58.5	1201	<i>SLC38A3</i>	62.9	322	<i>RNU6</i>	62.6	625
<i>QRFP</i>	58.5	801	<i>CLIC5</i>	58.1	635	<i>RP11-34F13.3</i>	58.5	1714
<i>MLIP-IT1</i>	58.5	1217	<i>EPC2</i>	60.7	336	<i>MRRF</i>	60.7	338
<i>SLC8A1</i>	58.5	1254	<i>PSD4</i>	60.0	309	<i>RP11-181K12</i>	57.2	568
<i>TTN</i>	59.5	1204	<i>EBP</i>	64.0	313	<i>RN7SKP279</i>	61.6	1276
<i>RP11-40A</i>	59.5	1202	<i>ABCB9</i>	63.1	316	<i>EXT1</i>	61.1	463
<i>CDK8</i>	60.1	1202	<i>MLLT6</i>	66.1	474	<i>FOXO3</i>	62.1	912
<i>RP11-556E</i>	60.1	1215	<i>RP11-506D12</i>	62.7	333	<i>ZC3HAV1</i>	62.5	945
<i>NAB1</i>	60.1	1253	<i>PGPR26</i>	58.3	673	<i>RPL11-TCEB3</i>	61.6	424
<i>RHOT2</i>	60.5	359	<i>RHOBTB2</i>	59.0	336	<i>ZNF720</i>	62.9	664

For PCR reactions, 10x dreamtaq buffer, 2.5 mM of each dNTP, 0.25 µM of the forward and reverse primer, 200 ng of the respective gDNA were combined with 1.25 U dreamtaq

polymerase. The PCR program was set to 95 °C for 3 min, followed by 35 cycles at 95 °C for 30 s, 30 s at the appropriate T_m of each primer pair and 1 min at 72 °C. The final extension was performed at 72 °C for 10 min, followed by storage at 4 °C until further processing. For the gene *RHOT2* optimisation of PCR conditions was required. Therefore, 5% DMSO was added to PCR reactions, PCR cycles were reduced from 35 to 30 and the extension time during the cycles was reduced from 1 min to 30 s. The PCR products were purified as described in section 5.3.4.4 with the High-Pure PCR product purification kit from Roche and subsequently sent to Eurofins for Sanger sequencing as described in section 5.3.4.4. The sequences were aligned to the sequence of the human genome in Snapgene. If point mutations were observed in the PCR products, PCRs and sequencings were repeated for the hiPSC control cell line to ensure that this cell line carries the same point mutation and avoid off-target effects induced by the Cas9.

5.4 Human-induced pluripotent stem cell derived cardiac myocytes

5.4.1 Cardiac monolayer differentiation

For differentiation of hiPSC into cardiac myocytes, hiPSC were cultured and passaged at least three times after thawing prior to cardiac myocyte differentiation induction. When cells were still in their growth phase, 550.000 cells were plated on 6-wells in FTDA (+FGF and Y-27632) on high-growth factor matrigel-coated 6-well plates. Beforehand, high-growth factor matrigel was diluted 1:60 in ice-cold RPMI and 1 mL per 6-well culture well plate were distributed and incubated for at least 1 h at 37 °C. Approximately 12 h in advance to mesoderm induction, Y-27632 was removed and cells were incubated with FTDA, supplied with FGF.

As soon as the cell layer reached approximately 60-70% confluency, the medium was aspirated and replaced by Stage 0 medium to induce mesoderm induction. From this time point onwards, cells were incubated in a normoxic incubator at 37 °C, 5% CO₂ and 20% O₂. Stage 0 medium was replaced by Stage 1 medium, 12-15 h post-mesoderm induction. Additional 48 h later, cells were washed with RPMI and the medium was replaced with Stage 2.1 medium to induce cardiac differentiation. On day 5, after another 48 h of incubation with Stage 2.1 medium, the medium was replaced by Stage 2.2 medium containing, in addition to Stage 2.1 medium, insulin. From day 7 onwards, hiPSC-derived cardiac myocytes received every second day fresh cardiac myocyte medium and were monitored daily for spontaneous beating. For each cell line, the best cardiac differentiation condition was tested, Therefore, for each cell line, cell densities of 500.000 cells/well, 550.000 cells/well and 600.000 cells/well as well as differentiation media with 8 ng/mL activin A or 12 ng/mL activin A concentration were tested. Based on the beating behaviour

and measured cardiac myocyte amounts by cTnT stainings and flow cytometry, the most appropriate condition for each cell line has been selected.

5.4.2 Dissociation of hiPSC-CMs from monolayer differentiation

When wave-like beating behaviour of hiPSC-derived cardiac myocytes could be observed, cells were dissociated with collagenase into single cells that were used for two-dimensional plating, generation of engineered heart tissues (EHTs) or freezing. The cardiac differentiation of *NRAP*-KD hiPSC, dissociation and generation and culture of EHTs was performed parallel to the differentiation of the *NRAP*-OE cell lines with the help of Vanessa Lewandowski.

Therefore, the medium was removed from 6-well plates and replaced with Hank's Balanced Salt Solution (HBSS). Beyond 2 min incubation, the HBSS washing solution was removed and the step was repeated once before adding 1 mL collagenase solution per well. After up to 2 h incubation at 90% relative humidity (rH), 5% CO₂, 20% O₂ when cells started to disaggregate, cells were gently triturated five times with a 5 mL serological pipette and transferred into 50 mL falcon tubes. An equal amount of blocking buffer was added to neutralise digestion. The cell suspension was centrifuged for 10 min at 100 g and resuspended in non-cardiac myocyte medium (NKM) by gently triturating 5 times with a serological pipette. The number of cells was counted and cells were again centrifuged and resuspended in appropriate amounts of NKM for further purposes such as the generation of EHTs or freezing cells.

5.4.3 Flow cytometry

In order to determine the successful differentiation of hiPSC into cardiac myocytes, cells were stained for the cardiac myocyte-specific marker cTnT, followed by cardiac myocyte proportion analysis by flow cytometry. For that purpose, 0.5 Mio dissociated cardiac myocytes were transferred into a flow cytometry tube with 2 mL PBS and centrifuged at 1000 rpm for 3 min. These centrifugation parameters were used in the following centrifugation steps of this chapter. The supernatant was removed, and cells were fixed with 0.5-1 mL Roti Histofix for 20 min on ice. After fixation, 4 mL PBS was added and cells were again centrifuged, followed by two washing and centrifugation steps with 0.5 mL flow cytometry permeabilisation buffer. The cells were kept light-protected in permeabilisation buffer overnight at 4 °C.

On the following day, samples were equally distributed to two flow cytometry tubes, centrifuged and resuspended in the appropriate isotype control antibody (1:50) or the cTnT APC antibody (1:50). After at least 45 min light-protected incubation at 4 °C, 2 mL

permeabilisation buffer were added, followed by centrifugation and washing of cells with 500 μ L permeabilisation buffer. In addition, one washing step with 1 mL PBS per tube was performed before samples were stored in 300 μ L PBS at 4 °C until flow cytometry analysis at the Canto II or Quanteon machine.

5.4.4 Freezing and thawing of cardiac myocytes

Subsequently to dissociation of cardiac myocytes after cardiac differentiation, cardiac myocytes were either used for two-dimensional culture, for the generation of EHTs or frozen. For freezing of cardiac myocytes, cells were washed once with PBS, and then centrifuged at 100 g for 10 min. After centrifugation, the supernatant was removed and cells were carefully resuspended in appropriate volumes of FBS, supplemented with 20% DMSO and transferred to cryotubes. In each cryotube, between 2-20 Mio cardiac myocytes were frozen. Cryotubes were inverted and stepwise frozen with a Mr. Frosty at -80 °C. On the following day, frozen cells were transferred to -150 °C for storage and to liquid nitrogen tanks for long-term storage.

For thawing of cardiac myocytes, cryopreserved cardiac myocytes were defrosted for 2-3 min in a waterbath at 37 °C until approximately 20% frozen cells remained. The cell suspension was gently transferred into a 50 mL falcon tube using a 2 mL serological pipette to avoid cell damage. The cryovial was rinsed with 1 mL pre-warmed cardiac myocyte thawing medium that was dropwise added over 90 s to the falcon tube with cells. This step was repeated once over 60 s before another 7 mL of the same medium was added over 30 s to the cell suspension. During that process, the proper mixing of the medium with the cells was ensured by swirling the 50 mL tube. The cells were counted using a Neubauer chamber and trypan blue and then centrifuged for 10 min at 100 g and RT. The cells were washed once in the same thawing medium and again centrifuged to remove the remaining collagenase from the dissociation process. After centrifugation, cells were carefully resuspended in the respective amount of EHT culture medium or NKM.

5.4.5 Culture of cardiac myocytes

In order to culture cardiac myocytes for downstream protein analysis or immunofluorescence, 35 mm dishes were coated with a layer of 1 mL of 1% (w/v) gelatine in PBS for 30 min at 37 °C. Prior to plating of cardiac myocytes, the 1% gelatine-coated 35 mm dishes were washed with PBS and either 400.000 cells for immunofluorescence staining or 1 Mio cells for protein analyses per 35 mm dish were plated in EHT culture medium. The hiPSC-derived cardiac myocytes were cultured for 7 days at 37 °C, 20% O₂ and 5% CO₂ with medium exchange three times a week.

5.5 Engineered heart tissues

5.5.1 Generation and culture of engineered heart tissues

Fibrin-based human-derived or NRVMs-derived EHTs were generated as previously described (Hansen et al. 2010, Breckwoldt et al. 2017). Initially, casting moulds were prepared in a 24-well plate format with 2% agarose solution in PBS and polytetrafluoroethylene (PTFE) spacer, allowing to generate a mould in which the EHTs can be embedded (**Figure 9 A, C**). After the agarose had solidified, transparent polydimethylsiloxane (PDMS) posts were placed into the casting moulds and 100 μ L of the master mix were pipetted into the agarose moulds (**Figure 9 B, C**). For human-derived EHTs, 1 Mio cardiac myocytes, 5.6 μ L 2x DMEM, 0.1% of 10 mM Y-27632, 2.5 μ L fibrinogen (200 mg/ml in NaCl 0.9%), 3 μ L thrombin and 97 μ L NKM per EHT were mixed. For NRVMs-based EHTs, NRVMs were directly used after isolation and before pre-plating. The EHT master mix contained 550.000 cells, 5.5 μ L 2x DMEM, 2.5 μ L fibrinogen and 3 μ L thrombin per calculated EHT. To allow polymerisation of the fibrin, the EHT plate was incubated at 37 °C, 7% CO₂, 40% O₂ and 98% relative humidity for 1.5-2 h. EHTs were overlaid for 30 min with 500 μ L pre-warmed NKM and then transferred into a new 24-well plate containing pre-warmed EHT culture medium. Three times a week, EHTs were transferred to a feeding plate with EHT culture medium that had been supplemented with 200 μ M tranexamic acid for matrix stabilisation.

5.5.2 Treatment of NRVMs-derived engineered heart tissues

NRVMs-derived EHTs were daily treated for 7 days in an early treatment from day 2-9 after casting or in a late treatment from day 14-21 after casting in EHT culture medium with 3 μ M of the pharmacological PKD inhibitor BPKDi in DMSO or DMSO only as the corresponding vehicle control in the presence or absence of 20 μ M of the pro-hypertrophic stimulus PE.

5.5.3 Video-optical contraction analysis

Approximately 7-10 days after EHT generation, a macroscopically visible beating pattern could be observed allowing video-optical contraction analysis of EHTs for different parameters such as force, frequency and contraction kinetics (Hansen et al. 2010; Schaaf et al. 2011). Three times a week, 1.5-2 h after the medium exchange, the 24-well plate with the EHTs was placed into a test system that allows automated video-optical analysis for the above described parameters.

This system contains an integrated incubator allowing controlled conditions for the EHTs at 37 °C, 7% CO₂, 72% N₂ and 21% O₂. The top of the integrated incubator includes a

glass area through which the above-placed XYZ-axis camera system can record movies of each EHT of the 24-well plate that is defined by specific XYZ coordinates in the corresponding software of the camera system (**Figure 9 A**).

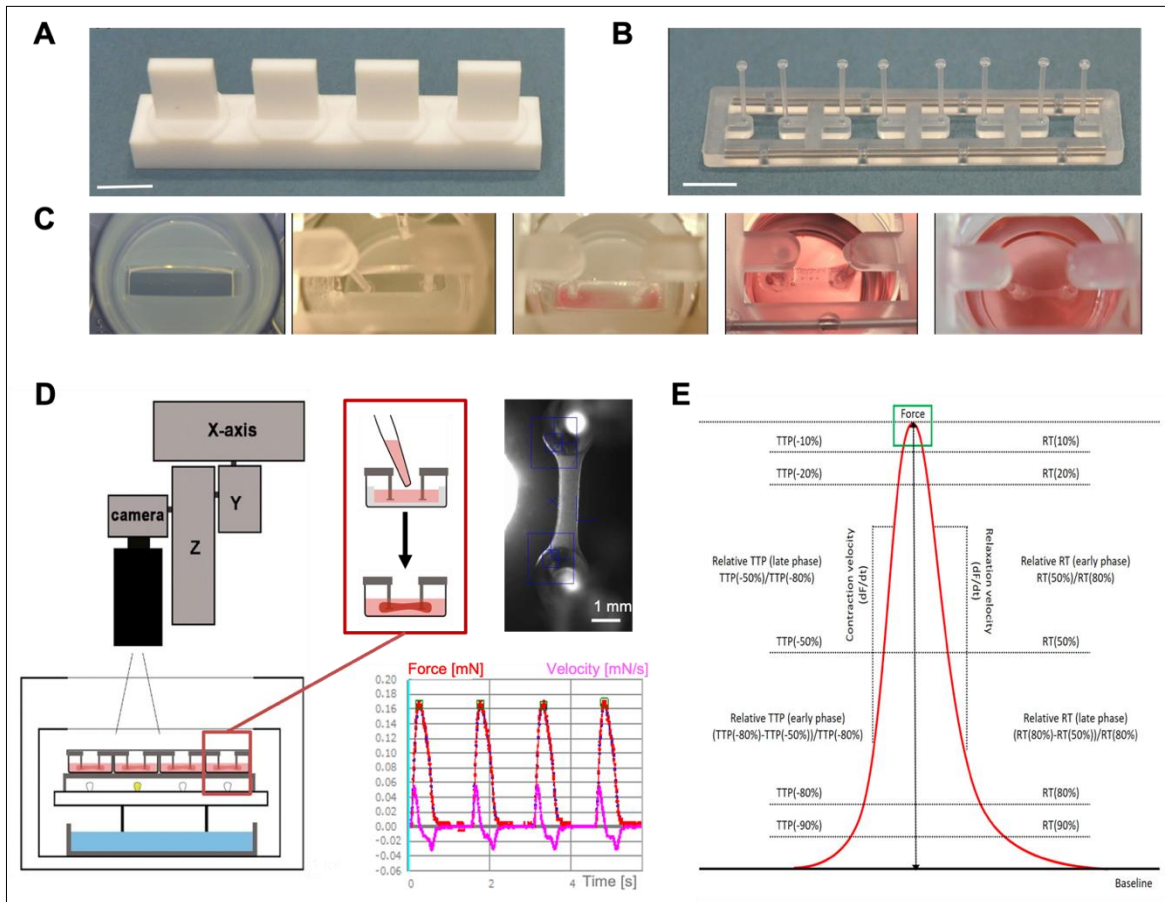


Figure 9: Generation of EHTs and video-optical EHT contraction analysis system. A) Polytetrafluorethylene (PTFE) spacer, **B)** polydimethylsiloxane (PDMS) rack, **C)** generation process of EHTs (from left to right). Represented are an agarose casting mould, the insertion of PDMS racks, the addition of the EHT master mix into moulds, the freshly transferred EHTs from casting moulds into medium and remodeled EHT after 15 days of culture. The scale bar is equal to 1 mm. Images **A-C)** are adapted from (Mannhardt et al. 2017). **D)** Schematic overview of the 24-well plate in the incubation system with the camera system on top. In the system the crosses can be set to the EHTs posts via the XYZ-axis system to measure contraction traces. The schematic illustration was modified from (Schaaf et al. 2011). **E)** The system uses the EHT shortening for the calculation of different contractile parameters such as force, frequency, time to peak (TTP) and relaxation time (RT).

In the customised software, x- and y-coordinates and the borders between posts and EHTs must be adjusted manually for each EHT to allow depicting the EHT shortening during contraction. The software then measures EHT shortening over time and calculates contractile parameters (e.g. force [mN], frequency [Beats per minute], contraction [s] and relaxation time [s] and RR scatter [s]) that result in output excel files with automatically calculated values by the software (**Figure 9 B**). The measurement of each EHTs varied between 10 s and 20 s for human EHTs and 60 s for NRVMs-derived EHTs since these

are beating in bursts. For the calculation of different parameters, at least four contraction peaks were required.

5.5.4 Electrical synchronisation

In order to allow analysis of force differences between different EHT groups, frequencies were electrically synchronised. For that purpose, EHTs were cultured on top of custom-made graphite pacing electrodes for 2 h with 2 mL EHT culture medium, at 37 °C, 7% CO₂, 72% N₂ and 21% O₂. Human EHTs were initially measured as above-described without electrical stimulation in the test system, followed by short-term electrical pacing as previously described with biphasic pulses (4 ms per direction) at 2 V (electrical field strength 2 V/cm) and a frequency of 0.5 to 4 Hz with increasing increments of 0.5 Hz (Hansen et al. 2010, Hirt et al. 2014).

However, due to a different beating behaviour and frequency in NRVMs-derived EHTs, these were electrically synchronised at 2.5 V, 4 ms biphasic pulses and 2-3 Hz with 0.5 Hz increasing increments. EHTs that could not be electrically synchronised were excluded from the analysis. After the finalisation of the electrical pacing, EHTs were used for downstream applications. For RNA or protein analyses, EHTs were washed once in PBS, transferred to 2 mL Eppendorf tubes and frozen in liquid nitrogen. The EHTs were kept at -80 °C until further processing.

5.5.5 Action potential measurements

Action potentials were kindly measured by Anna Steenpaß as previously described (Wettwer et al. 2013). For recordings, sharp microelectrode measurements of intact control EHTs, homozygous *NRAP/MYC*-OE EHTs or *NRAP*-KD EHTs were performed at an age of 28-42 days. In brief, EHTs were fixed in a recording chamber with two needles at the two ends of the EHTs and were superfused with a flow rate of 40 mL tyrode solution per 15 min at 37 °C. Sharp electrode measurements were performed using a tip resistance between 20 and 50 MQ (tip filled with 2.5 M KCl). The duration of the stimulation was set to 0.1x 6 ms and to 10x volts. For electrical stimulation of EHTs, the volts were adjusted to 1.5x threshold voltage. The data were analysed by the LabChart 5 software.

5.5.6 Frank-Starling measurements

Prior to Frank-Starling measurements, EHTs were cultured for three weeks and measured on day 22 of culture. The measurements were performed in a frequency-controlled (1 Hz) organ bath with four transducers in which the EHT silicon racks can be inserted allowing measurements of four EHTs at the same time. The preload of each EHT was set manually

in 10 μm steps without applying stretch to EHTs. The organ bath was perfused with Tyrode's solution, washed once with 0.6 mM CaCl_2 and then with 1.8 mM CaCl_2 for baseline measurements with constant diffusion with carbogen (95% O_2 and 5% CO_2) to stabilise the pH. The measurements and data analysis were performed with the LabChart software.

5.5.7 Transmission electron microscopy

For transmission electron microscopy, EHTs were fixed in 4% PFA and 1% glutaraldehyde in PBS overnight at 4 °C. The following steps of the transmission electron microscopy and measurement of lateral intercalated disc width were performed by Dr. Michaela Schweizer and Julie Lange. In brief, fixed EHTs were washed three times with 0.1 sodium cacodylate buffer at a pH of 7.2-7.4. The samples were rinsed with 1% osmium tetroxide in cacodylate buffer, dehydrated with increasing ethanol concentrations, washed twice in propylene oxide followed by embedding at 60 °C for 2 days. The mounted EHTs were used to prepare 60 nm thick sections and stained with uranyl acetate and lead citrate prior to observation with the EM902 electron microscope (Zeiss) using a TRS 2K digital camera.

5.5.8 Dissociation of engineered heart tissues

For dissociation of EHTs, EHTs were washed several times with HBSS and then incubated in papain solution for approximately 45 min at 37 °C, 90% humidity, 20% O_2 and 5% CO_2 . The digestion was regularly monitored and EHTs were gently triturated 4-5 times with a 1000 μL pipette. The cells were transferred to a falcon tube and the same amount of papain blocking buffer was added prior to centrifugation at 100 g for 10 min at RT. The cells were resuspended in HBSS, triturated and again centrifuged before dry-freezing cell pellets for further investigations. The papain dissociation was performed with the help of Hannah Münch.

5.5.9 Proteomics

For tryptic digestion, samples were dissolved in 100 mM triethyl ammonium bicarbonate and 1% w/v sodium deoxycholate buffer, followed by boiling at 95 °C for 5 min and sonification with a probe sonicator. Subsequently, disulfide bonds were reduced with (1 μL of 1 M) dithiothreitol for 30 min, alkylated in the presence of (4 μl of 0.5 M) iodoacetamide for 30 min in the dark and digested with (1.5 μL of 1 $\mu\text{g}/\mu\text{L}$ trypsin) at 37 °C overnight. Sodium deoxycholate was precipitated by the addition of 1% (v/v) formic acid followed by centrifugation at 16.000 g. The supernatant was transferred into a new tube and samples

were dried in a vacuum centrifuge. For LC-MS/MS analysis, samples were dissolved in 20 μ L 0.1% FA.

The digested peptides were analysed by LC-MS/MS by injection of the samples onto a nano-liquid chromatography system coupled via electrospray-ionisation to a mass spectrometer (MS) equipped with a quadrupole, a linear trap and an orbitrap. This was followed by injection of samples (5 μ L/min) into a column (Acclaim PepMap μ -precolumn, C18, 300 μ m x 5 mm, 5 μ m, 100 Å). The column was washed for 5 min with 2% of buffer B (5 μ L/min) (0.1% FA in ACN) prior to transfer of peptides to the separation column (200 nL/min) with a gradient of 2-30% in a time interval of 65 min (Acclaim PepMap 100, C18, 75 μ m x 250 mm, 2 μ m, 100 Å). The production of the spray occurred by a fused-silica emitter (10 μ m) at a capillary voltage of 1650 V. The measurement of mass spectra was performed in a positive ion mode and the analysis with the orbitrap Fusion in the data-dependent acquisition mode (DDA; 28% HCD collision energy, threshold of 0.00002, isolation width of 1.6 m/z, m/z range 400-1500, resolution of 120.000 FWHM at m/z 200, transient length of 256 ms, maximum injection time of 50 ms). The MS spectra were obtained from the ion trap (scan-rate of 66 kDa/s, maximum injection time of 200 ms, AGC target of 0.0001, underfill ratio of 10%, isolation width of 2 m/z).

The data analysis of the LC-MS/MS was carried out with the proteome discoverer 2.4.1.15. Proteins were identified and quantified using the search engine Sequest HT (homo sapiens SwissProt database) with the following settings: Precursor mass tolerance of 10 ppm, fragment mass tolerance of 0.2 Da, two missed cleavages allowed, carbamidomethylation on cysteine residues as a fixed modification and oxidation of methionine residues as a variable modification. Peptides with a FDR of 1% using Percolator were identified. At least two unique peptides per protein were used as a condition for a reliable identification. The tryptic digestion of samples, the LC-MS/MS procedure and the initial data analysis were kindly performed by Sönke Harder and Hannah Voß (UKE).

5.6 Molecular analyses

5.6.1 RNA isolation

Ribonucleic acid (RNA) was isolated from either two-dimensional cultured hiPSC-CMs or EHTs with TRIzolTM reagent, according to the manufacturer's instructions (Thermo Fisher Scientific). In brief, 0.5 or 1 mL TRIzolTM were added to each EHT or 6-wells with cells in order to lyse samples. Subsequent reactions were performed at 4 °C and amounts are per 1 mL TRIzolTM that was initially used for lysis. After homogenisation using a tissue lyser

(2x 30 s), samples were incubated for 5 min before 0.2 mL chloroform was added, followed by another 2-3 min incubation. Subsequently, samples were centrifuged for 15 min at 12.000 g. The aqueous phase was added to 0.5 mL isopropanol and incubated for 10 min prior to centrifugation for 10 min at 12.000 g. The pellet was resuspended in 1 mL 75% ethanol, vortexed and centrifuged for 5 min at 7500 g. The RNA pellet was air dried for 5-10, resuspended in 30 μ L RNase-free water and incubated for 10-15 min at 55-60 °C. The RNA concentration was determined with the NanoDrop™ 1000 spectrometer and stored at -80 °C until further processing for complementary deoxyribonucleic acid (cDNA) synthesis. The RNA isolation was performed with the help of Vanessa Lewandowski and Hannah Münch.

5.6.2 cDNA synthesis

Reverse transcription of RNA into cDNA was performed using the cDNA reverse transcription kit (Applied Biosystems). For each reaction, 2 μ L 10x reverse transcriptase buffer, 0.8 μ L 100 mM deoxynucleoside triphosphate (dNTPs), 2 μ L random primer, 4.2 μ L aqua destillata and 1 μ L reverse transcriptase were combined and mixed with 500 ng RNA sample. The PCR cycler was set for 10 min to 25 °C, for 120 min to 37 °C and then for 5 min to 85 °C. The cDNA was then stored until -20 °C until usage for experiments.

5.6.3 Realtime quantitative polymerase chain reaction (RT-qPCR)

Human and rat primers were designed with the National Centre for Biotechnology Information (NCBI) tool primer blast, matching the following criteria: exon-exon junction, ~20 nucleotides, ~60% guanine/cytosine content, low self-complementarity. The primer sequences are listed in the materials section (11.2). For rat and human samples, *GusB* was used as a housekeeping gene. Each 10 μ L sample was investigated in triplicates in a 384-well plate and included 100 nM of each forward and reverse primer, 5 μ L SYBR green/ROX mix and 50 ng cDNA or nuclease-free water for negative controls. SYBR green was used as a fluorescent marker binding double-stranded DNA fragments allowing to measure PCR product levels continuously during 40 cycles. Quantitative real-time PCR (RT-qPCR) was performed using the 7900HT fast real-time PCR system with the following amplification conditions: For initiation and denaturation the machine was set to 50 °C for 2 min and 95 °C for 10 min, followed by 40 cycles 95 °C for 15 s and 60 °C for 1 min. The final cycle was performed with the dissociation phase at 95 °C for 15 s, 60 °C for 15 s and 95 °C for 15 s.

To calculate the fold change, cycle threshold (CT) values of the respective housekeeping gene *GusB* were subtracted from CT values of the appropriate gene of interest. Afterwards, delta CT values were normalised to the mean of the control group (DMSO) to

calculate the delta delta CT. The fold change of the values was calculated by $2^{(-\text{delta delta CT})}$.

5.7 NRAP antibody development and validation

Considering that no appropriate human NRAP antibodies were available at the beginning of this project, a strategy to generate a polyclonal NRAP antibody was developed and produced with the help of the company Davids Biotechnology (Regensburg, Germany). Therefore, the peptide AKKAHELASDIKYRQDFNK was synthesised (2262.75 g/mol) and used for a five-step immunisation plan (**Figure 10**).

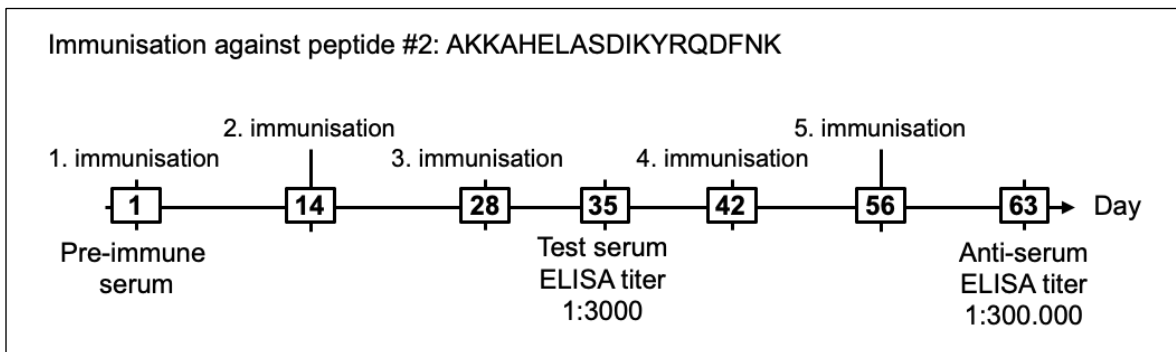


Figure 10: Immunisation plan for the development of a polyclonal rabbit anti human NRAP antibody. Rabbits received five immunisations in a 63-day protocol. On day 35, the titer of the test serum was tested by enzyme-linked immunosorbent assay (ELISA, titer: 1:3000). On day 63, the test serum was affinity- purified and the titer was again determined by ELISA (titer: 1:300.000). The development and preparation of the antibody was performed by the company Davids Biotechnology.

The immunisations were performed in intervals of two weeks. On day 35 and in the end, on day 63, the enzyme-linked immunosorbent assay (ELISA) titer was determined. The titer represents the concentration of the antibody in the blood and is stated as the highest dilution at which the antibody is still detectable.

The titer of the test serum at day 35 was 1:3000 while the final antiserum reached a titer of 1:300000. The final antiserum was then affinity-purified revealing an anti-NRAP concentration of 1.06 mg/mL. In order to validate the antibody, different dilutions were investigated for western immunoblotting and immunofluorescence for tissue derived from humans, mice and rats. The detailed procedure for antibody validation is described in section 5.7.

5.8 Protein analysis

5.8.1 Sample preparation and SDS-PAGE

Total protein extracts of cells for biochemical analysis were generated by scraping 1 Mio plated cells after appropriate culture from gelantine-coated 6-well culture well plates in 100-300 μ L 3x reducing sample buffer. The protein lysate was transferred into 1.5 mL reaction tubes. For human heart or mouse protein samples, frozen tissue was powdered using a metal device on liquid nitrogen and 10-20 mg of heart powder was transferred to cryotubes. To generate 10% heart homogenates, appropriate amounts of 100 mM Tris pH 7.4, supplemented with cComplete protease inhibitor, were added. Two metal beads per cryotube were added and homogenised twice for 20 s with the tissue lyser. Heart homogenates were then added to 3x reducing sample buffer or frozen at -80 °C. Prior to use, all protein samples were boiled at 95 °C for 5 min to denature proteins. All SDS samples were directly used for further applications or stored at -20 °C until further processing. For SDS-PAGE, equal amounts (2.5-25 μ L) of SDS samples and 5 μ L of Precise Plus protein marker (Bio-Rad) were run on 9% or discontinuous (5% and 10.5%) self-produced acrylamide gels.

5.8.2 Western immunoblot analysis

For western immunoblotting, SDS-gels were immunoblotted on polyvinylidenfluorid (PVDF) membranes after activation of membranes in methanol for 20 s. For initial testing of the custom-made human NRAP antibody, additionally nitrocellulose membranes were tested in combination with an antibody dilution series (1:100, 1:500, 1:1000, 1:2000 and 1:5000).

Prior to blotting, filter paper and membranes were washed in transfer buffer. Semi-dry blotting was performed at 45 mA per membrane for 2 h at RT. After the semi-dry blotting, proteins on nitrocellulose membranes were stained with Ponceau Red. Subsequently, un-specific binding sites were blocked by incubation of PVDF membranes for 1 h at RT with 10% non-fat dry milk or 3% BSA for nitrocellulose membranes in tris-buffered saline with 0.1% tween-20 (TBS-T) buffer. Afterwards, a sequential incubation with the appropriate primary antibodies overnight, four intermittent 15 min washing steps in TBS-T to remove unbound antibodies and incubation for 1 h with the species-matched secondary antibody in 1% non-fat dry milk or 0.3% BSA in TBS-T was performed. Another four 15 min washing steps in TBS-T followed this prior to analysis. Chemiluminescence reactions were visualised at the Chemidoc system (BioRad) using an ECL substrate. Afterwards, PVDF membranes were stained with coomassie for 15 min at RT to detect total proteins, followed by washing twice in destain solution for 15 min each.

5.9 Immunofluorescence

5.9.1 Preparation and immunofluorescent staining of heart sections

For the preparation of cryosections, frozen WT and *Mybpc3*-KI hearts (-80 °C) or frozen human heart tissue from a DCM patient (-80 °C) were embedded in Tissue Tek OCT medium and 10 µm thick sections were cut with a cryostat. The sections were immediately transferred to SuperFrost Plus adhesion microscope slides and incubated overnight at RT.

For fixation, sections were incubated for 5 min in ice-cold acetone at -20 °C and afterwards rehydrated in PBS for 5 min at RT. For initial testing of the NRAP antibody on DCM heart sections, additionally fixation with 4% paraformaldehyde (PFA) in PBS for 10 min at RT, followed by three washing steps with PBS was tested as well as fixation with ice-cold methanol for 5 min at -20 °C. In order to block unspecific binding sites, heart sections were blocked with 5% normal goat serum (NGS) in 1% BSA immunofluorescence buffer. All subsequent incubations were performed in a humidified chamber at RT while shaking. After 20 min incubation, the blocking solution was replaced by a primary antibody solution in 1% immunofluorescence buffer and incubated for 1 h. After three intermittent washing steps with PBS, sections were incubated with secondary antibodies in immunofluorescence buffer for 30-60 min. Subsequently to three more washing steps with PBS, heart sections were mounted with a mounting medium. Cover slips were added onto the mounting medium and fixed with nail polish. The sections were stored at 4 °C until analysis by microscopy.

5.9.2 Preparation and staining of engineered heart tissue sections

For the preparation of EHT sections, EHTs were first incubated in 30 mM butanedione monoxime (BDM) in PBS for 10-15 min at RT to allow relaxation of cardiac myocytes and then incubated in Roti Histofix for 12-16 h at 4 °C for fixation. EHTs were then removed from silicon posts and stored in TBS Azide at 4 °C until the preparation of EHT sections.

In order to prepare sections, fixed EHTs were embedded in agarose blocks. For that purpose, 4% agarose in PBS was prepared and filled in 24 well plates. The EHTs were immediately placed into the liquid agarose. After solidifying of the agarose, the agarose blocks were either overlaid with PBS, plates sealed with parafilm and stored at 4 °C or directly used for sectioning. Therefore, the agarose blocks were extracted from the plates, trimmed with a scapel and glued onto the vibratome plate. This was set into the reservoir which was filled up with PBS. For preparing the sections, the vibratome settings were set to 100 µm thick sections, the frequency to 5 and the speed to 7-8. The EHT sections were

placed each into a single PBS-filled well of a 24 well plate and stored at 4 °C until further processing.

For immunofluorescence staining of EHT sections, non-specific binding sites of antibodies were firstly blocked similarly with permeabilisation with 250 µL 0.3% Triton- X100 in immunofluorescence buffer per 24-well at RT for 60 to 90 min. The blocking buffer was removed and replaced by 250 µL primary antibody solution overnight at 4 °C on a shaker. After three intermittent washing steps in PBS for 5 min, sections were incubated with 250 µL secondary antibody solution, 4',6-Diamidin-2-phenylindol (DAPI) and wheat germ agglutinin (WGA) or phalloidin for 90 min at RT, followed by another three washing steps with PBS. The sections were then transferred to a glass slide, mounted with mounting medium and cover glasses. Until confocal microscopy, stained sections were stored at 4 °C. The immunohistochemical staining of EHT sections for dystrophin, the proliferation marker Ki67 and the apoptosis marker caspase 3 was performed by Kristin Hartmann from the mouse pathology facility at the UKE.

5.9.3 Immunofluorescence staining of cardiac myocytes

Cardiac myocytes were fixed with 4% PFA in PBS for 10 min at RT and washed three times with PBS prior to staining. Whereas cells that had been stained for MitoSPY, were pre-incubated with 250 nM MitoSPY in the culture medium for 30 min at 37 °C, washed with PBS and then fixed with Roti-histofix for 20 min. For storage, plates/dishes were covered with parafilm and kept in PBS at 4 °C.

For permeabilisation of cells, PBS was removed from wells and replaced with 0.2% Triton X-100 or 0.1% saponin in PBS for 5 min at RT. All incubation steps were performed in a humidified chamber at RT while shaking if not stated otherwise. After washing in PBS for 5 min, non-specific antibody binding sites were blocked with 5% NGS in IFB for 20 min, followed by primary antibody incubation overnight in IFB at 4 °C. On the next day, three washing steps with PBS were performed and replaced by secondary antibodies, 4',6-diamidino-2-phenylindole (DAPI) and phalloidin (F-actin) or WGA for 3 h. Thereafter, cells were washed three times with PBS and were then covered with mounting medium, coverslips and nail polish as previously mentioned. Samples were stored at 4 °C until microscopy.

5.9.4 Confocal microscopy

The Zeiss LSM 800 airyscan confocal microscope was used as imaging system and the Zeiss Zen software to analyse captured images. These were recorded with the 40x or 63x oil immersion objectives. In order to capture negative controls, respective controls were

only stained with secondary antibodies, DAPI and WGA or phalloidin for staining of actin and captured at the same laser and magnification settings.

5.10 Data analysis

5.10.1 Softwares

Data were analysed using Excel 2010, the BioRad software ImageLab, CanoScan, ImageJ, GelQuant, FlowJo, LAbChart and Zeiss ZEN software. The representation and statistical analysis were performed in GraphPad Prism 6.0. References were cited using the Endnote X6 software. Images were processed with ImageJ or the Zeiss ZEN software and visualised as single channels, overlays, or specific areas from the confocal dataset.

For qPCR analysis, the Sequence Detection System 2.4 was used. The raw data were exported in Excel files and the log₂ fold change was calculated by the comparative $\Delta\Delta C_t$ method, according to the description by Livak and Schmittgen in order to normalise the target to the reference mRNA amount of the reference gene Gsa or GusB (Livak and Schmittgen 2001). Western blots were analysed with the BioRad software ImageLab. For quantification of protein expression, ImageJ or GelQuant were used and subsequently normalised to actin loading controls using Excel 2010.

5.10.2 Statistical analysis

For analysis of significance, GraphPad Prism version 6.0 was used. If two groups were compared with each other, unpaired, non-parametric t-test was performed, while if more groups were compared to the mean of the control group, one-way ANOVA and Tukey's, Bonferroni's or Dunnett's posthoc test were performed. Values of $p < 0.05$ were considered as not significant. Values below $p < 0.05$ were indicated with one asterisk, $p < 0.01$ with two asterisks, $p < 0.001$ with three asterisks and $p < 0.0001$ with four asterisks for posthoc tests that were performed subsequently to one-way ANOVA. If t-test was performed, significances were depicted in the figures with hashes instead of asterisks. All quantitative data shown in this study are represented as means \pm standard error of the mean (SEM) of values that were obtained from at least three technical and biological replicates for each group.

6. Results

6.1 Impact of different culture conditions on hiPSC characteristics

At the beginning of the project, the impact of differences in culture conditions on hiPSC was investigated. Therefore, skin biopsies of 52 unrelated probands were reprogrammed into hiPSC by using a Sendai virus with pluripotency factors. The cells were subsequently cultured at 5% O₂ (defined as hypoxia) or 20% O₂ (defined as normoxia) and master cell banks were generated (**Figure 11 A**). Culture at normoxia had no impact on the morphology of cells but revealed chromosomal abnormalities in 50% of normoxic cultured hiPSC with 32% mosaic karyotypes and 18% chromosomal aberrations (**Figure 11 B-D**). In mosaic karyotypes different karyotypes appear in different cells. In comparison, 69% of hypoxic-cultured hiPSC showed a normal karyotype and only 31% of karyotypes were abnormal. The occurrence of karyotype abnormalities as a result of differences in passage number between conditions was ruled out (**Figure 11 E**).

For the investigation of hiPSC cell properties, pluripotency was assessed by measuring the stage-specific embryonic antigen 3 (SSEA3) levels. Hypoxic hiPSC culture resulted in significantly higher pluripotency compared to normoxic culture (**Figure 11 F**). As cellular hypoxia is characterised by induction of the hypoxia inducible factor 1 α (HIF1 α) pathway, western blot analysis was performed in order to validate the activation of this pathway. This resulted in significantly higher HIF1 α protein levels in hypoxic-cultured hiPSC compared to normoxic-cultured hiPSC (**Figure 11 G, H**).

Since the loss of pluripotency and increased mutations upon abnormal oxygen tensions have been associated with senescence (Busuttill et al. 2003; Kwon et al. 2017), the cellular senescence of normoxic- and hypoxic-cultured hiPSC was investigated. Therefore, the activity of the senescence marker SA- β -galactosidase was assessed by using its product 5-Bromo-4-chloro-3-indoxyl- β -D-galactopyranoside (X-gal). The hydrolysed end product produces a detectable blue colour in senescent cells allowing the detection and quantification by microscopy. Culture at normoxic oxygen tensions resulted in significantly increased X-gal staining compared to hypoxic-cultured hiPSC (**Figure 11 I**). To investigate whether the senescence might be induced by paracrine factors, the hypoxic and normoxic medium was exchanged after 12 h of culture to the respective other culture condition for another 24 h. This step was repeated once. Indeed, the exposure of hypoxic-cultured hiPSC to normoxic medium induced enhanced senescence in those cells whereas normoxic-cultured hiPSC that had been exposed to hypoxic-preconditioned medium, revealed no decrease in X-gal staining.

Results

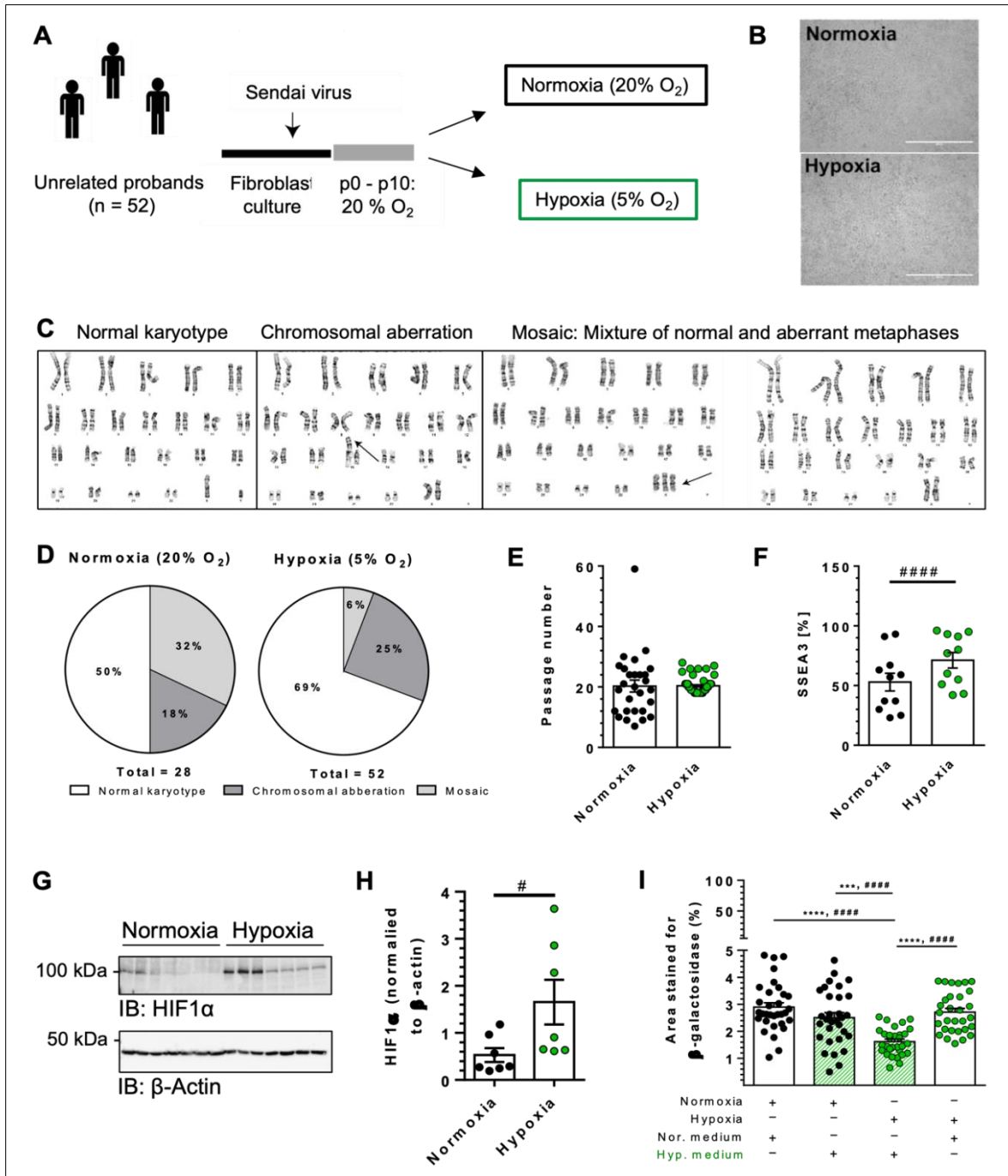


Figure 11: Generation and characterisation of human induced pluripotent stem cells (hiPSC) cultured at hypoxia (5% O₂) or normoxia (20% O₂). **A**) Experimental setup. Fibroblasts from 52 unrelated probands were reprogrammed by a Sendai virus containing pluripotency factors and subsequently incubated at 5% O₂ (hypoxia) or 20% O₂ (normoxia). Between passage 18 and 30, a master cell bank was generated and used for different approaches. **B**) Representative images of hypoxic and normoxic cultured hiPSC. Scale bars are equal to 400 μm. **C**) Karyotype analysis by Giemsa banding (n = 52 for hypoxia and n = 28 for normoxia). **D**) Quantification as parts of whole representing normal karyotypes (white) and abnormal karyotypes (grey) at hypoxic or normoxic culture. **E**) Passage number of hiPSC. **F**) Stage-specific embryonic antigen 3 (SSEA3) quantification as a marker for pluripotency. Paired t-test, ##### = p < 0.0001. **G**) Western blot for HIF1α and β-actin (n = 7), and **H**) quantification of HIF1α western blot normalised to β-actin (n = 3). **I**) Area stained for the β-galactosidase (green bars represent culture with hypoxic medium). Unpaired t-test, # = p < 0.05. This figure was adopted from the manuscript Raabe et al. (*in preparation*).

Results

To investigate underlying abnormalities resulting in altered pluripotency, HIF1 α levels and senescence in normoxic-cultured hiPSC compared to hypoxic-cultured hiPSC, RNA sequencing was performed. Among the top-upregulated gene expressions, NADH-dehydrogenase 1 alpha-subkomplex, 4-like 2 (*NDUFA4L2*) was identified (**Figure 12 A**). Upon hypoxic conditions, *NDUFA4* is inhibited and HIF1 α induced, leading to further induction of *NDUFA4L2* which then inhibits the complex I of the respiratory chain (Tello et al. 2011). The increased *NDUFA4L2* and *HIF1A* levels in hypoxic culture conditions compared to normoxic culture conditions were validated by real-time quantitative PCR (RT-qPCR) analysis (**Figure 12 B**). Subsequently, the RNA sequencing results were matched with assay for transposase-accessible chromatin (ATAC) sequencing to further investigate if posttranslational modifications of *NDUFA4L2* occur upon cultivation at hypoxic or normoxic conditions. Results from the ATAC sequencing showed that hypoxic-cultured cells had a higher accessibility of the chromatin structure of the promoter region in the *NDUFA4L2* gene (**Figure 12 C**).

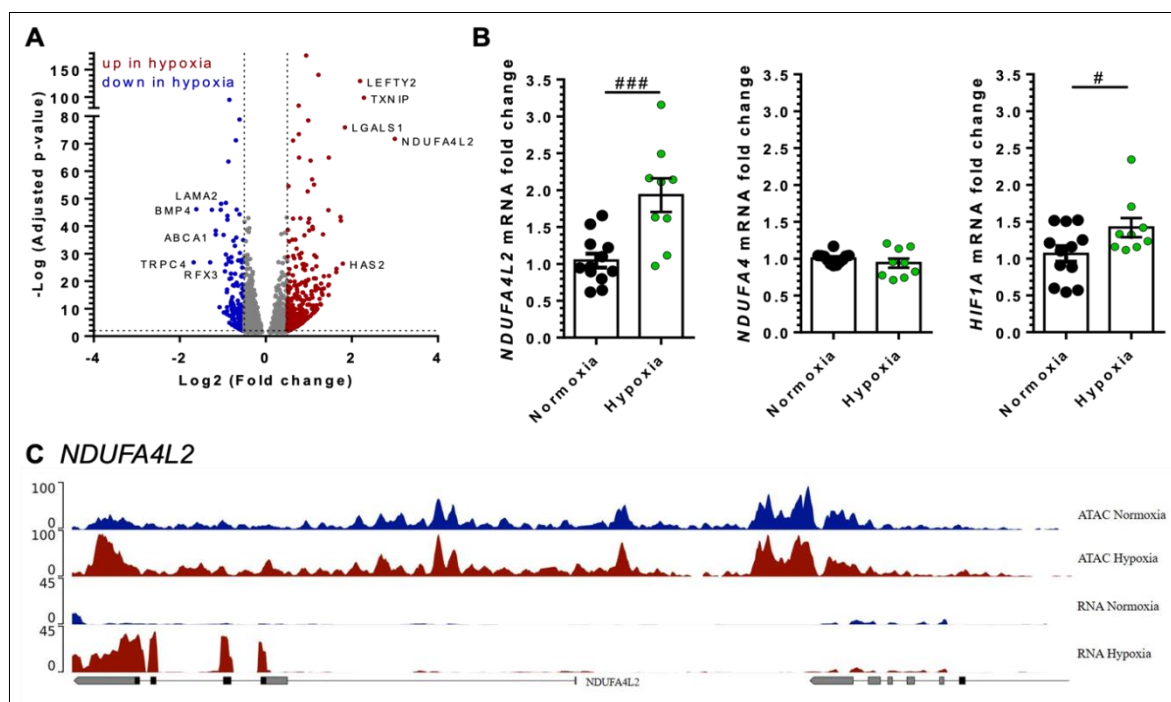


Figure 12: RNA- and ATAC sequencing of hypoxic (5% O₂) and normoxic (20% O₂)-cultured hiPSC. **A**) Representation the 5 top significant up- (red) and downregulated (blue) genes in hypoxic cells compared to normoxic-cultured cells. **B**) mRNA fold change of *NDUFA4L2*, *NDUFA4* and *HIF1A*. **C**) Plots of the RNAseq and ATACseq for *NDUFA4L2* (n = 3). For statistics, unpaired t-test compared to hypoxic-cultured hiPSC was performed (# = p<0.05, ### = p<0.001). This figure was adopted from the manuscript Raabe et al. (*in preparation*).

Since *NDUFA4L2* has previously reported to be a part of the respiratory chain complex IV (Balsa et al. 2012; Tello et al. 2011), we performed a blue native analysis followed by mitochondrial complexome analysis. Quantification of blue native band intensity showed only a trend towards lower band intensity in S1 in hypoxic compared to normoxic hiPSC

Results

(Figure 13 A, B). Interestingly, in contrast to what has been published in the literature, the mitochondrial complex analysis revealed NDUFA4L2 not as an integral component of respiratory chain complex IV, since NDUFA4L2 was not associated with a mitochondrial complex (Figure 13 C). Moreover, in the complexome analysis NDUFA4L4 was not detected in normoxic cells but in hypoxic-cultured hiPSC.

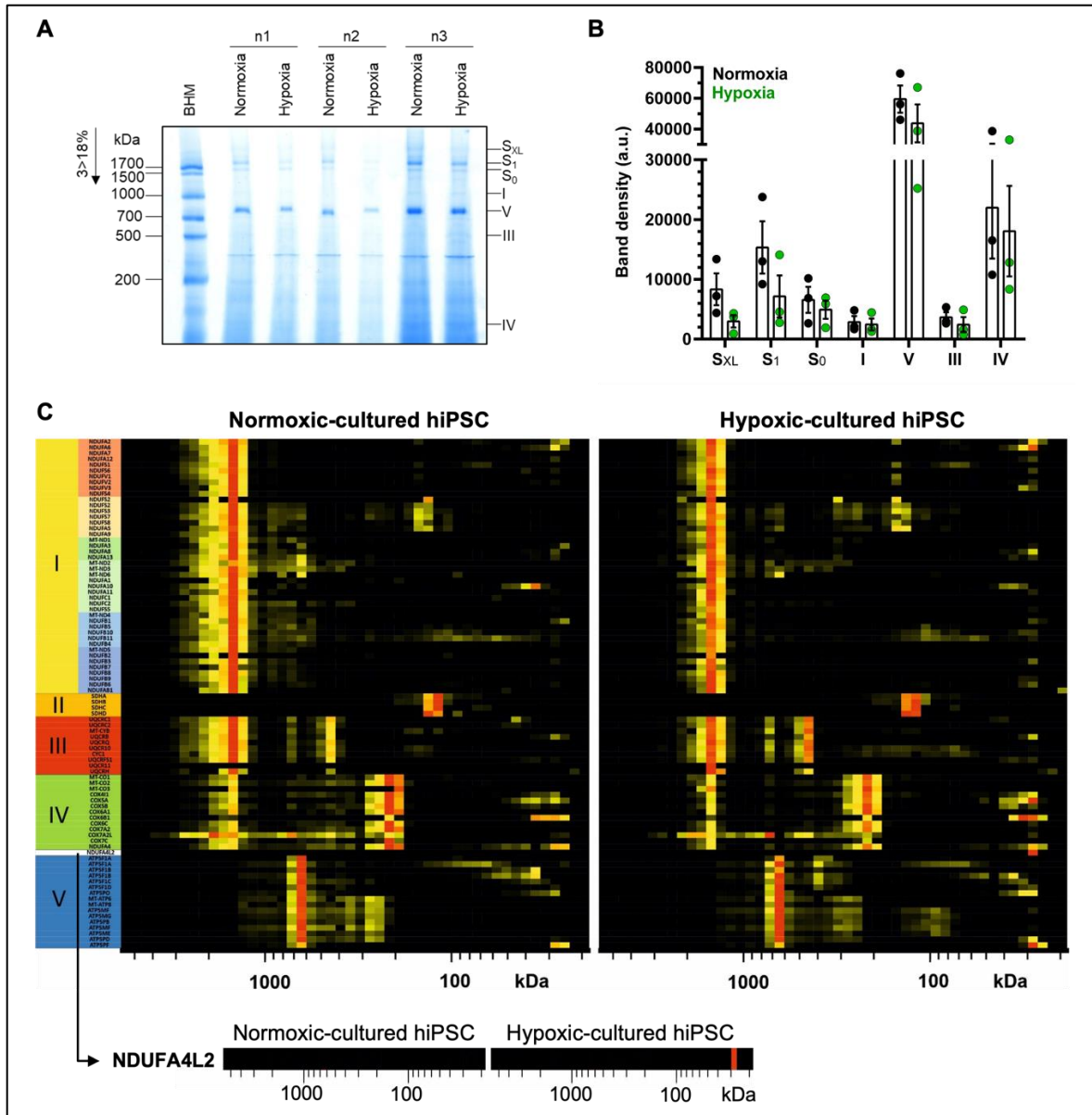


Figure 13: Analysis of the composition of the mitochondrial respiratory chain complexes in hypoxic (5 %O₂) and normoxic (20% O₂)-cultured hiPSC by blue native (BN) PAGE. A) Image of the BN PAGE (3-18%) for n = 3 pairs of hypoxic and normoxic samples. The band pattern obtained from isolated bovine heart mitochondria (BHM) was used as a mass ladder. **B)** Quantification of band intensities (AU; arbitrary units) of mitochondrial chain complexes. **C)** Mitochondrial complex analysis with magnified representation of NDUFA4L2. This figure was adopted from the manuscript Raabe et al. (*in preparation*).

The first chapter of this thesis investigated the impact of oxygen on hiPSC viability, and pluripotency during time in culture. Since culture in 20% O₂ resulted in increased

karyotype abnormalities and senescence, reduced pluripotency and mitochondrial activity, hiPSC were consequently cultured at 5% O₂ during experiments in this thesis.

6.2 NRAP antibody development and validation

6.2.1 Western immunoblot analysis

Since there were no commercial antibodies against human NRAP available at the beginning of this thesis, we initially aimed to develop our own NRAP antibody with cross-reactivity in mice and rats. The antibody was designed and produced with the help of the company Davids Biotechnology in Germany. Therefore, a polyclonal rabbit antibody was produced in a 63-day immunisation plan with five immunisations using the peptide AKKAHELASDIKYRQDFNK. To allow the detection of all human NRAP isoforms, a peptide that is identical to the NRAP protein sequence of all human NRAP isoforms from amino acid 322-340, was chosen. After the finalisation of the antibody production, the NRAP antibody was affinity purified by the company and delivered as a solution containing 0.2% Na-Azide. On day 35 and day 63, the antisera were used to determine the enzyme-linked immunosorbent assay (ELISA) titer. On day 35 the measure ELISA titer was 1:3000 and on day 65 1:300000.

Initially, the optimal conditions of the antibody for western immunoblotting purposes were investigated. For this, different conditions such as type of membrane and blocking reagent as well as various antibody concentrations were tested. Therefore, either nitrocellulose membranes in combination with blocking of unspecific antibody binding sites with 5% bovine serum albumin (BSA) or polyvinylidene difluoride (PVDF) membranes and 10% milk in Tris-buffered saline with Tween20 (TBS-T) were investigated as well as different NRAP antibody concentrations ranging from dilutions between 1:100 and 1:5000 for western immunoblot analysis (**Figure 14 A**).

On both membranes with human heart samples, derived from DCM patients, NRAP could be detected up to antibody dilutions of 1:2000. Indeed, the background of unspecific signals was higher on nitrocellulose membranes compared to PVDF membranes. The best signal intensity to low background signal ratio was detected with PVDF membranes and an antibody dilution of 1:500. Therefore, these conditions were used for further analyses with this antibody. Since the molecular weight for NRAP is 197 kDa, and thereby close to the molecular weight of myosin heavy chain (MHC) at 200 kDa which can often lead to cross reactivities of produced antibodies, another western blot for NRAP and MHC was performed. This revealed that the MHC band was above the detected molecular weight band of NRAP (**Figure 14 B**).

Results

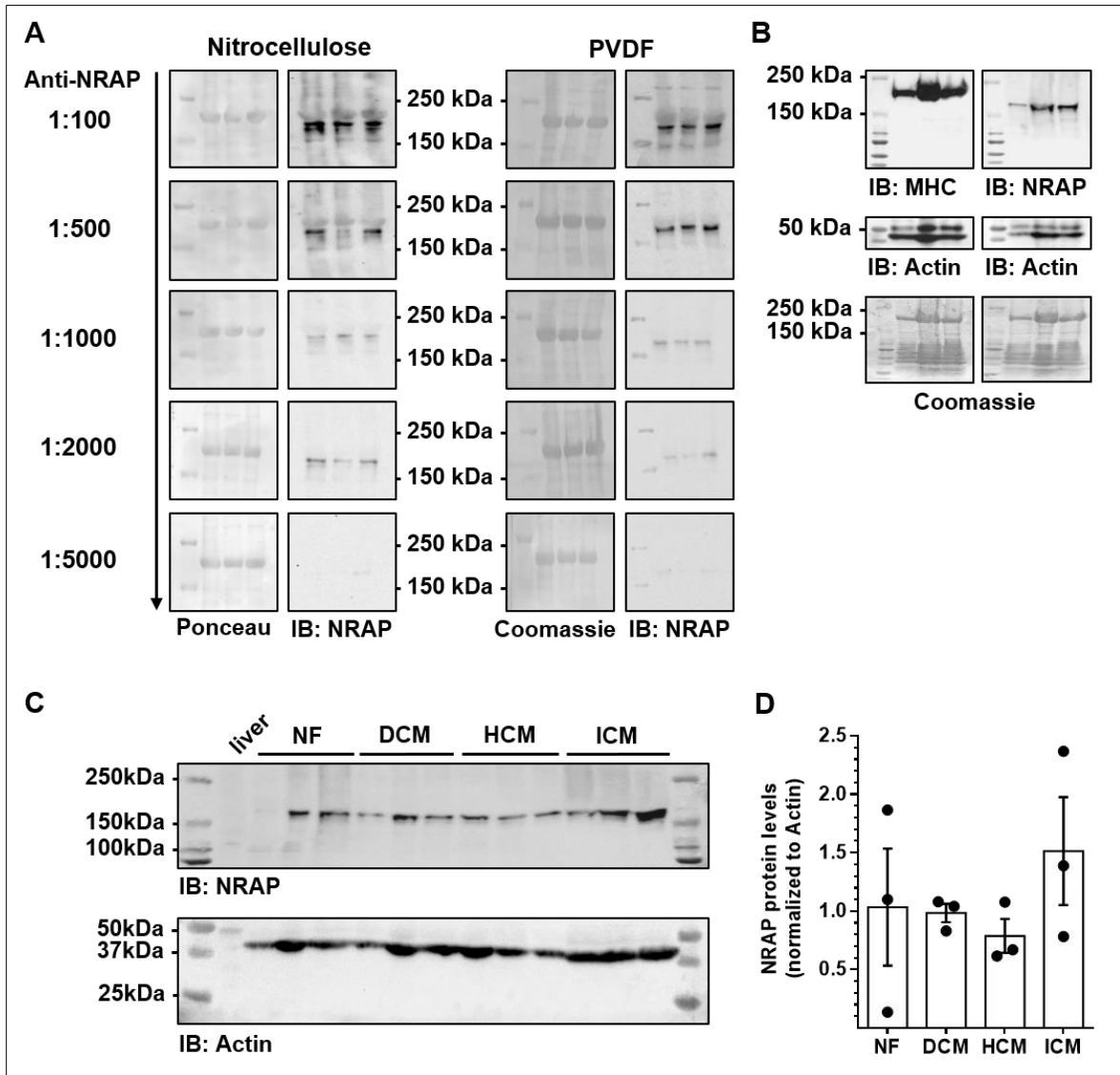


Figure 14: Validation of anti-NRAP for western immunoblot applications in human heart samples. **A)** Testing of 1:100-1:5000 dilutions of anti-NRAP on either nitrocellulose or PVDF membranes. Heart samples from three different patients with dilated cardiomyopathy (DCM) were used. For detection of total protein level, nitrocellulose membranes were stained with Ponceau Red and PVDF membranes were stained with Coomassie blue. **B)** Immunoblot (IB) for myosin heavy chain (MHC) or NRAP (1:500). Cardiac actin served as loading control and protein levels were stained with coomassie. **C)** Anti-NRAP detection in three human heart samples each for non-failing, DCM, hypertrophic cardiomyopathy (HCM) or ischemic cardiomyopathy (ICM) hearts. Mouse liver tissue was used as a negative control and cardiac actin as loading control, and **D)** quantification of NRAP protein levels normalised to actin.

In order to investigate if differences in NRAP protein levels could be detected in different forms of cardiomyopathies in the human heart, a western blot with ventricular tissue samples from non-failing (NF) hearts or explanted samples from patients with DCM, HCM and ischemic cardiomyopathy (ICM) was performed.

The quantification of the NRAP protein levels, normalised to cardiac actin as loading control, revealed no significant difference in protein levels (**Figure 14 C, D**). However, due

Results

to limitation of available human heart tissue, only three samples for each group could be produced indicating that there might be an increase in NRAP protein level for ICM if more samples would be available. Subsequently, due to high sequence similarity, we aimed to investigate whether the NRAP antibody can additionally detects NRAP mouse and rat isoforms as there is no reliable prediction for cross-reactivities with other species (**Figure 15**).

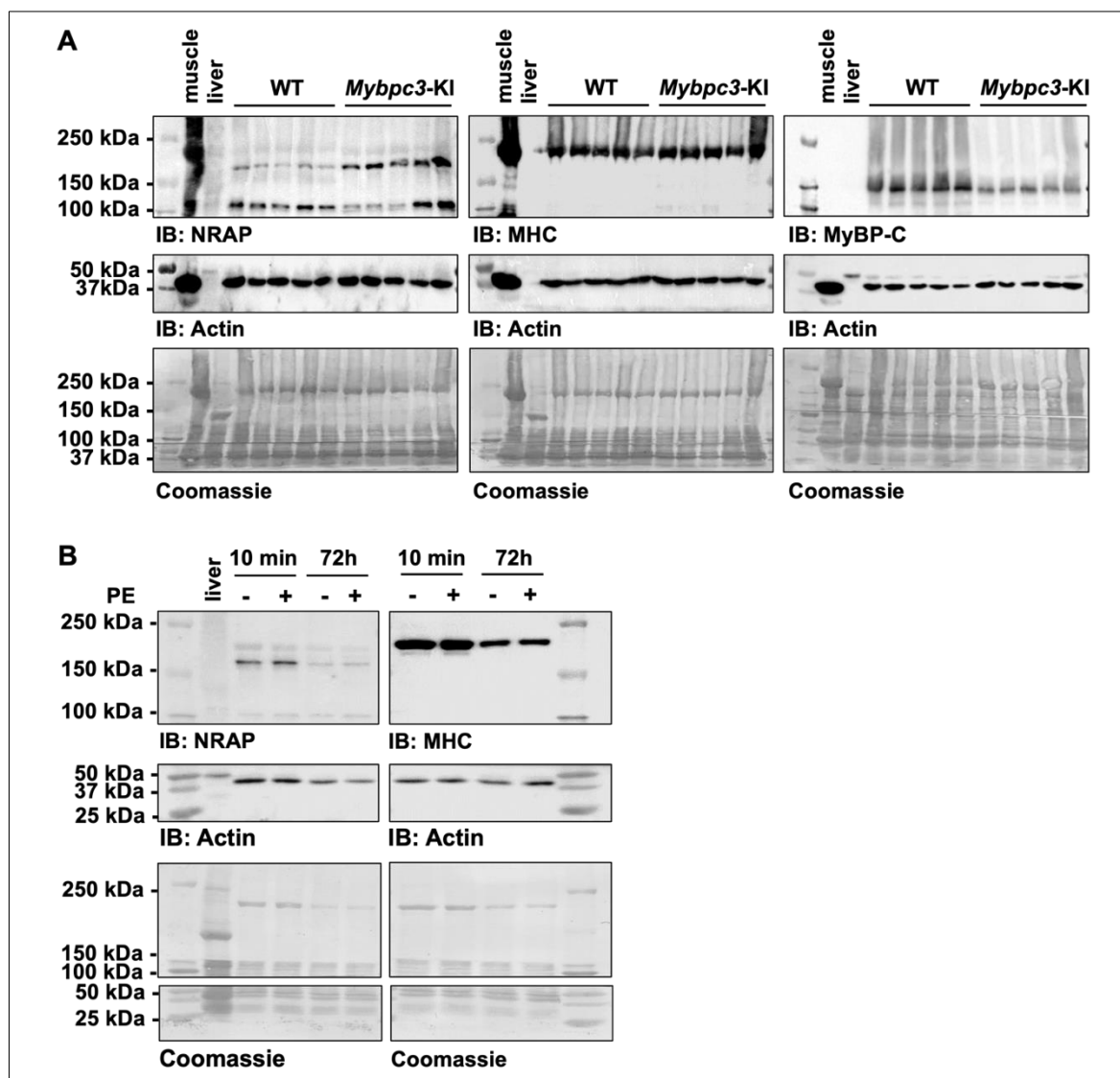


Figure 15: Validation of anti-NRAP for western immunoblot applications in mouse and rat heart samples. A) Testing of anti-NRAP (1:500), anti-Myosin Heavy Chain (MHC) and anti-myosin-binding protein C (MyBP-C) on PVDF membranes for mouse heart samples derived from WT- and Myosin binding protein C-Knock in (*Mybpc3-KI*) mice (n = 5). Skeletal mouse tissue was used as a positive control for NRAP while mouse liver samples were used as negative control for NRAP. Loading controls were performed using cardiac actin and membranes were subsequently stained for coomassie. **B)** Anti-NRAP (1:500) and anti-MHC were tested on PVDF membranes in heart samples derived from neonatal rat ventricular myocytes (NRVMs). Mouse liver was used as a negative control, anti-cardiac actin as loading control and membranes were stained with coomassie for total protein.

Results

For the mouse heart samples, wildtype (WT) and *Mybpc3*-knock-in (KI) mouse samples were used as the *Mybpc3*-KI develops a HCM phenotype and previous results showed that NRAP levels are increased in *Mybpc3*-KI mice compared to wildtype (WT) mice. The increase in NRAP levels could be corroborated for *Mybpc3*-KI mouse samples while an additional band was detected at a molecular weight of 100 kDa that had not been detected prior in human heart samples (**Figure 15 A**). As a positive control, mouse skeletal muscle tissue was used while liver tissue was used as a negative control. While there was a high reactivity for the antibody with the skeletal muscle tissue sample, NRAP was not detected in the liver sample. Moreover, a cross-reactivity of the NRAP antibody with MyBP-C could be excluded while a low cross-reactivity with MHC was detected.

In order to investigate the antibody in rat heart samples, NRVMs were treated for 10 min or 72 h with the pro-hypertrophic stimulus phenylephrine (PE) as previous results had indicated that this stimulation results in increased NRAP protein levels (**Figure 15 B**). The correct band of NRAP could be detected with higher protein levels at the earlier time point. In addition to the detection of NRAP, a faint band at 100 kDa was detected. Moreover, in rat heart samples, MHC was detected at the same size as a faint band after immunoblotting with the NRAP antibody.

Taken together, the custom-made human NRAP antibody was successfully validated for western immunoblot analysis in human heart tissue, but showed cross-reactivity with MHC and another unidentified protein at approximately 100 kDa in NRVMs and mouse heart tissue.

6.2.2 Immunofluorescence

Furthermore, the NRAP antibody was tested in immunofluorescence experiments to investigate NRAP localisation in cardiac myocytes. Due to the limited availability of human heart tissue from healthy probands, human explanted DCM hearts from transplantations were used for the generation of cryosections.

For optimisation, different fixation methods were investigated. Therefore, cryosections were fixed with either acetone, methanol or 4% PFA and stained with dilutions of the NRAP antibody ranging from 1:50 to 1:1000 (**Figure 16**). The best signal and structure of myofilaments from the heart sections could be detected with acetone fixation (**Figure 16 A**) while especially PFA resulted in wave-like sections (**Figure 16 C**). The most appropriate intercalated disc signal for NRAP and myofilament structure was detected in heart sections that were fixed with acetone and stained with a 1:500 dilution of the NRAP antibody (**Figure 16 A**). This concentration revealed an appropriate signal for NRAP and a low background signal. Therefore, for heart sections acetone fixation was used for further

Results

immunofluorescence stainings. For all following immunofluorescence applications, the NRAP antibody was used in 1:500 dilution.

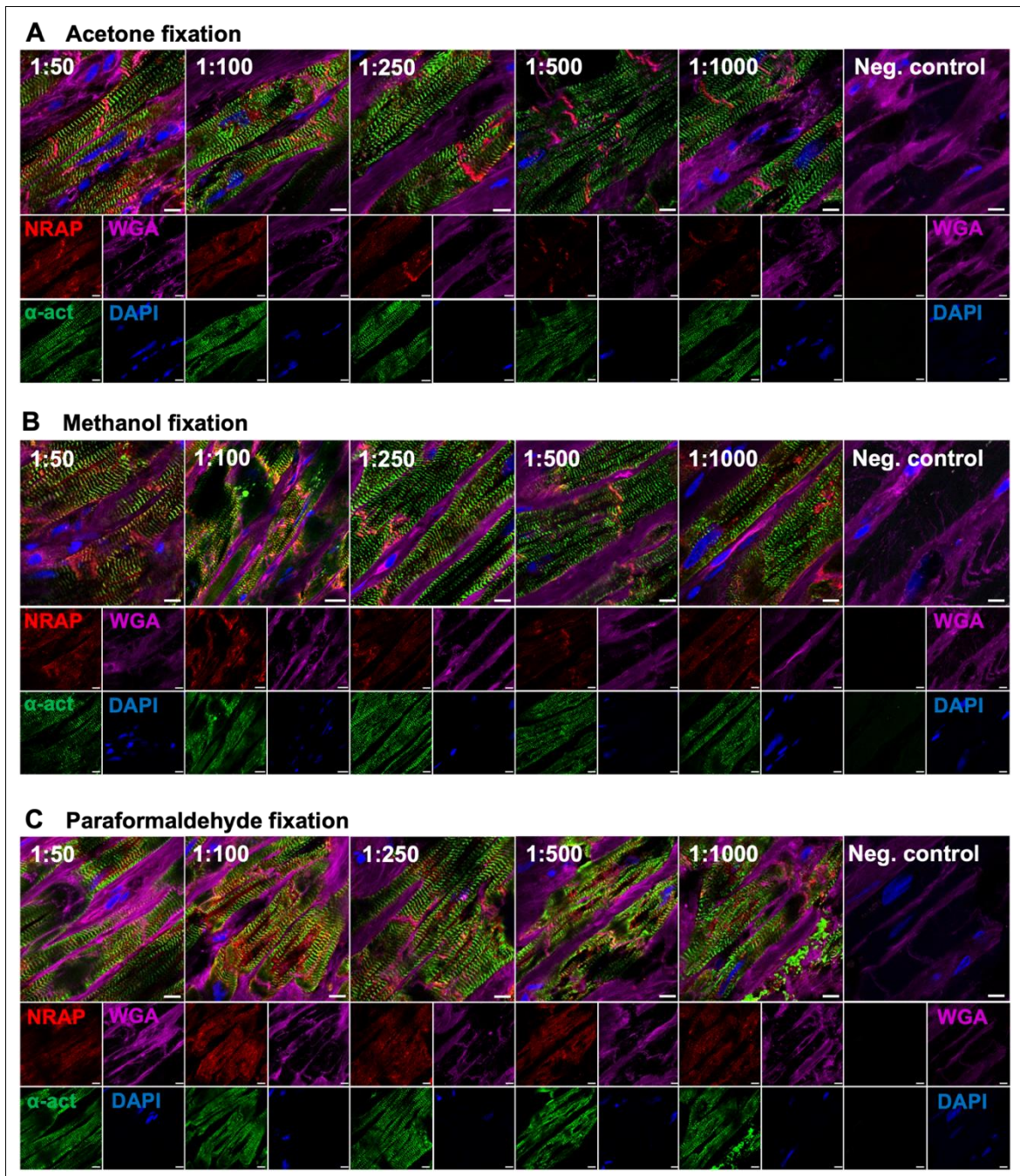


Figure 16: Validation of anti-NRAP for immunofluorescence in human heart sections from dilated cardiomyopathy patients. Anti-NRAP was investigated in dilutions ranging from 1:50 to 1:1000 (red) concomitantly for staining Z-discs with α -actinin (green), F-actin with phalloidin (purple) and nuclei with DAPI (blue). Heart sections of patients with dilated cardiomyopathy (DCM) were investigated for three different fixation methods. Sections were fixed with **A**) acetone, **B**) methanol or **C**) 4% paraformaldehyde. For each fixation setup negative controls were performed that were only incubated with the appropriate secondary antibodies. Scale bars are equal to 20 μ m.

Results

Moreover, the NRAP antibody was investigated in different human model systems such as hiPSC-derived cardiac myocytes and EHTs as well as in tissue from different organisms such as mice and rats. The staining of hiPSC-derived cardiac myocytes depicts an organised myofilament structure with paralleled orientation of α -actinin and F-actin (**Figure 17 A**). The localisation of detected NRAP by the antibody was distributed throughout the entire cell similarly to NRAP distribution in the EHT section with no specific NRAP localisation at cell-cell borders (**Figure 17 B**). Investigation of different fixation methods has no impact on NRAP staining with the antibody (**Supplementary figure 1**).

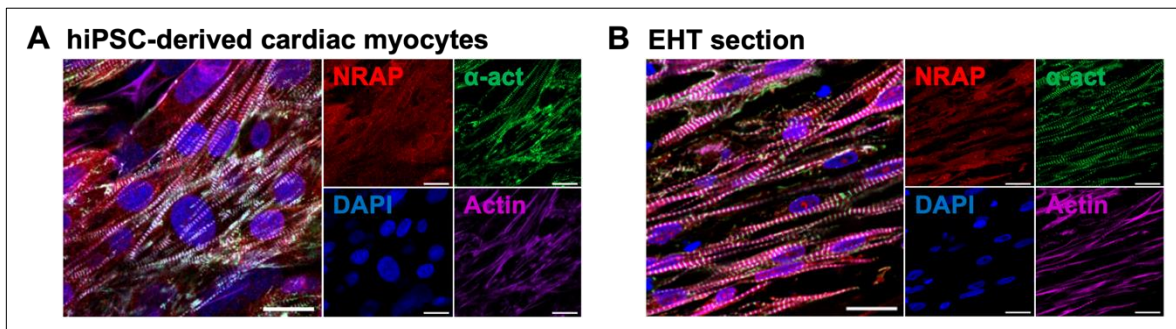


Figure 17: Validation of anti-NRAP in hiPSC and EHT samples by immunofluorescence. Cells were fixed with 4% paraformaldehyde and stained for NRAP (1:500; red), Z-discs with α -actinin (green), F-actin with phalloidin (purple) and nuclei with DAPI (blue). Staining of **A**) human-induced pluripotent stem cell (hiPSC)-derived cardiac myocytes, and **B**) human engineered heart tissues (EHTs). Scale bars are equal to 10 μ m for EHT sections and 20 μ m for hiPSC-derived cardiac myocytes.

In contrast, in WT and *Mybpc3*-KI mice heart sections, NRAP was detected at the intercalated disc (**Figure 18**).

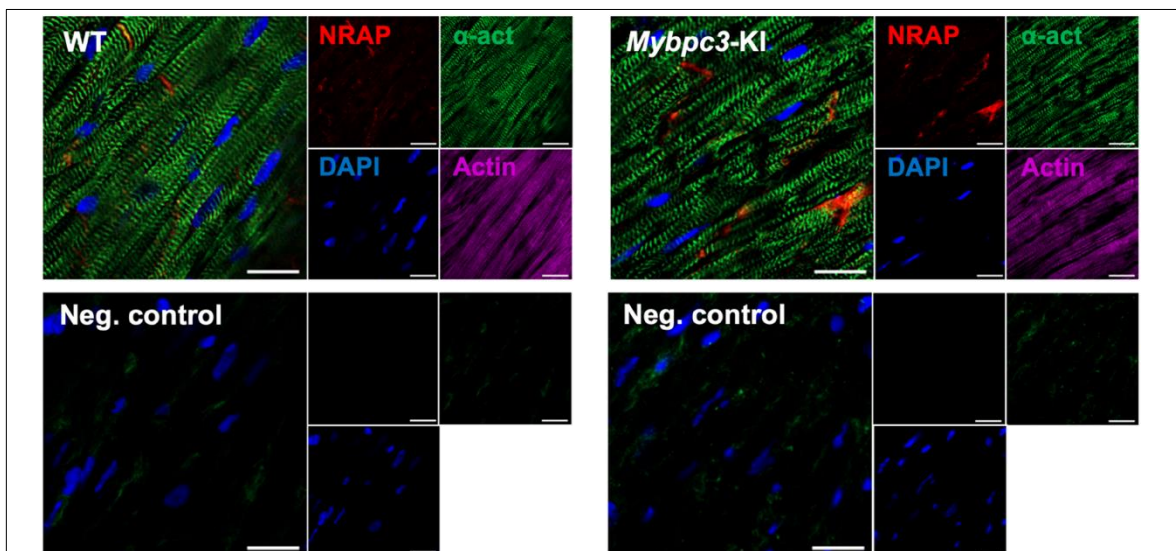


Figure 18: Validation of anti-NRAP in WT- and *Mybpc3*-KI mouse heart sections by immunofluorescence. Myosin-binding protein C (*Mybpc3*)-wildtype (WT) and -Knock-in (KI) 10 μ m thick heart sections were fixed with acetone and stained for NRAP (1:500; red), Z-discs with α -actinin (green), F-actin with phalloidin (purple) and nuclei with DAPI (blue). The respective negative controls have only been stained with secondary antibodies. Scale bars are equal to 20 μ m.

Results

The localisation in WT heart sections was exclusively restricted to the intercalated disc area and in *Mybpc3*-KI heart sections NRAP accumulated at the intercalated disc as in accordance with previous results (**Supplementary figure 2**).

In order to test the antibody additionally on rat cells by immunofluorescence, NRVMs were isolated and either cultured for 48 h in the presence or absence of the pro-hypertrophic stimulus PE. In control cardiac myocytes, NRAP was mostly located at the nuclear and perinuclear cytosolic areas (**Figure 19**). However, pro-hypertrophic stimulation of NRVMs resulted in the maturation of cardiac myocytes as indicated by increased structured α -actinin and actin staining. In these cells, NRAP was detected in close proximity to actin filaments and the intercalated disc.

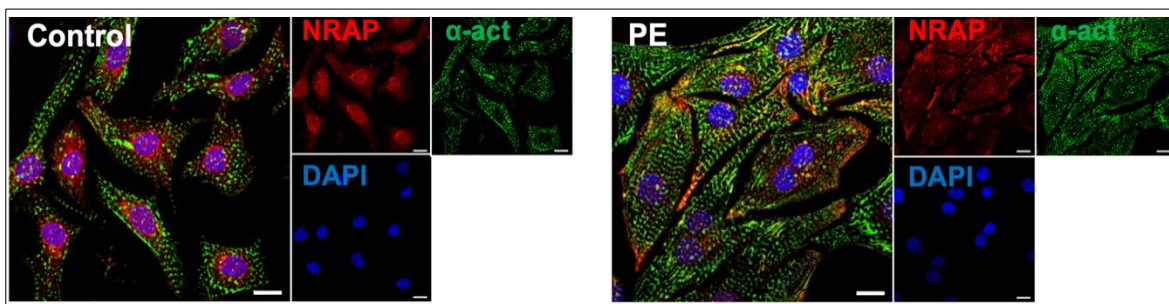


Figure 19: Validation of anti-NRAP in neonatal rat ventricular cardiac myocytes for immunofluorescence. Neonatal rat ventricular myocytes (NRVMs) were incubated for 48 h incubation without (control) or with 10 μ M of the pro-hypertrophic stimulus phenylephrine (PE), fixed with 4% paraformaldehyde and stained for NRAP (1:500; red), Z-discs with α -actinin (green), F-actin with phalloidin (purple) and nuclei with DAPI (blue). Scale bar are equal 20 μ m.

Investigation of NRAP-localisation in human, mouse and rat cardiac myocytes by immunofluorescence revealed NRAP localisation in human acetone-fixed heart tissues, NRVMs and mice heart sections as expected, but not in hiPSC and EHTs.

6.3 Development of *NRAP*-OE and -KD hiPSC lines

In order to investigate the contribution of gain-of-function or loss-of-function NRAP protein levels to the development and progression of human heart disease, a *NRAP*-OE and *NRAP*-KD hiPSC line were generated.

6.3.1 Generation of a *NRAP*/MYC-OE hiPSC line

For this purpose, a *NRAP*-MYC-OE hiPSC line was developed by CRISPR-Cas9 technology. For that purpose, a plasmid with right and left homology arm with identical sequence to the protein phosphatase 1 regulatory subunit 12C (*PPP1R12C*) gene on chromosome 19 of the human genome was designed (**Figure 20**). With the selection of the genomic location, it is important that neither essential genes are disrupted nor that the KI affects the pluripotency of hiPSC. Therefore, the *PPP1R12C* gene was used for targeting as KI

Results

into this gene locus has been successfully shown to not lead to adverse effects in cells, postulating this gene locus as a “safe harbour” (Smith et al. 2007). The name adeno-associated virus integration site 1 (AAVS1) safe harbour locus originates from the observation that the adeno-associated virus 2 (AAV2) was able to integrate into this gene (Kotin et al. 1992). The resulting transgenes were shown to be stably expressed in human embryonic stem cells and hiPSC (Luo et al. 2014; Smith et al. 2007).

The area between the left and right homology arm was used to design a gRNA for targeting the Cas9 nuclease to this locus and to induce a site-specific double-strand break followed by homology-directed repair. This allows the stable integration of plasmids into the human genome without affecting or disrupting other gene loci (Oceguera-Yanez et al. 2016).

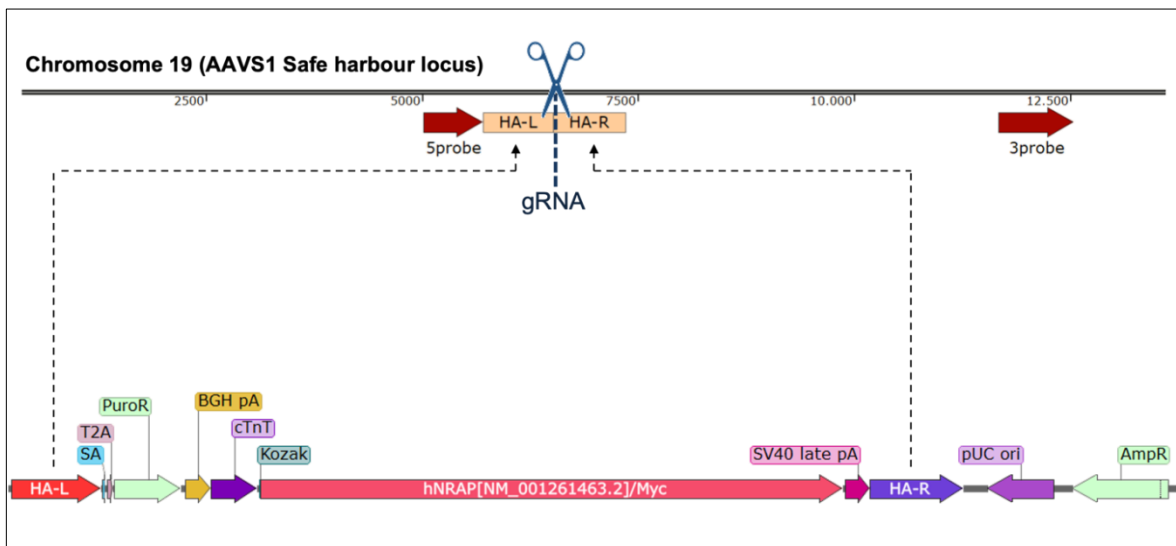


Figure 20: Gene editing approach for stable overexpression of NRAP in human-induced pluripotent-derived cardiac myocytes. The gene editing approach was performed by the CRISPR-Cas9 system. Therefore, the Cas9, the AAVS1-cTnT-NRAP/MYC-OE plasmid and a specific gRNA, that targets the AAVS1 safe harbour locus on chromosome 19 of the human genome, were used for nucleofection of human-induced pluripotent stem cells. The plasmid was self-designed and produced by VectorBuilder. It contains a left and right homology arm that are identical to those homology arms on the human genome allowing the stable integration mediated by homology-directed repair (HDR). Moreover, the plasmid contains a puromycin resistance, enabling the selection of successfully edited cells, a cardiac-specific troponin T (cTnT) promoter, a Kozak sequence, the NRAP mRNA of NRAP isoform 1, that includes all NRAP exons, coupled to a MYC-tag allowing to distinguish between endogenous and artificial NRAP. Moreover, that part of the plasmid that is not integrated into the genome contains an ampicillin resistance for specific amplification of the plasmid in *Escherichia coli*.

For the generation of the plasmid, the mRNA of NRAP isoform 1 was integrated since this isoform contains all exons of the NRAP gene. Upstream of the NRAP mRNA, a cTnT promoter was integrated that is only active in cardiac myocytes but not in hiPSC allowing increased NRAP expression in cardiac myocytes (Figure 21 A). Additionally, at the C-

Results

terminus of the *NRAP* mRNA a *MYC*-tag was integrated. This enables to distinguish between endogenously expressed *NRAP* and heterologous *NRAP*-OE in cardiac myocytes.

Initially, the plasmid was validated by restriction digestion. Both enzymes, BamHI and BglII revealed the correct restriction band pattern of the plasmid with 3735 bp, 2956 bp, 1791 bp, 1682 bp and 474 bp for digestion with BamHI and 4808 bp, 3248 bp and 2586 bp for digestion with BglII (**Figure 21 B**). Subsequently to validation by restriction digestion, the entire plasmid was sequenced revealing the correct sequence (**Figure 21 C**).

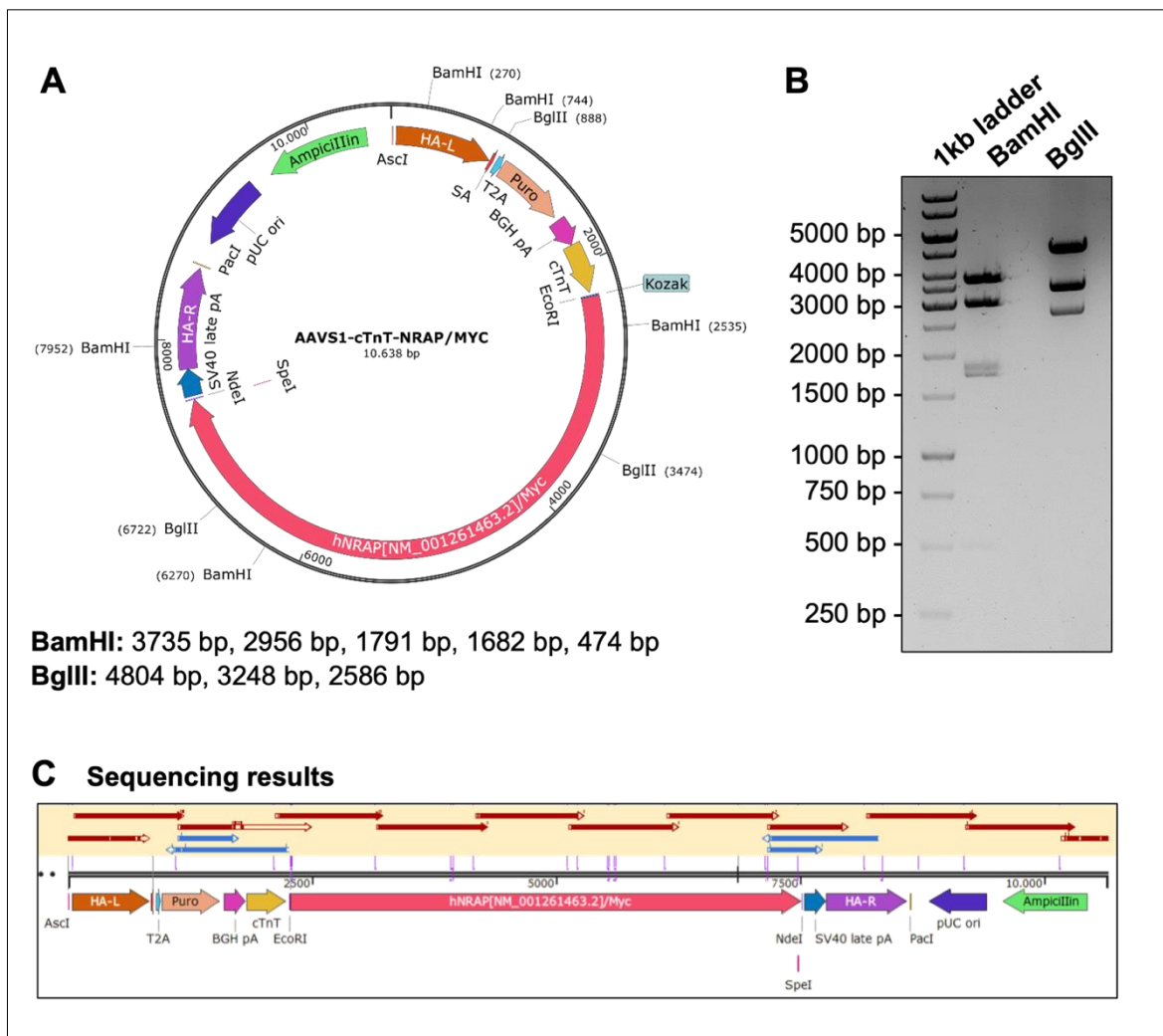


Figure 21: Validation of the AAVS1-cTnT-NRAP/MYC plasmid for stable integration into the human genome. A) Plasmid map with the respective restriction sites for BamHI (3735 bp, 2956 bp, 1791 bp, 1682 bp, 474 bp) and BglII (4804 bp, 3248 bp, 2586 bp). **B)** Agarose gel after plasmid restriction digest with BamHI and BglII. **C)** Sanger sequencing for validation of the correct sequence of the plasmid are indicated by red arrows.

Since the plasmid revealed the correct sequence, the integration of this plasmid into the safe harbour locus was performed by CRISPR-Cas9. Three days post-nucleofection, the

Results

plated cells were incubated with 10 μ M puromycin for three days with a daily medium exchange. While untreated control cells reached a confluency of the cell layer after two days, fewer control cells were observed after incubation in the presence of puromycin due to missing resistance to puromycin (**Figure 22**). After three days of exposure to puromycin, no control cells were left. However, approximately 20% of post-nucleofected cells remained attached after three days of incubation with puromycin. These pre-selected cells were used for the generation and propagation of single-cell clones.

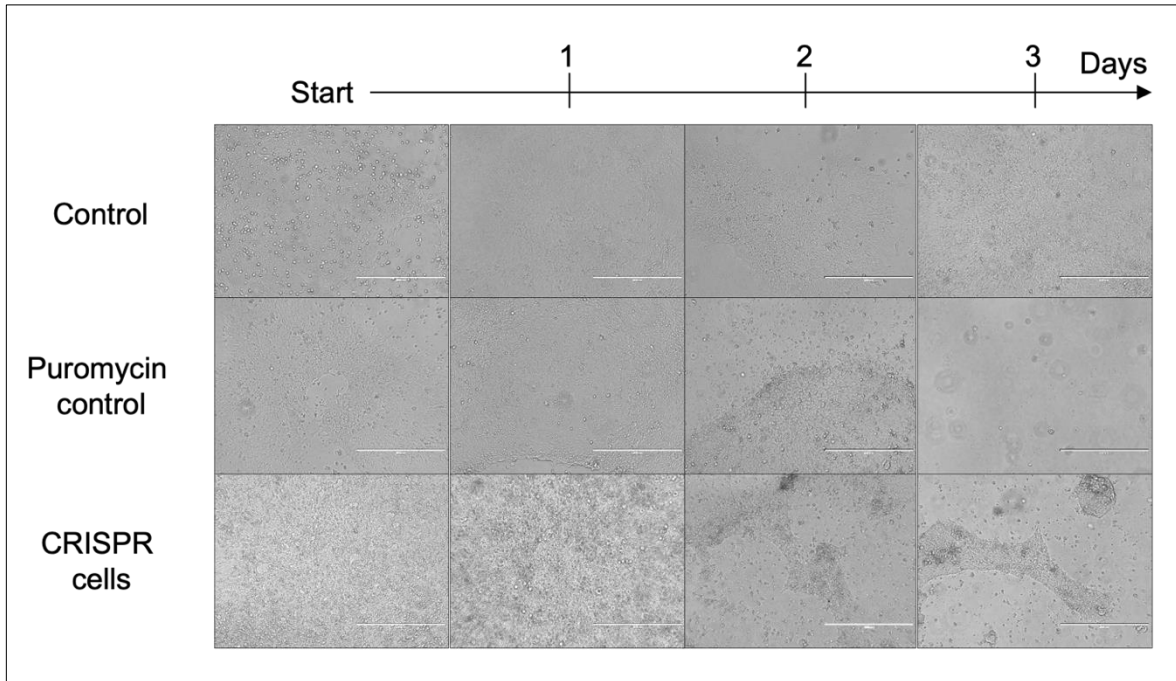


Figure 22: Puromycin selection of successfully nucleofected human-induced pluripotent stem cells (hiPSC) with the *AAVS1-cTnT-NRAP/MYC* plasmid. Represented are either non-nucleofected or cells 3 days post-nucleofected cells. Images show daily treatment of the puromycin control and CRISPR cells with 0.5 μ g/mL puromycin for 72 h or control cells that were not treated with puromycin. Images were taken with the EVOS microscope and scale bars are equal to 1 mm.

Among these cell clones, a heterozygous and homozygous *NRAP/MYC*-OE clone of the successfully-edited clones were used for further investigations. For both clones, various control PCRs were performed to validate the successful integration of the plasmid into the safe harbour locus (**Figure 23**).

First, the overlapping sequence parts between plasmid and genome were validated (as indicated by the numbers 1 and 4), followed by the amplification of internal parts of the plasmid (as indicated by the numbers 2 and 3). Since these primers recognise an exon-exon junction, the smaller fragments at 201 bp and 323 bp represent the amplification from the plasmid while the upper band results at 1458 bp and 1164 bp from amplification of genomic *NRAP*. To identify whether the clones are hetero- or homozygous, an

Results

amplification of the entire plasmid insert spanning from the left homology arm to the right homology arm was performed.

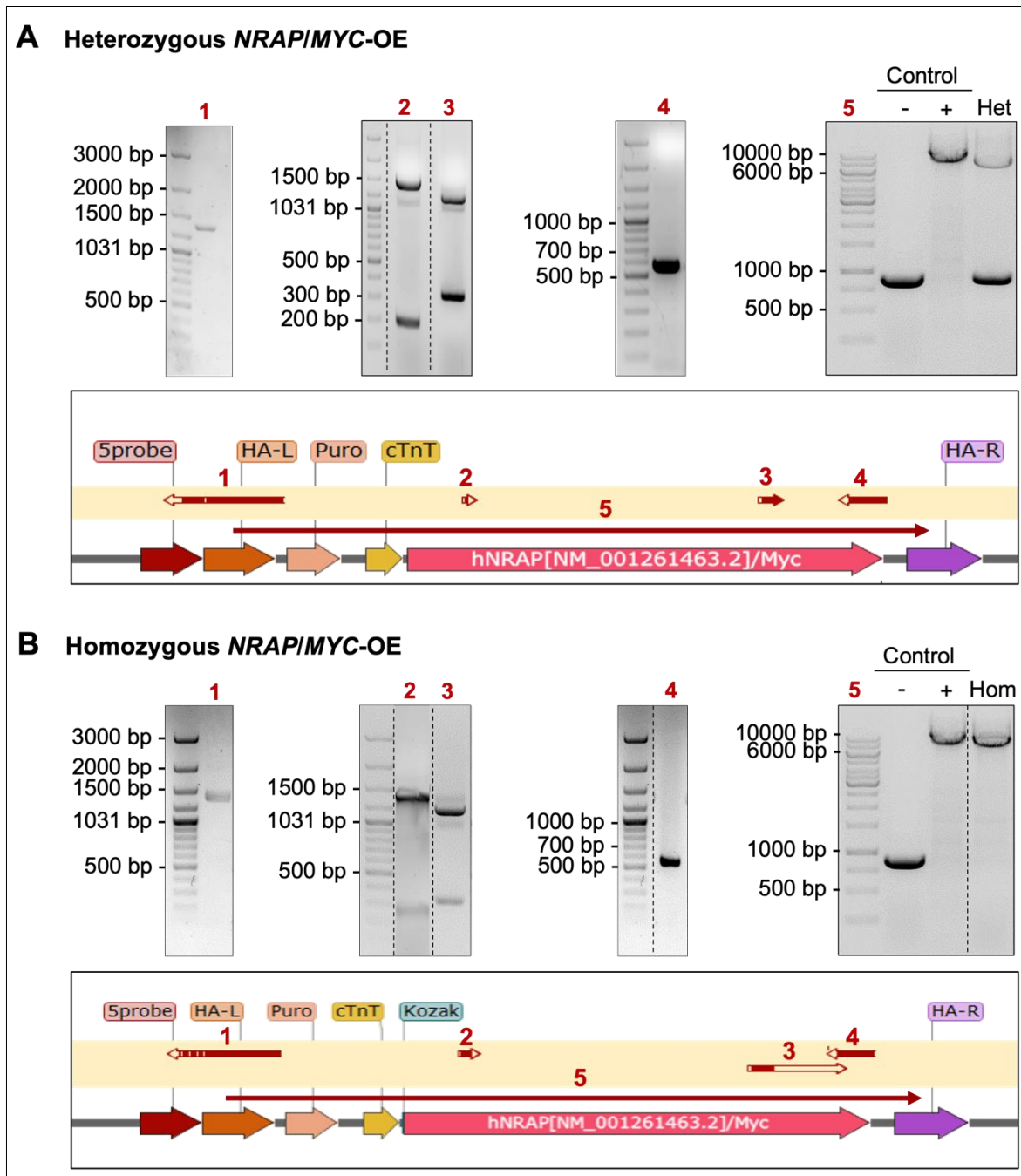


Figure 23: Validation of heterozygous and homozygous *NRAP/MYC*-overexpressing human-induced pluripotent stem cell (hiPSC) clones. Different PCRs with Sanger sequencing were performed to validate either the plasmid-genome overlapping parts (1 = 1323 bp, 4 = 572 bp) or parts in the plasmid (2 = 201 and 1458 bp, 3 = 323 and 1164 bp). Additionally, long-range PCRs (5 = 7843 bp) from the left homology arm (HA-L) to the right homology arm (HA-R) were performed to investigate the genotype of the **A**) heterozygous (het) *NRAP/MYC*-overexpressing (OE) or **B**) homozygous (hom) *NRAP/MYC*-OE clone. The control hiPSC line served as a negative control (-) and the plasmid as a positive control (+) in order to validate the successful setup of the long-range PCR. Successful sequencings are represented as red arrows over the plasmid/genome map for the appropriate clone.

Results

Since these homology arms are part of the genomic safe harbour locus, the primers bind to those homology arms independently of the success of the plasmid integration. As a negative control for the insertion of the plasmid, gDNA derived from the control hiPSC line was used. For the positive control and for initial optimisation of the long-range PCR, the *AAVS1-cTnT-NRAP/MYC* plasmid was used. In case of unsuccessful insertion of the plasmid, the PCR reveals a 926 bp amplicon while successful insertion results in a 7843 bp long PCR amplicon. Therefore, for the heterozygous *NRAP/MYC*-OE clone, two bands were detected at 7843 bp and 926 bp (**Figure 23 A**). Instead, for the homozygous *NRAP/MYC*-OE clone only one band at 7843 bp was detected (**Figure 23 B**).

From the hetero- and homozygous *NRAP/MYC*-OE cell clones, master and working cell banks were produced. These were subjected to an array of quality controls (**Figure 24**).

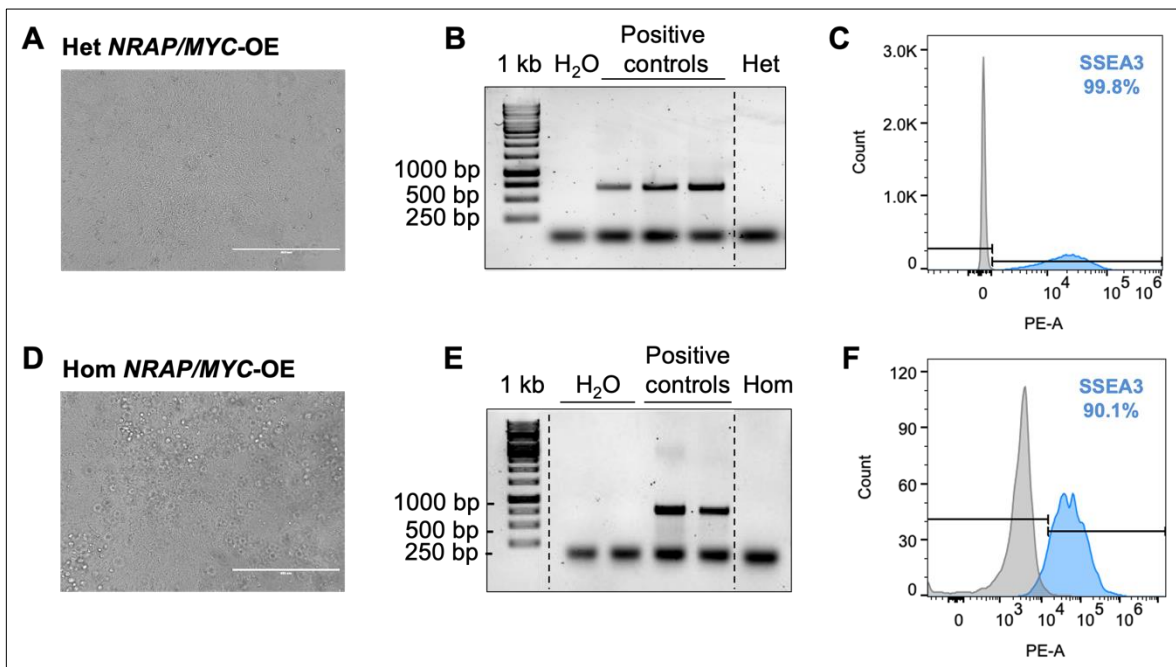


Figure 24: Quality controls for the heterozygous and homozygous *NRAP/MYC*-overexpressing human-induced pluripotent stem cell (hiPSC) lines. For quality control, different characteristics of the master cell bank were determined for **A, B, C**) the heterozygous (het) and **D, E, F**) the homozygous (hom) *NRAP/MYC*-overexpressing hiPSC clone (*NRAP/MYC*-OE). **A, D**) Images of the master cell bank were taken with the EVOS microscope to capture the morphology of hiPSC. Scale bars are equal to 1 mm. **B, E**) Agarose gel representing the result of mycoplasma testing with water as negative control and previously positive-revealed samples as positive control. **C, F**) Stage-specific embryonic antigen 3 (SSEA3) measurements by flow cytometry to determine pluripotency of hiPSC.

First, the cell supernatant during the production of the master cell banks was used to exclude a contamination by mycoplasma since these bacteria would not be visible under the microscope due to their small size. For both cell lines, the mycoplasma test was negative as depicted in the agarose gel that revealed no PCR product for the cell clones (**Figure 24 B, E**).

Results

To investigate the quality of the post-nucleofected hiPSC lines, the pluripotency was assessed. This was performed by staining of cells for the pluripotency marker SSEA3 followed by flow cytometry analysis. For the heterozygous cell line, a pluripotency of 99.4% and for the homozygous cell line a pluripotency of 90.71% was measured (**Figure 24 C, F**).

As the CRISPR-Cas9 technology might lead to karyotype abnormalities (Kosicki et al. 2018), karyotype analysis was performed for both genotypes. This showed in average only two duplicates for each chromosome and revealed no detectable trisomy (**Figure 25 A, B**).

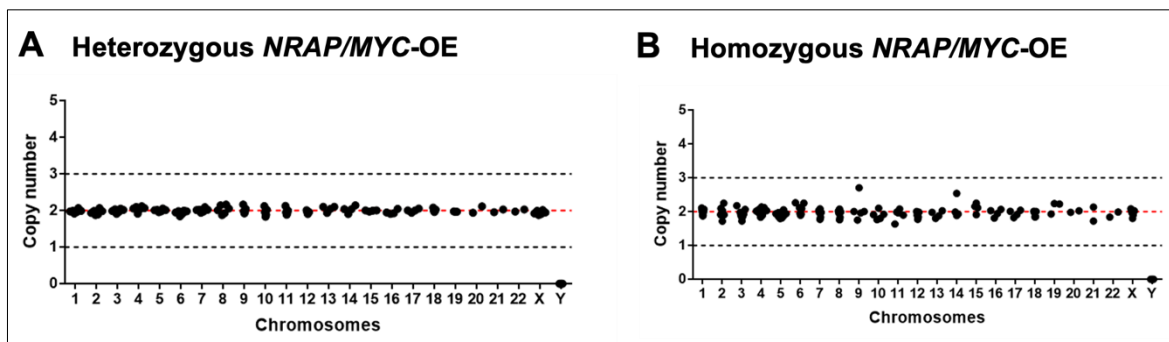


Figure 25: Karyotype analysis of the heterozygous and homozygous *NRAP/MYC*-overexpressing human-induced pluripotent stem cell (hiPSC) clones. For investigation of genetic abnormalities, **A, B**) karyotypes were analysed to exclude alterations in the number of chromosomes for the **A**) heterozygous and the **B**) homozygous *NRAP/MYC*-overexpressing (*NRAP/MYC*-OE) hiPSC clone. This analysis was performed by Elisabeth Krämer and Niels Pietsch.

Nevertheless, not only the chromosomes can be affected by the CRISPR-Cas9 technology. Each gRNA could potentially lead to introduction of off-target modification when the Cas9 binds to a similar sequence at an undesired genomic locus in the genome. In order to exclude the unspecific induction of double-strand breaks at different loci than the safe harbour locus, an off-target analysis was performed. Using the CRISPOR website tool, the top ten most likely off-targets sites were predicted for each gRNA.

For each of those off-target sites, PCRs from the heterozygous and homozygous clones were performed and purified PCR products were sequenced by Sanger sequencing to validate that the genomic sequence was not affected at the wrong site by the Cas9 (**Figure 26**). The sequencing revealed no alterations in the human genomic sequence of the studied off-target gene loci. Exclusively for the gene *APPL2*, a point mutation was detected by sequencing of the off-target region, but the sequencing of the proband control hiPSC line revealed the same point mutation prior to gene editing suggesting that this mutation is a silent mutation in this proband hiPSC line (**Figure 26**).

Results

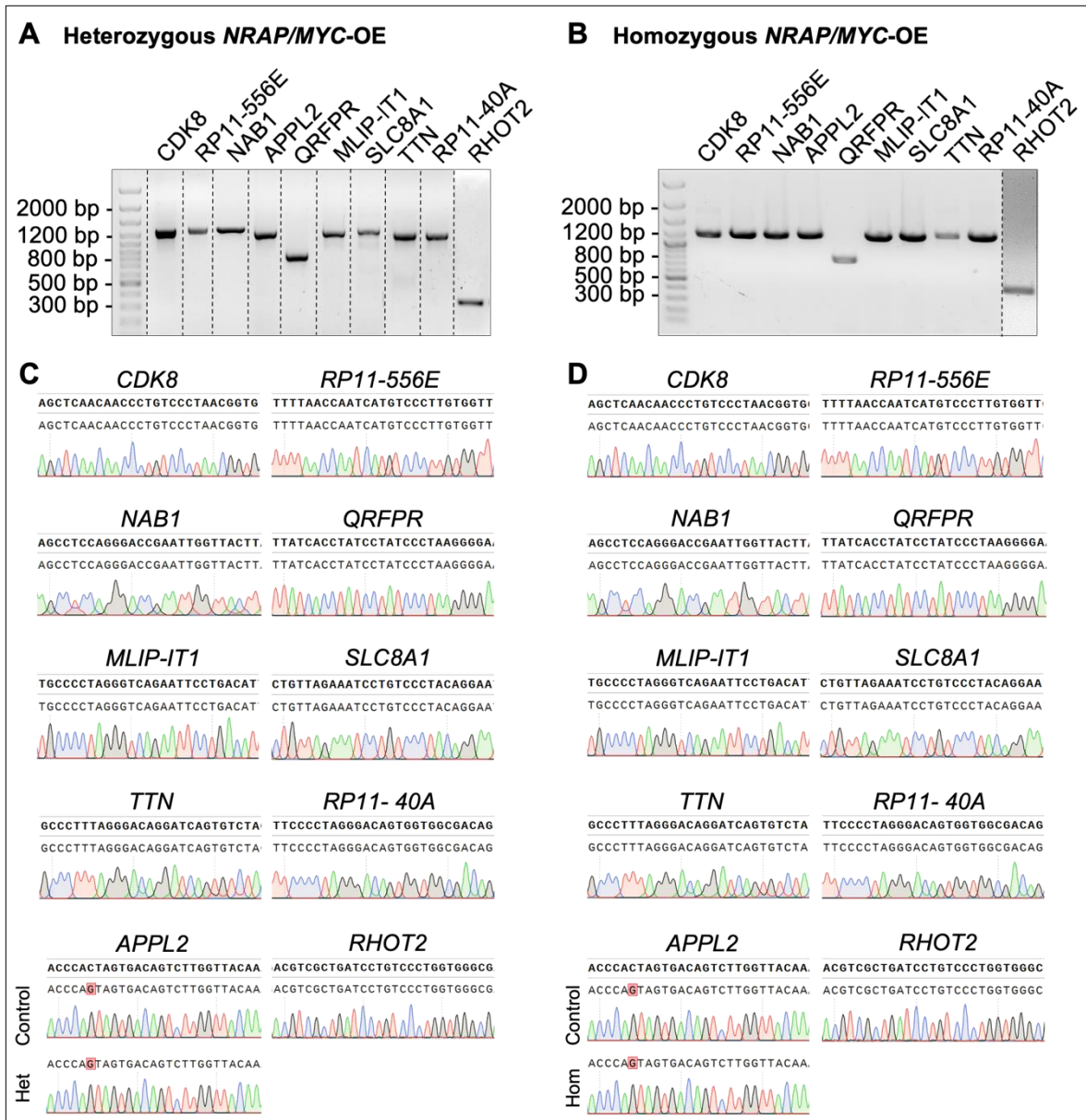


Figure 26: Validation of the top ten off-targets of the heterozygous and homozygous *NRAP/MYC*-overexpressing human-induced pluripotent stem cell (hiPSC) lines. The top ten predicted off-targets sites were identified by the CRISPOR website and investigated by **A, B**) polymerase chain reaction and subsequent **C, D**) Sanger sequencing for the **A, C**) heterozygous (het) and the **B, D**) homozygous (hom) *NRAP/MYC*-overexpressing hiPSC cell lines.

6.3.2 Generation of a *NRAP/GFP*-OE hiPSC line

Since *NRAP* is not only increased in cardiomyopathies, but also plays a crucial role during myofibrillogenesis (Carroll et al. 2004), additionally a *NRAP*-OE hiPSC line with a C-terminal GFP reporter was generated by CRISPR-Cas9 technology. This allows to directly detect the *NRAP* localisation by live-cell imaging. Therefore, the initial *AAVS1-cTnT-NRAP/MYC* plasmid was used to remove the *MYC* tag by restriction digestion and replace it by a *GFP* (**Figure 27 A**). In order to validate the construct, the plasmid was digested with the enzymes BamHI and BglIII (**Figure 27 B**).

Results

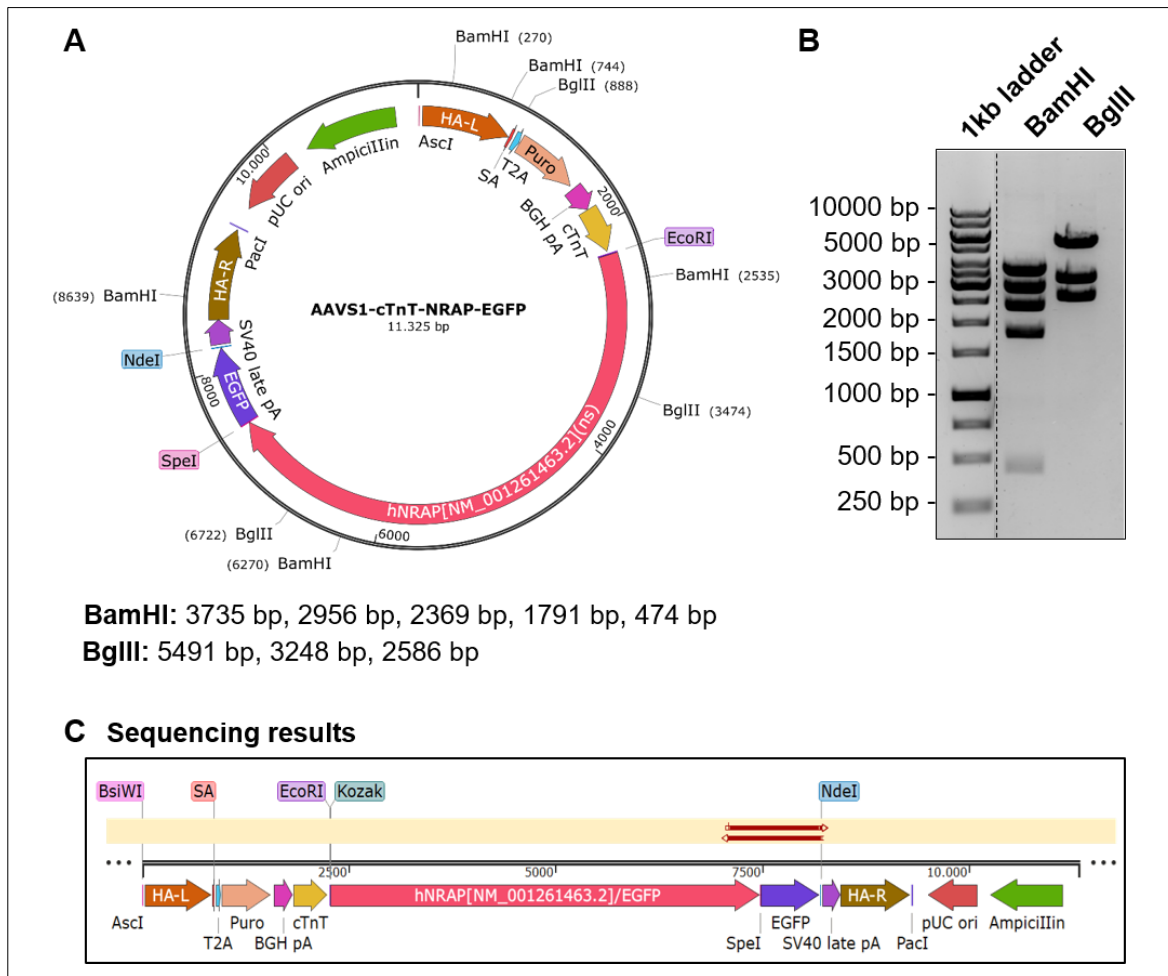


Figure 27: Validation of the *AAVS1-cTnT-NRAP/GFP* plasmid for stable integration into the human genome. **A) Plasmid map with the respective restriction sites for BamHI (3735 bp, 2956 bp, 2369 bp, 1791 bp, 474 bp) and BglII (5491 bp, 3248 bp, 2586 bp). The plasmid was self-designed and produced by VectorBuilder. It contains a left and right homology arm that are identical to those homology arms on the human genome allowing the stable integration mediated by homology-directed repair (HDR). Moreover, the plasmid contains a puromycin resistance, enabling the selection of successfully edited cells, a cardiac-specific troponin T (cTnT) promoter, a Kozak sequence, the *NRAP* mRNA of *NRAP* isoform 1, that includes all *NRAP* exons, coupled to a green fluorescent protein (GFP). Moreover, that part of the plasmid that is not integrated into the genome contains an ampicillin resistance for specific amplification of the plasmid in *Escherichia coli*. **B)** Agarose gel after plasmid restriction digest with BamHI and BglII. **C)** Sanger sequencing for validation of the correct GFP sequence of the plasmid is indicated by red arrows.**

The digestion with BamHI revealed the correct band sizes at 3735 bp, 2956 bp, 2369 bp, 1791 bp and 474 bp and the digestion with BglII at 5491 bp, 3248 bp and 2586 bp. Due to different restriction fragments of the *AAVS1-cTnT-NRAP/MYC* and *AAVS1-cTnT-NRAP/GFP* plasmids, the successful generation of the *GFP*-containing plasmid could be validated. Additionally, the sequence from the C-terminus of *NRAP* involving the *GFP* and part of the right homology arm was successfully validated by Sanger sequencing (**Figure 27 C**).

Results

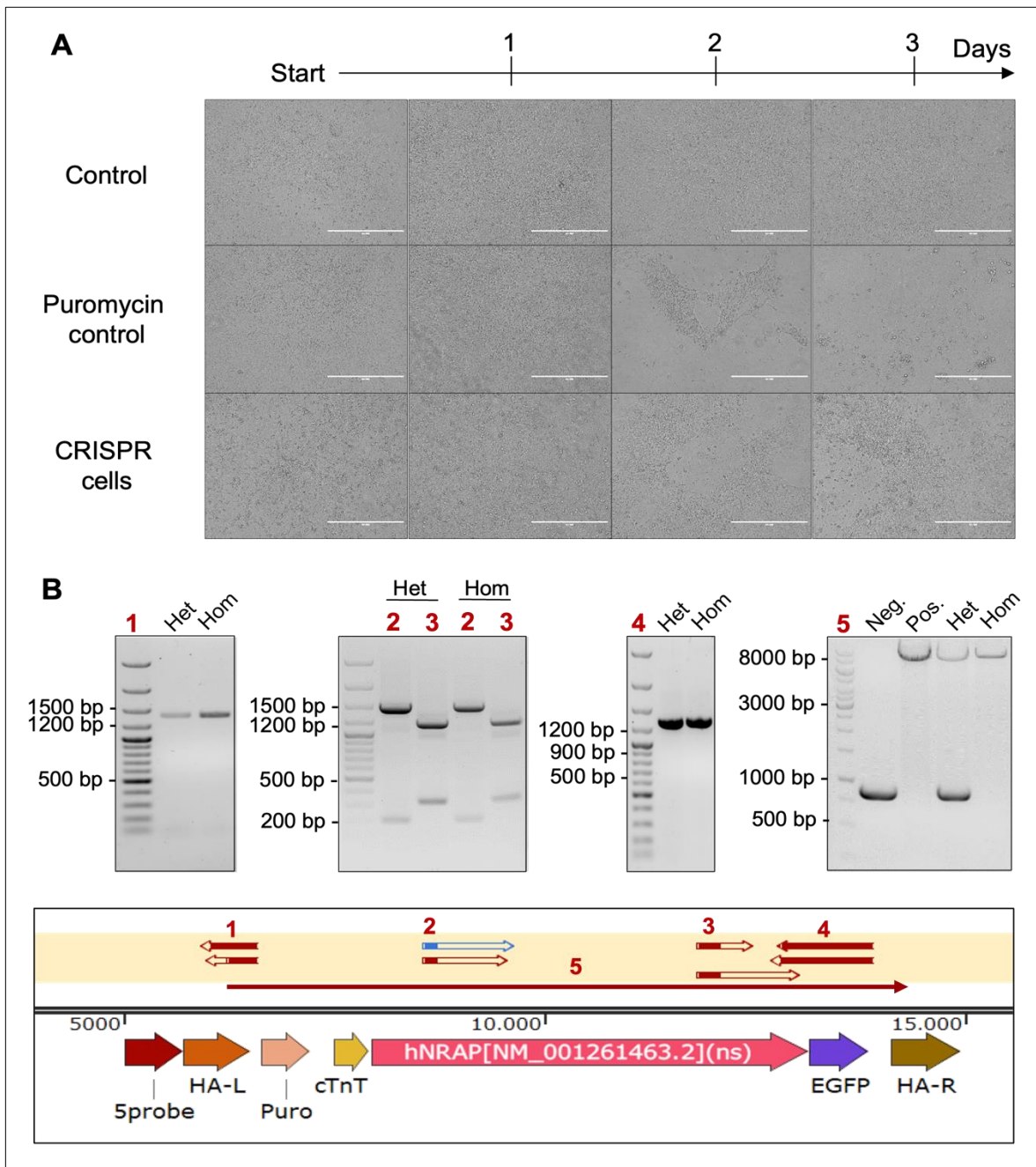


Figure 28: Puromycin selection and validation of heterozygous and homozygous *NRAP*/*GFP*-overexpressing human-induced pluripotent stem cell (hiPSC). **A)** Represented are either non-nucleofected or 3 days post-nucleofected cells. Images show daily treatment of the puromycin control and CRISPR cells with 0.5 $\mu\text{g}/\text{mL}$ puromycin for 72 h. Control cells were not treated with puromycin. Images were taken with the EVOS microscope and scale bars are equal to 1 mm. **B)** Different PCRs with Sanger sequencing were performed to validate either the plasmid-genome overlapping parts (1 = 1323 bp, 4 = 1259 bp) or parts in the plasmid (2 = 201 and 1458 bp, 3 = 323 and 1164 bp). Additionally, long-range PCRs (5 = 8474 bp and 926 bp) from the left homology arm (HA-L) to the right homology arm (HA-R) have been performed to investigate the genotype of the heterozygous (het) and homozygous (hom) *NRAP*/*GFP*-overexpressing clone. The control hiPSC line served as a negative control (neg) and the plasmid as a positive control (pos) in order to validate the successful setup of the long-range PCR. Successful sequencings are represented as red arrows over the plasmid/genome map for the appropriate clone.

Results

After validation of the correct plasmid, the safe harbour locus was used as mentioned above with the similar strategy to integrate the plasmid stably into the human genome (**Figure 28**). Subsequently, hiPSC were nucleofected with the plasmid, the Cas9 and the gRNA targeting the safe harbour locus. Three days post-nucleofection, hiPSC were treated with puromycin for 72 h until only successfully nucleofected control cells were remaining (**Figure 28 A**). The remaining puromycin-resistant hiPSC were used as mentioned above to generate single-cell clones. Similar to the validation approach of the successful integration of the *AAVS1-cTnT-NRAP/MYC* plasmid into the safe harbour locus, the overlapping parts between the human genome and integrated plasmid as well as parts in the plasmid region were validated by PCR and Sanger sequencing. Long-range PCRs were performed to validate heterozygous and homozygous clones (**Figure 28 B**). The analysis of single cell clones revealed a heterozygous and a homozygous *NRAP/GFP-OE* clone.

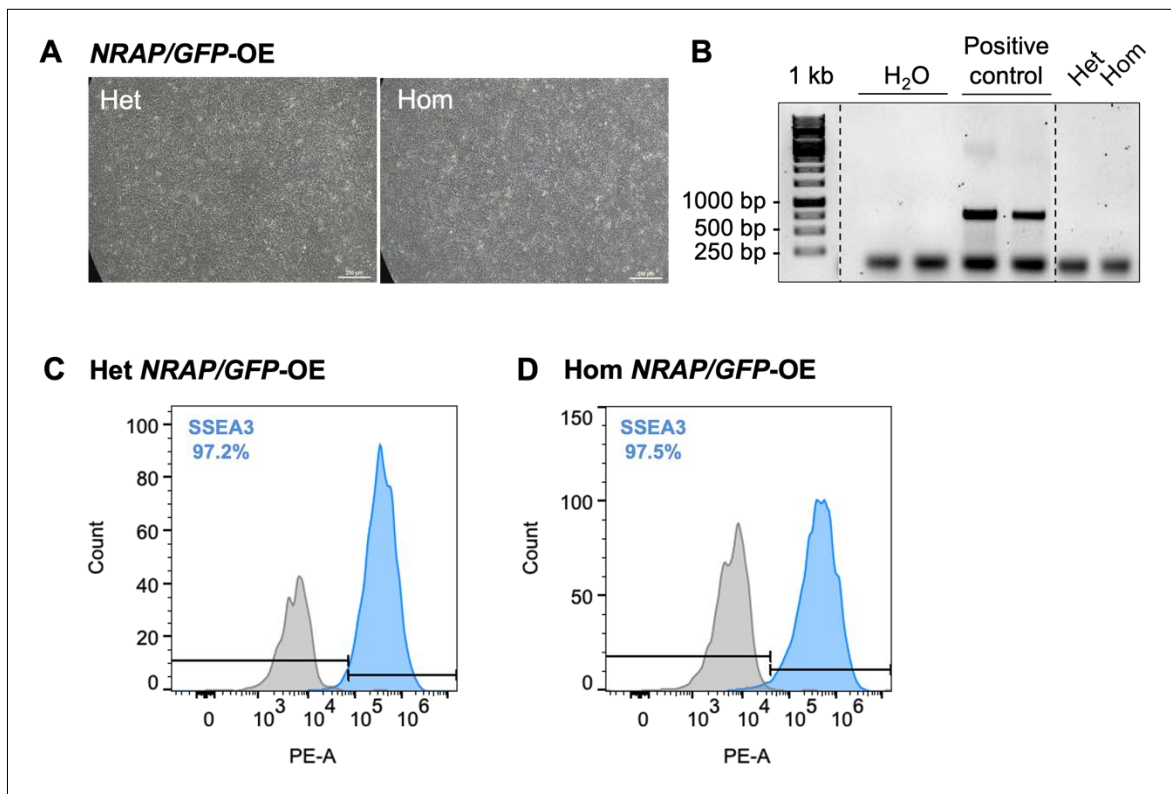


Figure 29: Quality controls for the heterozygous and homozygous *NRAP/GFP-over-expressing* human-induced pluripotent stem cell (hiPSC) clones. A, B) Images of the master cell bank were taken with the EVOS microscope to capture the morphology of hiPSC. Scale bars are equal to 1 mm. B) Agarose gel representing the result of mycoplasma testing with water as negative control and previously positive-revealed samples as a positive control. Measurement of the stage-specific embryonic antigen 3 (SSEA3) by flow cytometry to determine pluripotency of C) heterozygous (het) and D) homozygous (hom) *NRAP/GFP-OE* hiPSC.

For the negative control, the control hiPSC line was amplified (926 bp) and for the positive control, the *AAVS1-cTnT-NRAP/GFP* plasmid was used (8474 bp). For the heterozygous

Results

NRAP/GFP-OE cell line, the PCR consisted of two PCR products, one at a size of 8474 bp and one at 926 bp. However, the PCR of the homozygous *NRAP/GFP*-OE clone only revealed one PCR product at 8474 bp. After successful validation of the plasmid integration into the human genome, master and working cell banks were generated from the heterozygous and homozygous *NRAP/GFP*-OE clones (**Figure 29 A, B**).

The morphology of all cell lines was similar to that of the original hiPSC control cells and the media supernatant revealed no contamination by mycoplasma (**Figure 29 B**). To prove the hiPSC quality and pluripotency, the SSEA3 levels were determined by flow cytometry analysis. The pluripotency of the heterozygous *NRAP/GFP*-OE cell bank was 94.63% and for the homozygous *NRAP/GFP*-OE cell bank 98.87% (**Figure 29 C, D**). In addition, karyotype analysis was performed to exclude CRISPR/Cas9-induced chromosomal abnormalities. This revealed no karyotype abnormalities in the heterozygous and homozygous *NRAP/GFP*-OE hiPSC line (**Figure 30**).

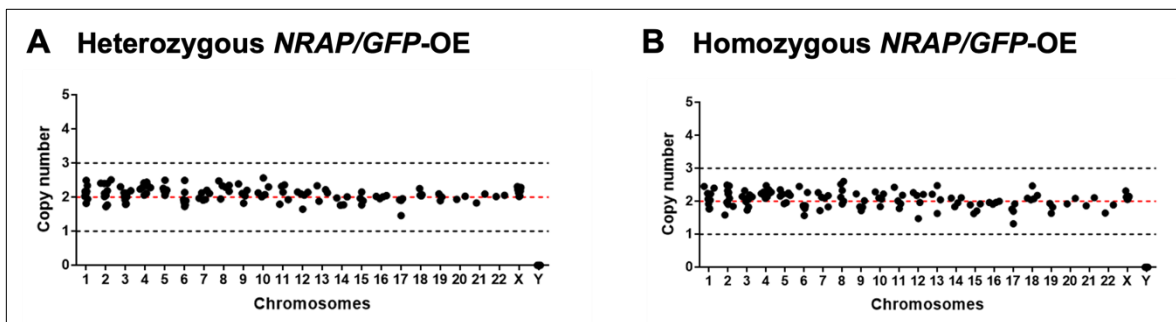


Figure 30: Karyotype analysis of the heterozygous and homozygous *NRAP/GFP*-overexpressing human-induced pluripotent stem cell (hiPSC) clones. For investigation of genetic abnormalities, **A, B** karyotypes were analysed to exclude alterations in the number of chromosomes for the **A**) heterozygous and the **B**) homozygous *NRAP/GFP*-overexpressing (OE) hiPSC clone.

Moreover, the potential top ten off-targets as predicted by the website tool CRISPOR were investigated. Amplification of all off-target loci resulted in successful amplification of PCR products after optimisation (**Figure 31 A, B**). Sanger sequencing analysis of purified PCR products revealed no Cas9-induced genetic modifications such as insertions or deletions (**Figure 31 C, D**) except the gene locus for *APPL2*. Since a point mutation was detected in the heterozygous and homozygous *NRAP/GFP*-OE clones, in addition also here the *APPL2* locus of the human control hiPSC line was sequenced. The same mutation was detected in control and genetically-modified *NRAP* hiPSC lines (**Figure 31 C, D**).

Due to time limitation, the heterozygous and homozygous *NRAP/GFP*-OE cell lines were only developed and all quality controls were successfully performed, but the cell lines were not further investigated by cardiac differentiation and downstream functional studies so far.

Results

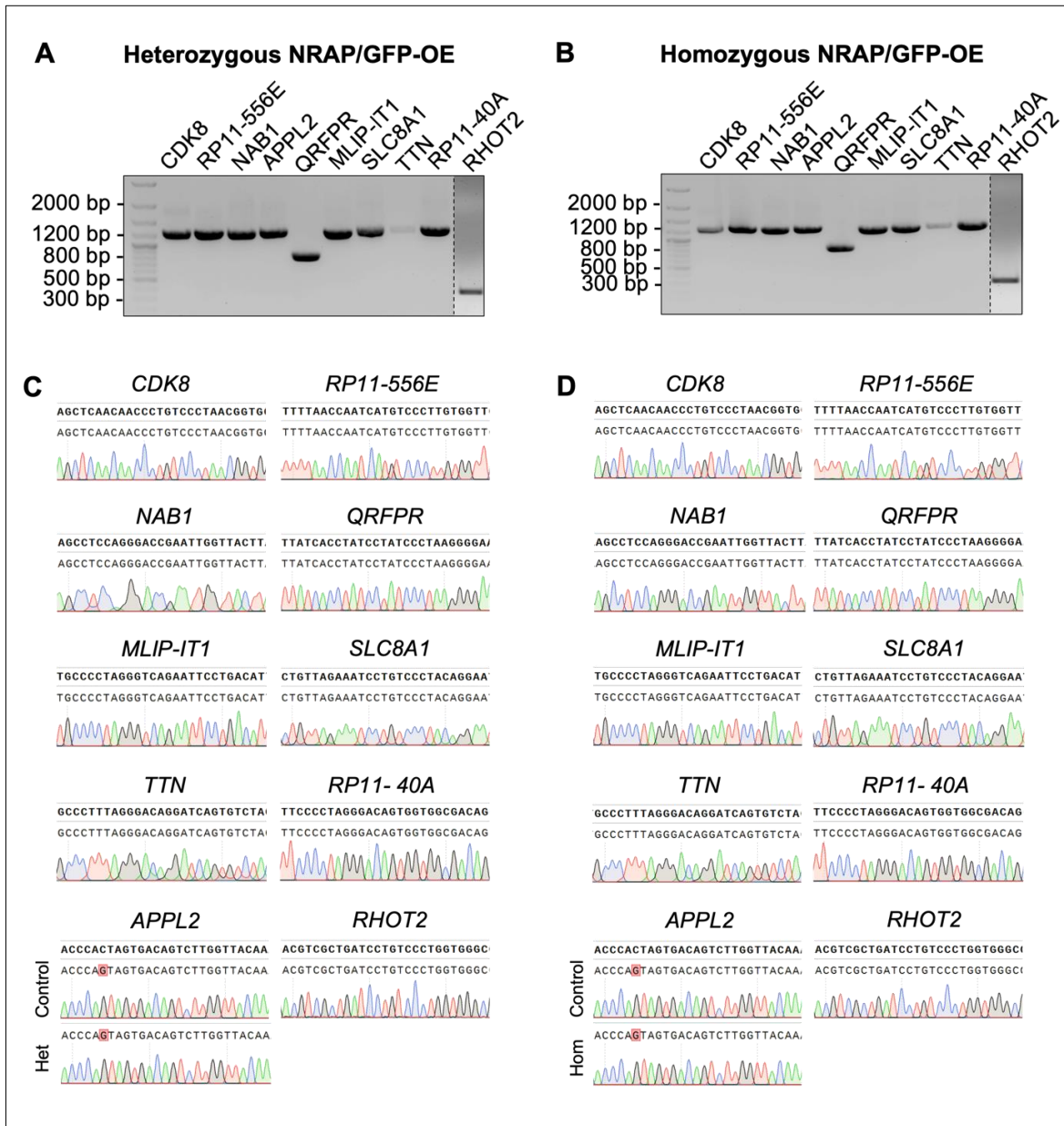


Figure 31: Validation of the top ten off-targets of the heterozygous and homozygous *NRAP/GFP*-overexpressing human-induced pluripotent stem cell (hiPSC) lines. The top ten predicted off-targets sites were identified by the CRISPOR website and investigated by **A, B**) polymerase chain reaction and subsequent **C, D**) Sanger sequencing for the **A, C**) heterozygous (het) and the **B, D**) homozygous (hom) *NRAP/GFP*-overexpressing hiPSC cell lines.

6.3.3 Generation of a *NRAP*-KD hiPSC line

In order to enable the study of the loss-of-*NRAP*-function, in addition to the *NRAP*-OE cell lines, a KO of *NRAP* was performed that affects all four known human *NRAP* isoforms. For this purpose, two gRNAs were generated that match the 5' site of the promoter flanking region and the 3' site of the promoter (**Figure 32 A, B**). With this strategy, the generation of non-sense mRNA and non-sense mediated mRNA decay could be avoided. At the same time, by removal of the promoter flanking region and promoter region, including the start codon and the first exons, *NRAP* expression was prevented.

Results

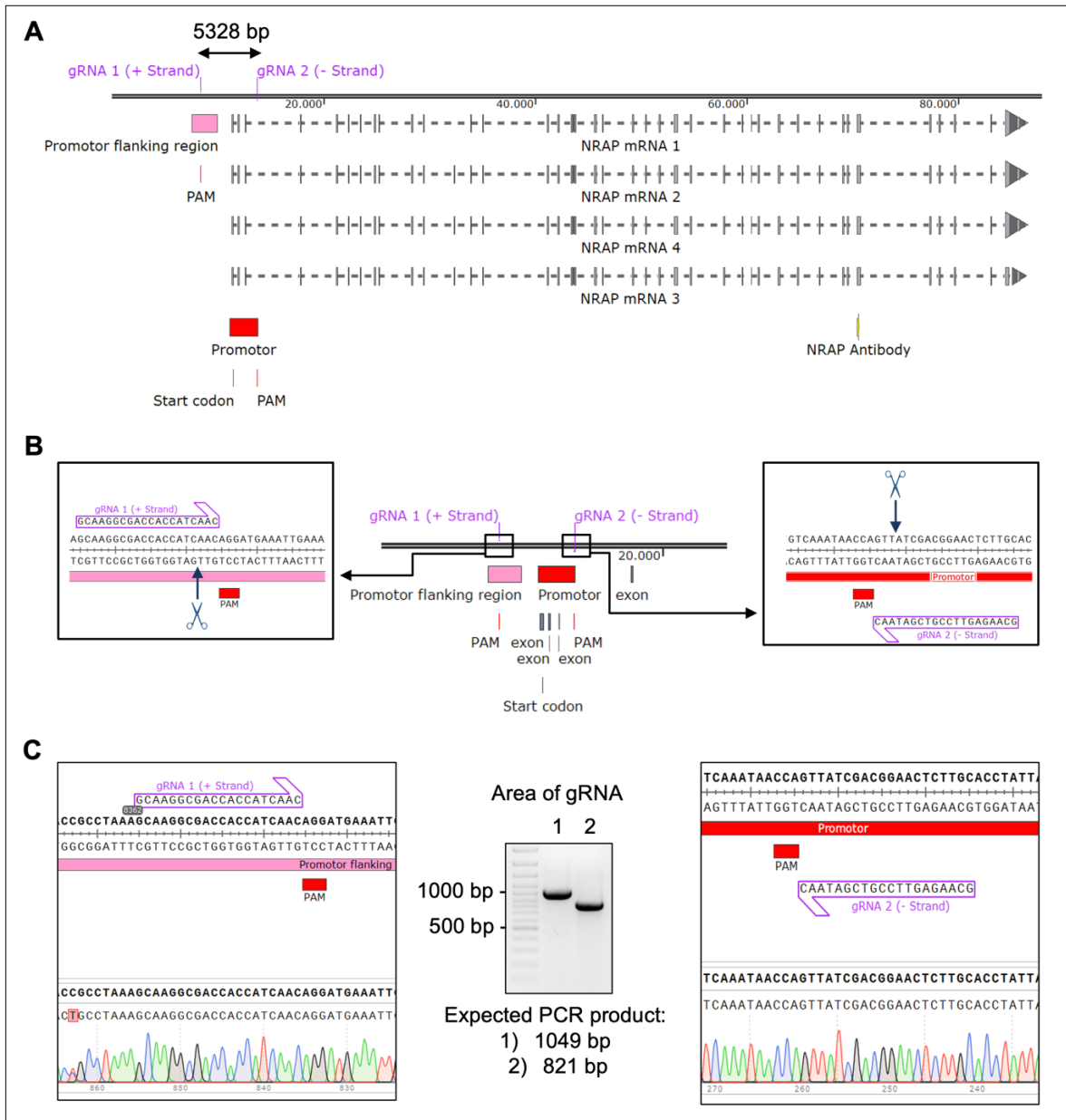


Figure 32: Gene editing approach for stable knock-out (KO) of NRAP in human-induced pluripotent-derived cardiac myocytes. The gene editing approach was performed by the CRISPR-Cas9 system. Therefore, the Cas9 and two specific gRNAs were used for the nucleofection of human-induced pluripotent stem cells. **A)** The gRNA 1 targets the 5' site of the promoter-flanking region and the gRNA 2 targets the 3' site of the promoter. With this strategy, NRAP expression should be prevented by removing the initiation site and start site. The four NRAP isoforms are represented and the vertical lines represent the 42 exons of NRAP. **B)** Sequences representing the protospacer adjacent motif (PAM) sequences and cutting sites by the Cas9. **C)** Polymerase chain reaction and Sanger sequencing to prevent silent point mutations on the genomic sequence of the control hiPSC line that could impair gRNA binding to genomic DNA.

To ensure that there were no silent mutations around the PAM sites that might disable binding of gRNAs, the sequence at those areas was first validated by Sanger sequencing (**Figure 32 C**). After successful validation of the sequence, hiPSC were nucleofected with the Cas9 and the two gRNAs to induce double strand breaks at the anticipated genomic areas of the chromosome 10, followed by cell mediated repair by non-homologous end

Results

joining. At 48 h post-nucleofection, single cell clones were generated from the hiPSC pool. For validation of a successful removal of 5328 bp, the area upstream of the 5' PAM site and downstream of the 3' PAM site were used for amplification. In comparison to the control hiPSC line that only revealed amplification of a 5805 bp PCR product, the PCR amplification of the CRISPR pool additionally revealed an amplification of a 477 bp fragment (**Figure 33 A, B**).

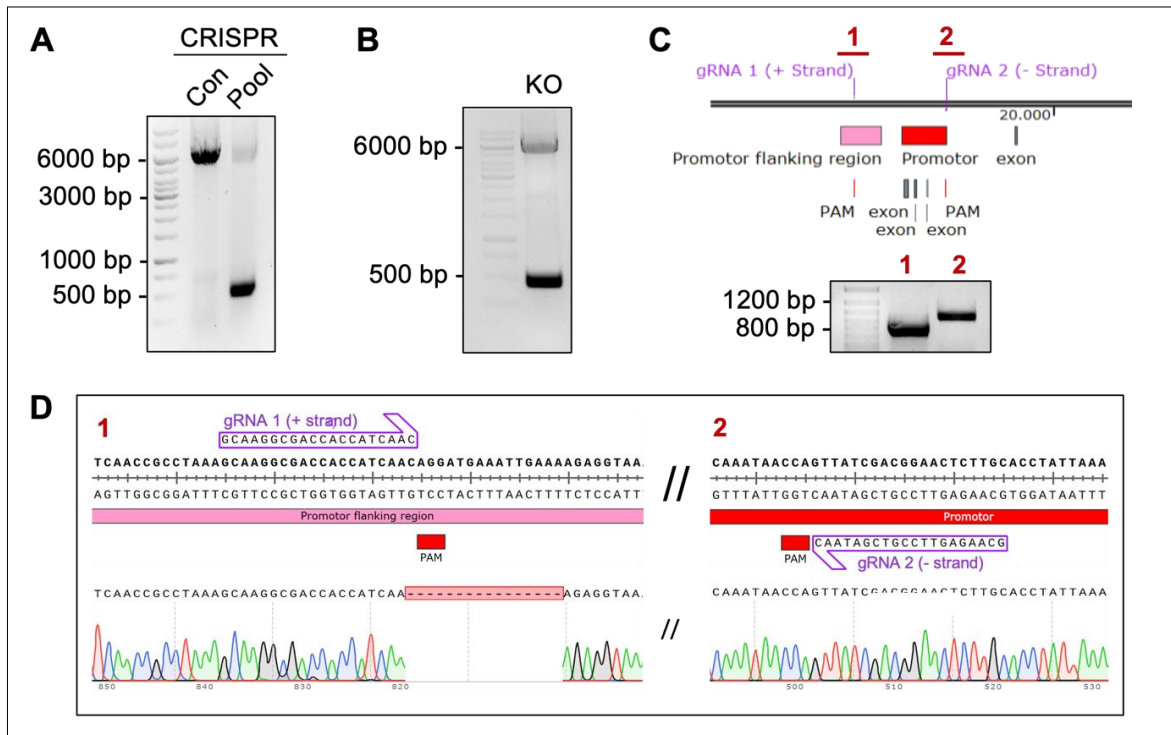


Figure 33: Validation of successful generation of a *NRAP*-knock-down (KD) in human-induced pluripotent stem cells (hiPSC). **A**) Analysis of gene editing efficiency with gDNA derived from control (Con) or CRISPR-pool (Pool) cells by amplification. **B**) Amplification of a heterozygous clone. **C**) Amplification of sequence parts covering the sequences around the two protospacer adjacent motif (PAM) sites (1, 2 (red), and **D**) sequencing of the purified PCR products. The validation of CRISPR clones was performed by Vanessa Lewandowski under my supervision.

As previously described for validation purposes of the sequences around the PAM sites, the same PCRs were performed to investigate the sequences on the non-affected allele after successful nucleofection. This revealed no alteration of the sequence for gRNA 2 in the promoter region but showed alterations around the PAM site of gRNA 1 in the promoter-flanking region (**Figure 33 C, D**). In that region, a 16 bp deletion starting +1 upstream of the PAM site and ending -12 downstream of the PAM site was detected. Since no homozygous clones could be identified and all heterozygous clones of the 150 screened clones showed deletions around the PAM site, this *NRAP*-knock down (KD) clone was used for further investigations. Similar to the previously described genetically modified cell lines, quality controls for the *NRAP*-KD master cell bank were performed with

Results

a determined pluripotency of 78.7%. This revealed the absence of mycoplasma, excluded karyotype abnormalities and off-target modification.

Overall, these data demonstrate successful generation of *NRAP/MYC-OE* and *NRAP/GFP-OE* hiPSC lines. Among many screened clones, not a single homozygous *NRAP-KO* could be detected. Since the aim was to study *NRAP* loss-of-function, a *NRAP-KD* hiPSC line with one successfully edited allele and a deletion on the other allele was generated. All cell banks showed a correct karyotype. Morphological alterations, mycoplasma contamination and CRISPR off-targets were ruled out. The pluripotency was sufficiently high in all lines.

6.4 *NRAP/MYC-OE* and *NRAP-KD* hiPSC-derived cardiac myocytes

6.4.1 Cardiac differentiation of *NRAP/MYC-OE* and *NRAP-KD* hiPSC

In order to investigate the gain- and loss-of-function of NRAP in cardiac myocytes, *NRAP-OE* or *NRAP-KD* hiPSC were optimised for a cardiac monolayer differentiation.

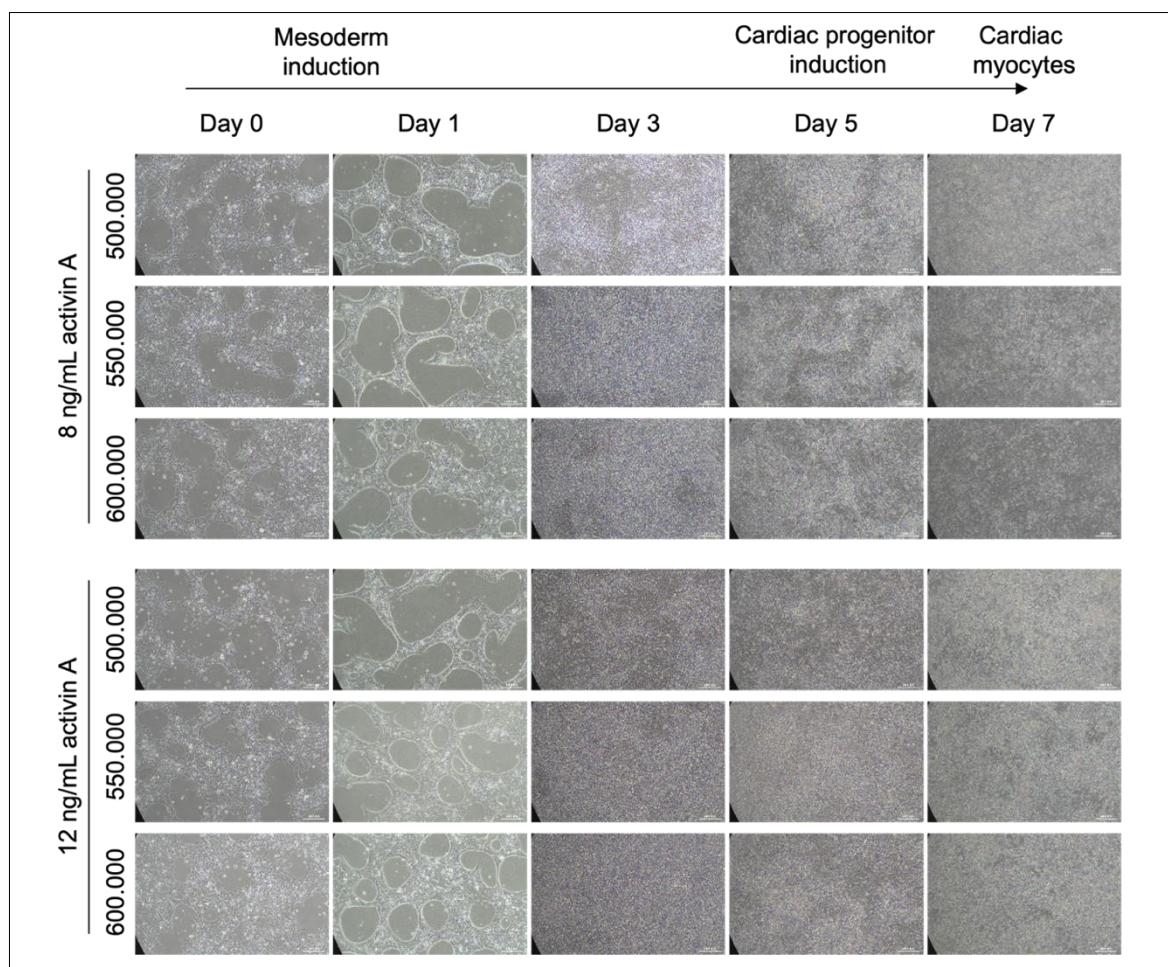


Figure 34: Testing of different conditions for cardiac monolayer differentiation. Different amounts of activin A (8 ng/mL or 12 ng/mL) were used and cell densities of 500.000, 550.000 or 600.000 cells for each 35 mm dish were used. Images were taken after every medium change. These images are representative for the control cell line and images of cardiac differentiation for other genetically-modified cell lines can be found in the supplements. The scale bars are equal to 200 μ m.

Therefore, for each cell line, including control hiPSC, different cell densities of 500.000, 550.000 and 600.000 hiPSC as well as different concentrations of the growth factor activin A were tested. For mesoderm induction, either 8 ng/mL activin A or 12 ng/mL activin A were used (**Figure 34**). Compared to the control hiPSC line, no morphological alterations could be observed either for the *NRAP/MYC-OE* or for the *NRAP-KD* hiPSC line. Importantly, all cell lines formed a typical colonies on day 1 during this two-dimensional cardiac differentiation (**Figure 34**).

Results

Subsequently to differentiation of hiPSC into cardiac myocytes, cells were dissociated as soon as wave-like beating of the cell layer could be observed. To analyse the efficiency of the differentiation, cells were stained for the cardiac-specific marker cTnT and cTnT-positive cells were quantified by flow cytometry (**Figure 35**).

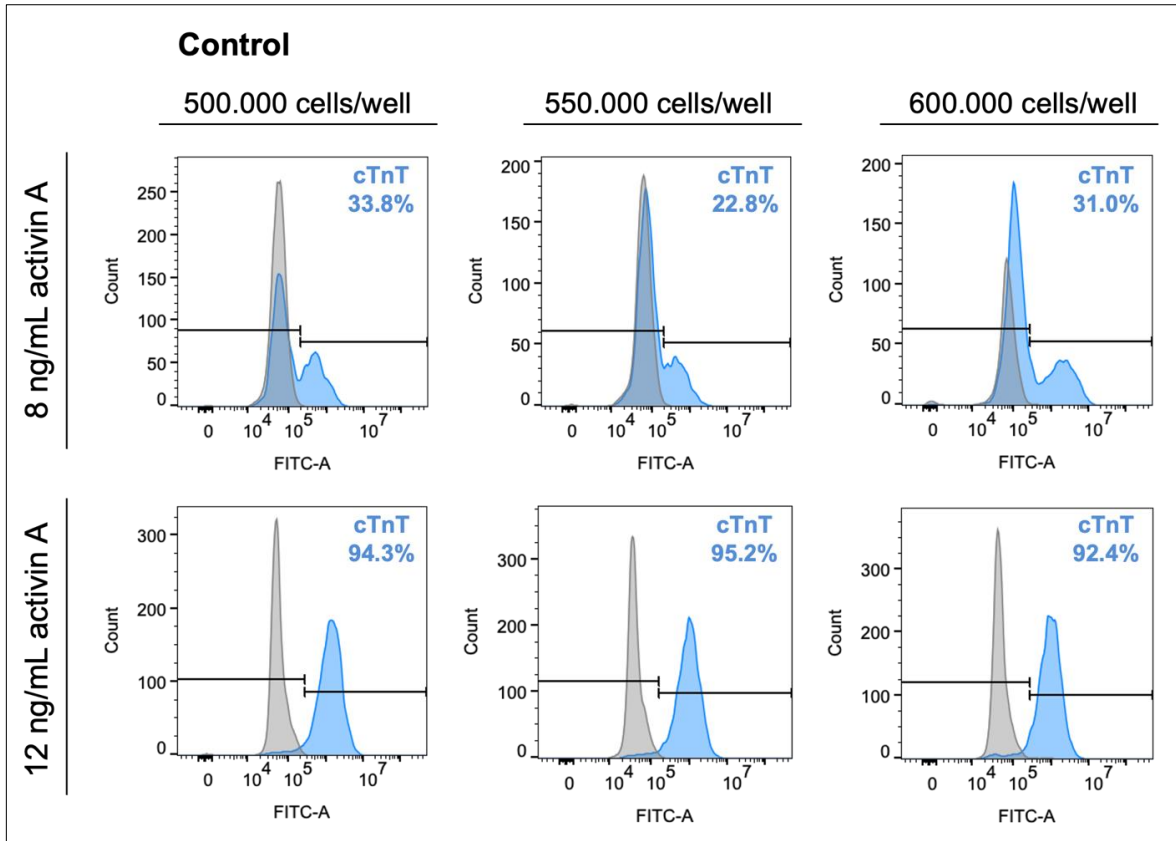


Figure 35: Cardiac troponin T values for testing of different conditions for cardiac monolayer differentiation of the control cell line. Different amounts of activin A (8 ng/mL or 12 ng/mL) and cell densities of 500.000, 550.000 or 600.000 cells for each 35 mm dish were used. The cardiac-specific marker troponin T (cTnT) was measured by flow cytometry. Data were analysed using the FlowJo software.

For the control cell line, low cTnT values, ranging between 22.8 and 33.8% cTnT-positive cells for the different cell densities, were detected when 8 ng/mL activin A was used during the differentiation. In contrast, 12 ng/mL activin A revealed higher percentages of cTnT-positive cells, ranging between 92.4 to 95.2%. The optimal differentiation efficiency was achieved with 95.2% cTnT-positive cells when 550.000 control cells were seeded on 6-well culture plates and 12 ng/mL activin A were used for differentiation.

For the *NRAP*-KD cell line, differentiation with 8 ng/mL activin A resulted in 45.5 to 69% cTnT-positive cells whereas differentiation with 12 ng/mL activin A led to cTnT values between 66.7 and 80.1% (**Figure 36**). The optimal cardiac differentiation efficiency for the *NRAP*-KD cell line was reached by plating of 550.000 cells on 6-well culture plates and differentiation with 12 ng/mL activin A resulting in 80.1% positive cells.

Results

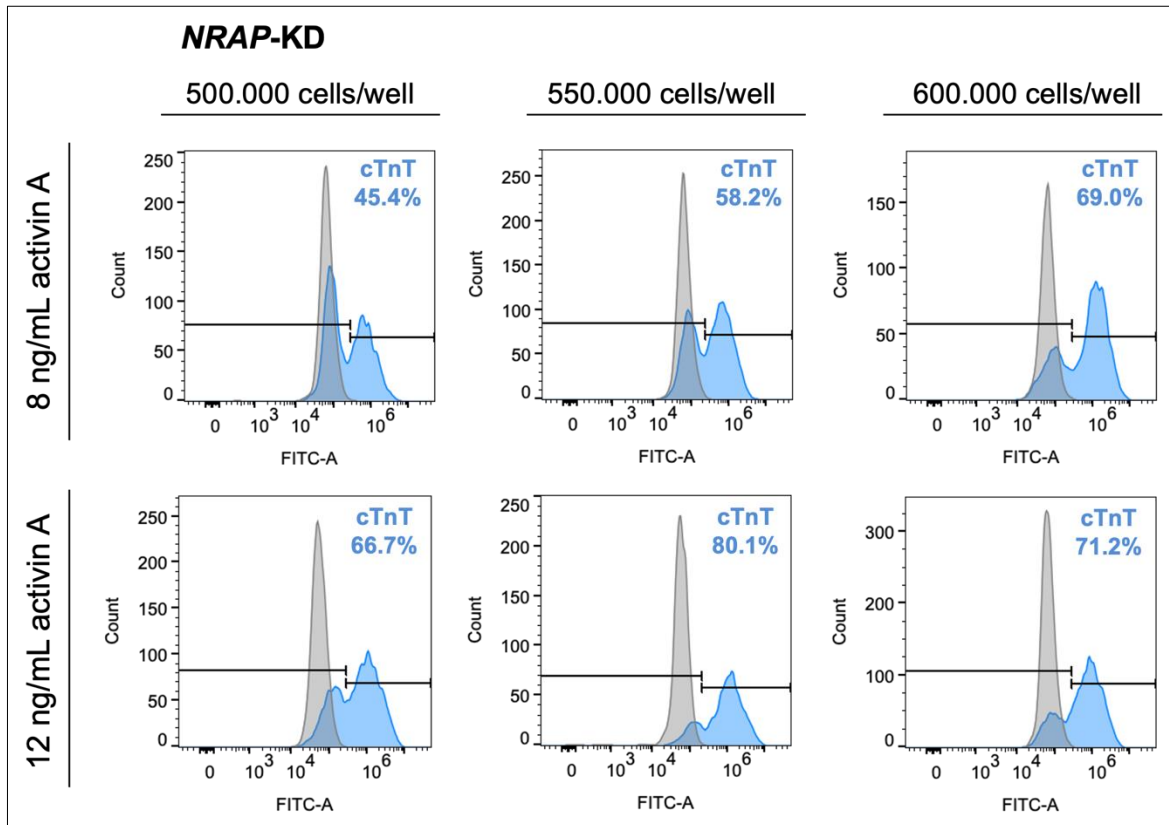


Figure 36: Cardiac troponin T values for testing of different conditions for cardiac monolayer differentiation of the *NRAP-KD* cell line. Different amounts of activin A (8 ng/mL or 12 ng/mL) and cell densities of 500.000, 550.000 or 600.000 cells for each 35 mm dish were used. The cardiac-specific marker troponin T (cTnT) was measured by flow cytometry. Data was analysed using the FlowJo software.

For the heterozygous *NRAP/MYC-OE* cell line, differentiation with 8 ng/mL activin A resulted in cTnT values between 24.4 and 33.5% while differentiation with 12 ng/mL activin A led to 80.5 to 88.2% cTnT-positive cells (**Figure 37**). The optimal conditions for differentiation were plating of 550.000 hiPSC to 6-well culture plates and usage of 12 ng/mL activin A resulting in 88.2% cTnT-positive cells. For the homozygous *NRAP/MYC-OE* cell line, the higher activin A concentration revealed higher cTnT values although the difference of cTnT-positive cells was less than for the other cell lines between the different activin A concentrations.

A concentration of 8 ng/mL activin A resulted in 73.7 to 83.9% cTnT-positive cells while 12 ng/mL activin A resulted in values ranging from 80.1 to 95.7% (**Figure 37**). The highest cTnT value of 95.7% was reached with a cell density of 500.000 cells and an activin A concentration of 12 ng/mL.

Results

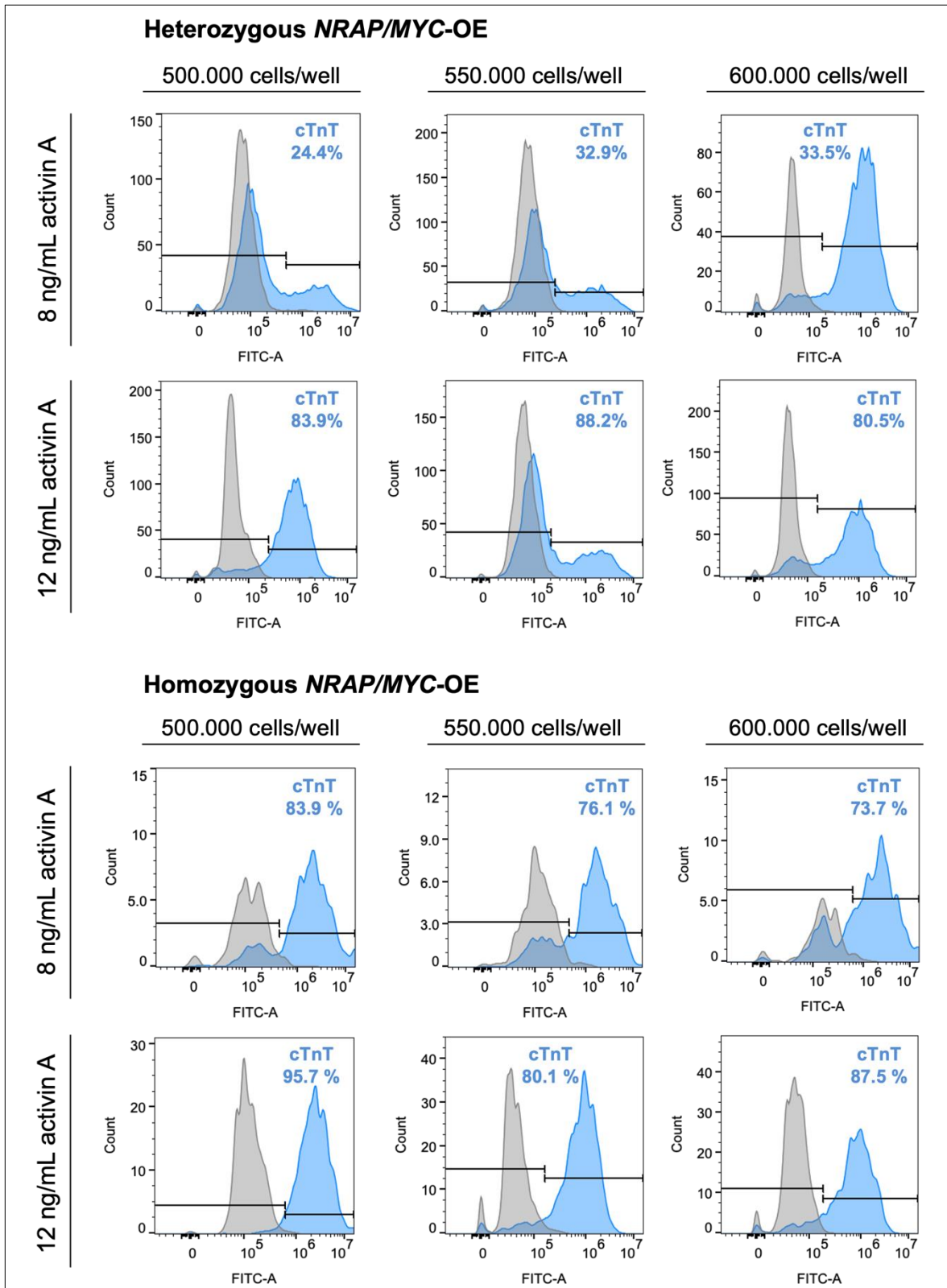


Figure 37: Cardiac troponin T values for testing of different conditions for cardiac monolayer differentiation of heterozygous and homozygous *NRAP/MYC-OE* cell line. Different amounts of activin A (8 ng/mL or 12 ng/mL) were used and cell densities of 500.000, 550.000 or 600.000 cells for each 35 mm dish were used. The cardiac-specific marker troponin T (cTnT) was measured by flow cytometry. Data was analysed using the FlowJo software.

Results

Overall, the aim was to identify one optimal differentiation condition suitable for all investigated hiPSC lines. Since 12 ng/mL activin A and a cell density of 550.000 cells on 6-well culture vessels revealed the highest cTnT values, this condition was used for further propagation.

6.4.2 NRAP RNA and protein levels

Initially after successful differentiation of control, *NRAP/MYC*-OE and *NRAP*-KD hiPSC to cardiac myocytes, the cell lines were investigated for mRNA and protein levels to analyse if the genetic editing of hiPSC resulted in a detectable NRAP gain- and loss-of-function.

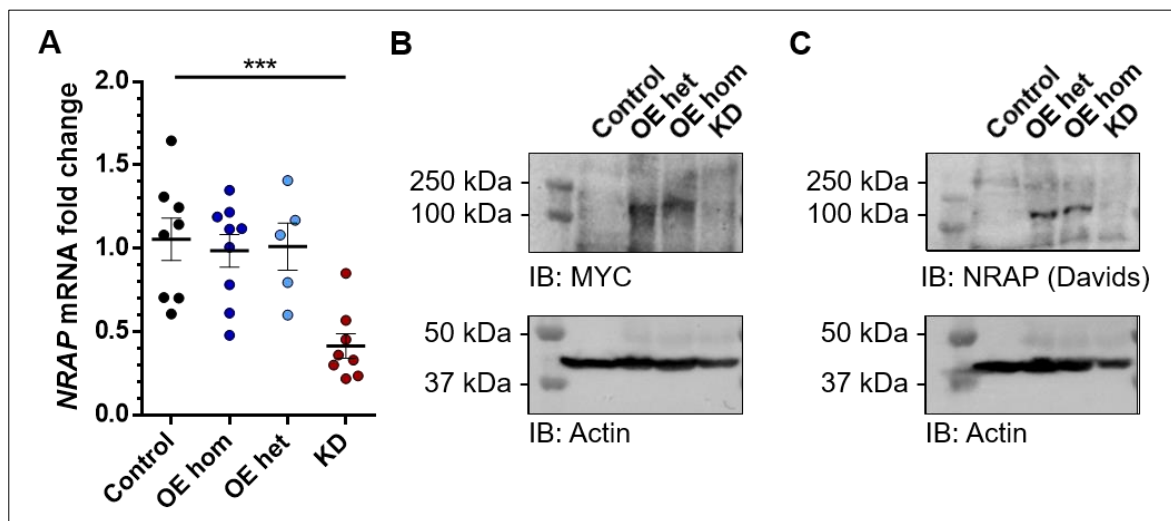


Figure 38: NRAP mRNA and protein levels in *NRAP*-overexpressing and knock-down hiPSC-derived cardiac myocytes. A) *NRAP* mRNA levels normalised to GusB in control, heterozygous (het) and homozygous (hom) *NRAP/MYC*-overexpressing (OE) or *NRAP*-knock-down (KD) EHTs after 21 days of culture. Data are represented as dots for each EHT and mean \pm standard error mean (SEM) from $n = 8$ (control, KD), $n = 9$ (OE hom) or $n = 5$ (OE het) EHTs from three independent differentiations. For statistics, one-way ANOVA, followed by Dunnett's posthoc test was performed (***) = $p < 0.001$). **B-C)** Western immunoblot for MYC and NRAP (Davids Biotechnology). Cardiac actin served as a loading control from control, het or hom *NRAP*-OE or *NRAP*-KD hiPSC-derived cardiac myocytes after 7 days of culture.

Since NRAP is only expressed in heart and muscle tissue but not in other cell types such as hiPSC and the cTnT promoter of the *NRAP/MYC*-OE hiPSC line is only active in cardiac myocytes, the differentiation of those cell lines to cardiac myocytes was required before testing for NRAP protein abundance and ultimate confirmation of successful generation of NRAP gain- and loss-of-function cell lines.

For mRNA analysis, RNA was isolated from EHTs after 21 days of culture when EHTs had reached their force plateau. Despite high variance between different EHTs, no differences in mRNA fold change were detected for heterozygous and homozygous *NRAP/MYC*-OE EHTs compared to control EHTs but 60% lower *NRAP* mRNA was detected in *NRAP*-KD EHTs compared to control EHTs (**Figure 38 A**).

For investigation of NRAP protein levels, cardiac myocytes were cultured for 7 days in 2D prior to protein analysis by western immunoblotting since isolation of proteins from EHTs was unsuccessful. This revealed the detection of the MYC-tag in both *NRAP/MYC-OE* hiPSC-derived cardiac myocytes (**Figure 38 B**). Concomitantly, higher NRAP protein levels were detected in *NRAP/MYC-OE* compared to *NRAP-KD* cardiac myocytes and control cardiac myocytes (**Figure 38 C**). Recently, a NRAP antibody had been developed by Merck that has been validated by the company for immunostaining. This antibody was additionally tested for western immunoblotting of the same samples, revealing unspecific protein detection in cardiac myocytes (**Supplementary figure 3**).

In essence, 60% less mRNA was detected in *NRAP-KD* EHTs and higher protein abundance in both heterozygous and homozygous *NRAP/MYC-OE* cardiac myocytes.

6.4.3 Myofilament structure

Considering that NRAP is not only involved in mechanotransduction, but has additionally been shown to be involved in the assembly of myofibrils, the aim was to study the impact of a NRAP gain- or loss-of-function on NRAP localisation and myofilament structure in cardiac myocytes. Therefore, two-dimensional control, heterozygous or homozygous *NRAP/MYC-OE* as well as *NRAP-KD* cardiac myocytes were stained for F-actin and Z-discs by staining of α -actinin, NRAP and DAPI for nuclei. In addition to the produced antibody by Davids Biotechnology, the commercial NRAP antibody from Merck, was investigated since the initial validation of the custom-made antibody showed a diffuse and non-specific signal for NRAP in hiPSC or hiPSC-derived EHTs.

In control hiPSC-derived cardiac myocytes, structured myofilaments could be detected as indicated by F-actin and α -actinin staining of Z-discs. NRAP staining with both antibodies revealed signals in close proximity to Z-discs (**Figure 39 A, B**). However, in heterozygous *NRAP/MYC-OE* cardiac myocytes, differences between the two antibodies were observed. While the NRAP antibody from Davids Biotechnology resulted in mainly nuclear and additionally cytosolic staining of NRAP (**Figure 39 A**), the NRAP antibody from Merck showed staining of NRAP at the cellular periphery of cardiac myocytes (**Figure 39 B**). However, in both conditions, the myofilament structure was not as structured and paralleled as in the respective control cardiac myocytes.

In contrast, homozygous *NRAP/MYC-OE* cardiac myocytes displayed more aligned and parallel myofilament structures. The detection of NRAP by the antibody from Davids Biotechnology was almost exclusively located in the nucleus (**Figure 39 A**) while the commercial antibody detected NRAP mainly at membrane-like structures and myofibril insertion sites (**Figure 39 B**). The myofilament structure of *NRAP-KD* hiPSC-CMs was

Results

comparable with those of control cardiac myocytes. Similar to control cardiac myocytes, NRAP was located in the nuclear and cytosolic area as demonstrated with the antibody from Davids Biotechnology (**Figure 39 A**) and in close proximity to Z-discs with the commercial NRAP antibody from Merck (**Figure 39 B**).

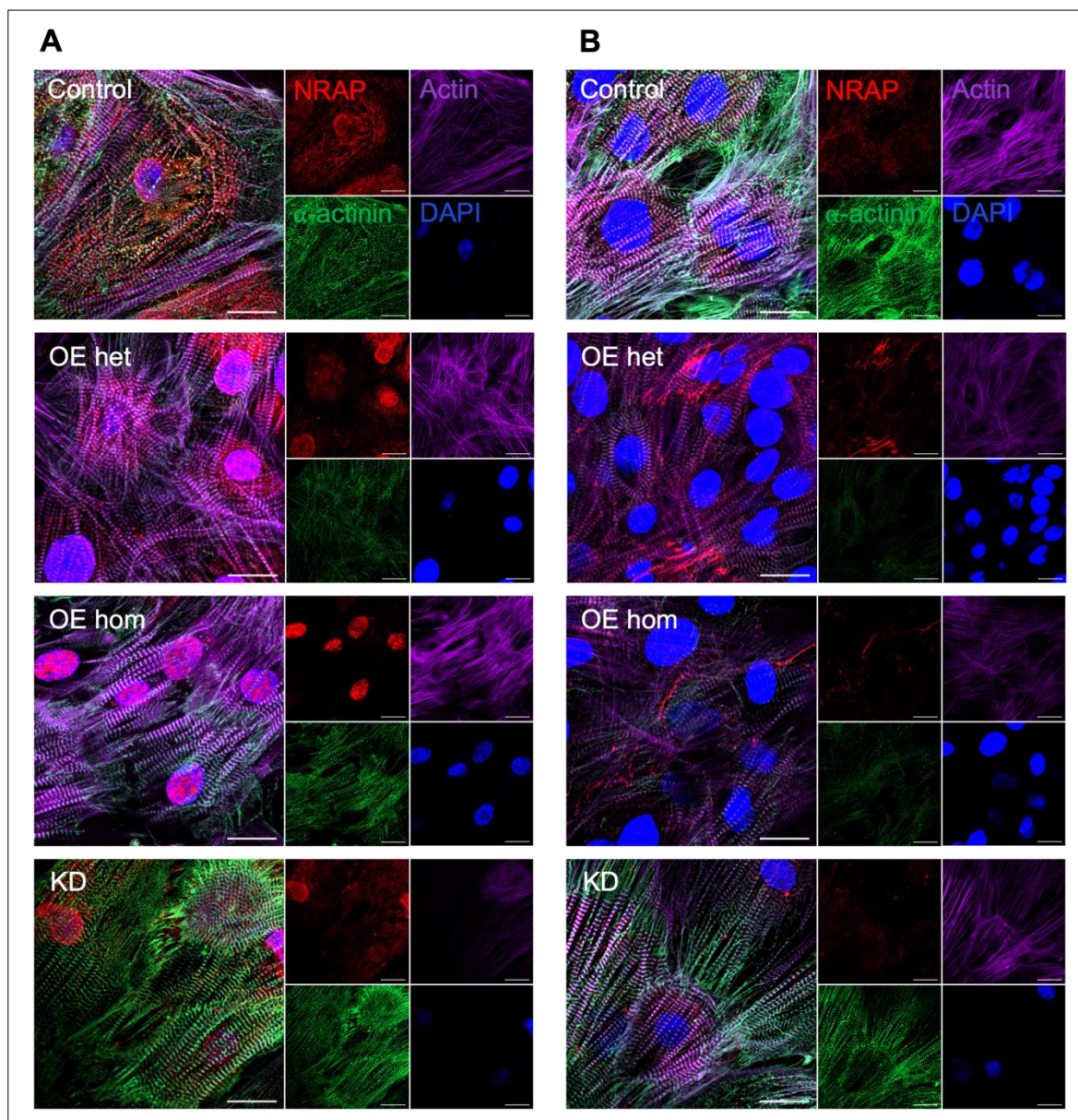


Figure 39: NRAP protein levels and localisation in *NRAP*-overexpressing and -knock-down hiPSC-derived cardiac myocytes. A, B Immunofluorescence of control, heterozygous (OE het) *NRAP/MYC*-OE, homozygous (OE hom) *NRAP/MYC*-OE or *NRAP*-knock-down (KD) hiPSC-derived cardiac myocytes. Cells were stained for α -actinin (green), F-actin (purple), nuclei (DAPI, blue) and NRAP (red). NRAP was stained with the **A**) NRAP antibody by DAVIDS biotechnology or **B**) the commercial NRAP antibody from Merck. Scale bars are equal to 20 μ m ($n = 1$).

Investigation of the myofilament structure revealed phenotypical similarities between control and *NRAP*-KD cardiac myocytes with NRAP localisation in close proximity to Z-discs. In contrast, NRAP was detected at the lateral borders in *NRAP/MYC*-OE cardiac

myocytes as shown with the commercial Merck antibody. Instead, the custom-made NRAP antibody did not work in hiPSC-derived cardiac myocytes.

6.5 Impact of NRAP gain- and loss-of-function in EHTs

6.5.1 Contractile function

In order to study the impact of a NRAP gain- and loss-of-function on contractile function in a gene-dosis-dependent effect, control, hetero- and homozygous *NRAP/MYC-OE* and *NRAP-KD* hiPSC-derived cardiac myocytes were embedded in a three-dimensional EHT format that allows investigating different contractile parameters. Therefore, EHTs were monitored and measured over a time period of 21 days as EHTs reached their force plateau after approximately 14 days.

On days 5-6 after the generation of EHTs, the mean beating frequency \pm SEM of control (44.2 ± 3.3 BPM), heterozygous *NRAP/MYC-OE* (47.1 ± 7.3 BPM) and homozygous *NRAP/MYC-OE* (34.9 ± 1.5 BPM) EHTs was lower compared to *NRAP-KD* EHTs (86.5 ± 4.4 BPM) (**Figure 40 A**). Over time, the beating frequency increased for control (60.2 ± 2.6 BPM), heterozygous *NRAP/MYC-OE* (79.7 ± 3.7 BPM) and homozygous *NRAP/MYC-OE* (80.7 ± 2.7 BPM) EHTs while the frequency decreased until culture day 21 for *NRAP-KD* EHTs (65.5 ± 2.1 BPM). The mean force on day 5 was relatively low for control (0.07 ± 0.006 mN), heterozygous (0.089 ± 0.014 mN) and homozygous (0.096 ± 0.010 mN) *NRAP/MYC-OE* and *NRAP-KD* (0.045 ± 0.004 mN) EHTs (**Figure 40 B**).

Over time, the mean force only increased marginally with no differences in spontaneous beating force between the genetically-modified *NRAP*-EHTs and control EHTs. Additionally, no differences in the time to peak (-80 %) were observed between different cell lines (**Figure 40 C**).

However, the relaxation time (80%) was lower in the heterozygous (0.231 ± 0.013 s) and homozygous (0.258 ± 0.008 s) *NRAP/MYC-OE* EHTs as well as in *NRAP-KD* EHTs (0.187 ± 0.006 s) compared to control EHTs (0.289 ± 0.008 s) (**Figure 40 D**). During 21 days of culture, the relaxation time increased for all cell lines to 0.343 ± 0.011 s for control EHTs, 0.223 ± 0.012 s for heterozygous *NRAP/MYC-OE* EHTs, 0.231 ± 0.011 s for homozygous *NRAP/MYC-OE* EHTs and 0.265 ± 0.007 s for *NRAP-KD* EHTs.

Results

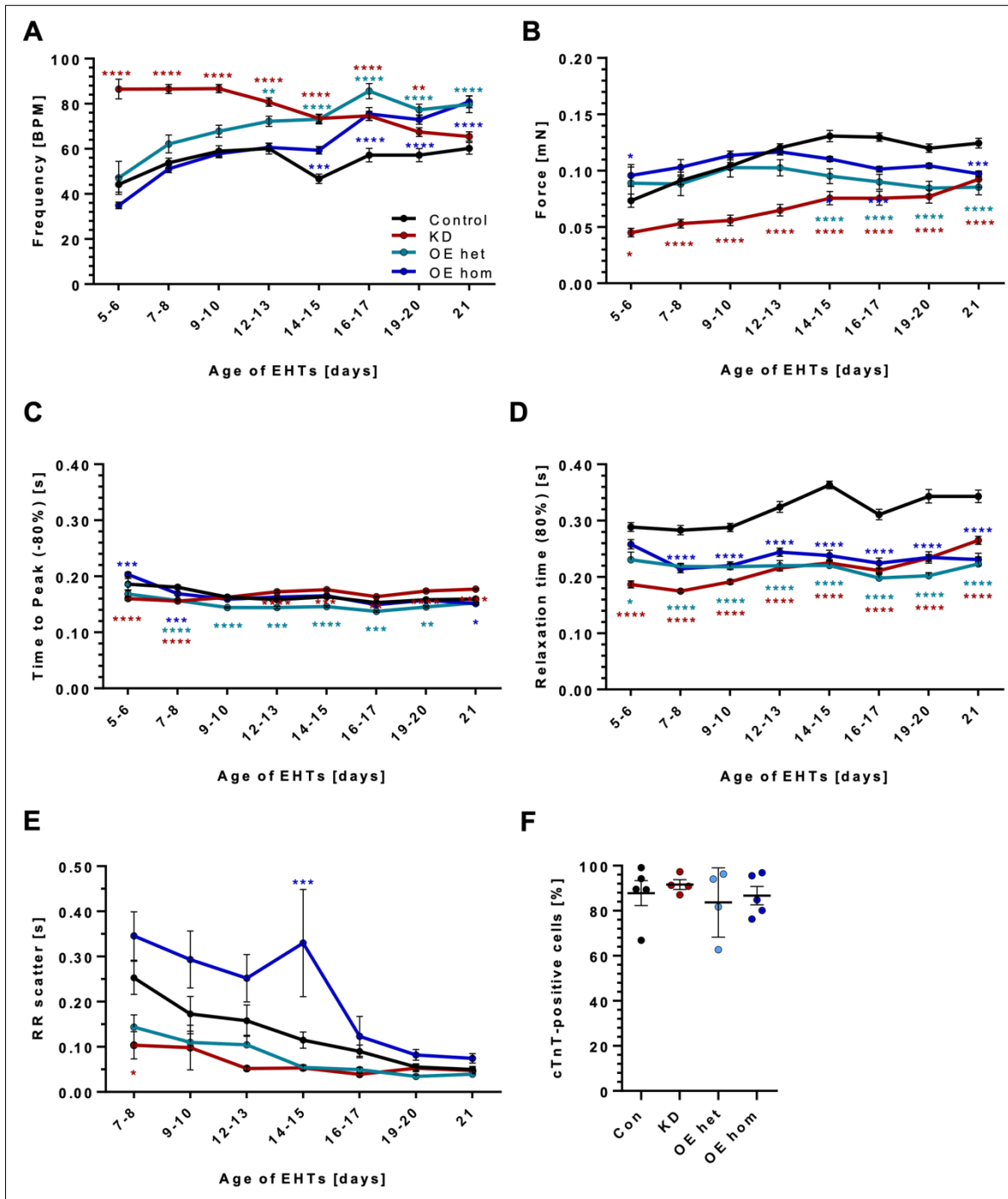


Figure 40: Contractile measurements of genetically-modified NRAP-EHTs. Control (black), heterozygous (OE het; light blue) and homozygous *NRAP/MYC*-overexpressing (OE hom; dark blue) or *NRAP*-KD (KD; red) hiPSC-derived cardiac myocytes were embedded in engineered heart tissues (EHTs). EHTs were cultured for 21 days and measured three times a week for contractile parameters such as **A**) frequency [beats per minute/BPM], **B**) force [mN], **C**) time to peak (-80%) [s], **D**) relaxation time (80%) [s] and **E**) RR scatter (time between beating peaks) [s] over time [days]. Data are represented as mean \pm standard error mean (SEM) from 5 (control/OE hom) or 4 (OE het/KD) batches. N = 98 for control EHTs, n = 82 for KD EHTs, n = 51 for OE het EHTs and n = 99 for OE hom EHTs. **F**) Differentiation efficiency measured by cardiac troponin T (cTnT) positive cells [%]. For statistical analysis, two-way ANOVA, followed by Bonferroni's posthoc test was performed (* = $p < 0.05$, ** = $p < 0.01$, *** = $p < 0.001$ and **** = $p < 0.0001$).

Results

During the measurement of EHTs, irregularities in *NRAP/MYC*-OE EHTs beating behaviour compared to control EHTs were observed. Therefore, the RR scatter, which describes the time between contraction peaks, was analysed. The homozygous *NRAP/MYC*-OE EHTs showed a significant increase of time between contraction peaks after 14 days of culture (**Figure 40 E**). However, the RR scatter was initially high for control EHTs but decreased during the incubation time. To ensure that the detected effects in EHTs were not due to different amounts of cardiac myocyte populations, cTnT-positive cells were depicted for all differentiation runs that were included in these EHT data (**Figure 40 F**).

Considering the force-frequency relationship, electrical stimulation of EHTs is required to synchronise beating frequencies and enable the detection of differences in force. Therefore, EHTs were stimulated with 2 V biphasic pulses and stimulation frequencies ranging from 0 to 4 Hz with 0.5 Hz increments for each measurement after 21 days of EHT culture (**Figure 41**).

This allows to detect to which extent EHTs of different cell lines with different *NRAP* expression levels are able to follow the electrical stimulation and which stimulation might be best suitable for analysis of contractile parameters. During this process termed pacing, the beating frequency increases with increasing frequency stimulation while force decreases with increasing stimulation frequency. Some control EHTs (**Figure 41 A, B**), *NRAP*-KD EHTs (**Figure 41 C, D**), heterozygous *NRAP/MYC*-OE (**Figure 41 E, F**) and homozygous *NRAP/MYC*-OE (**Figure 41 G, H**) EHTs were able to follow the stimulation until a pacing frequency of 4 Hz. For analysis of electrically synchronised frequencies to distinguish between other contractile parameters, a pacing frequency of 2 Hz was used. EHTs that were not following the stimulation were excluded from this analysis (**Figure 42**).

Results

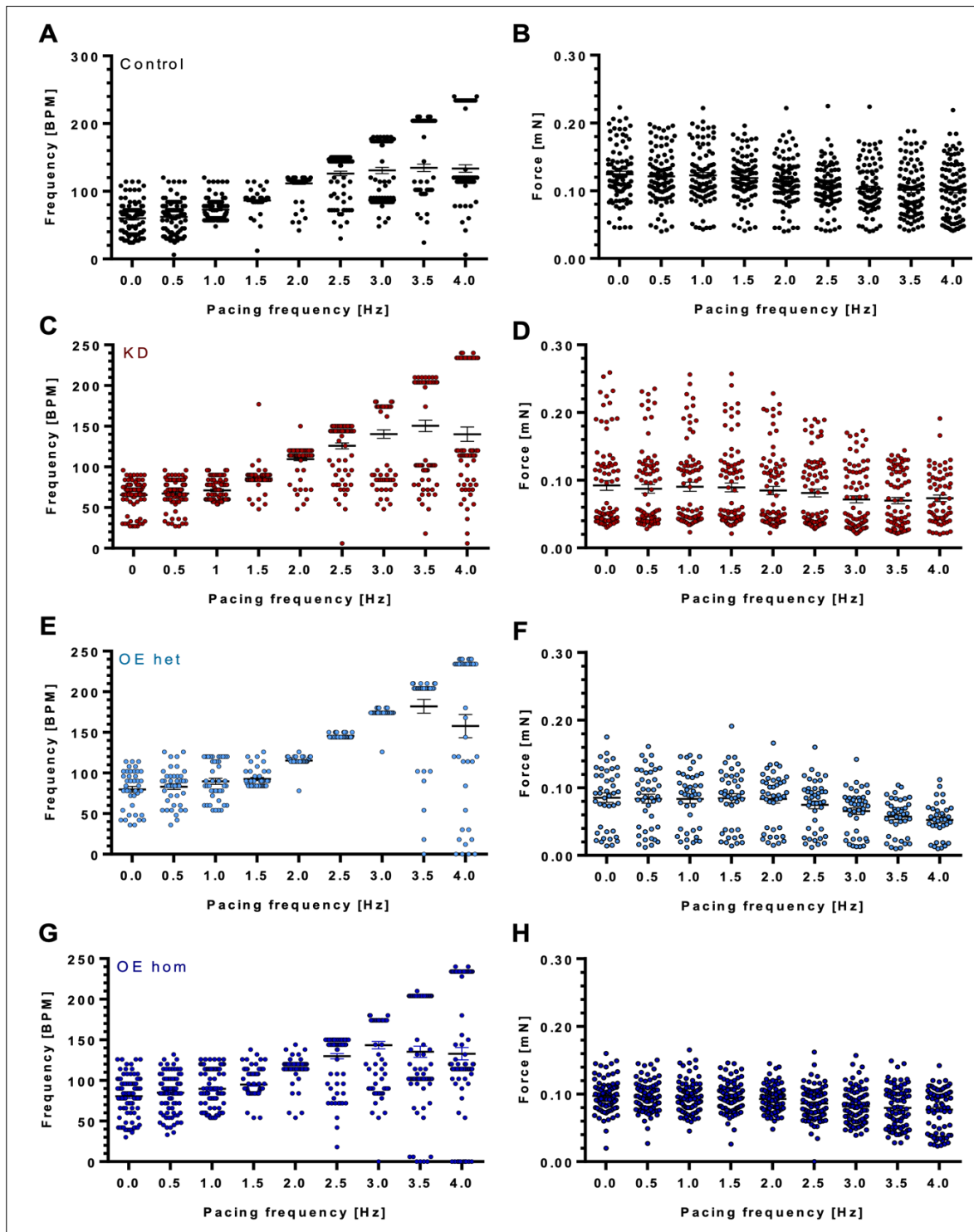


Figure 41: Electrical synchronisation of frequency in genetically-modified *NRAP*-EHTs. **A, B)** Control (black), **C, D)** *NRAP*-KD (KD; red), **E, F)** heterozygous *NRAP/MYC*-overexpressing (OE het; light blue) or **G, H)** homozygous *NRAP/MYC*-overexpressing (OE hom; dark blue) hiPSC-derived cardiac myocytes were embedded in engineered heart tissues (EHTs). EHTs were cultured for 21 days prior to electrical synchronisation of frequency at 2 V and stimulation frequencies of 0-4 Hz with 0.5 Hz increments for each measurement. The parameters **A, C, E, G)** frequency [beats per minute/BPM], **B, D, F, H)** force [mN] were measured. Represented are single measurements for each EHT and as mean \pm standard error mean (SEM) from 5 (control/OE hom) or 4 (OE het/KD) batches. N = 98 for control EHTs, n = 82 for KD EHTs, n = 51 for OE het EHTs and n = 99 for OE hom EHTs.

Results

Since modification of NRAP levels resulted in impaired force generation (**Figure 42 B**) and reduced relaxation time (**Figure 42 D**) and concomitantly only in *NRAP*-KD EHTs to increased time to peak (80%; **Figure 42 C**) in comparison to control EHTs, different parameters of contraction peaks from spontaneously beating EHTs were analysed. This revealed significant lower resting length in *NRAP*-KD (4.308 ± 0.097 mm) and heterozygous *NRAP/MYC*-OE (4.400 ± 0.133 mm) but not in homozygous *NRAP/MYC*-OE (4.860 ± 0.054 mm) compared to control EHTs (4.759 ± 0.049 mm) (**Figure 43 A**). Regarding the peak velocities, the contraction velocity of *NRAP*-KD (0.776 ± 0.065 mN/s), heterozygous (0.796 ± 0.057 mN/s) and homozygous (0.882 ± 0.019 mN/s) *NRAP/MYC*-OE was significantly lower compared to control EHTs (1.152 ± 0.043 mN/s) (**Figure 43 B**) while the relaxation velocity was not altered (**Figure 43 C**).

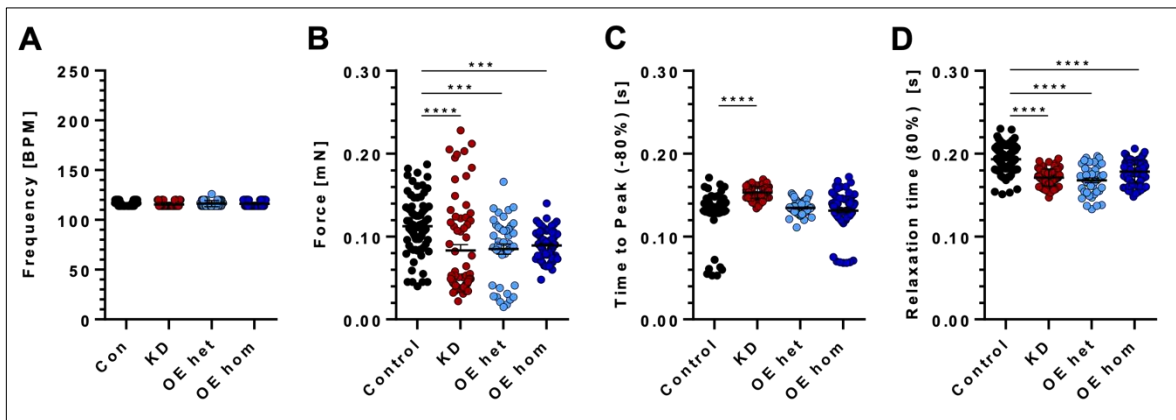


Figure 42: Contractile measurements of genetically-modified *NRAP*-EHTs after electrical synchronisation. Control (black), heterozygous *NRAP/MYC*-overexpressing (OE het; light blue), homozygous *NRAP/MYC*-overexpressing (OE hom; blue) or *NRAP*-KD (KD; red) hiPSC-derived cardiac myocytes were embedded in engineered heart tissues (EHTs). EHTs were cultured for 21 days prior to electrical synchronisation of frequency at 2 V and stimulation frequency at 2 Hz. Contractile parameters such as **A**) frequency [beats per minute/BPM], **B**) force [mN], **C**) time to peak (-80%) [s] and **D**) relaxation time (80%) [s] over time [days] were measured. EHTs that were not following the electrical stimulus were excluded from the data analysis. Data are represented as dots for each included EHTs and mean \pm standard error mean (SEM) from 5 (control/OE hom) or 4 (OE het/KD) batches. N = 89 control EHTs, n = 78 KD EHTs, n = 44 OE het EHTs and n = 88 OE hom EHTs. For statistical analysis, one-way ANOVA, followed by Dunnett's posthoc test was performed (* = $p < 0.05$, ** = $p < 0.01$, *** = $p < 0.001$ and **** = $p < 0.0001$).

As the data revealed significant alterations for all *NRAP*-modified EHTs compared to the control, the relative early and late relaxation time were investigated. This showed an increased relatively early and lower late relaxation time for *NRAP*-KD EHTs compared to control EHTs (**Figure 43 D**). Interestingly, investigation of the relative early and late time to peak showed increased early and lowered late time to peak for *NRAP/MYC*-OE EHTs (**Figure 43 E**).

Results

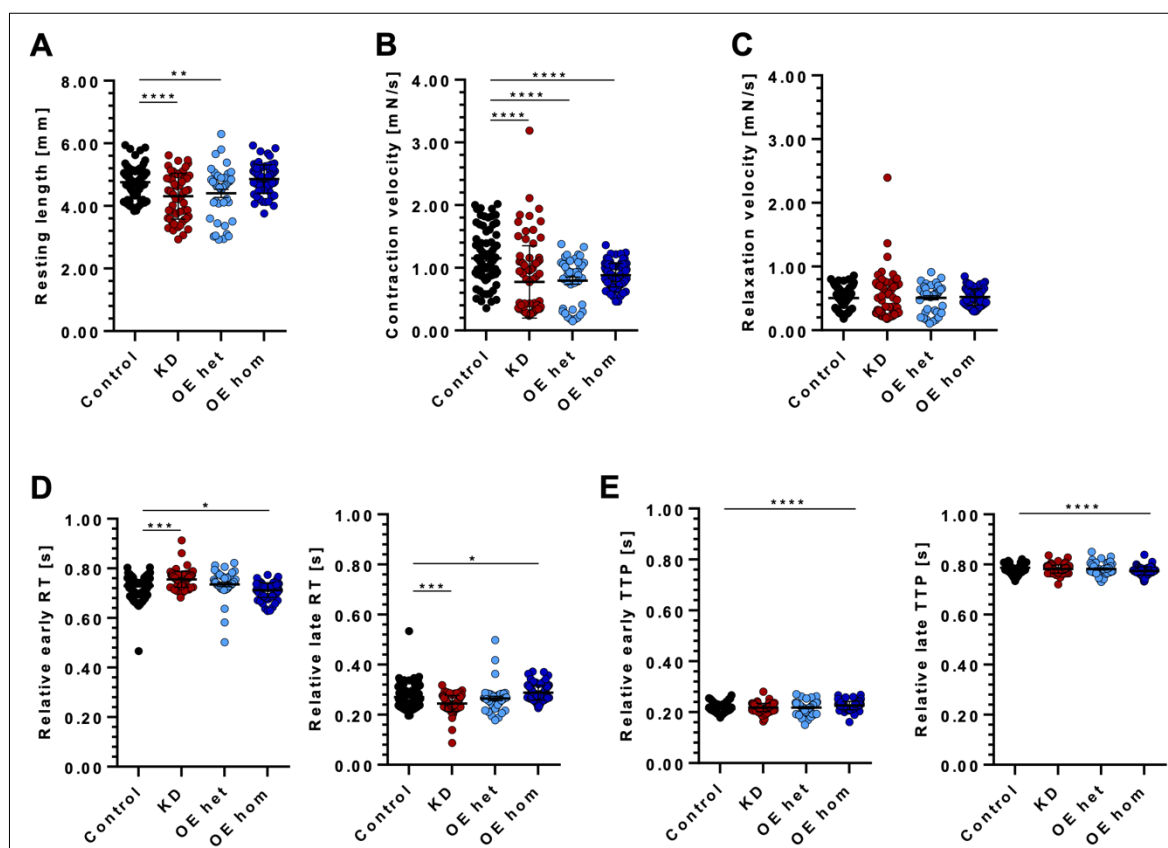


Figure 43: Impact of modified NRAP levels on contractility parameters. Contractile measurements of spontaneously beating genetically-modified NRAP-EHTs. Control (black), heterozygous (OE het; light blue) and homozygous *NRAP/MYC*-overexpressing (OE hom; dark blue) or *NRAP*-KD (KD; red) hiPSC-derived cardiac myocytes were embedded in engineered heart tissues (EHTs). Spontaneously-beating EHTs were investigated for different contractile parameters on day 21 of culture, such as **A**) resting length [mm], **B**) contraction velocity [mN/s], **C**) relaxation velocity [mN/s], **D**) relative early time to peak (TTP) and relative late TTP [s], and **E**) relative early relaxation time (RT) and relative late RT [s]. Data are represented as mean \pm standard error mean (SEM) from 5 (control, OE hom) or 4 (OE het/KD) batches. N = 98 control EHTs, n = 82 KD EHTs, n = 51 OE het EHTs and n = 99 OE hom EHTs. For statistical analysis, one-way ANOVA, followed by Dunnett's posthoc test was performed (*** = $p < 0.001$ and **** = $p < 0.0001$).

Considering that modification of NRAP levels resulted in alterations in force, time to peak and relaxation time, conduction was investigated by measuring action potentials. This revealed a less negative take-off potential (TOP) in homozygous *NRAP/MYC*-OE EHTs (-54.6 ± 4.2 mV) compared to control EHTs (-69.0 ± 3.9 mV) (**Figure 44**). In addition, the action potential amplitude (APA; 81.5 ± 7.7 mV) and maximal change of voltage over time (V_{max} ; 19445.7 ± 2421.7 mV/s) were lowered in homozygous *NRAP/MYC*-OE EHTs compared to control EHTs (99.5 ± 3.6 mV; 89626 ± 30335 mV/s) (**Figure 44**).

The action potential duration at 90% (APD_{90}) relaxation was not altered in any of the cell lines and the maximal diastolic potentials (MDP) were less negative in homozygous *NRAP/MYC*-OE EHTs (56.8 ± 4.4 mV) compared to control EHTs (75.0 ± 3.2 mV) (**Figure**

Results

44). Overall, *NRAP*-KD EHTs were not altered in any of the action potential characteristics.

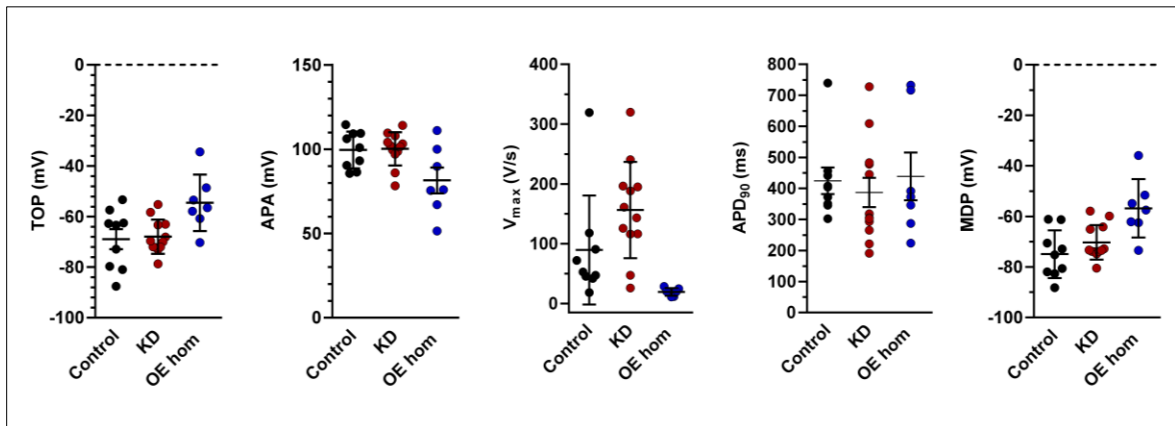


Figure 44: Action potential measurements. Control, *NRAP*-KD and homozygous *NRAP/MYC*-overexpressing (OE) EHTs were investigated between day 28 and 41 of culture for the following action potential characteristics: Take-off potential (TOP) [mV], action potential amplitude (APA) [mV], maximal change of voltage over time (V_{max}) [V/s], action potential duration at 90% relaxation (APD_{90}) and maximal diastolic potentials (MDP) [mV]. Data are from two independent EHT batches with $n = 9$ control EHTs, $n = 12$ *NRAP*-KD EHTs and $n = 7$ homozygous *NRAP/MYC* EHTs. Represented are single EHT measurements as well as means \pm SEM.

Overall, during electrical synchronisation of *NRAP/MYC*-OE and *NRAP*-KD, EHTs developed lower force and revealed shorter relaxation time and contraction velocity in spontaneously beating EHTs compared to controls. In spontaneously beating *NRAP*-KD EHTs, the resting length was shorter and early and late relaxation time were altered. However, in homozygous *NRAP/MYC*-OE EHTs, both the relatively early and late time to peak and relaxation time were altered, which was accompanied by a less negative TOP and MDP and lower V_{max} .

6.5.2 Mechanical stretch

In the adult heart, NRAP is located at the intercalated disc where it is thought to act as a mechanosensing protein. To investigate the impact of NRAP during mechanical stretch, control, homozygous *NRAP/MYC*-OE and *NRAP*-KD EHTs were analysed for their mechanical stretch-force relationship applying the Frank-Starling mechanism. The difference between the initial force and the force after applying stretch is represented as delta force. This showed high scattering for control and *NRAP*-KD EHTs but revealed a trend towards lower delta force in the *NRAP/MYC*-OE EHTs compared to control EHTs (**Figure 45 A**). Moreover, the applied stretch length over the initial force was calculated which revealed an overall trend towards a lower ratio for the *NRAP/MYC*-OE compared to the control (**Figure 45 B**). As depicted in the representative mechanograms, after applying stretch to the EHTs, homozygous *NRAP/MYC*-OE EHTs consequently stopped following the

Results

electrical stimulation and instead showed an irregular beating behaviour (**Figure 45 C**). This was observed in all EHTs of this genotype but not in control or *NRAP*-KD EHTs.

Taken together, *NRAP*-KD EHTs showed a higher ability to respond to mechanical stretch compared to control EHTs. To the contrary, homozygous *NRAP/MYC*-OE EHTs were not able to compensate alterations in mechanical stretch, resulting in an irregular beating behaviour.

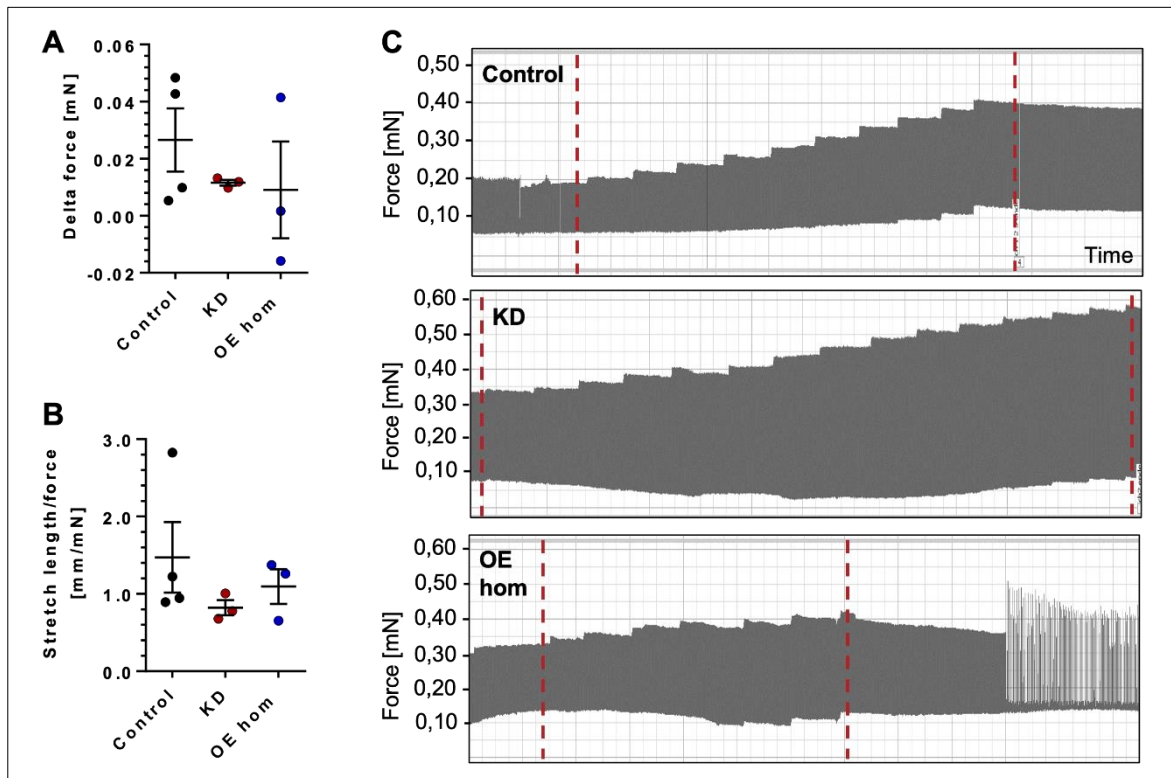


Figure 45: Frank-Starling mechanism. Control, *NRAP*-knock-down (KD) and homozygous *NRAP/MYC*-overexpressing (OE hom) EHTs were investigated on day 22 of culture before electrical stimulation at a frequency of 1 Hz in a Frank-Starling apparatus. EHTs were stretched with inter-mittent stretching steps of 20 $\mu\text{m}/2$ min to which EHTs respond with a force increase. Represented are the **A**) delta force [mN], **B**) the stretch length/force [mm'/mN] and **C**) exemplary stretch-force traces of one batch of EHTs with $n = 4$ control EHTs and $n = 3$ *NRAP*-KD and homozygous *NRAP/MYC*-OE EHTs from one cardiac differentiation (start and end of stretch are indicated by red dashed lines).

6.5.3 Proteome

In order to investigate the underlying molecular pathways resulting in altered force, electrophysiology and response to mechanical stretch in homozygous *NRAP/MYC*-OE versus *NRAP*-KD EHTs, mass spectrometry of EHTs was performed. In total, 2479 proteins were identified, of which 182 were significantly different between control, *NRAP/MYC*-OE and *NRAP*-KD EHTs.

Results

Clustering the samples from control, *NRAP*-KD and *NRAP/MYC*-OE EHTs in a principal component analysis (PCA) revealed that control EHTs clustered closer to *NRAP*-KD EHTs than to *NRAP/MYC*-OE EHTs (**Figure 46 A**). Concomitantly, the heatmap of all higher and lower abundant proteins showed a more similar protein expression pattern between control and *NRAP*-KD EHTs while the expression pattern in homozygous *NRAP/MYC*-OE EHTs was diametrically opposed (**Figure 46 B**).

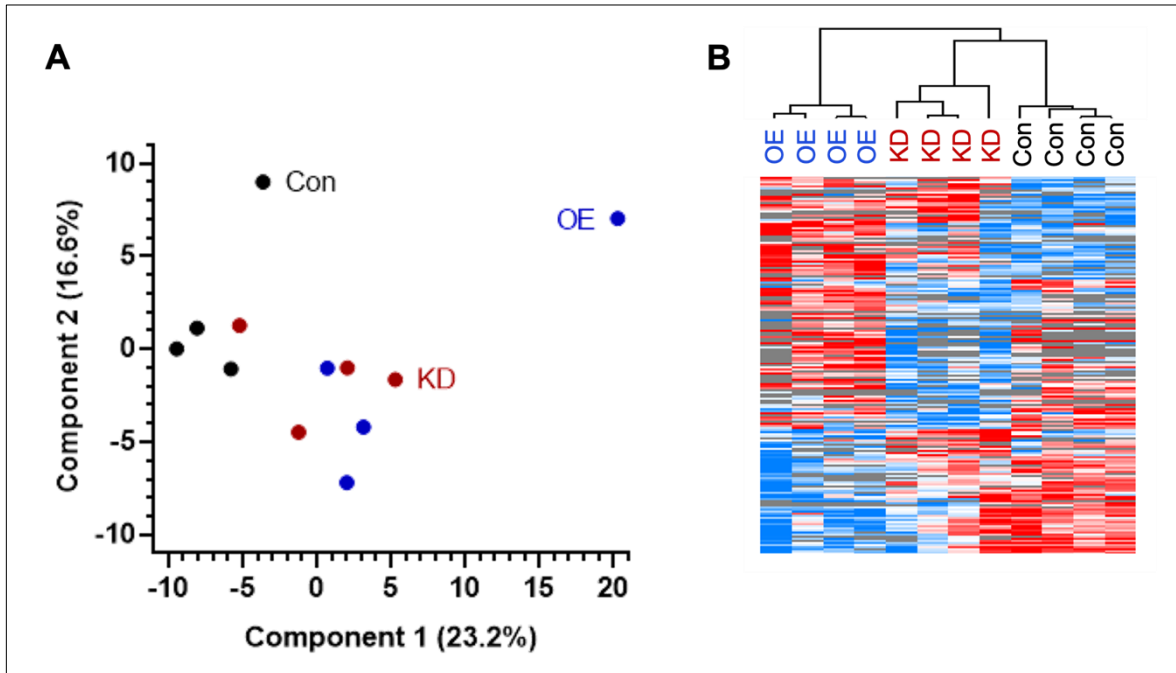


Figure 46: Quantitative proteomic analysis of EHTs. **A)** Principal component analysis (PCA) of control (blue), *NRAP*-KD (dark red) and homozygous *NRAP/MYC*-OE (blue) EHTs and **B)** heatmap representing top higher (red) or lower (blue) abundant proteins. Each dot represents one sample that consists of three EHTs and originates from a separate differentiation ($n = 4$ differentiations).

Significantly higher and lower abundant proteins in *NRAP*-KD versus *NRAP/MYC*-OE EHTs in comparison to control EHTs was visualised in volcano plots. In *NRAP*-KD EHTs, among the highest abundant proteins, glutathione peroxidase 4 (GPX4) and glycogen phosphorylase (PYGM) that are related to metabolism or myosin heavy chain 6 (MYH6) that is linked to cardiac contraction, were identified. In addition, the developmental proteins SH3 domain binding glutamate rich protein like (SH3BGRL) and growth factor receptor bound protein 2 (GRB2) were enhanced in *NRAP*-KD compared to control EHTs (**Figure 47 A**). Analysis of Kyoto Encyclopedia of Genes and Genomes (KEGG) metabolic pathways identified a connection of abundant proteins to various pathways including adrenergic signalling in cardiac myocytes, cardiac contraction, DCM and HCM (**Figure 47 C**).

Results

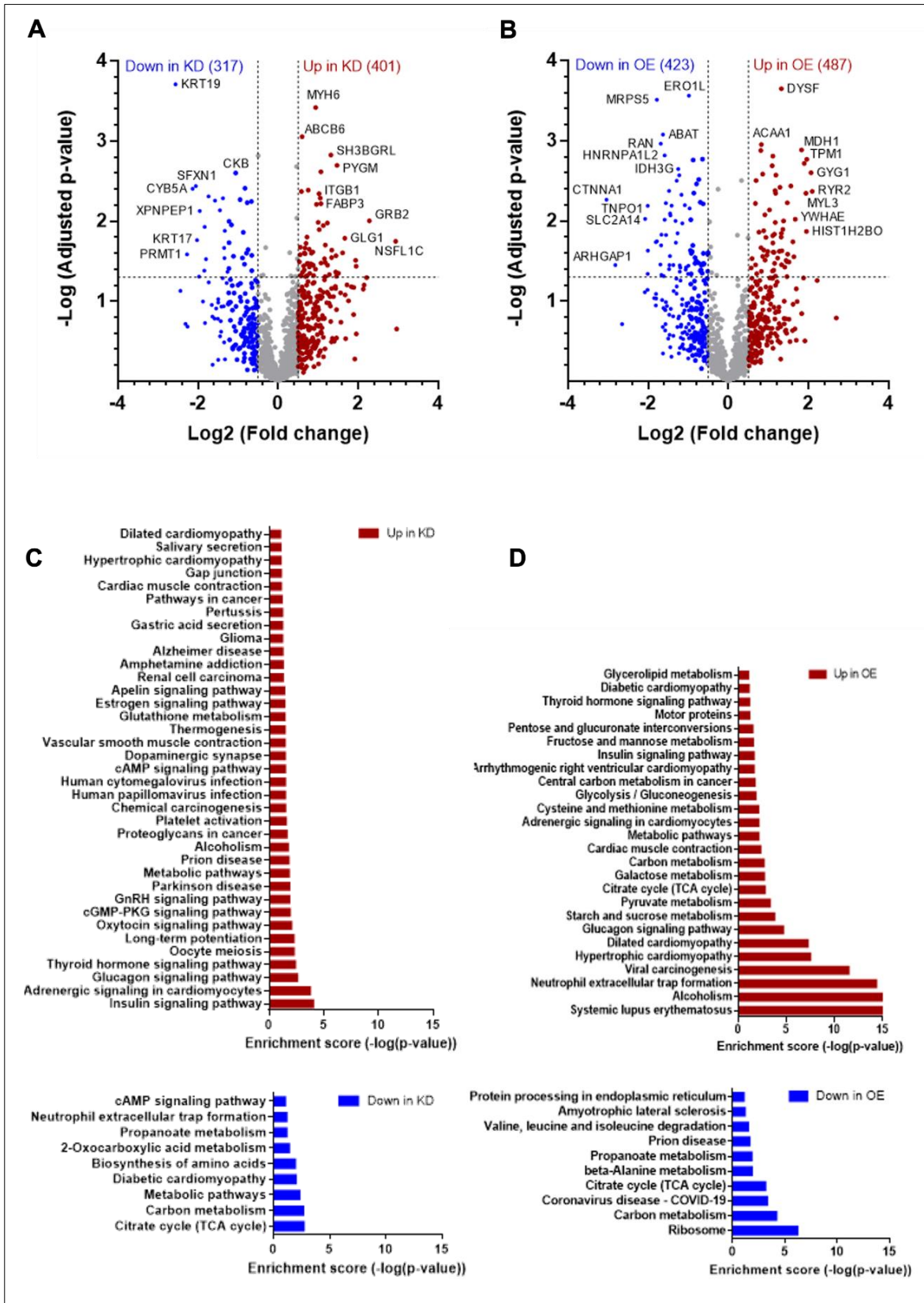


Figure 47: Volcano plot and enrichment analysis of proteins identified by proteomic analysis. A, B) Volcano plots representing the most differentially higher or lower abundant proteins in *NRAP*-knock-down (*NRAP*-KD) or *NRAP*-overexpressing (*NRAP*-OE) EHTs and **C, D)** KEGG pathways of enriched proteins that were significantly ($p < 0.05$) higher or lower abundant in **C)** *NRAP*-KD or **D)** *NRAP*-OE EHTs. The data derive from four independent differentiations ($n = 4$) with each sample comprising three EHTs.

Results

Among the lowest abundant proteins sideroflexin 1 (SFXN1) and cytochrome B5 type A (CYB5A) and protein arginine methyltransferase 1 (PRMT1) were identified. KEGG pathway analysis depicted an association to the citrate cycle and various metabolic pathways (Figure 47 C).

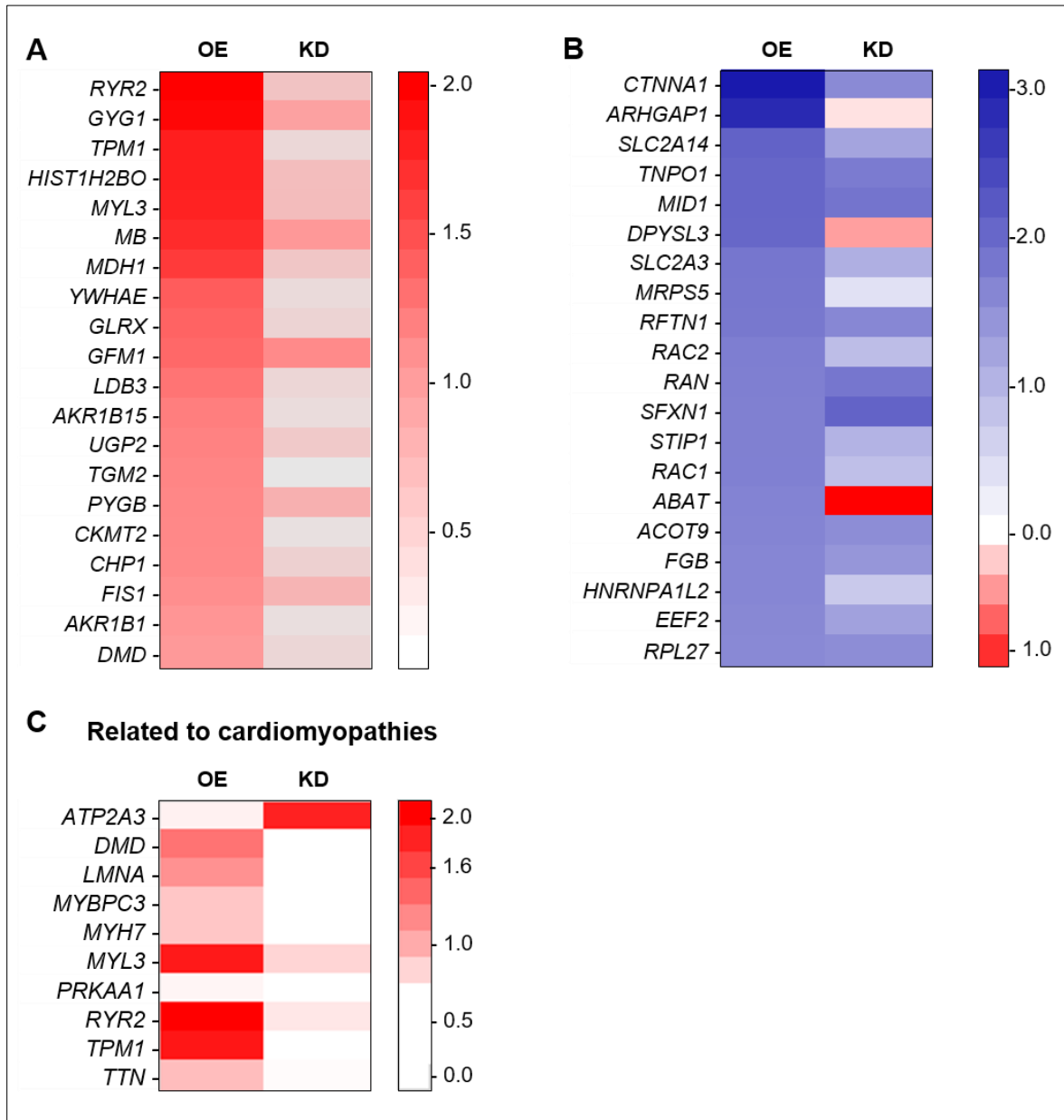


Figure 48: Clustering analysis of top higher and lower abundant proteins in *NRAP*-over-expressing (OE) EHTs. Heatmaps represent the relative abundance as indicated by log2fold changes of highest (red) to lowest (blue) abundant proteins of *NRAP/MYC*-OE and *NRAP*-knock-down (KD) proteins. **A**) Top 20 higher abundant proteins in *NRAP/MYC*-OE EHTs and comparison to *NRAP*-KD EHTs, and **B**) top 20 lower abundant proteins in *NRAP/MYC*-OE EHTs. **C**) Regulation of proteins involved in cardiomyopathies. Mean of four independent differentiations ($n = 4$) with each sample comprising three EHTs. Only values with $p < 0.05$ were included into the analysis.

Among the top higher abundant proteins in homozygous *NRAP/MYC*-OE EHTs were dysferlin (DYSF), tyrosine 3-monooxygenase/tryptophan 5-monooxygenase activation

Results

protein epsilon (YWHAE), the contraction-associated proteins tropomyosin 1 (TPM1), ryanodine receptor 2 (RYR2) and myosin light chain 3 (MYL3), metabolic proteins such as malate dehydrogenase 1 (MDH1) and glycogenin 1 (GYG1) were detected (**Figure 47 B**). Interestingly, KEGG pathway analysis of homozygous *NRAP/MYC*-OE EHTs revealed that higher abundant proteins were linked to metabolic pathways and different forms of cardiomyopathies including HCM, DCM, ARVC and diabetic cardiomyopathy (**Figure 47 D**). Among the top lower significantly different proteins, the endoplasmic reticulum oxidoreductin-1-like (ERO1L) is associated with the ER while other lower abundant proteins such as mitochondrial ribosomal protein S5 (MRPS5) and isocitrate dehydrogenase 3 non-catalytic subunit gamma (IDH3G) are linked to mitochondria or transportin 1 (TNPO1) and Ras-related Nuclear Protein (RAN) to nuclear import and export (**Figure 47 B**). Pathway analysis of lower abundant proteins showed involvement of ribosomes, the ER and citrate cycle (**Figure 48 D**). To further investigate the impact of RNA expression, transcriptomic analysis could be performed in addition.

Clustering the top 20 higher and lower abundant proteins of *NRAP/MYC*-OE EHTs showed that the RYR2 was the highest abundant protein while CTNNA1 was lowest abundant (**Figure 48 A, B**). In comparison to *NRAP*-KD EHTs, a differential protein expression pattern was observed. Since the KEGG pathway analysis revealed an association to cardiomyopathies in both *NRAP/MYC*-OE and *NRAP*-KD EHTs, the proteomic profile of related proteins was depicted in a heatmap (**Figure 48 C**). In *NRAP/MYC*-OE EHTs, many cardiomyopathy-related proteins were higher abundant while in *NRAP*-KD EHTs only MYL3 and ATPase sarcoplasmic/endoplasmic reticulum Ca²⁺ transporting 3 (ATP2A3) were higher abundant compared to control EHTs (**Figure 48 C**).

In conclusion, both *NRAP* gain- and loss-of-function has been associated with a cardiomyopathy-protein signature. Thereby, *NRAP*-KD EHTs display more similarities to control EHTs than to homozygous *NRAP/MYC*-OE EHTs. Although overexpression of *NRAP* impacted contractile parameters, *NRAP* localisation and electrophysiology, it remains unknown how *NRAP* might be regulated upon progression to cardiac disease.

6.6 Impact of protein kinase D inhibition on *NRAP*

Previous reports of a yeast-2-hybrid screen from a human cardiac library for PKD1 revealed *NRAP* as a potential substrate or interaction partner (unpublished data from the publication; Haworth et al. 2004). PKD1 has been characterised as a central hub in fetal and hypertrophic signalling in cardiac myocytes by regulating various functions via MEF2-dependent transcriptional regulation and target protein phosphorylation (Avkiran et al. 2008). Therefore, the aim was to investigate whether PKD impacts *NRAP* expression,

NRAP localisation and phosphorylation and how this might be altered upon neurohumoral activation of the PKD1-mediated myocyte enhancer factor 2 (MEF2)-dependent gene transcription. For this purpose, NRVMs were used as they allow studying this concomitantly in a developing and diseased model.

6.6.1 NRAP localisation and protein levels

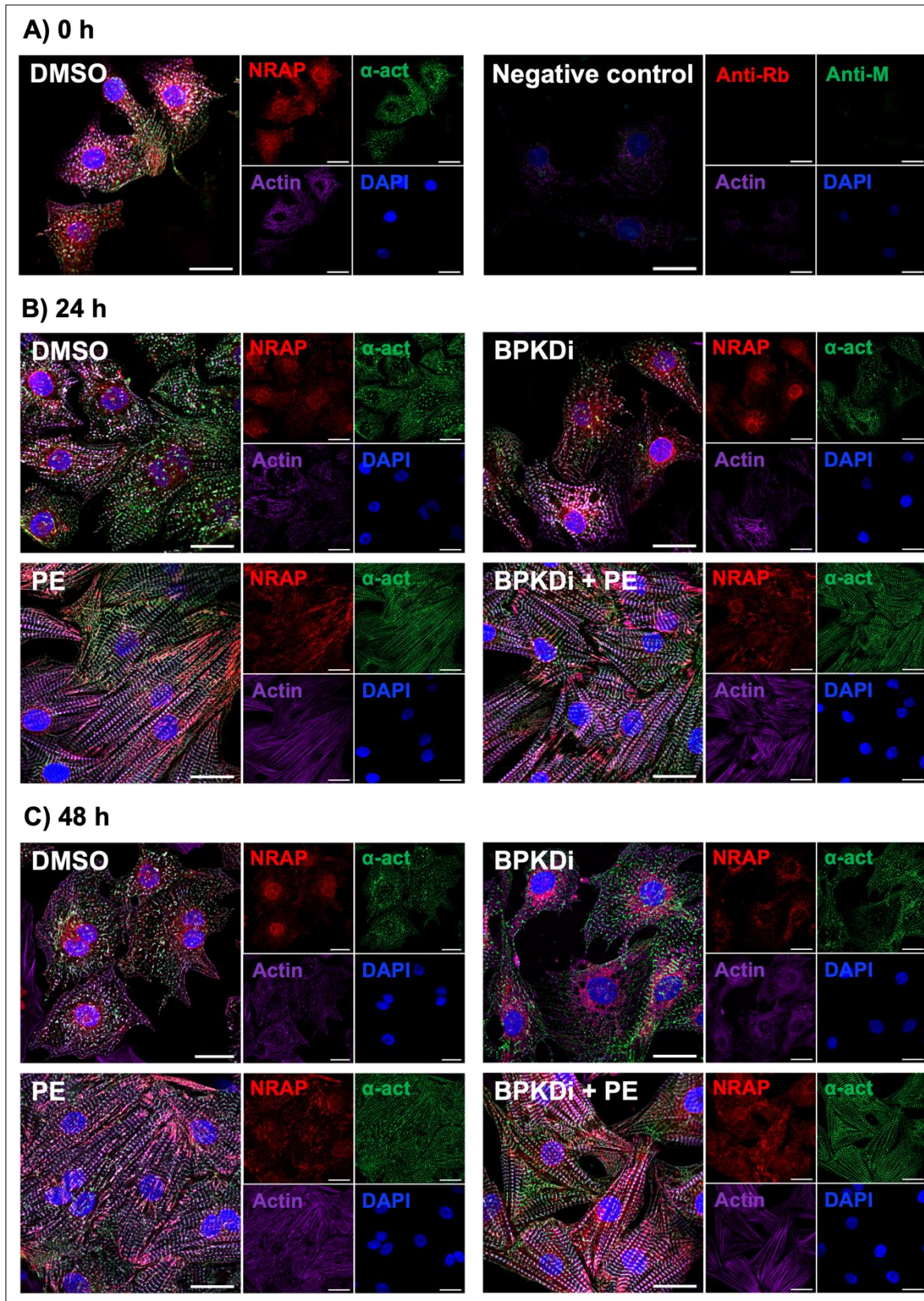
Initially, NRVMs were exposed daily for up to 96 h to the pharmacological PKD inhibitor BPKDi and/or the pro-hypertrophic stimulus phenylephrine (PE). Every 24 h of treatment, immunofluorescent staining was performed. Over time, DMSO-treated NRVMs were increasing in maturation as indicated by the localisation and intensity of the Z-disc marker α -actinin or F-actin staining (**Figure 49**). NRAP was mainly located in the nuclear and perinuclear areas. However, exposure to BPKDi initially showed nuclear and perinuclear localisation of NRAP after 24 h of treatment but was distributed more to the cytosol after 96 h of treatment (**Figure 49**). The NRAP staining in the perinuclear area was characterised by distinct holes within the regular myofilament lattice. The maturation of NRVMs that had been exposed to BPKDi was similar to the control cells that had been exposed to DMSO. However, myofibrillar disarray was observed when PKD activity was inhibited in NRVMs (**Figure 49**).

Exposure to the pro-hypertrophic stimulus PE matured myofilament structure as indicated by distinct α -actinin staining as well as parallel and cross-striated F-actin staining (**Figure 49**). The staining of NRAP was located close to actin filaments and at later time points such as 72 h and 96 h in close proximity to the intercalated disc regions. Combined exposure of NRVMs to PE and BPKDi, resulted in sarcomere rupture after 24 h incubation with more frequently disrupted areas with increasing incubation times (**Figure 49**). Interestingly, NRAP was accumulating in those disrupted areas.

Since PKD inhibition altered the localisation of NRAP, the impact of PKD overexpression simultaneously with or without pro-hypertrophic stimulation by PE and/or isoprenaline (ISO) on NRVMs was investigated by immunofluorescence. While exposure to PE enhanced maturation and resulted in NRAP localisation along actin filaments, exposure to ISO led to retained NRAP accumulation in the perinuclear area (**Figure 50 A**). To achieve PKD overexpression, a PKD-overexpressing adenovirus was used for transduction at the beginning of the treatment. Due to a GFP-tag, the heterologously expressed PKD could be distinguished from the endogenous PKD.

Control NRVMs that had been transduced with the PKD-overexpressing adenovirus revealed more structured and paralleled Z-discs as indicated by α -actinin stainings (**Figure 50 B**).

Results



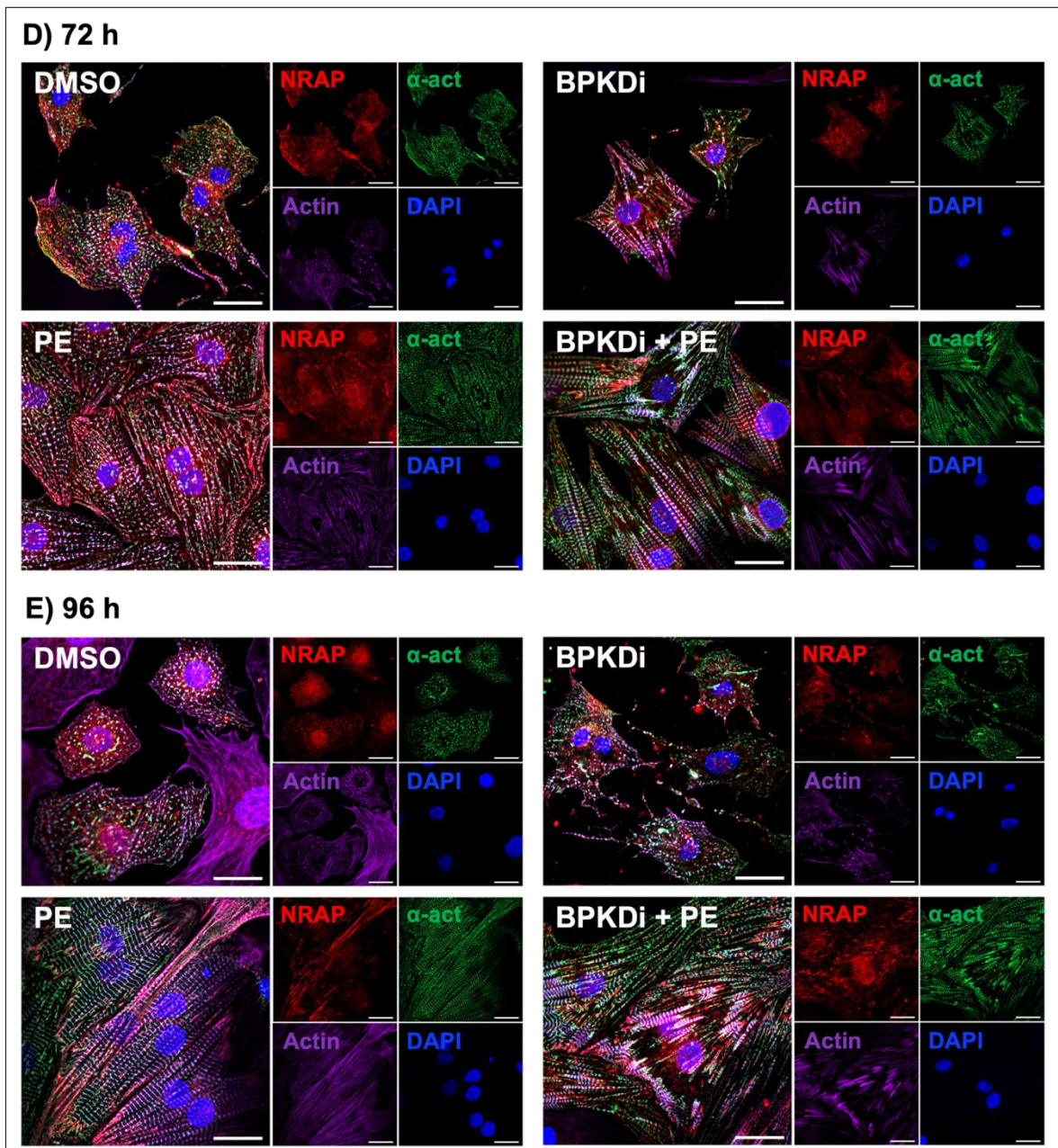


Figure 49: Impact of protein kinase D inhibition and pro-hypertrophic stimulation on myofilament structure. Neonatal rat ventricular myocytes (NRVMs) were incubated for 0-96 h with DMSO or 3 μ M BPKDi in presence or absence of 10 μ M phenylephrine (PE). NRVMs were fixed with 4% paraformaldehyde and stained for NRAP (red), α -actinin (green), F-actin (purple) and nuclei (DAPI, blue). For negative controls, cells were only incubated with secondary antibodies. Scale bars are equal to 20 μ m. The immunofluorescence images are representative images and have been performed three times from three independent NRVMs isolations (n = 3).

The NRAP localisation was altered by PKD overexpression and was localised more towards the cell-cell borders of cardiac myocytes. Additional exposure to PE resulted in accumulation of NRAP in vacuole-like structures (**Figure 50 B**). Interestingly, no nuclei were observed in those vacuole-like structures. Combined exposure to PE and ISO led to NRAP accumulation in aggregates and altered sarcomere structure (**Figure 50 B**).

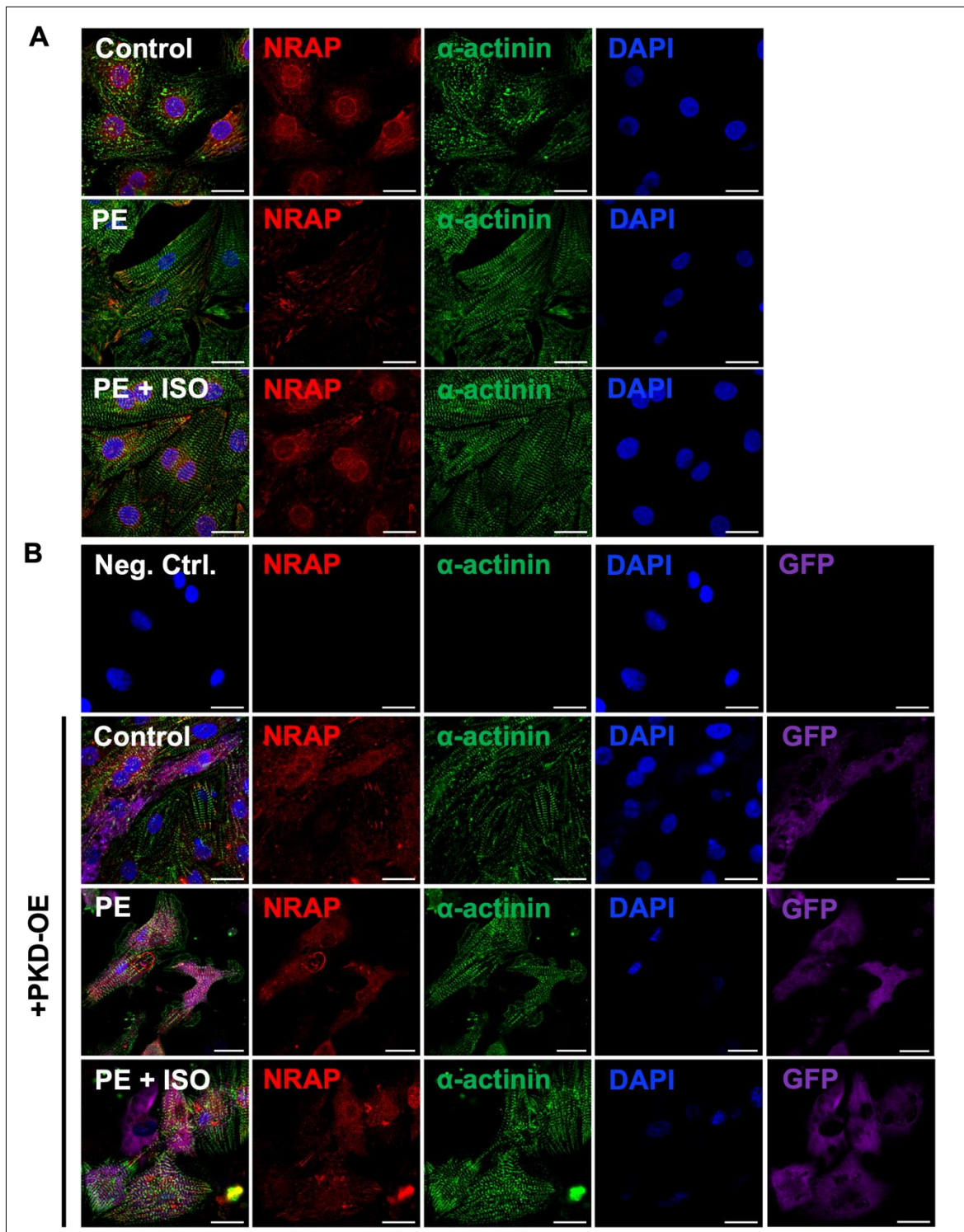


Figure 50: Impact of protein kinase D (PKD) overexpression in neonatal rat ventricular myocytes. Neonatal rat ventricular myocytes (NRVMs) were incubated for 72 h with DMSO or 3 μ M BPKDi in presence or absence of 10 μ M phenylephrine (PE) and/or 10 nM isoprenaline (ISO). Cells were fixed with 4% paraformaldehyde and stained for NRAP (1:500; red), Z-discs with α -actinin (green), F-actin with phalloidin (purple) and nuclei with DAPI (blue). Staining of **A**) NRVMs treated with PE or ISO and **B**) additional exposure to 5 μ L PKD-overexpressing adenovirus to each 35 mm dish for 24 h. Scale bar are equal to 20 μ m. For negative controls, cells were only incubated with secondary antibodies. The immunofluorescence images are representative images and have been performed two times from two independent NRVMs isolations (n = 2).

Results

Subsequently, NRAP protein levels were investigated by western immunoblot analysis with the same treatment conditions over 96 h (**Figure 51 A**). Overall, this revealed no significant changes in NRAP protein levels although with high a standard error means in three investigated samples derived from three independent NRVM isolations. However, a slight increase in NRAP abundance over time with the highest levels at 96 h of treatments, especially after exposure to the pro-hypertrophic stimulus PE was observed (**Figure 51 B**).

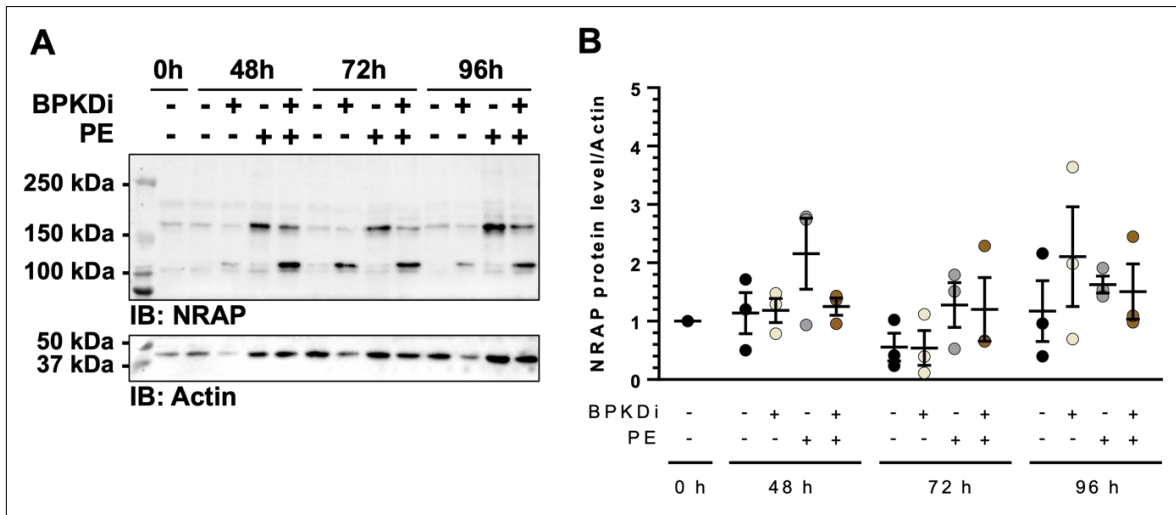


Figure 51: Impact of protein kinase D inhibition and pro-hypertrophic stimulation on NRAP protein levels. Neonatal rat ventricular myocytes (NRVMs) were incubated for up to 96 h with DMSO or 3 μ M BPKDi in the presence or absence of 10 μ M phenylephrine (PE). **A**) Representative western immunoblot for NRAP and actin as a loading control, and **B**) quantification of NRAP protein level normalised to cardiac actin (n = 3).

Investigation of the structural and transcriptional regulation of NRAP by PKD revealed that pharmacological inhibition PKD activity in NRVMs resulted in perinuclear, punctate-like accumulation of NRAP. In contrast, PKD-overexpression revealed NRAP accumulation in vacuole-like structures. Exposure of NRVMs to the pro-hypertrophic stimulus PE led to NRAP translocation towards the lateral cardiac myocyte borders and concomitant PKD inhibition revealed sarcomere rupture with NRAP translocation to these areas. Western immunoblotting of NRAP revealed only a trend towards higher NRAP protein levels upon pro-hypertrophic stimulation.

6.6.2 Contractile function

To assess the functional consequences of disturbed sarcomeric structure, cardiac cells from neonatal rat hearts were isolated and assessed in a three-dimensional EHT format. For investigation of the impact of PKD on the developing and diseased heart, NRVMs-derived EHTs were exposed to the PKD inhibitor BPKDi and/or the pro-hypertrophic stimulus PE at two different culture time points. For the early treatment timepoint, EHTs

Results

were treated with the respective stimuli from day 2 after the EHT generation and for the late treatment from day 14 when the EHTs achieved their force plateau. After 7 days of treatment, the EHTs were electrically synchronised to parallel the beating frequency of all EHTs. Due to the force-frequency relation, this allowed to detect differences in force.

In early-treated NRVMs-derived EHTs, the force was significantly increased in BPKDi-treated EHTs (0.13 ± 0.02 mN) compared to DMSO control EHTs (0.08 ± 0.1 mN) or the PE-treated EHTs (0.09 ± 0.01 mN; **Figure 52 A**). However, when NRVMs-derived EHTs were exposure to PE alone or additionally no alteration in force was detected compared to the DMSO control. Moreover, no significant impact on time to peak or relaxation time was determined. The contraction pattern in early-treated EHTs was not altered as the NRVMs-derived EHTs were beating as known for rats in bursts.

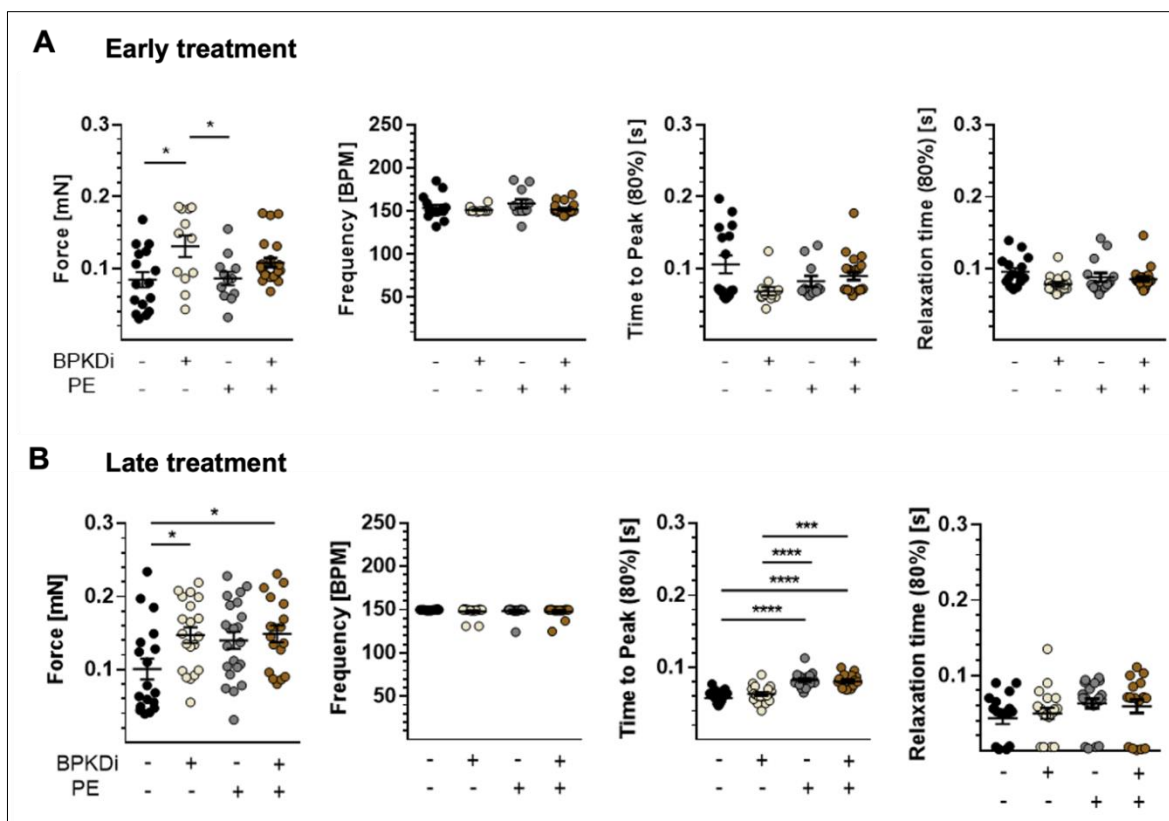


Figure 52: Impact of protein kinase D (PKD) inhibition and pro-hypertrophic stimulation on the contractile force. Neonatal rat ventricular myocytes (NRVMs)-derived engineered heart tissue (EHT) were treated daily with DMSO or 3 μ M of the pharmacological PKD inhibitor BPKDi, in presence or absence of 20 μ M of the pro-hypertrophic stimulus phenylephrine (PE). The treatment was performed as an **A**) early treatment from day 2-9 after the generation of EHTs or **B**) as a late treatment from day 14-21 after the generation of EHTs when EHTs reached their force plateau. Represented are different contractile parameters such as force [mN], frequency [beats per minute = BPM], time to peak (-80%) [s] or relaxation time (80%) [s] after electrical stimulation at 2.5 V and 2.5 Hz. For statistical analysis, one-way ANOVA, followed by Tukey's posthoc test was performed (* = $p < 0.05$, *** = $p < 0.001$ and **** = $p < 0.0001$). These experiments have been performed three times from three independent NRVMs isolations ($n = 3$).

Results

Compared to the early treatment, the late treatment revealed improved force in all four treatment conditions. In late treated NRVMs-derived EHTs, BPKDi treatment (0.15 ± 0.01 mN) resulted in higher force development compared to DMSO control EHTs (0.10 ± 0.01 mN) but not to PE-treated EHTs (0.14 ± 0.01 mN; **Figure 52 B**). In contrast to early-treated NRVMs-derived EHTs, combined BPKDi and PE exposure of late-treated EHTs (0.15 ± 0.01 mN) revealed significantly higher force compared to the respective DMSO control. Additionally, the duration to reach the contraction peaks was significantly higher in PE- and combined PE and BPKDi late treated EHTs compared to DMSO- or BPKDi-treated EHTs as indicated by the time to peak (TTP; **Figure 52 B**). For the relaxation time no alterations between the treatment groups were detected. Interestingly, exposure of late-treated NRVMs-derived EHTs to BPKDi resulted in impaired full relaxation during the burst phase as depicted by the deteriorating contraction force traces (**Figure 53**).

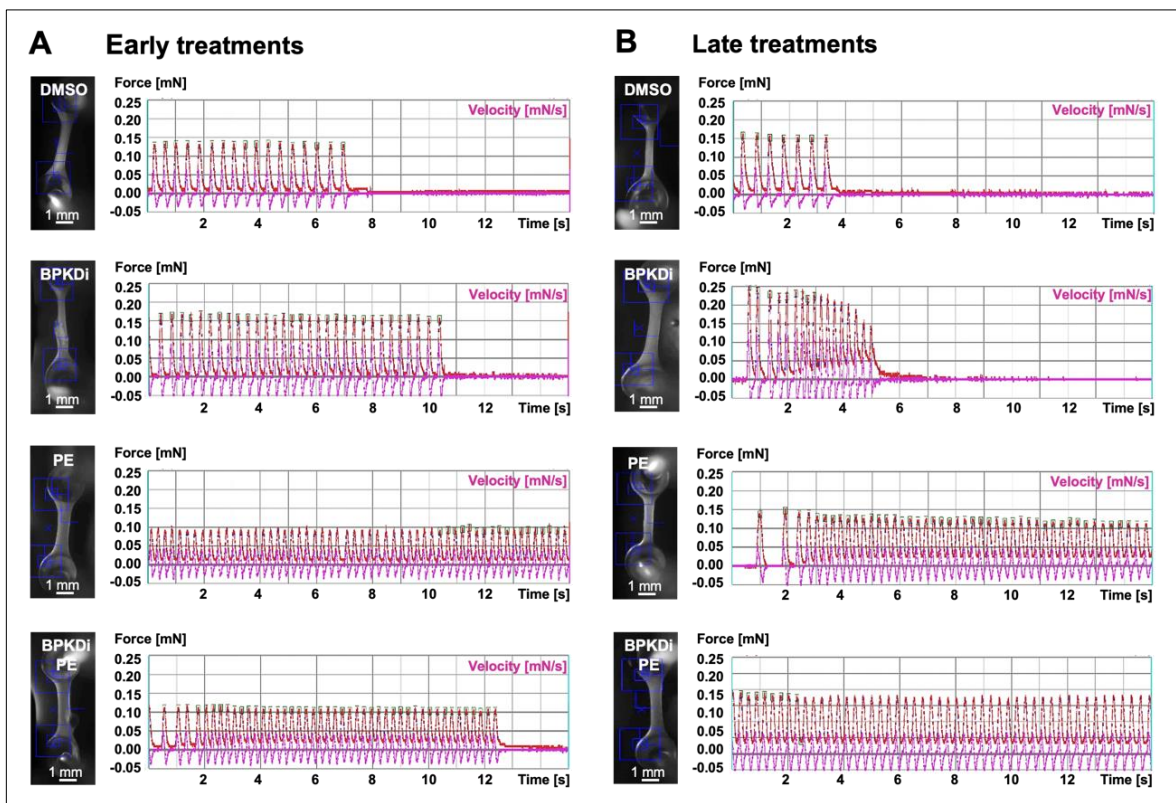


Figure 53: Impact of protein kinase D (PKD) inhibition and pro-hypertrophic stimulation on contractility. Neonatal rat ventricular myocyte (NRVMs)- derived engineered heart tissue (EHT) were treated daily with DMSO or $3\ \mu\text{M}$ of the pharmacological PKD inhibitor BPKDi, in presence or absence of $20\ \mu\text{M}$ of the pro-hypertrophic stimulus phenylephrine (PE). The treatment was performed as an **A**) early treatment from day 2-9 after the generation of EHTs or **B**) as a late treatment from day 14-21 after the generation of EHTs when EHTs reached their force plateau. Represented are pictures of EHTs taken during the contractility measurement and representative force recordings of spontaneously beating EHTs. The red line depicts the force [mN] and the purple line the velocity [mN/s]. Scale bars are equal to 1 mm. These experiments have been performed three times from three independent NRVM isolations ($n = 3$).

Investigating the impact of pharmacological PKD inhibition in early- and late-treated NRVMs-EHTs resulted in increased force in early while in late-treated EHTs the beating behaviour was altered. Additional exposure to PE in late-treated NRVMs-EHTs resulted in increased force and longer time to peak.

6.6.3 Structural impact

In order to investigate the structural impact of the treatments on NRVMs-derived EHTs, 100 μm thick EHT sections were investigated by immunofluorescence.

6.6.3.1 Sarcomeres

All EHT sections showed improved maturation compared to respective two-dimensional NRVMs controls (**Figure 54**). Combined exposure to PE and BPKDi during the early treatment, resulted similarly to experiments in two-dimensional treated NRVMs, to sarcomere disruption as almost no α -actinin but still some disorganised F-actin were detected in the distorted area (**Figure 54 A**). Interestingly, NRAP was accumulating in this area. In comparison to the early-treated NRVMs-EHTs, the late-treatment induced further maturation with parallel aligned sarcomere structures (**Figure 54 B**). Apart from that no altered localisations were detected except from NRVMs that had been exposed to the combined treatment of late-treated EHTs with PE and BPKDi (**Figure 54 B**). In contrast to early-treated NRVMs-EHTs no sarcomere disruption was observed when EHTs were treated at a later timepoint after they EHTs had already achieved their force plateau.

As it has previously been shown that dystrophin deficiency results in impaired contractile tension of myofibrils and is related to Duchenne muscular dystrophy cardiomyopathy (Pioner et al. 2020), immunohistochemical staining of dystrophin in EHT sections was performed. In the early-treated NRVMs-derived EHTs, a tendency towards more dystrophin staining in EHTs, that had been exposed to the pro-hypertrophic stimulus PE, was observed and quantified by removal of the background (**Figure 55 A**). In contrast, in late-treated NRVMs-derived EHTs exposure to this stimulus seemed to result in lower dystrophin staining (**Figure 55 B**).

However, this experiment was only been performed once. Investigation of other immunohistochemical markers such as the apoptosis marker caspase3 or the proliferation marker Ki67 revealed no alterations between the different treatment groups even though in the late treated NRVMs-derived EHTs the caspase3 staining appeared less compared to early-treated NRVMs-derived EHTs when exposed to BPKDI and/or PE (**Supplementary figure 10**).

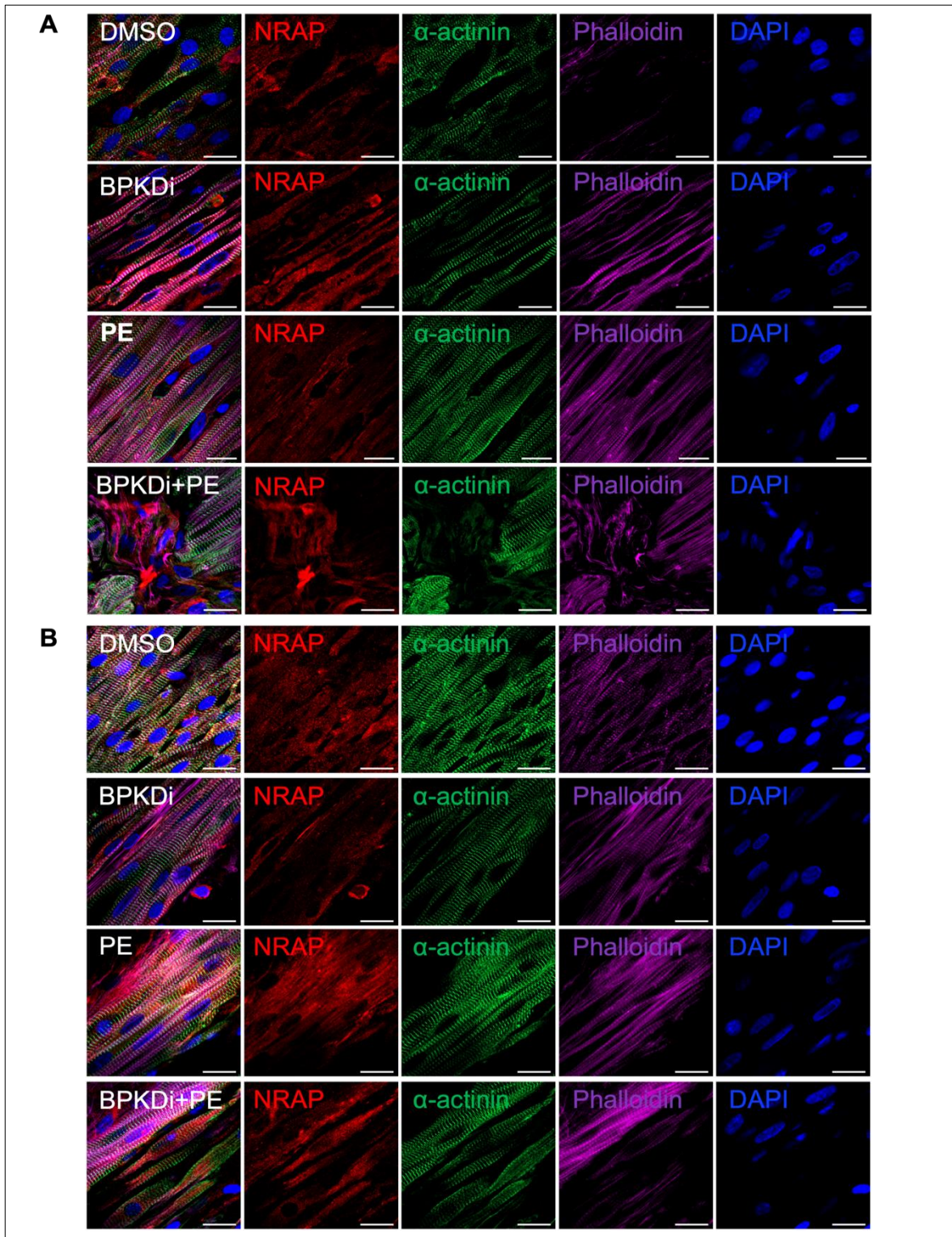


Figure 54: Impact of protein kinase D (PKD) inhibition and pro-hypertrophic stimulation on myofilament structure. Neonatal rat ventricular myocyte (NRVMs)- derived engineered heart tissue (EHT) were treated daily with DMSO or 3 μ M of the pharmacological PKD inhibitor BPKDi, in presence or absence of 20 μ M of the pro-hypertrophic stimulus phenylephrine (PE). The treatment was performed as an **A**) early treatment from day 2-9 after the generation of EHTs or **B**) as a late treatment from day 14-21 after the generation of EHTs when EHTs reached their force plateau. The EHTs were used for sectioning to 100 μ m thick sections using the vibratome and subsequently stained for NRAP (red), α -actinin (green), F-actin (purple) or nuclei (DAPI, blue). Scale bars are equal to 20 μ m. This immunofluorescence of EHT sections has been performed once (n = 1).

Results

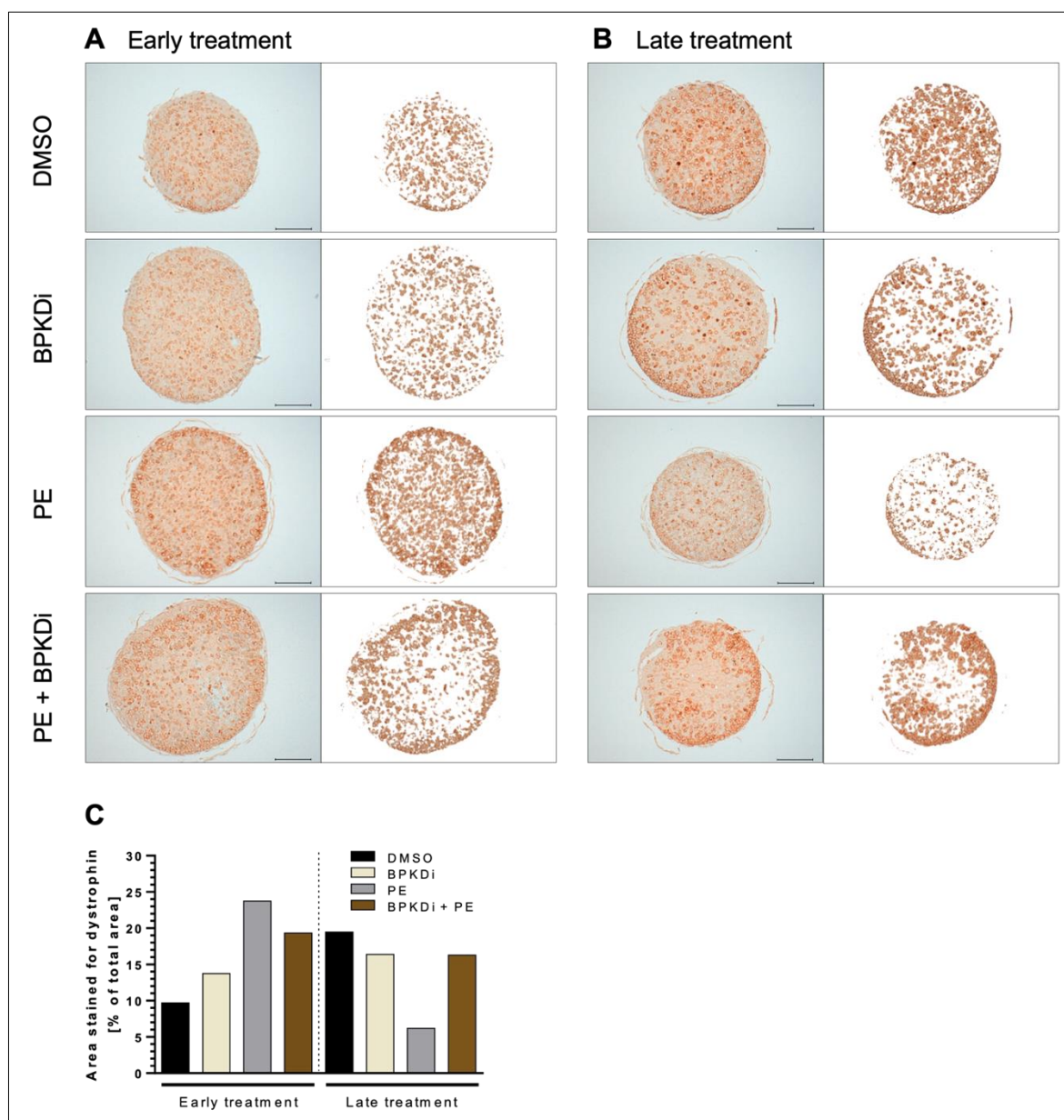


Figure 55: Detection of dystrophin in NRVMs-derived EHTs after protein kinase D (PKD) inhibition and pro-hypertrophic stimulation. Neonatal rat ventricular myocyte (NRVMs)-derived engineered heart tissue (EHT) were treated daily with DMSO or 3 μ M of the pharmacological PKD inhibitor BPKDi, in presence or absence of 20 μ M of the pro-hypertrophic stimulus phenylephrine (PE). The treatment was performed as an **A**) early treatment from day 2-9 after the generation of EHTs or **B**) as a late treatment from day 14-21 after the generation of EHTs when EHTs reached their force plateau. The EHTs were used for immunohistochemical staining of dystrophin. The background was removed and **C**) the dystrophin signal was quantified using ImageJ and represented as percent of stained area/total area ($n = 1$). Scale bars are equal to 100 μ m.

Structural analysis of NRVMs-derived EHTs showed that exposure of late-treated NRVMs-EHTs to BPKDi and PE induced sarcomere rupture. Exposure to the pro-hypertrophic stimulus PE resulted in enhanced dystrophin staining in early-treated and less dystrophin staining in late-treated NRVMs-derived EHTs.

6.6.3.2 Mitochondria and lateral width of intercalated discs

Since pharmacological inhibition of PKD resulted in increased force in both, early- and late-treated NRVMs-derived EHTs, mitochondria were investigated due to their crucial role in energy provision. Transmission electron microscopy of early- and late-BPKDi-treated NRVMs-derived EHT sections showed altered mitochondrial structures resembling roundish structures in all EHTs that had been exposed to BPKDi and enlarged mitochondria upon PE exposure (**Figure 56 A**).

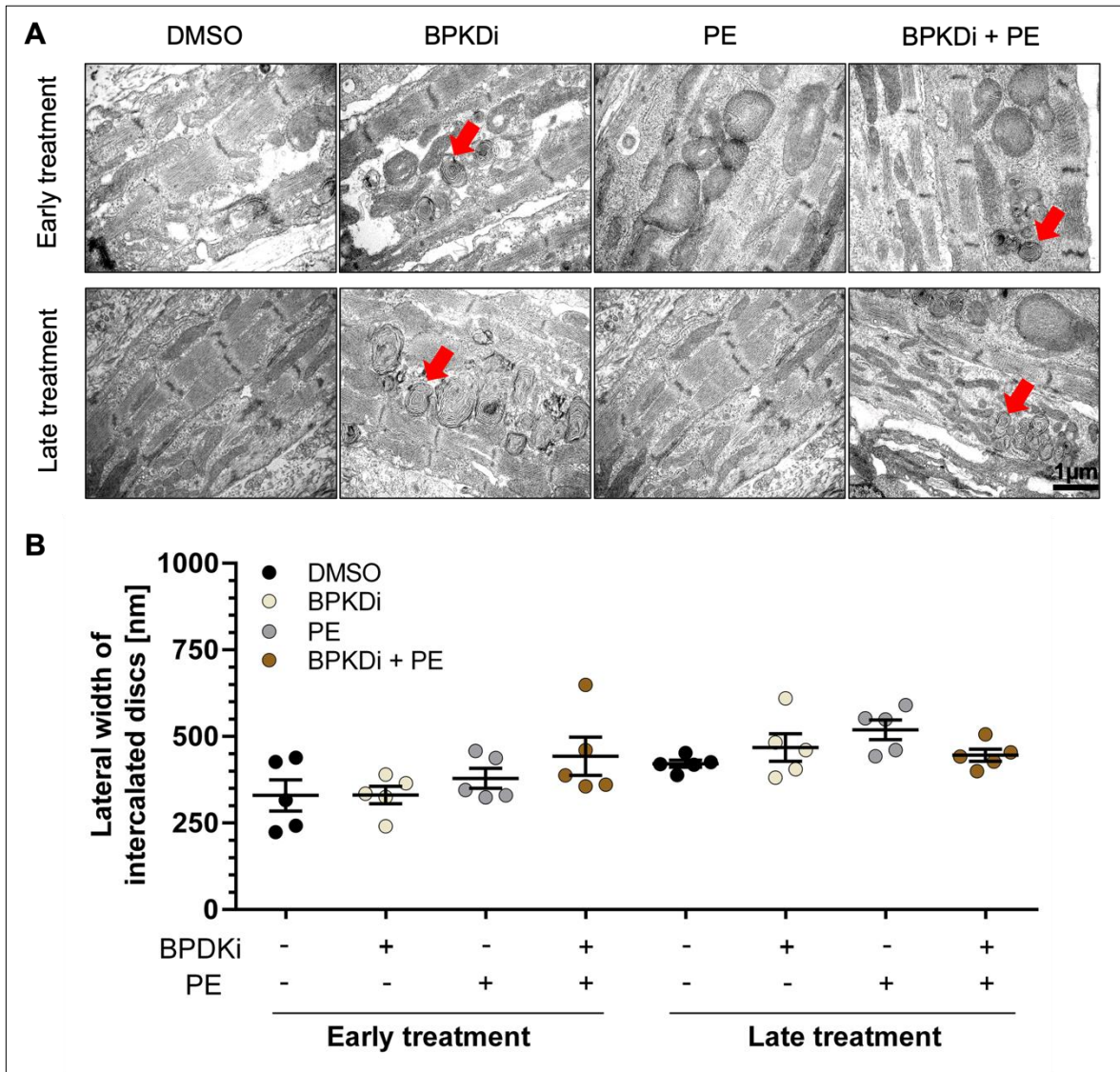


Figure 56: Structural alterations by inhibition of protein kinase D (PKD) and pro-hypertrophic stimulation. A) Transmission electron microscopy (TEM) of neonatal rat ventricular myocytes (NRVMs)-derived engineered heart tissues (EHTs) after daily treatment with DMSO or 3 μ M of the pharmacological PKD inhibitor BPKDi, in presence or absence of 20 μ M of the pro-hypertrophic stimulus phenylephrine (PE). The early treatment was performed from day 2-9 after generation of EHTs or as a late treatment from day 14-21 after generation of EHTs when EHTs reached their force plateau. **B)** Measurements of lateral intercalated disc width in NRVMs-derived EHT sections ($n = 1$). Scale bars are equal to 1 μ m.

Results

Additionally, alterations in intercalated disc width of these NRVMs-derived EHT sections were observed. Therefore, images of different regions were used to measure the intercalated disc width as previously described (Wilson et al. 2014; **Figure 56 B**). This quantification revealed a tendency in early-treated NRVMs-derived EHT sections towards laterally wider intercalated discs when EHTs had been exposed to the pro-hypertrophic stimulus PE. Similar results were measured in late-treated NRVMs-derived EHTs. Overall, the measured intercalated discs were wider in late-treated compared to early-treated NRVMs-derived EHT sections (**Figure 56 B**).

Further, the mitochondrial alterations that were observed in TEM, were additionally assessed in two-dimensional NRVMs after treatment with or without BPKDi in the presence or absence of the pro-hypertrophic stimulus PE with the live-cell stain MitoSPY to investigate mitochondrial localisation by immunofluorescence (**Figure 57**).

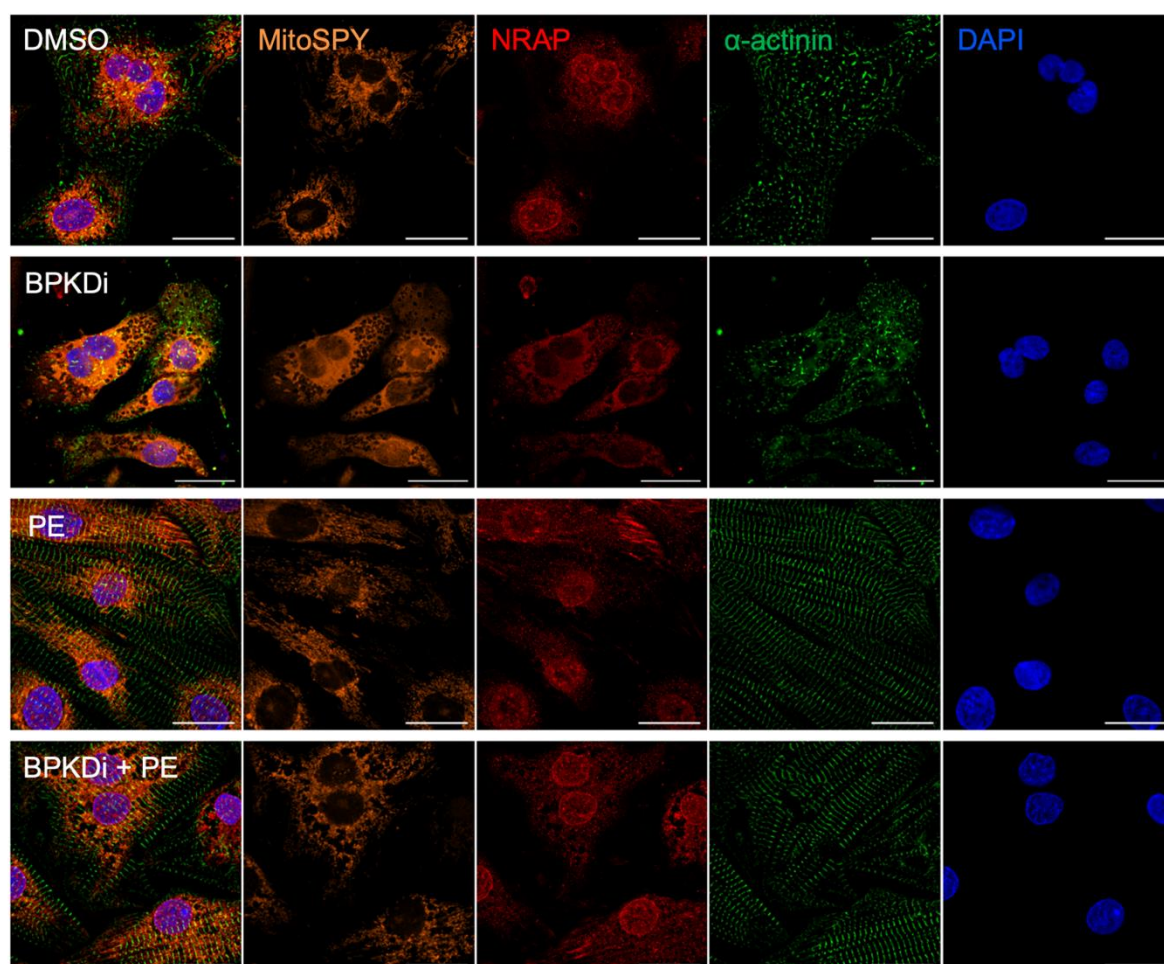


Figure 57: Impact of protein kinase D (PKD) inhibition and pro-hypertrophic stimulation on mitochondria. Neonatal rat ventricular cardiac myocytes (NRVMs) after daily treatment with DMSO or 3 μ M of the pharmacological PKD inhibitor BPKDi, in presence or absence of 10 μ M of the pro-hypertrophic stimulus phenylephrine (PE). Cells were stained for NRAP (red), α -actinin (green), MitoSPY (orange) or nuclei (DAPI, blue) ($n = 2$). Scale bars are equal to 20 μ m.

In control NRVMs, that were only incubated with DMSO, a perinuclear mitochondrial network was detected while exposure to BPKDi resulted in a more diffuse and distributed mitochondrial signal throughout the cell. Exposure to the pro-hypertrophic stimulus PE led to mitochondria distribution along myofilament and additional exposure to BPKDi seemed to disturb the mitochondrial network in a similar manner to the punctate localisation of NRAP.

Overall, pharmacological inhibition of PKD activity led to structural alterations of mitochondria in NRVMs and NRVMs-derived EHTs. Exposure of NRVMs-derived EHTs to the pro-hypertrophic stimulus PE or longterm culture of EHTs showed a trend towards wider intercalated disc dimensions.

6.6.4 Impact on protein expression

Investigation of contractile parameters and structural analysis in NRVMs-derived EHTs revealed that pharmacological inhibition of PKD activity resulted in increased force and concomitantly altered localisation of NRAP with sarcomere disruption upon additional stimulation with the pro-hypertrophic stimulus PE. Hence, alteration of protein translation and turnover were investigated in parallel to the functional consequences by mass spectrometry. Prior to pharmacological treatment, NRVMs were cultured in SILAC light medium. This was followed by exposure of NRVMs to BPKDi in presence or absence of the pro-hypertrophic stimulus PE in SILAC heavy medium. In contrast to the SILAC light medium, this medium contains the heavily-labelled amino acids arginine and lysine allowing to specifically identify newly synthesised proteins.

Analysis of protein expression revealed that PKD inhibition resulted in less NRAP expression (fold change = -1.15), whereas exposure to the pro-hypertrophic stimulus PE (fold change = 1.84) or combined exposure to PE and ISO (fold change = 1.38) increased NRAP protein synthesis significantly (**Figure 58 A**). Combined exposure of those stimuli in presence of BPKDi revealed a non-significantly trend towards lower NRAP expression.

Regarding other significantly regulated proteins, exposure to PE as well as combined exposure to PE and ISO led to decreased protein synthesis of proteins that are related to mitochondria (e.g Echs1, Hspd1, Decr1, Ndufs4, Ndufa7, Coq9; **Figure 58 B, D**). In contrast, more abundantly expressed proteins were related to actin organisation (e.g Xirp2, Tagln2, Pdlim3, Enah).

Results

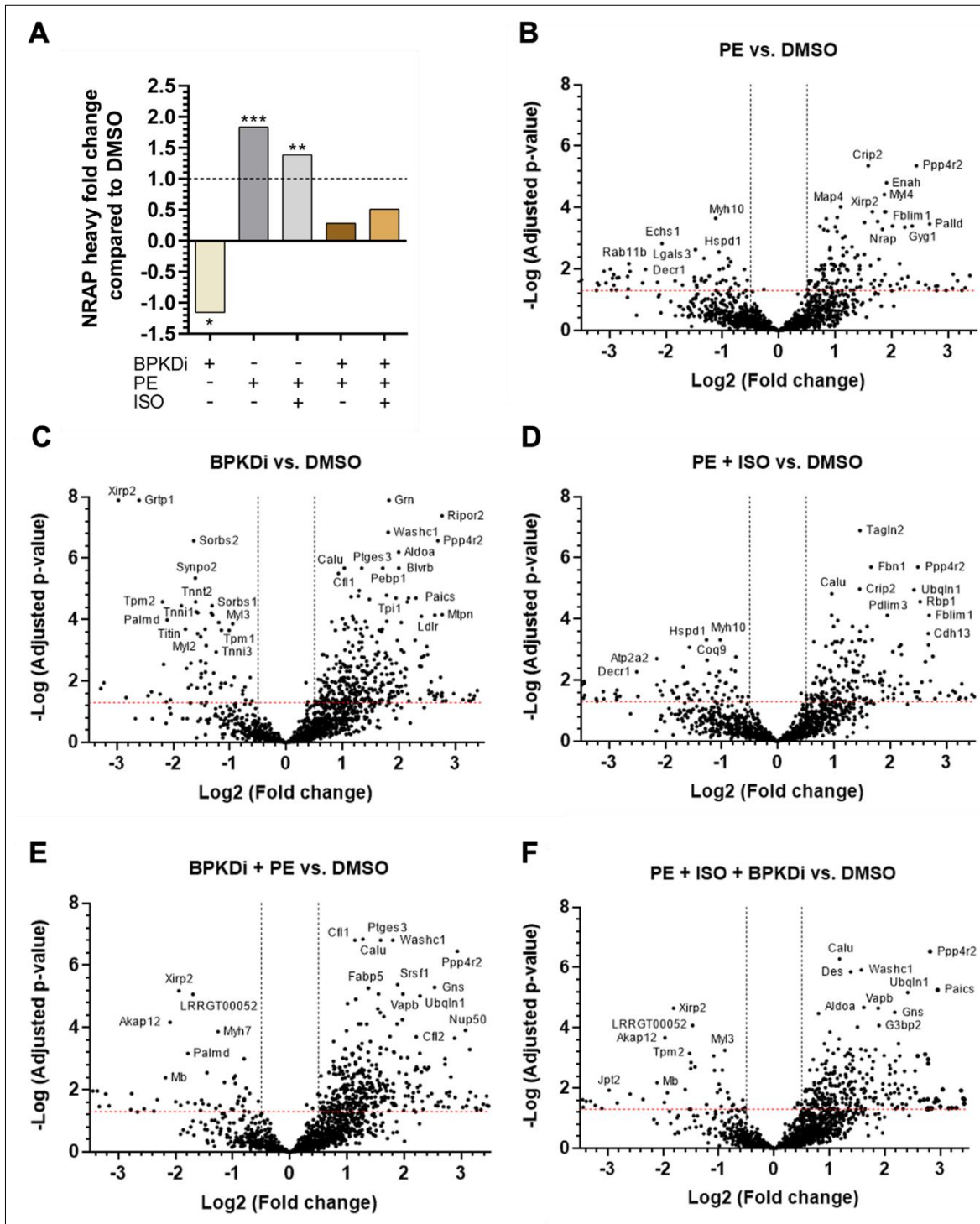


Figure 58: Impact of protein kinase D (PKD) inhibition and pro-hypertrophic stimulation on protein expression. Neonatal rat ventricular myocytes (NRVMs) were treated daily for 72 h in stable isotope labelling by/with amino acids in cell culture (SILAC) heavy medium with DMSO or 3 μ M of the pharmacological PKD inhibitor BPKDi, in the presence or absence of 10 μ M of the pro-hypertrophic stimulus phenylephrine (PE) and/or 10 nM isoprenaline (ISO). Subsequently, mass spectrometry was performed. **A**) NRAP expression compared to DMSO after treatment and volcano plots after treatments with **B**) PE, **C**) BPKDi, **D**) PE and ISO, **E**) BPKDi and PE, or **F**) PE, ISO and BPKDi. Represented are some of the proteins that were most significantly more or less abundant. Proteins above the dashed red lines represent a p-value below 0.05. For statistical analysis, one-way ANOVA, followed by Dunnett's posthoc test was performed (* = $p < 0.05$, ** = $p < 0.01$, *** = $p < 0.001$). These experiments have been performed three times ($n = 3$).

Results

However, pharmacological PKD inhibition reduced synthesis of proteins related to actin organisation related proteins (e.g Xirp2, Synpo2, Myh7, Ldb3) and cytoskeletal proteins (e.g Tnnt2, Tnni, Tpm2, Myoz2) while inducing synthesis of some ER/Golgi-related proteins such as Calu and Rps21 and proteins involved in pathway regulation (e.g Ptges3, Pepb1, Ppp4r2, Paics, Fabp5; **Figure 58 C**). When cells were additionally exposed to pro-hypertrophic stimulation, less proteins of actin organisation were affected but instead the protein Srsf1 that is related to splicing was higher abundant (**Figure 58 E**).

Furthermore, using the database for annotation, visualisation and integrated discovery (DAVID) was used to categorise regulated protein expressions to related KEGG metabolic pathways (**Figure 59**). Interestingly, BPKDi treatment significantly increased protein expression of proteins that are involved in spliceosomal, phagosomal or lysosomal pathways but also processes related to the Golgi and ER network while lower abundant proteins are associated with cardiomyopathies and cardiac muscle contraction (**Figure 59 A**).

As the aim was to investigate the direct impact of PKD inhibition as well as the impact of pro-hypertrophic stimulation on NRVMs, the top 20 more and less abundant proteins derived from the SILAC data set were sorted for treatment with BPKDi or treatment with PE (**Figure 60 A**). Among the top higher expressed proteins upon pharmacological PKD inhibition, mainly proteins related to the coat protein complex II (COPII) that ensure the transport from the ER to the Golgi network or ER-Golgi intermediate compartment (ERCIC) were found. These included S24, COP9 signalosome subunit 3 (COPS3), S61g, sorting nexin 5 (SNX5) and sorting nexin 1 (SNX1). Moreover, proteins such as pyruvate kinase (Pkm) or sulfiredoxin (Srx) that are related to mitochondria were more abundant only if cells had been treated with BPKDi. Regarding the top 20 lower abundant proteins after treatment with BPKDi, proteins such as Nedd8 and stress-induced protein kinase CK1 delta (Csnk1d) were related to proteasomal degradation, while again mitochondria-related proteins such as NADH dehydrogenase 1 beta subcomplex subunit 7 (Ndufb7) and Reticulon-3 (Rtn3) were detected (**Figure 60 A**). However, most of the top hits were related to sarcomere and actin organisation. This included the proteins tropomyosin alpha-1 chain (Tpm1), Calponin-1 (Cnn1), LIM Domain Binding 3 (LDB3) and telethonin (Tcap).

The top 20 upregulated hits after PE treatment were related to ribosomes (EH1ax, Tsr2), epigenetic modifications (Chromobox *Protein* Homolog 1 (Cbx), trinucleotide repeat containing adaptor 6B (Tnrc6b)), transcriptional processes (specificity protein 1 (Sp1), signal-retaining autophagy indicator (Sra1); **Figure 60 B**).

Results

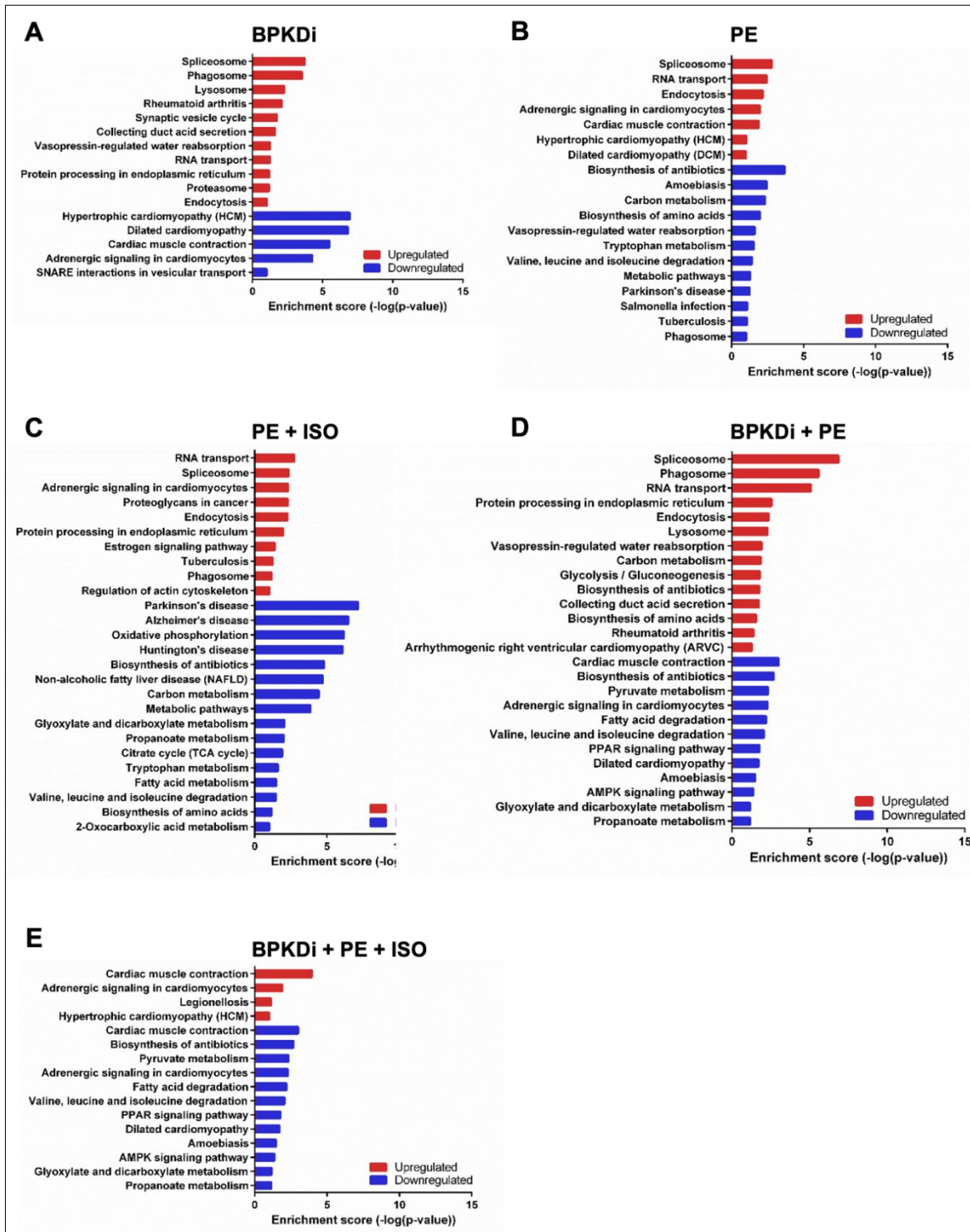


Figure 59: KEGG pathway analysis of the SILAC proteome. Neonatal rat ventricular myocytes (NRVMs) were treated daily for 72 h in stable isotope labelling by/with amino acids in cell culture (SILAC) heavy medium with DMSO or 3 μ M of the pharmacological PKD inhibitor BPKDi, in the presence or absence of 10 μ M of the pro-hypertrophic stimulus phenylephrine (PE) and/or 10 nM isoprenaline (ISO). Subsequently, mass spectrometry was performed and results were annotated with the Database for Annotation, Visualization and Integrated Discovery (DAVID). Top higher and lower expressed proteins were clustered to KEGG pathways for NRVMs treated with **A)** BPKDi, **B)** PE, **C)** PE and ISO, **D)** BPKDi and PE, **E)** BPKDi and PE and ISO. These experiments have been performed in three times ($n = 3$).

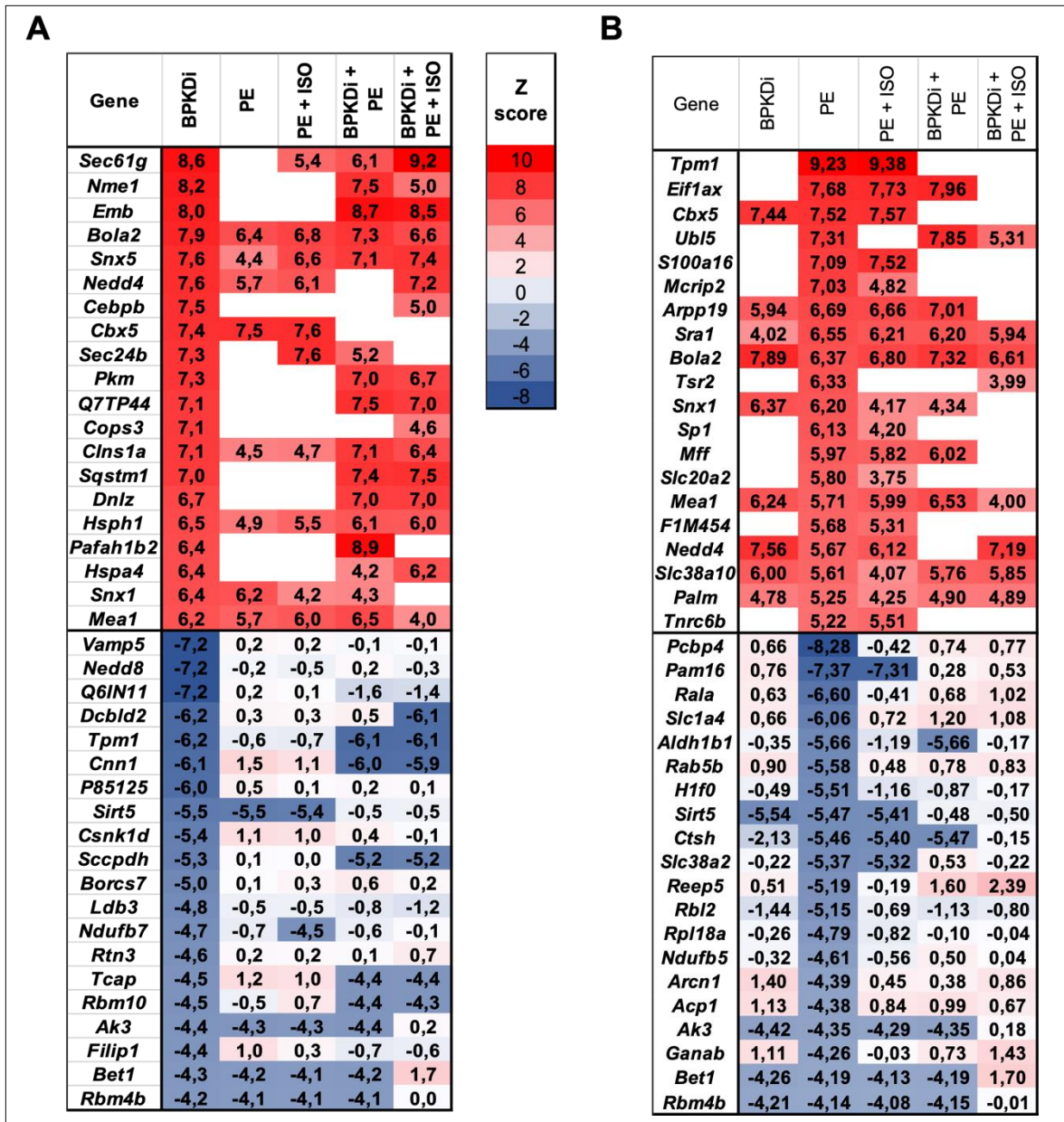


Figure 60: Top 20 higher and lower abundant proteins after protein kinase D (PKD) inhibition and pro-hypertrophic stimulation. Neonatal rat ventricular myocytes (NRVMs) were treated daily for 72 h in stable isotope labeling by/with amino acids in cell culture (SILAC) heavy medium with DMSO or 3 μ M of the pharmacological PKD inhibitor BPKDi, in the presence or absence of 10 μ M of the pro-hypertrophic stimulus phenylephrine (PE) and/or 10 nM isoprenaline (ISO). Subsequently, mass spectrometry was performed. The top 20 most more and less abundant proteins are represented as indicated with the z score with a Z score of 10 as most abundant and a Z score of -8 as the less abundant. Log2 fold change of the top 20 proteins sorted according to cells treated with **A**) BPKDi or **B**) PE. These experiments have been performed three times (n = 3).

The top 20 lower expressed proteins were related to cell cycle (Poly(RC) binding protein 4 (Pcbp4), Ras-related protein A (Ral-A), RB transcriptional corepressor like 2 (Rbl2)) and vesicle trafficking (Ral-A, Archain 1 (Arcn1), Bet1).

Altogether, BPKDi-mediated inhibition of PKD activity decreased NRAP expression in NRVMs while exposure to the pro-hypertrophic stimuli PE and ISO increased NRAP expression. Pathway analysis demonstrated that BPKDi exposure increased abundance of proteins related to degradational pathways.

6.6.5 Regulation of degradational pathways by protein kinase D

Since the SILAC proteome analysis revealed that in BPKDi-treated NRVMs proteins with involvement in vesicle transport were more abundant, NRVMs were treated with BPKDi and/or PE and stained with a Golgi marker by immunofluorescence (**Figure 61**). In control or BPKDi-treated NRVMs, the staining of the Golgi network was detected in close proximity and on one site of the nucleus. In PE-treated NRVMs, the staining of the Golgi network seemed to be in more distance to the nucleus but close to NRAP staining while additional exposure to BPKDi resulted as previously described in sarcomere disruption.

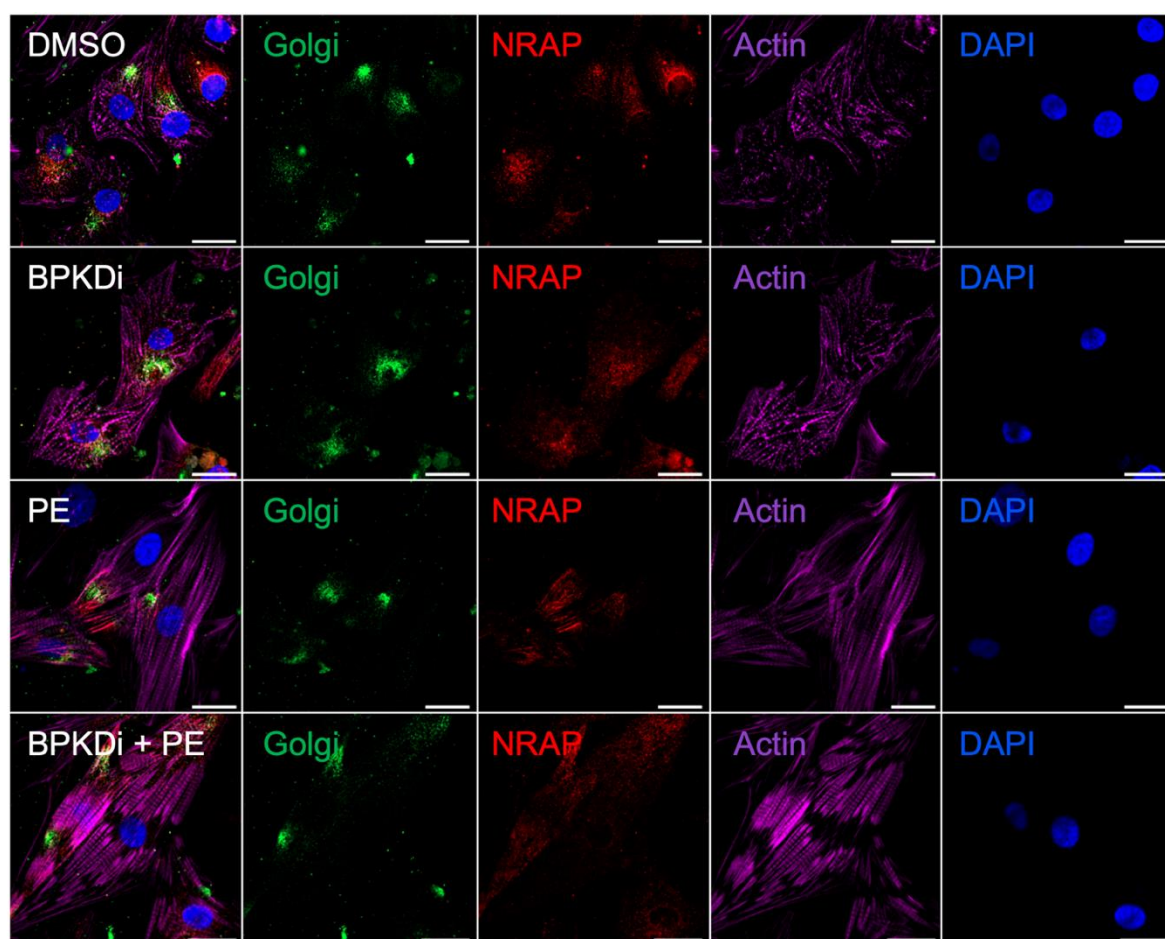


Figure 61: Impact of protein kinase D inhibition and pro-hypertrophic stimulation on the Golgi network. Neonatal rat ventricular myocytes (NRVMs) were incubated for 72 h with DMSO or 3 μ M BPKDi in presence or absence of 10 μ M phenylephrine (PE). NRVMs were fixed with 4% paraformaldehyde and stained for NRAP (red), α -actinin (green), F-actin (purple) and nuclei (DAPI, blue). For negative controls, cells were only incubated with secondary antibodies. Scale bars are equal to 20 μ m. This experiment has been performed once ($n = 1$).

Results

Interestingly, the staining of the Golgi network was similar to NRAP detected within the disrupted areas. Conclusively, pharmacological PKD inhibition impacted Golgi localisation.

Furthermore, a higher abundance of proteins involved in degradation pathways was observed in the SILAC proteome. Therefore, the impact of inhibiting the UPS or autophagy system on NRAP protein levels were investigated while concomitantly treating NRVMs with BPKDi and/or PE (**Figure 62**). Quantification of NRAP protein level revealed a tendency towards increased NRAP protein levels when the UPS system was inhibited by MG132 but not when the autophagy was inhibited in cells. When PKD was inhibited in NRVMs and the UPS system was inhibited by MG132, this resulted in significantly higher NRAP protein levels.

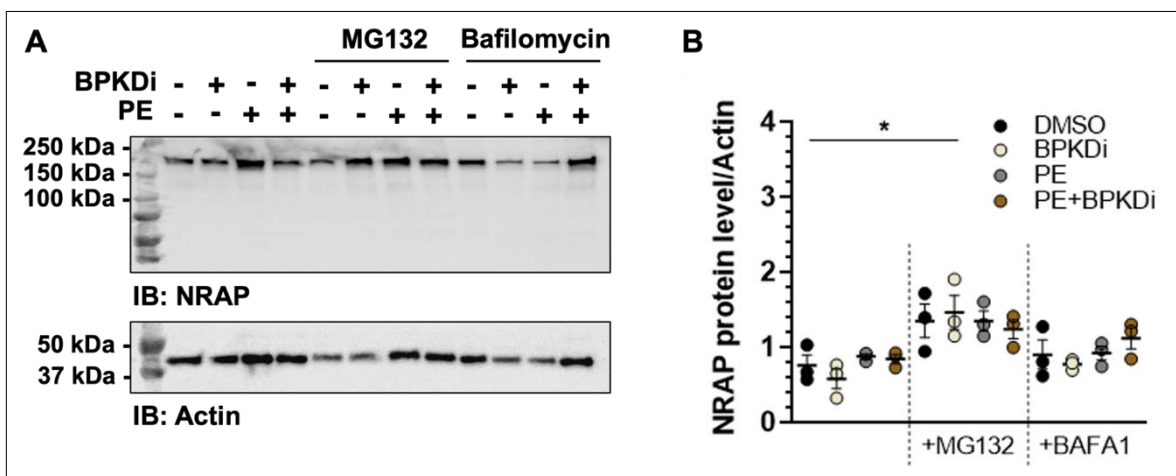


Figure 62: Impact of protein kinase D inhibition and pro-hypertrophic stimulation on the degradational pathways. Neonatal rat ventricular myocytes (NRVMs) were incubated for 72 h with DMSO or 3 μ M BPKDi in the presence or absence of 10 μ M phenylephrine (PE). Additionally, NRVMs were incubated for 24 h with 1 μ M of the proteasome inhibitor MG132 or 3 h with 50 nM of the autophagy inhibitor bafilomycin (BAFA1). **A**) Representative western immunoblot for NRAP and actin as a loading control, and **B**) quantification of NRAP protein level normalised to cardiac actin ($n = 3$). For statistical analysis, one-way ANOVA, followed by Dunnett's posthoc test was performed (* = $p < 0.05$).

Overall, NRAP protein levels increased upon inhibition of the UPS degradation system by MG132, while inhibition of autophagy had no obvious impact on NRAP protein levels, suggesting that the UPS regulates NRAP protein degradation.

6.6.6 Immunoprecipitation of NRAP

In order to investigate if PKD might impact NRAP by direct phosphorylation, NRVMs that had been treated with or without BPKDi in the presence or absence of PE, were investigated by immunoprecipitation using the NRAP antibody from Davids Biotechnology followed by western immunoblotting (**Figure 63 A**). The immunoprecipitation process showed high NRAP levels in the input and crude lysate whereas no NRAP was detected

Results

in the insoluble pellet (**Figure 63 B**). In the immunoprecipitated NRAP fraction (labelled as IP) NRAP was detected at approximately 200 kDa but additionally in the control and NRVMs that were treated with BPKDi and PE a signal at 80 kDa was detected. Moreover, three bands below 50 kDa were detected in all four samples. However, almost no NRAP could be detected in the final supernatant fraction.

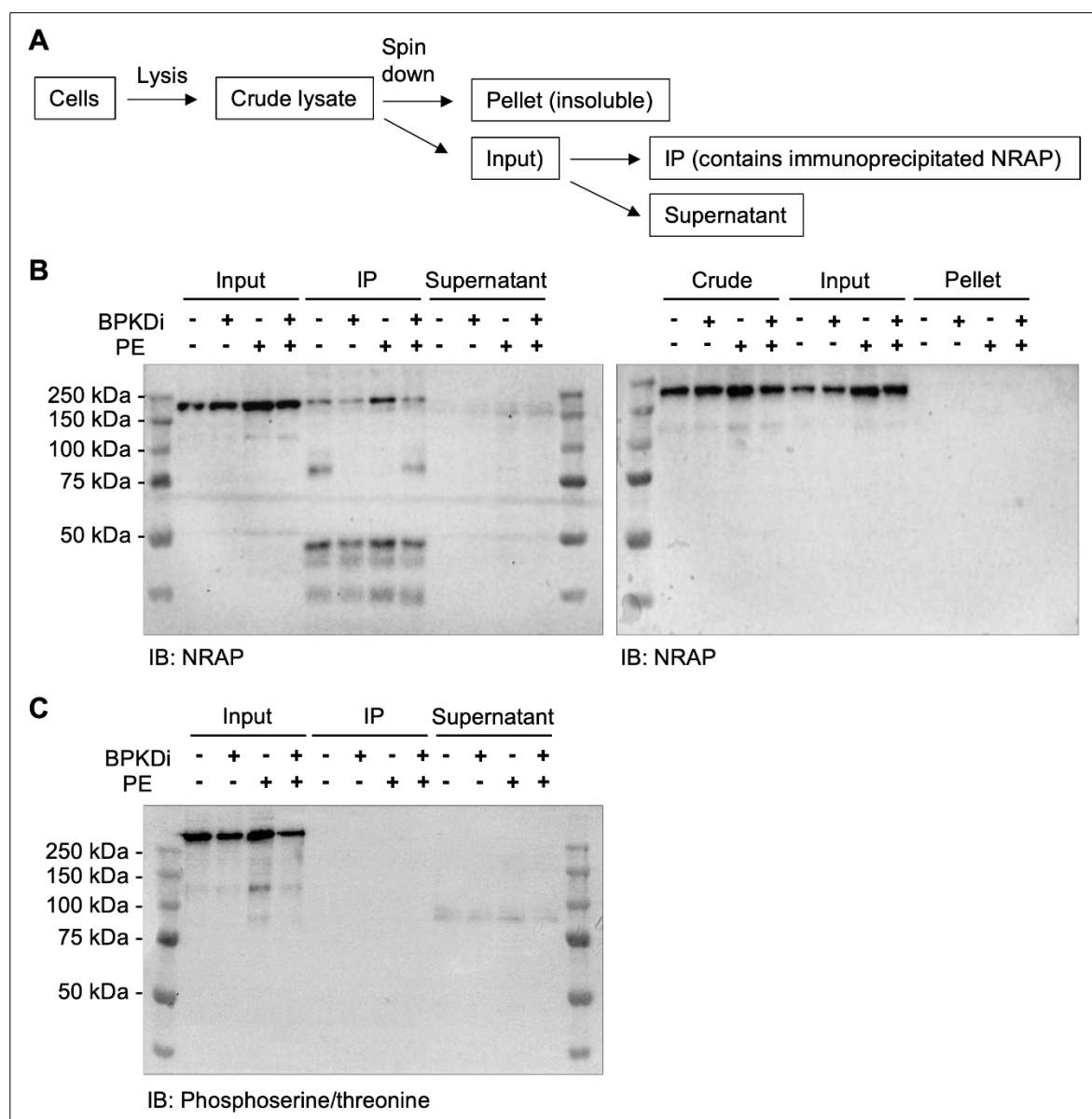


Figure 63: Immunoprecipitation of NRAP after pro-hypertrophic stimulation and inhibition of the protein kinase D in neonatal rat ventricular myocytes (NRVMs). **A)** Schematic overview of the immunoprecipitation (IP) procedure. NRVMs were treated for 72 h with DMSO or 3 μ M BPKDi or 10 μ M of the pro-hypertrophic stimulus phenylephrine (PE). The cells were lysed and NRAP was immunoprecipitated (1:200 anti-NRAP) according to the scheme. The IP fraction contained the immunoprecipitated NRAP. **B)** Western immunoblot for NRAP of different samples taken during the immunoprecipitation procedure to ensure successful immunoprecipitation of NRAP. **C)** Western blot for a phosphoserine/threonin-specific antibody. This experiment has been performed once (n = 1).

Results

Due to successful immunoprecipitation of NRAP, these samples were probed by western immunoblotting with an phosphoserine/threonine antibody to detect potential posttranslational modification. The antibody detected a band in the input sample above 250 kDa and 125 kDa while in the supernatant a band at approximately 90 kDa was detected (**Figure 63 C**). However, in none of the immunoprecipitated samples containing NRAP, a signal by the antibody was detectable, suggesting no phosphorylation of NRAP or difficulties in the detection of NRAP phosphorylation.

The immunoprecipitation of NRAP was successful, but phosphorylation of NRAP by western immunoblotting was not detectable with the available tools. Therefore, unbiased phosphoproteomic analysis followed by mass spectrometry was performed with analysis still ongoing.

7. Discussion

Previous studies reported that mutations and altered expression of intercalated disc proteins have been associated with the development of HCM, DCM and ARVC (Zhao et al. 2019). A prominent intercalated disc protein is NRAP. Its loss-of-function has been suggested to cause DCM (Koskenvuo et al. 2021). Since the precise molecular (patho) physiological role of NRAP in cardiac disease development remains unknown to date, the overarching aim of this thesis was to investigate whether NRAP protein abundance impacts the development of cardiac disease development and whether the function of NRAP might be regulated by posttranslational modifications. To achieve these aims, contractile function and response to mechanical stretch was studied in a gene-dose dependent manner in *NRAP/MYC-OE* and *NRAP-KD* hiPSC-derived cardiac myocytes and EHTs as well as in NRVMs and NRVM-derived EHTs.

7.1 Normoxic oxygen tensions impact on hiPSC characteristics

The tissue culture model that this thesis was based on are hiPSC. To start, the impact of oxygen on hiPSC culture was studied. Tissue-resident stem cells reside in hypoxic niches (Shooter and Gey 1952). Cultivation of stem cells at oxygen conditions that differ from their physiological niche results in chromosomal abnormalities and decreased pluripotency. Accordingly, a study of human embryonic stem cells showed that culture at 20% O₂ resulted in significantly increased spontaneous chromosomal aberrations in comparison to cells that had been incubated at 2% O₂ (Forsyth et al. 2006).

Generally, it is presumed that proliferating stem cells can quit the G₁ phase of the cell cycle by either entering a reversible and quiescent G₀ phase or an irreversible G₀ phase that might result in differentiated or senescent cells (Cheung and Rando 2013). For hematopoietic stem cells, it has been shown that those cells can reside in the quiescent G₀ phase to overcome conditions abnormal to their physiological niche (Shima et al. 2010). In the quiescent phase, hematopoietic stem cells accumulate more mutations due to less efficient DNA repair mechanisms (Beerman et al. 2014). This indicates that normoxic-cultured hiPSC might acquire a quiescent state. However, compared to incubation at hypoxic conditions, cultivation of hiPSC at normoxic oxygen tension resulted in increased levels of senescence compared to hypoxic incubation as indicated by the detection of increased levels of the senescence marker SA- β -galactosidase. However, senescent cells lose their proliferative properties and ability to re-enter the cell cycle (Campisi 2011). Interestingly, the normoxia-induced senescence could be partially reversed by culture in pre-conditioned hypoxic medium. This suggests that paracrine

factors released in the cell culture media induce senescence and that cells potentially partially reside in the senescent G₀ phase and partially in the quiescent G₀ phase.

Since senescence or apoptosis might be the consequence of high oxygen concentrations and thus the production of ROS (Balaban et al. 2005), mitochondrial complexes were further investigated. An important oxygen-dependent regulator of the hypoxia-inducible gene expression pattern is HIF1 α (Lee et al. 2004). As expected, HIF1 α mRNA and protein expression was lower upon normoxic culture of hiPSC and this coincided with lower *NDUFA4L2* expression and decreased accessibility of the chromatin structure of the *NDUFA4L2* gene. In murine embryonic fibroblasts, it has been reported that *NDUFA4L2* is a downstream target of HIF1 α , which inhibits mitochondrial complex I activity, thus resulting in lower ROS production during hypoxic culture conditions (Tello et al. 2011). In addition, a reduction in mitochondrial respiration and ROS formation was observed upon adenoviral *NDUFA4L2* expression in skeletal mouse muscle (Liu et al. 2021b). The *NDUFA4L2* protein sequence shares a high similarity with the sequence of *NDUFA4* and is therefore postulated as a paralog of *NDUFA4* (Tello et al. 2011). Previously, *NDUFA4* was considered to be related to the mitochondrial complex I (Tello et al. 2011), however it has been shown by complexome analysis of mouse cells that *NDUFA4* is a subunit of the mitochondrial complex IV (Balsa et al. 2012). In contrast, mitochondrial complexome analysis of normoxic- and hypoxic-cultured hiPSC could not detect *NDUFA4L2* as an integral part of the mitochondrial complex IV at least in this experiment system. Interestingly, *NDUFA4L2* was only detected in hypoxic- but not in normoxic-cultured hiPSC. *NDUFA4L2* might only associate with complex IV without being an internal part of it or might contribute to the mitochondrial complex IV in mice but not in human hiPSC.

7.2 Successful generation and validation of a human NRAP antibody

Since previous studies reported an involvement of NRAP in the developing and diseased heart, the advantages of hiPSC differentiation to cardiac myocytes was used to enable studying NRAP on a human genetic background. Human *NRAP* mutations resulting in a loss-of-function were correlated with the human DCM phenotype (Truszkowska et al. 2017; Zhang et al. 2023) while DCM mouse models such as the *MLP*-KO mouse led to accumulation of NRAP protein (Ehler et al. 2001). NRAP protein levels were investigated in human samples of NF, DCM, HCM or ICM. However, NRAP abundance was not significantly altered between samples. The discrepancy might be caused due to a limited availability of patient samples and in consequence high variability. Especially in the NF heart samples the variability between different patient samples was high. Although the accessibility to human heart tissue is limited, analysis of more samples would provide

more reliable results on whether NRAP protein levels correlate with the type of heart disease.

Furthermore, we used our custom-made NRAP antibody to investigate subcellular distribution of NRAP in DCM heart sections as well as in hiPSC-derived cardiac myocytes or EHT sections. Application of the antibody for immunofluorescence enabled detection of NRAP at intercalated discs in DCM heart sections whereas NRAP localisation in hiPSC-derived cardiac myocytes or EHT sections was distributed throughout the cell. Investigation of different fixation methods did not impact this signal. Since immunofluorescence staining revealed correct localisation and detection of NRAP in DCM heart sections, but not in hiPSC-derived cardiac myocytes and EHTs, this suggests that NRAP might be distributed in the cytosol due to immaturity of hiPSC cardiac myocytes. The absence of intercalated discs in hiPSC-derived cardiac myocytes seems to be a general disadvantage of this model. In experimental murine models, the formation of intercalated discs have been shown to mainly occur postnatally and is thereby considered as a feature of maturity (Hirschy et al. 2006; Pieperhoff and Franke 2007). The immaturity of hiPSC has been previously reported as a limiting aspect in hiPSC models and different strategies have been developed to enhance hiPSC cardiac myocyte maturation (Thomas et al. 2022). This includes prolonged culture time, metabolic maturation by medium supplementation with hormones, physical treatments such as electrical stimulation or rotation or culture in three dimensional EHT formats.

Although the antibody was developed based on detection of human NRAP, the aim was to also test its ability to detect NRAP in mouse and rat heart tissue due to high sequence homology. In cardiac mouse and rat tissue, the antibody detected the correct NRAP band but also cross-reacted with MHC and an additional band at approximately 100-115 kDa while the immunofluorescence showed the NRAP localisation towards the intercalated discs. However, during preparation of SDS samples for western immunoblotting, tertiary protein structures are destroyed while they are maintained during their *in situ* detection by immunofluorescence which might explain the cross-reactivity observed by western blotting. Immunological cross-reactivity has previously been described if the antibody epitope and binding sites share homologous amino acids (Kharrazian et al. 2020). Especially in polyclonal antibodies, the cross-reactivity results from multiple epitope recognition but can be lowered by affinity purification of the antibody (Ascoli and Aggeler 2018).

The immunisation of the NRAP antibody was performed by using a peptide sequence against a N-terminal nebulin repeat. However, other family members of the nebulin family,

such as nebullette, share a homology to these nebulin repeats (Pappas et al. 2011). The molecular weight of human nebullette is 107 kDa (Pappas et al. 2011). The mouse isoforms are described on the NCBI website to consist of 102 kDa (917 amino acids) and 30 kDa (270 amino acids) while rats only express one nebullette isoform of 106 kDa (952 amino acids). This suggests that the detected cross-reactivity at 100-115 kDa could possibly be caused by binding of the NRAP antibody to a nebulin-repeat in the protein nebullette (**Supplementary figure 9**).

7.3 Impact of NRAP modulation on hiPSC-derived cardiac myocytes

The combination of the CRISPR-Cas9 engineering technology and the hiPSC cell technology constitutes an ideally-suited opportunity to unravel disease mechanisms on a human genetic background. To study whether altered NRAP levels are associated with cardiac myocyte dysfunction, stable homo- and heterozygous *NRAP/MYC-OE* and *NRAP/GFP-OE* cell lines and a *NRAP-KD* hiPSC line were successfully generated.

However, these technologies are accompanied by side effects such as undesired genetic alterations or variabilities. The CRISPR-Cas9 system might induce chromosomal rearrangements and karyotype abnormalities if the DNA re-ligates after double-strand breaks induced by the Cas9 (Liu et al. 2022). To overcome this issue, CRISPR-Cas9-induced chromosomal rearrangements were ruled out by several quality controls. CRISPR-induced chromosomal aberrations and insertions or deletions were excluded by karyotyping and sequencing of the appropriate DNA loci around the PAM sites. Although the Cas9 reliably generates DNA double-strand breaks after base pairing between a desired gene locus adjacent to a PAM site and the custom-designed sgRNA, off-target effects occur if the Cas9 cleaves untargeted genomic sites (Jinek et al. 2012; Pacesa et al. 2022; Wang et al. 2016). To minimise off-target effects, RNP-based nucleofection was preferred over gRNA- and Cas9-containing plasmids allowing constant expression for days compared to RNP complexes that are rapidly degraded (Gaj et al. 2012; Kim et al. 2014). Further, the ten most likely predicted off-target loci for each gRNA locus were validated by sequencing. This reduces the probability of selecting a cell clone with unspecific DNA double-strand breaks induced by the Cas9. Opportunities to further reduce the incidence of using cell clones with off-targets might be Southern blotting or whole genome sequencing. However, by whole genome sequencing it has been shown that the probability of off-target effects in hiPSC induced by Cas9 is rather low (Veres et al. 2014).

7.3.1 *NRAP*-OE

For the generation of a stable *NRAP*-OE cell line, transgene integration into the safe harbour locus was performed since this has not been shown to negatively impact cell viability or chromatin structure (Ogata et al. 2003; Smith et al. 2007). Transgene integration can be achieved by using homology arms that range between 50 bp and 2 kbp depending on the inserted gene of interest (Byrne et al. 2015; Orlando et al. 2010). In this thesis, the homology arms were each approximately 800 bp long, which is in accordance with successfully and commonly used homology arms in the literature (Oceguera-Yanez et al. 2016).

Targeting of the *AAVS1* locus by CRISPR/Cas9 has been reported to lead to editing efficiencies in iPSC between 0.1 and 4% (Mali et al. 2013; Roberts et al. 2017). To enhance the percentage of positively edited hiPSC, puromycin resistance of the simultaneously integrated gene inserted into the safe harbour locus was used (Luo et al. 2014; Oceguera-Yanez et al. 2016). The application of puromycin as a selection marker results in only a few surviving cells with high chance of selection of successfully edited cells (Lyu et al. 2018). Even though CRISPR efficiencies were not determined due to the absence of a marker protein such as GFP, many of the remaining cells after puromycin selection were positively edited, suggesting a high efficiency of this CRISPR strategy.

In order to achieve overexpression of *NRAP* exclusively in cardiac myocytes, in addition to the protein expressed from the endogenous *NRAP* gene, *NRAP* expression from the transgene was driven by the cTnT promoter, which has been shown to achieve cardiac-specific expression (Kolwicz et al. 2016). Hence, this allows specific expression of *NRAP* in cardiac myocytes, but not in other undefined cell types that are routinely present at low percentage after cardiac differentiation. In addition, the MYC-tag or the GFP-tag at the C-terminus of the integrated *NRAP* allowed to distinguish between endogenous and transgenic *NRAP* in cardiac myocytes. For validation of successful integration into the safe harbour locus, long-range PCRs were combined with sequencing of different genomic parts of the insert as well as overlapping DNA parts of genomic and plasmid origin. However, this validation process is error-prone if no long-range amplicon is expressed or plasmids are integrated into a different locus. A more reliable opportunity to confirm the genotype is Southern blotting (Oceguera-Yanez et al. 2016). This allows to distinguish between hetero- and homozygous clones and unveils whether additional plasmid rearrangements occurred (Oceguera-Yanez et al. 2016).

7.3.2 *NRAP*-KD

For the generation of a *NRAP*-KD, the promotor-flanking region, the promotor and the DNA sequence covering the first exons of *NRAP*, including the start codon, were removed to prevent the production of a truncating protein or the activation of nonsense-mediated decay. The induction of two double-strand breaks to remove the desired 5328 bp of the DNA sequence was used since the induction of only one double-strand break has several disadvantages. In the latter case, frameshift mutations might occur, destroying the reading frame (Zimmer et al. 1994). If the open reading frame is too short, the frameshift mutation might only lead to the reintegration of a downstream start codon (Zimmer et al. 1994). Instead, if the frameshift mutation is located downstream of the start codon, this might result in a premature stop codon that activates the cellular nonsense-mediated decay preventing the translation of the mRNA into a protein (Hug et al. 2016). If the premature stop codon is in the final exon, the expression of a truncated and partially functional protein might occur (Hug et al. 2016). For induction of a more predictable gene KO in hiPSC, two double-strand breaks were induced, followed by NHEJ that resulted in an efficient opportunity to generate loss-of-function cell lines (Liu et al. 2016).

However, the DNA sequence of 5328 bp was only removed on one allele while 8 bp from the other allele around the PAM sequence were removed. This indicates a successful DNA double-strand break on one allele around the PAM site in the promotor flanking region but not at the second PAM site in the *NRAP* exon. The 8 bp induced deletion in gRNA1 might be causative due to NHEJ occurring and indicate that the gRNA2 in the *NRAP* exon might have a lower on-target score. This could explain why no homozygous *NRAP*-KO clone was identified among all 150 screened hiPSC clones except one clone that died during production of a master cell bank. Another explanation could be that homozygous *NRAP*-KO hiPSC might not be viable. The homozygous KO of intercalated disc proteins was shown to often result in embryonic lethality around the onset of cardiac myocyte differentiation (Perriard et al. 2003). To our knowledge, there are no established *NRAP*-KO animal models described in the literature. This might suggest that these animals might not be viable and supports the importance of *NRAP* for proper formation and functioning of myofibrils.

However, the validation of the cell clone by whole genome sequencing would be more reliable since no allelic dropout could occur as recently described for PCR-based validation methods (Simkin et al. 2022). In this study, 33% of previously correctly validated hiPSC clones by PCR and Sanger sequencing, showed on-target genomic defects by whole genome sequencing.

Since the aim was to study NRAP in a gene-dose dependent manner, the *NRAP*-KD hiPSC clone with a 5328 bp deletion on one allele and a 8 bp deletion on the other allele was used to study the loss-of-function effects of NRAP. Because the 8 bp deletion occurs around the PAM site in the promotor-flanking region, it is not expected to result in a truncating or functionally impaired protein.

7.3.3 Differentiation into hiPSC-derived cardiac myocytes

Since NRAP has been described to be exclusively expressed in skeletal and cardiac muscle tissue, the differentiation of genetically-edited *NRAP*-hiPSC lines to ventricular cardiac myocytes was urgently required. The established cardiac differentiation protocol in our institute for cardiac differentiation includes the incubation with 8 ng/mL activin A. However, this resulted in low differentiation efficiencies. Higher activin A concentrations (12 ng/mL) promote the differentiation of hiPSC to ventricular cardiac myocytes while lower activin A concentrations rather result in the differentiation of atrial cardiac myocytes (Lee et al. 2017). Therefore, the differentiation protocol was explicitly optimised for the *NRAP* hiPSC lines. To this end, a concentration of 12 ng/mL activin A in combination with different cell densities was applied, resulting in higher efficiencies of cardiac myocyte differentiation as indicated by high values of cTnT-positive cells measured by flow cytometry.

Despite several quality controls and the usage of the same cell densities and growth factors during parallel differentiations, high variabilities of differentiation efficiencies were observed in hiPSC and hiPSC-derived cardiac myocytes. A large-scale study using genome-wide profiling of 711 hiPSC lines from overall 301 healthy probands found phenotypical and differentiation efficiency variabilities of 5-46%, which are caused by the different genetic backgrounds of the probands (Kilpinen et al. 2017). Moreover, high batch-to-batch variability was reported for hiPSC-derived cardiac myocyte expression of cardiac ion channels which might impact contractile parameters (Huo et al. 2016). In addition, these high variabilities between batches could be further assessed in the EHT format (Mannhardt et al. 2020). Therefore, several differentiations and EHT batches were included to allow reliable conclusions to be drawn regarding the observed structural and functional alterations between different *NRAP* cell lines. To further ensure the impact of *NRAP* gain- and loss-of-function on cardiac contractility, more than one clone per genotype should be investigated, which was beyond the scope of this thesis due to time and cost limitations.

7.3.4 NRAP mRNA and protein expression

Prior to analyse the structural and functional consequences of *NRAP/MYC*-OE and *NRAP*-KD hiPSC-derived cardiac myocytes, the priority at first was to ascertain overexpression or knockdown of NRAP in cardiac myocytes. In *NRAP*-KD EHTs, *NRAP* mRNA was 60% decreased, which indicates that the 8 bp deletion in the promotor-flanking region might impact *NRAP* gene expression since a 50% mRNA reduction would be expected for a heterozygous *NRAP*-KO line. Therefore, inclusion of more than the here investigated 5-9 EHTs from three batches are required to strengthen these observations. Interestingly, on a protein level, NRAP was not detectable in *NRAP*-KD or control hiPSC-derived cardiac myocytes. In contrast, a robust signal for NRAP was detectable by western blotting with simultaneous detection of the C-terminal MYC-tag in *NRAP/MYC*-OE cardiac myocytes. This proves increased protein expression of the transgene *NRAP/MYC* and thereby successful generation of *NRAP/MYC*-OE hiPSC-derived cardiac myocytes.

However, no difference in *NRAP* mRNA levels could be detected between *NRAP/MYC*-OE and control EHTs. To corroborate this observation, it would be necessary to include more EHTs in the gene expression analysis. An explanation for this apparent discrepancy between mRNA and protein levels might originate from different culture conditions and consequently differences in maturity since *NRAP* mRNA fold changes were determined from EHTs after three weeks of culture suggesting higher levels of maturity compared to two dimensional cardiac myocytes that were used for NRAP protein quantification. Moreover, the discrepancies between mRNA and protein levels might be caused by differences in degradation processes for mRNA and proteins since NRAP has previously been shown to be targeted by UPS-mediated degradation (Witt et al. 2005). Another explanation for the absence of increased mRNA levels in *NRAP*-OE EHTs could be that a fast translation of the transgenic *NRAP/MYC* mRNA to protein occurs since no alternative splicing or modification of the transgenic NRAP is required.

7.3.5 Modulation of NRAP lead to structural alterations in cardiac myocytes

Structural alterations after NRAP gain- and loss-of-function were investigated in two-dimensional cultured hiPSC-derived cardiac myocytes. The custom-made NRAP antibody revealed mainly nuclear staining, which might represent an artefact and indicates that this antibody is not properly functioning in this cell system. In contrast, the commercial human NRAP antibody showed NRAP localisation at Z-discs in control and *NRAP*-KD EHTs, similarly to our previous observations in heart sections of DCM patients as exemplified in the section containing the antibody validation process. This indicates that *NRAP*-KD

cardiac myocytes are either undergoing the fetal gene program or that this program is induced upon hypertrophy as previously reported (Taegtmeyer et al. 2010).

Indeed, in heterozygous and homozygous *NRAP/MYC-OE* cardiac myocytes, translocation of NRAP towards the lateral cell borders was detectable suggesting potentially enhanced maturation. Similar NRAP localisation has been observed when immature NRVMs were exposed to the pro-hypertrophic stimulus PE. The myofilament structure appeared disorganised in *NRAP/MYC-OE* cardiac myocytes in comparison to control cardiac myocytes or *NRAP-KD* cardiac myocytes where myofilaments were aligned in a parallel manner. Since NRAP has a crucial role in I-Z-I band assembly in early myofibrillogenesis (Carroll et al. 2004), overexpression of NRAP might impact the correct alignment of newly formed sarcomeres.

7.3.6 Gain- and loss-of-function of NRAP impacts contractile parameters

For the investigation of a gene-dose-dependent impact of NRAP on contractile parameters, genetically modified *NRAP-EHTs* were investigated. Commonly, EHTs are generated from differentiated hiPSC-derived cardiac myocytes with a cardiomyocyte content within the cells of a differentiation between 60-90% (Mannhardt et al. 2016). Accordingly, hiPSC-derived cardiac myocyte fractions with more than 60% cTnT-positive cells were considered acceptable to enrol into the EHT generation. Although mean cTnT values varied between single EHT batches and cell lines, the mean cTnT value of all batches was similar between different cell lines allowing to detect differences in structural and contractile functions.

In spontaneously-beating *NRAP-KD*, hetero- and homozygous *NRAP/MYC-OE* EHTs shorter relaxation time (80%) and enhanced contraction velocity was detected compared to control EHTs. These contractile characteristics have been previously observed in neonatal, heterozygous *Mybpc3-KI* mice-derived EHTs that develop a HCM phenotype (Stöhr et al. 2013).

Interestingly, *NRAP-KD* EHTs developed a slower relative early RT but faster late RT than control EHTs whereas homozygous *NRAP/MYC-OE* EHTs developed a slower relative early TTP and faster relative late TTP. The functional observations in *NRAP/MYC-OE* EHTs are in accordance with the action potential measurements that revealed a less negative diastolic potential in comparison to control EHTs that is defined as MDP. This has been associated with low densities of the inward rectifier current (I_{K1}) and originates from immaturity of hiPSC-derived cardiac myocytes (Ma et al. 2011). In addition a less negative TOP and a lower V_{max} was detected in homozygous *NRAP/MYC-OE* EHTs compared to

control EHTs. These findings combined with altered time to peak durations indicate that altered sodium current (I_{Na}) activity might be involved in these electrophysiological alterations in homozygous *NRAP/MYC-OE* EHTs (Ismaili et al. 2023).

Assessment of electrically synchronised EHTs revealed significantly lower force and relaxation time (80%) in all genetically-modified *NRAP* EHTs compared to their respective control group. Additionally, *NRAP-KD* EHTs showed a faster time to peak (-80%) than control EHTs. In a study of severe childhood cardiomyopathies, a homozygous nonsense variant (c.1344T>A) in *NRAP* was detected leading to a premature stop codon and truncating protein (Vasilescu et al. 2018). Thus the truncating *NRAP* mRNA was not degraded and resulted in a dysfunctional protein suggested to cause severe childhood cardiomyopathies with enlarged left ventricle and decreased ejection fraction. Another study detected a homozygous *NRAP* loss-of-function variant (c.259delC) that caused left ventricular non-compaction cardiomyopathy (LVNC) in a patient, phenotypically characterised by dilated left atrium and ventricle accompanied by decreased heart function (Zhang et al. 2023). This variant was modelled in a zebrafish resulting in disorganised cardiac myocytes and lower gene expression related to cardiac development emphasising the importance of *NRAP* on unperturbed contraction (Zhang et al. 2023).

On the opposite, these genes were upregulated in *NRAP-OE* mice which were associated with the development of right ventricular cardiomyopathy resulting right ventricular dilation and decreased ejection fraction with minor impact on left ventricular performance (Lu et al. 2011). In essence, *NRAP* loss-of-function has been reported to affect the left ventricle function while *NRAP* gain-of-function predominantly affected the right ventricle with both cases enhancing fetal and hypertrophic gene expression and developing dysfunctional ejection fraction. This is in accordance with our observations in *NRAP-KD* and *NRAP/MYC-OE* EHTs that developed significantly less force than their isogenic control EHTs.

7.3.7 NRAP impacts mechanical stiffness

Exposing EHTs to increased mechanical stretch unveiled that homozygous *NRAP-OE* EHTs responded to mechanical stretch with inability to follow the electrical pacing. Interestingly, *NRAP* upregulation has been linked to the most common form of cardiac arrhythmia, the atrial fibrillation (Liu et al. 2021a). This is corroborated by our observations of alterations in electrophysiological parameters such as less negative MDP, RMP and higher RR-scatter in homozygous *NRAP/MYC-OE* EHTs, confirming indeed a causal link between *NRAP* protein abundance and the pro-arrhythmic phenotype.

In contrast, *NRAP*-KD EHTs demonstrated unperturbed contractility during increased mechanical stretch even better than isogenic control EHTs. Myocardial stiffness depends on cardiac myofilament characteristics such as the isoform abundance of titin (Linke 2008). Variations of titin stiffness has been linked to different forms of cardiomyopathies. In HCM, titin-dependent stiffness was increased (Herwig et al. 2020), while titin-dependent stiffness was lower in DCM (Nagueh et al. 2004). This indicates that *NRAP* loss-of-function might also result in decreased stiffness allowing to compensate higher mechanical stretch.

7.3.8 *NRAP/MYC*-OE and -KD enhance cardiomyopathy-related proteins

Proteome and subsequent bioinformatic KEGG pathway analysis of *NRAP/MYC*-OE and *NRAP*-KD revealed that both, gain- and loss-of-function lines were associated with over-representation of cardiomyopathy signalling pathways. Interestingly, this association was more pronounced in *NRAP/MYC*-OE EHTs compared to *NRAP*-KD EHTs, which showed a protein expression pattern more similar to control EHTs than to *NRAP/MYC*-OE EHTs.

Since higher and lower *NRAP* protein levels enhance cardiomyopathy-signalling pathways, this indicates that *NRAP* protein expression must be tightly controlled for proper functioning of cardiac myocytes. This is supported by similar observations that have been made upon modulation of the adherens junctional protein N-cadherin. Homozygous N-cadherin KO mice died early during embryonic development, whereas N-cadherin overexpressing transgenic mice developed a DCM phenotype (Ferreira-Cornwell et al. 2002; Radice et al. 1997). In a different study, either KO mice with a deletion of ventricular adherens junctional protein β -catenin or β -catenin-overexpressing mice with a non-degradable form of β -catenin by removal of phosphorylation sites were generated. The β -catenin overexpressing mice developed DCM with premature death at the age of 6 months and displayed enhanced *NRAP* expression, but not other intercalated disc proteins (Hirschy et al. 2010). The KO mice did not show overt phenotypically alterations in contrast to other mouse models such as cardiac-specific KO of vinculin or α -E-catenin, that resulted in DCM or sudden cardiac death (Sheikh et al. 2006; Zemljic-Harpf et al. 2007).

In addition, *NRAP/MYC*-OE EHTs showed increased protein abundance of MYH7, RYR2 and higher abundant proteins association with mitochondria, which has also been linked to maturation of cardiac myocytes (Guo and Pu 2020). However, *NRAP/MYC*-OE EHTs concomitantly showed increased protein levels of slow skeletal troponin I (TNNI1) that has been associated with immaturity of cardiac myocytes (Hunkeler et al. 1991). During

cardiac myocyte maturation, a switch from the TNNI1 isoform to the TNNI3 isoform has been reported (Guo and Pu 2020; Hunkeler et al. 1991). However, TNNI3 was not detected in *NRAP/MYC-OE* EHTs and instead significantly lower abundant in *NRAP-KD* EHTs. Moreover, *NRAP-KD* EHTs were associated with MYH6 instead of MYH7, suggesting an immaturity of *NRAP-KD* EHTs (Guo and Pu 2020). Due to the representation of mixed features of immature and mature cardiac myocytes in *NRAP/MYC-OE*, NRAP gain-of-function might enhance maturation since NRAP was also translocated towards the lateral borders of hiPSC-derived cardiac myocytes, which occurs during the maturation process of cardiac myocytes.

Overall, this indicates the importance of a tight protein expression control of intercalated disc proteins within cardiac myocytes, and that impaired control mechanisms might result in pathophysiological phenotypes. In this work, NRAP gain-of-function had a more severe impact on cardiac myocyte function than NRAP loss-of-function. However, both NRAP gain- and loss-of-function resulted in pathophysiological phenotypes indicating that molecular control mechanisms governing protein composition in critical microdomains in the cell are required to balance the physiological NRAP protein levels. Thus far, it remains elusive how physiological NRAP levels might be regulated and how dysfunctional regulation leads to the progression of cardiac disease.

7.4 PKD-mediated regulation in the developing and diseased heart

7.4.1 Impact of PKD inhibition on NRAP expression and phosphorylation

Since NRAP was identified as a putative substrate or interaction partner of PKD1 (unpublished data from the publication Haworth et al. 2004) and PKD1 has been identified as a central signalling hub controlling fetal and hypertrophic gene expression (Avkiran et al. 2008), the direct impact of PKD1 activity on NRAP expression, localisation and phosphorylation was investigated by using BPKDi, a pharmacological PKD inhibitor. This inhibitor has been shown to prevent PKD autophosphorylation efficiently, thus inhibiting its activation and downstream HDAC5 phosphorylation upon GPCR stimulation by endothelin-1 and PE (Monovich et al. 2010; Stathopoulou et al. 2014). BPKDi selectively inhibits PKD1 with an IC_{50} of 1 nM leading to abolished PKD1 levels upon exposure to 1 μ M of the inhibitor (Monovich et al. 2010).

The Inhibition of PKD activity significantly decreased NRAP protein expression suggesting that PKD1 is involved at least in the regulation of NRAP expression. PKD1 has been shown to promote fetal and hypertrophic gene transcription by phosphorylation of HDAC5 (Vega et al. 2004). The latter results in the nuclear export of HDAC5 and thus the

disinhibition of MEF2-regulated gene transcription (**Figure 64 A**; Lu et al. 2000). MEF2 has been described as a crucial transcription factor in the cardiac gene program during embryogenesis and cardiac hypertrophy (Akazawa and Komuro 2003). Hypertrophic gene expression can be induced by the GPCR agonist PE that promotes activation of the PKD1/HDAC5/MEF2 signalling axis (Simsek Papur et al. 2018). Since exposure of NRVMs to PE increased NRAP protein abundance but not when PKD activity was inhibited, strongly suggests that NRAP expression might be regulated by PKD1 via the HDAC5/MEF2 axis (**Figure 64 A, B**). However, another study identified the transcription factor Prox1 to induce *Nrap* transcription while cardiac-specific *Prox1* KO mice displaying reduced *Nrap* expression (Risebro et al. 2009). Prox1 is important in the maintenance and maturation of cardiac myocytes but not during the initial stages of myofibrillogenesis since at that stage no phenotypic defects are observed in cardiac-specific *Prox1* KO mice (Risebro et al. 2009). This suggests a differential regulation of *NRAP* expression in the fetal and maturing heart.

Since PKD1 has been shown to impact contractile function by phosphorylation of myofilament proteins (Cuello et al. 2007; Haworth et al. 2004), posttranslational modifications of NRAP were investigated. Immunoprecipitated NRAP from NRVMs, that had been pre-exposed to BPKDi and/or PE, was investigated by western immunoblotting. NRAP was detected in the immunoprecipitated fractions but no phosphorylation of NRAP was detectable using a pan-pSer/THr antibody. Recently, the *Nrap* isoform 3 was shown to be phosphorylated at a serine in the protein at position 1450 in a DCM mouse model with arginine to cysteine transition at residue 9 in phospholamban (Kuzmanov et al. 2016). Therefore, the failure to detect NRAP phosphorylation in our experiments could be a limitation of the antibody in detecting phosphorylated NRAP, as these antibodies often only detect a selection of highly abundant proteins that are phosphorylated at multiple sites (Murray et al. 2013). To overcome this issue, NRVMs were pre-treated with PE to activate PKD1 with or without BPKDi. The samples are currently analysed by unbiased phosphoproteomic analysis. This will allow to identify if PKD1 directly impacts NRAP phosphorylation.

7.4.2 NRAP translocation in response to modulation of PKD protein level

Localisation studies of NRAP revealed an association with a punctuate-appearing α -actinin structure in control NRVMs with increasing parallel alignment of myofilaments and Z-discs during the time in culture. The punctuate structure of α -actinin and association with NRAP has been previously described in the developing chicken heart (Ehler et al. 1999; Manisastry et al. 2009). However, transduction with a PKD-overexpressing virus

enhanced myofilament maturation as indicated by parallel aligned myofilaments and NRAP translocation towards lateral borders of cardiac myocytes. This might occur by promoting the HDAC5/MEF2-dependent pro-hypertrophic gene expression. Additional pro-hypertrophic stimulation resulted in vacuole-like stainings for NRAP. Since PKD has been shown to regulate the vesicular transport from the trans-Golgi network to membranes (Hausser et al. 2005; Wakana and Campelo 2021) and immunofluorescence revealed staining of NRAP in close proximity to the Golgi marker, an explanation might be a more general role for PKD in the regulation of cargo transport that also impacts translocation of NRAP.

In contrast, pro-hypertrophic stimulation of NRVMs with PE alone resulted in initial NRAP localisation along actin fibres after 24 h of treatment and redistribution of NRAP towards the lateral cell borders over time. Exposure to PE might enhance hypertrophic growth and maturation since cardiac myocytes switch from hyperplastic growth to hypertrophic growth during maturation (Hirschy et al. 2006). During the mouse heart development, NRAP is initially associated with premyofibril structures and translocates to Z-discs and M-bands during the maturation process (Lu et al. 2005). In the adult mouse heart, NRAP was absent from sarcomeres and exclusively located at the intercalated discs (Lu et al. 2005). Investigation of lateral intercalated disc width showed a trend towards wider intercalated discs after exposure to PE or longer culture times in the EHT format. In MLP-null mice that develop a DCM phenotype wider intercalated disc were measured after 6 months of age compared to control mice although during the age-dependent maturation process a general increase in intercalated disc width was determined (Wilson et al. 2014).

Exposure of NRVMs to BPKDi resulted in perinuclear, punctate accumulation of NRAP while additional exposure to PE led to myofibrillar rupture with NRAP accumulation close to the disrupted areas indicating a regulatory role for PKD1 in NRAP localisation via impacting on cargo transport (**Figure 64 B**). Interestingly, this disrupted myofibril structure was additionally observed in early-treated but not in late-treated NRVMs-derived EHTs. In accordance with this, a previous study showed myofibril disruption of hiPSC-derived cardiac myocytes upon overstretching with 35 kPa stiff substrates (Ribeiro et al. 2015). This suggests that the myofibril disruption in BPKDi-treated NRVMs might occur due to an impaired ability to compensate for the hypertrophic growth induced by PE. Since this impairment only occurred during early treatments but not after late treatments define again early and late, this highlights a crucial role for PKD1 in embryogenesis and myofibrillogenesis.

7.4.3 PKD negatively impacts contractile force

To investigate the underlying mechanisms of myofibril disruption and structural alterations upon PKD inhibition in the developing and diseased heart, contractile properties were investigated in early- and late-treated NRVMs-derived EHTs. Inhibition of PKD increased force while the exposure to the pro-hypertrophic stimulus PE only enhanced force in late-treated EHTs but not during the early treatment. Upon pathological stress, compensatory mechanisms such as increasing cell size, alterations in sarcomeres to increase contractility and the fetal gene transcription are activated (Chien 1999; Marks 2003). Previously, the homozygous loss-of-function of *Prkd1* in mice was shown to result in embryonic lethality (Fielitz et al. 2008), supporting a crucial role for PKD1 during embryogenesis. However, in accordance with increased contractile force upon inhibition of PKD activity, the phenotype of cardiac myocyte-specific *Prkd1*-KO mice represented less hypertrophy, fibrosis and fetal gene expression in response to pressure overload (Fielitz et al. 2008). Additionally, reducing PKD protein abundance by siRNA-mediated silencing improved cardiac hypertrophy and dysfunction in mice by increasing autophagy (Zhao et al. 2017).

Due to the continuous energy demand of cardiac myocytes to enable actin-myosin cross bridge cycling, functional mitochondria are invaluable representing the power stations in cardiac myocytes. The mitochondrial shape and maintenance is continuously altered upon various stimuli and regulated by the fission and fusion of mitochondria (Galloway et al. 2012). The shape maintenance is important for appropriate function upon (patho)physiological conditions and abnormal balance results in ROS production (Yu et al. 2008). The exposure of NRVMs-derived EHTs to the pro-hypertrophic stimulus PE led to mitochondria enlargement. Alterations in mitochondrial morphology have been previously observed upon induction of cardiac hypertrophy (Xue et al. 2019; Yang et al. 2022).

Interestingly, the inhibition of PKD resulted in alteration of mitochondrial shape in NRVMs-derived cardiac myocytes and EHTs independently of the treatment time point. Recently a study showed that PKD activation upon α -adrenergic stimulation leads to phosphorylation of the dynamin-like protein 1 (DLP1) resulting in mitochondrial fragmentation and ROS production (Jhun et al. 2018). Controversially, the opposite was recently shown by other groups. According to their findings, PKD regulates RhoA which induces mitophagy and prevent apoptosis (Brand et al. 2018; Tu et al. 2022). Altogether, these studies suggests an important role of PKD in mitochondrial homeostasis.

7.4.4 Involvement of PKD1 in degradational pathways

Investigation of the underlying mechanisms of PKD-mediated regulation of NRAP showed by KEGG pathway analysis that PKD inhibition results in an increase of degradation pathways and processes and proteins related to the Golgi and ER network. The highest abundant proteins were related to the coat protein complex II (COPII) which is involved in vesicle transport from the ER to the Golgi network or ERCIC (Barlowe et al. 1994). PKD1 was previously linked to trafficking processes from the trans-Golgi network to the plasma membrane (Hausser et al. 2005). Since translocation of NRAP occurred similarly to altered Golgi staining upon pharmacological PKD inhibition, PKD might impact NRAP localisation by affecting vesicle trafficking. Accordingly, Vamp5 was identified as the top lower abundant protein which has been shown to be involved in membrane trafficking of vesicles and localisation at intercalated discs (Takahashi et al. 2013).

Consistent with previous findings of abnormal mitochondrial structures in BPKDi-treated NRVMs-derived EHTs, top higher and lower abundant proteins upon BPKDi stimulation were associated with mitochondrial proteins. Among the top lower abundant proteins were proteins relating to the proteasome system. PKD1 phosphorylates HDAC5 which leads to its export and thereby to a derepression of the TFEB-mediated expression of MuRF1 which is involved in UPS-mediated degradation (Pablo Tortola et al. 2020). In addition, MurF1/2 has been shown to target NRAP for ubiquitination (**Figure 64 A**; Witt et al. 2005). Nedd8 was identified as one of the top lower abundant proteins which has a crucial role in activation and function of ubiquitination (Baek et al. 2020).

However, pro-hypertrophic and α -adrenergic stimulation with PE increased protein abundance related to cardiomyopathies, cardiac muscle contraction, spliceosome and RNA transport. Previous studies suggested the involvement of splicing in cardiomyopathies (Watanabe et al. 2018) and regulation of this process through RNA interaction with the transcription factor GATA4 (Zhu et al. 2022). Although heterogenous expression of higher and lower abundant proteins, some of the higher abundant proteins were related to transcriptional and translational processes. This might occur due to activation of the HDAC5/MEF2-mediated pro-hypertrophic gene expression. Additional exposure to the β -adrenergic stimulus ISO increased protein abundance related to protein processing in the ER and actin cytoskeleton. PKD has been shown to regulate actin remodelling by directly interacting with F-actin (Eiseler et al. 2007).

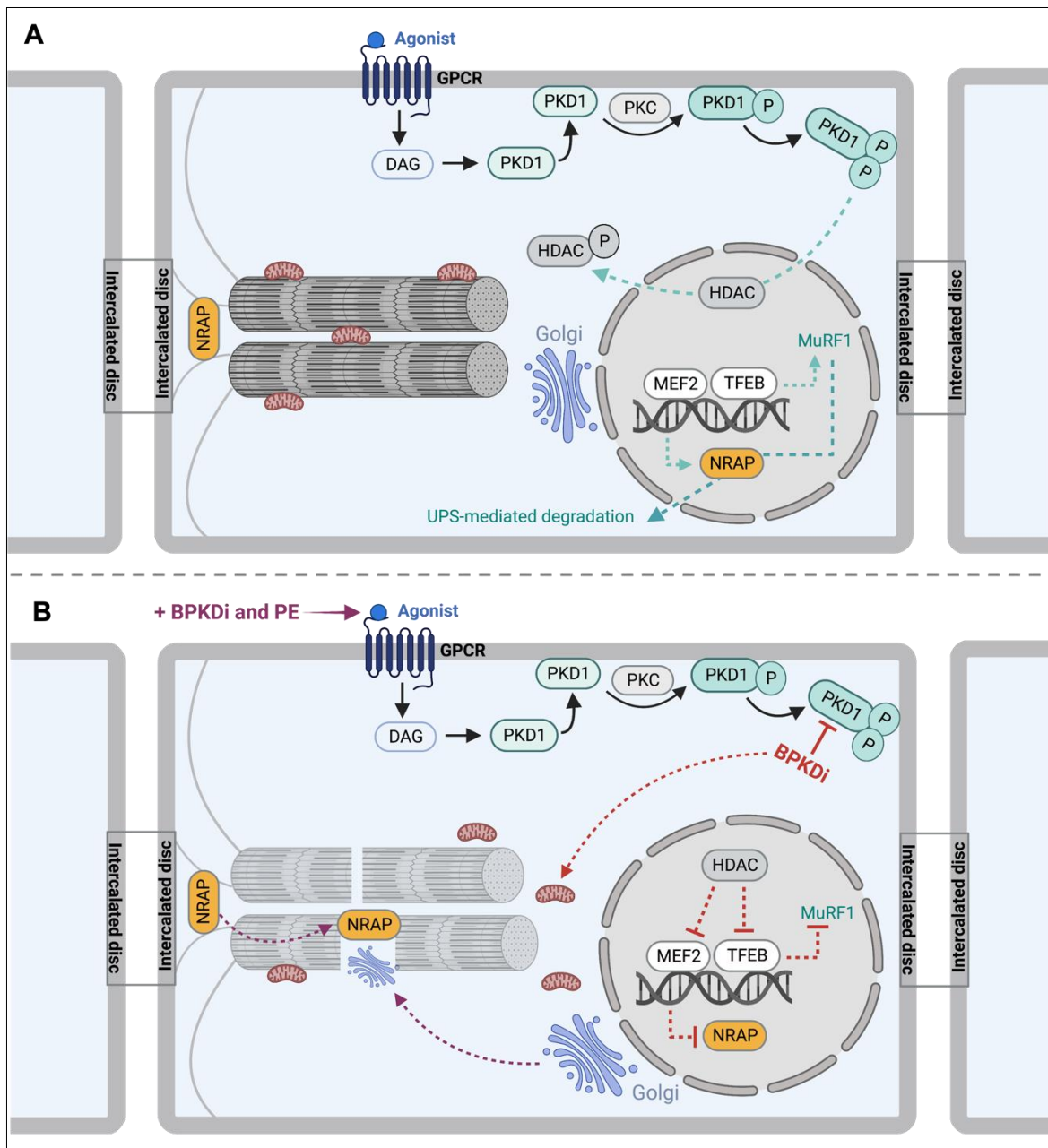


Figure 64: Schematic overview of hypothesised PKD1 and NRAP signalling. A) PKD1 signalling at physiological conditions. Upon G-protein coupled receptor (GPCR) activation, diacylglycerol (DAG) binds cytosolic PKD1 leading to PKD1 translocation to the membrane where it is first phosphorylated by protein kinase C (PKC) and then autophosphorylated. Activated PKD1 phosphorylates histone deacetylases (HDAC) leading to their export into the cytosol and a derepression of the myocyte enhancer factor 2 (MEF2) or the transcription factor EB (TFEB) dependent gene transcription. **B)** Hypothesised regulation of NRAP by PKD1. Inhibition with the PKD inhibitor BPKDi results in HDAC-dependent repression of MEF2 and TFEB gene expression and thus NRAP and muscle ring finger protein 1 (MuRF1) expression. MuRF1 has been shown to target NRAP for degradation by the ubiquitine proteasome system (UPS). Moreover, altered mitochondria localisation has been observed upon PKD inhibition. Additional pro-hypertrophic stimulation with phenylephrine (PE) resulted in sarcomere disrupture with accumulation of NRAP and Golgi staining within the disrupted areas. This illustration was generated with BioRender.

Discussion

However, the combined exposure to BPKDi and PE revealed a mixed phenotype of pathways involved in BPKDi exposure and pathways involved in PE stimulation. Interestingly, the combined exposure to PE and BPKDi or exposure to only BPKDi enhanced protein abundance of prostaglandin E synthase 3 (PTGES3) which mediates prostaglandin E2 (PGE2) production (Nakatani and Kudo 2008). Prostaglandin E2 has been linked to inflammation and additionally shown to induce MEF2 activation and thereby linking inflammation to cardiac remodeling (Tóth et al. 2018).

8. Conclusion

In conclusion, the results showed that both, NRAP gain- and loss-of-function results has pathophysiological consequences. Assessment of *NRAP/MYC*-OE cardiac myocytes and EHTs resulted in decreased contractile force and relaxation time, NRAP translocation towards intercalated discs, and less negative TOP and diastolic membrane potentials. Moreover, increased abundance of cardiomyopathy-related and metabolic proteins was detectable that was combined with the inability to compensate changes in mechanical stretch. In contrast, *NRAP*-KD EHTs responded to mechanical stretch with increased force production, but also showed increased abundance of cardiomyopathy-related proteins, lower contractile force and relaxation time. Overall, the *NRAP*-KD phenotype resembled the control group more than the *NRAP/MYC*-OE. This suggests that both, NRAP gain- and loss-of-function lead to cardiac disease progression with a more severe impact of *NRAP/MYC*-OE than *NRAP*-KD. This indicates that tight control of a physiological NRAP abundance is a prerequisite for cardiac health and that modulation of NRAP levels in either direction consequently promote cardiac disease development.

In order to investigate, which factors and pathways might regulate the switch from physiological to pathophysiological NRAP expression, the regulation of NRAP was investigated by studying its relation to PKD1 which represents a central hub in fetal and hypertrophic signalling via regulation of the HDAC5/MEF2 signalling axis. This revealed a PKD1-mediated regulation of NRAP expression and localisation with functional consequences. However, in order to identify whether PKD1 directly targets NRAP, it is required to investigate posttranslational modifications of NRAP. To identify PKD1 phosphorylation targets, a phosphoproteome analysis is currently in progress. The outcome will further our knowledge about the role of PKD1 and the regulatory mechanisms governing NRAP expression in health and disease.

9. Further perspectives

In this thesis, *NRAP/MYC-OE* and *NRAP-KD* lines were successfully generated and basally characterised. In order to overcome the impact of batch-to-batch variability and reliably demonstrate the impact of *NRAP-OE* and *-KD* on contractile parameters, inclusion of data from more EHT batches is required. The impact on electrophysiological parameters will further be investigated by analysing the impact of sodium and potassium channels and currents by patch-clamp analysis in *NRAP/MYC-OE* EHTs.

Already the physiological assessment of *NRAP* gain- and loss-of-function resulted in dramatic functional differences. Therefore, the functional and structural consequences of increased mechanical stretch will be investigated in EHTs. For this purpose, the silicon posts, on which the EHTs are attached at both ends can be stepwise increased in their stiffness and thereby allow to increase the mechanical resistance against which the EHTs have to beat, so called afterload enhancement. In order to investigate additionally the contributing role of *NRAP* to cardiac disease progression, pathophysiological conditions can be mimicked by a combined exposure to the pro-hypertrophic stimuli PE and endothelin-1.

Moreover, the impact of mechanical stretch on structural alterations of cardiac myocytes will be assessed in a two-dimensional format. Therefore, cardiac myocytes will be cultured on different coatings of varying stiffness by modulating the ratio between acrylamide and bisacrylamide. Structurally, cell size, myofilament structure and formation of intercalated discs in *NRAP/MYC-OE* and *NRAP-KD* will be analysed. Potential alterations in ID organisation will be determined by using stimulated emission depletion (STED) super-resolution and alterations in cellular stiffness by applying atomic force measurements.

In order to further study how the expression and localisation of *NRAP* is regulated, the phosphoproteome that is currently underway will allow to identify phosphorylation targets of PKD1 and to inform whether *NRAP* is a direct phosphorylation target of PKD1. Since not only *NRAP* might be regulated by the HDAC5/MEF2 axis, but also MuRFs have been shown to be regulated by the PKD1/HDAC5/TFEB signalling axis, which might be involved in *NRAP* degradation, the link between proteasomal degradation of *NRAP* by MuRFs will be investigated. This will be performed by studying the localisation and expression in modulated *NRAP/MYC-OE* and *NRAP-KD* hiPSC-derived cardiac myocytes and in *MuRF1/3*-double-KO mice. This will enhance the knowledge about *NRAP* stability and regulation and how this regulation might contribute to cardiac disease progression.

Further perspectives

Moreover, NRAP has been shown to be essential in the regulation of myofibrillogenesis. Therefore, the successfully generated *NRAP/GFP*-OE hiPSC line will be differentiated to cardiac myocytes to track the GFP-tagged NRAP by live cell imaging. Further, dynamic properties of the GFP-tagged NRAP will be analysed by using fluorescence recovery after photobleaching (FRAP) to assess the contribution of NRAP to *de novo* myofibrillogenesis as well as upon exposure to pathophysiological stress such as exposure to combined PE and endothelin-1.

The outcome is anticipated to further identify the specific functional role of NRAP during the cardiac myocyte response to mechanical stress and how the regulation of NRAP contributes to the pathophysiological development of cardiac disease.

10. References

- Aasen T, Raya A, Barrero MJ, Garreta E, Consiglio A, Gonzalez F, Vassena R, Bilić J, Pekarik V, Tiscornia G, Edel M, Boué S, Izpisua Belmonte JC (2008) Efficient and rapid generation of induced pluripotent stem cells from human keratinocytes. *Nat Biotechnol* 26(11):1276-84.
- Ahmed RE, Tokuyama T, Anzai T, Chanthra N, Uosaki H (2022) Sarcomere maturation: function acquisition, molecular mechanism, and interplay with other organelles. *Philos Trans R Soc Lond B Biol Sci* 377(1864):20210325.
- Akazawa H, Komuro I (2003) Roles of cardiac transcription factors in cardiac hypertrophy. *Circ Res* 92(10):1079-88.
- Alfares AA, Kelly MA, McDermott G, Funke BH, Lebo MS, Baxter SB, Shen J, McLaughlin HM, Clark EH, Babb LJ, Cox SW, DePalma SR, Ho CY, Seidman JG, Seidman CE, Rehm HL (2015) Results of clinical genetic testing of 2,912 probands with hypertrophic cardiomyopathy: expanded panels offer limited additional sensitivity. *Genet Med* 17(11):880-8.
- Anastasi G, Cutroneo G, Gaeta R, Di Mauro D, Arco A, Consolo A, Santoro G, Trimarchi F, Favalaro A (2009) Dystrophin-glycoprotein complex and vinculin-talin-integrin system in human adult cardiac muscle. *Int J Mol Med* 23(2):149-59.
- Anders S, Pyl PT, Huber W (2015) HTSeq--a Python framework to work with high-throughput sequencing data. *Bioinformatics* 31(2):166-9.
- Anderson CA, Kovar DR, Gardel ML, Winkelman JD (2021) LIM domain proteins in cell mechanobiology. *Cytoskeleton (Hoboken)* 78(6):303-311.
- Aoi T, Yae K, Nakagawa M, Ichisaka T, Okita K, Takahashi K, Chiba T, Yamanaka S (2008) Generation of pluripotent stem cells from adult mouse liver and stomach cells. *Science* 321(5889):699-702.
- Ascoli CA, Aggeler B (2018) Overlooked benefits of using polyclonal antibodies. *BioTechniques* 65(3):127-136.
- Avkiran M, Rowland AJ, Cuello F, Haworth RS (2008) Protein kinase d in the cardiovascular system: emerging roles in health and disease. *Circ Res* 102(2):157-63.
- Baek K, Krist DT, Prabu JR, Hill S, Klügel M, Neumaier LM, von Gronau S, Kleiger G, Schulman BA (2020) NEDD8 nucleates a multivalent cullin-RING-UBE2D ubiquitin ligation assembly. *Nature* 578(7795):461-466.
- Balaban RS, Nemoto S, Finkel T (2005) Mitochondria, oxidants, and aging. *Cell* 120(4):483-95.
- Balsa E, Marco R, Perales-Clemente E, Szklarczyk R, Calvo E, Landázuri MO, Enríquez JA (2012) NDUFA4 is a subunit of complex IV of the mammalian electron transport chain. *Cell Metab* 16(3):378-86.
- Bang ML, Bogomolovas J, Chen J (2022) Understanding the molecular basis of cardiomyopathy. *Am J Physiol Heart Circ Physiol* 322(2):H181-h233.
- Barlowe C, Orci L, Yeung T, Hosobuchi M, Hamamoto S, Salama N, Rexach MF, Ravazzola M, Amherdt M, Schekman R (1994) COPII: a membrane coat formed by Sec proteins that drive vesicle budding from the endoplasmic reticulum. *Cell* 77(6):895-907.

References

- Barrangou R, Fremaux C, Deveau H, Richards M, Boyaval P, Moineau S, Romero DA, Horvath P (2007) CRISPR provides acquired resistance against viruses in prokaryotes. *Science* 315(5819):1709-12.
- Barth E, Stämmler G, Speiser B, Schaper J (1992) Ultrastructural quantitation of mitochondria and myofilaments in cardiac muscle from 10 different animal species including man. *J Mol Cell Cardiol* 24(7):669-81.
- Basso C, Thiene G, Corrado D, Angelini A, Nava A, Valente M (1996) Arrhythmogenic right ventricular cardiomyopathy. Dysplasia, dystrophy, or myocarditis? *Circulation* 94(5):983-91.
- Bays JL, Peng X, Tolbert CE, Guilluy C, Angell AE, Pan Y, Superfine R, BurrIDGE K, DeMali KA (2014) Vinculin phosphorylation differentially regulates mechanotransduction at cell-cell and cell-matrix adhesions. *J Cell Biol* 205(2):251-63.
- Beerman I, Seita J, Inlay MA, Weissman IL, Rossi DJ (2014) Quiescent hematopoietic stem cells accumulate DNA damage during aging that is repaired upon entry into cell cycle. *Cell Stem Cell* 15(1):37-50.
- Beisaw A, Wu C-C (2022) Cardiomyocyte maturation and its reversal during cardiac regeneration. *Dev. Dyn.* 1-20.
- Bennett PM (2012) From myofibril to membrane; the transitional junction at the intercalated disc. *FBL* 17(3):1035-1050.
- Bennett PM, Ehler E, Wilson AJ (2016) Sarcoplasmic reticulum is an intermediary of mitochondrial and myofibrillar growth at the intercalated disc. *J. Muscle Res. Cell Motil* 37(3):55-69.
- Bennett PM, Maggs AM, Baines AJ, Pinder JC (2006) The transitional junction: a new functional subcellular domain at the intercalated disc. *Mol Biol Cell* 17(4):2091-100.
- Berger J, Berger S, Li M, Jacoby AS, Arner A, Bavi N, Stewart AG, Currie PD (2018) In Vivo Function of the Chaperonin TRiC in α -Actin Folding during Sarcomere Assembly. *Cell Rep* 22(2):313-322.
- Bergmann O, Bhardwaj RD, Bernard S, Zdunek S, Barnabé-Heider F, Walsh S, Zupicich J, Alkass K, Buchholz BA, Druid H, Jovinge S, Frisén J (2009) Evidence for cardiomyocyte renewal in humans. *Science* 324(5923):98-102.
- Borrmann CM, Grund C, Kuhn C, Hofmann I, Pieperhoff S, Franke WW (2006) The area composita of adhering junctions connecting heart muscle cells of vertebrates. II. Colocalizations of desmosomal and fascia adhaerens molecules in the intercalated disk. *Eur J Cell Biol* 85(6):469-85.
- Bossuyt J, Borst JM, Verberckmoes M, Bailey LRJ, Bers DM, Hegyi B (2022) Protein Kinase D1 Regulates Cardiac Hypertrophy, Potassium Channel Remodeling, and Arrhythmias in Heart Failure. *J Am Heart Assoc* 11(19):e027573.
- Bossuyt J, Chang CW, Helmstadter K, Kunkel MT, Newton AC, Campbell KS, Martin JL, Bossuyt S, Robia SL, Bers DM (2011) Spatiotemporally distinct protein kinase D activation in adult cardiomyocytes in response to phenylephrine and endothelin. *J Biol Chem* 286(38):33390-400.
- Brand CS, Tan VP, Brown JH, Miyamoto S (2018) RhoA regulates Drp1 mediated mitochondrial fission through ROCK to protect cardiomyocytes. *Cell Signal* 50:48-57.
- Braunwald E, Morrow AG, Cornell WP, Aygen MM, Hilbish TF (1960) Idiopathic hypertrophic subaortic stenosis: Clinical, hemodynamic and angiographic manifestations. *Am J Med* 29(6):924-945.

References

- Breckwoldt K, Letuffe-Breniere D, Mannhardt I, Schulze T, Ulmer B, Werner T, Benzin A, Klampe B, Reinsch MC, Laufer S, Shibamiya A, Prondzynski M, Mearini G, Schade D, Fuchs S, Neuber C, Kramer E, Saleem U, Schulze ML, Rodriguez ML, Eschenhagen T, Hansen A (2017) Differentiation of cardiomyocytes and generation of human engineered heart tissue. *Nat Protoc* 12(6):1177-1197.
- Broussard JA, Getsios S, Green KJ (2015) Desmosome regulation and signaling in disease. *Cell Tissue Res* 360(3):501-12.
- Buenrostro JD, Giresi PG, Zaba LC, Chang HY, Greenleaf WJ (2013) Transposition of native chromatin for fast and sensitive epigenomic profiling of open chromatin, DNA-binding proteins and nucleosome position. *Nat Methods* 10(12):1213-8.
- Burridge PW, Keller G, Gold JD, Wu JC (2012) Production of de novo cardiomyocytes: human pluripotent stem cell differentiation and direct reprogramming. *Cell Stem Cell* 10(1):16-28.
- Busuttill RA, Rubio M, Dollé ME, Campisi J, Vijg J (2003) Oxygen accelerates the accumulation of mutations during the senescence and immortalization of murine cells in culture. *Aging Cell* 2(6):287-94.
- Byrne SM, Ortiz L, Mali P, Aach J, Church GM (2015) Multi-kilobase homozygous targeted gene replacement in human induced pluripotent stem cells. *Nucleic Acids Res* 43(3):e21.
- Calderon D, Bardot E, Dubois N (2016) Probing early heart development to instruct stem cell differentiation strategies. *Dev Dyn* 245(12):1130-1144.
- Calore M, Lorenzon A, De Bortoli M, Poloni G, Rampazzo A (2015) Arrhythmogenic cardiomyopathy: a disease of intercalated discs. *Cell and Tissue Research* 360(3):491-500.
- Campisi J (2011) Cellular senescence: putting the paradoxes in perspective. *Curr Opin Genet Dev* 21(1):107-12.
- Carlisle C, Prill K, Pilgrim D (2017) Chaperones and the Proteasome System: Regulating the Construction and Demolition of Striated Muscle. *Int J Mol Sci* 19(1).
- Carra S, Seguin SJ, Landry J (2008) HspB8 and Bag3: a new chaperone complex targeting misfolded proteins to macroautophagy. *Autophagy* 4(2):237-9.
- Carroll S, Lu S, Herrera AH, Horowitz R (2004) N-RAP scaffolds I-Z-I assembly during myofibrillogenesis in cultured chick cardiomyocytes. *J Cell Sci* 117(Pt 1):105-14.
- Carroll SL, Horowitz R (2000) Myofibrillogenesis and formation of cell contacts mediate the localization of N-RAP in cultured chick cardiomyocytes. *Cell Motil Cytoskeleton* 47(1):63-76.
- Casey JG, Kim ES, Joseph R, Li F, Granzier H, Gupta VA (2023) NRAP reduction rescues sarcomere defects in nebulin-related nemaline myopathy. *Hum. Mol. Genet.* 32(10):1711-1721.
- Chen J, Nekrasova OE, Patel DM, Klessner JL, Godsel LM, Koetsier JL, Amargo EV, Desai BV, Green KJ (2012) The C-terminal unique region of desmoglein 2 inhibits its internalization via tail-tail interactions. *J Cell Biol* 199(4):699-711.
- Chereau D, Boczkowska M, Skwarek-Maruszewska A, Fujiwara I, Hayes DB, Rebowski G, Lappalainen P, Pollard TD, Dominguez R (2008) Leiomodin is an actin filament nucleator in muscle cells. *Science* 320(5873):239-43.
- Cheung TH, Rando TA (2013) Molecular regulation of stem cell quiescence. *Nat Rev Mol Cell Biol* 14(6):329-40.
- Chien KR (1999) Stress Pathways and Heart Failure. *Cell* 98(5):555-558.

References

- Choi HJ, Gross JC, Pokutta S, Weis WI (2009) Interactions of plakoglobin and beta-catenin with desmosomal cadherins: basis of selective exclusion of alpha- and beta-catenin from desmosomes. *J Biol Chem* 284(46):31776-88.
- Chu M, Gregorio CC, Pappas CT (2016) Nebulin, a multi-functional giant. *J Exp Biol* 219(Pt 2):146-52.
- Ciarambino T, Menna G, Sansone G, Giordano M (2021) Cardiomyopathies: An Overview. *Int J Mol Sci* 22(14).
- Cuello F, Bardswell SC, Haworth RS, Yin X, Lutz S, Wieland T, Mayr M, Kentish JC, Avkiran M (2007) Protein kinase D selectively targets cardiac troponin I and regulates myofilament Ca²⁺ sensitivity in ventricular myocytes. *Circ Res* 100(6):864-73.
- D'Avila F, Meregalli M, Lupoli S, Barcella M, Orro A, De Santis F, Sitzia C, Farini A, D'Ursi P, Erratico S, Cristofani R, Milanesi L, Braga D, Cusi D, Poletti A, Barlassina C, Torrente Y (2016) Exome sequencing identifies variants in two genes encoding the LIM-proteins NRAP and FHL1 in an Italian patient with BAG3 myofibrillar myopathy. *J Muscle Res Cell Motil* 37(3):101-15.
- De Masi C, Spitalieri P, Murdocca M, Novelli G, Sangiuolo F (2020) Application of CRISPR/Cas9 to human-induced pluripotent stem cells: from gene editing to drug discovery. *Human Genomics* 14(1):25.
- Delmar M, McKenna WJ (2010) The Cardiac Desmosome and Arrhythmogenic Cardiomyopathies. *Circulation Research* 107(6):700-714.
- Di Lisa F, De Tullio R, Salamino F, Barbato R, Melloni E, Siliprandi N, Schiaffino S, Pontremoli S (1995) Specific degradation of troponin T and I by mu-calpain and its modulation by substrate phosphorylation. *Biochem J* 308(Pt 1):57-61.
- Dobin A, Davis CA, Schlesinger F, Drenkow J, Zaleski C, Jha S, Batut P, Chaisson M, Gingeras TR (2013) STAR: ultrafast universal RNA-seq aligner. *Bioinformatics* 29(1):15-21.
- Donald L, Lakatta EG (2023) What makes the sinoatrial node tick? A question not for the faint of heart. *Philos Trans R Soc Lond B Biol Sci* 378(1879):20220180.
- Doudna JA (2020) The promise and challenge of therapeutic genome editing. *Nature* 578(7794):229-236.
- Ehler E (2016) Cardiac cytoarchitecture - why the "hardware" is important for heart function! *Biochim Biophys Acta* 1863(7 Pt B):1857-63.
- Ehler E, Horowitz R, Zuppinger C, Price RL, Perriard E, Leu M, Caroni P, Sussman M, Eppenberger HM, Perriard JC (2001) Alterations at the intercalated disk associated with the absence of muscle LIM protein. *J Cell Biol* 153(4):763-72.
- Ehler E, Rothen BM, Hämmerle SP, Komiyama M, Perriard JC (1999) Myofibrillogenesis in the developing chicken heart: assembly of Z-disk, M-line and the thick filaments. *J Cell Sci* 112 (Pt 10):1529-39.
- Eiseler T, Schmid MA, Topbas F, Pfizenmaier K, Hausser A (2007) PKD is recruited to sites of actin remodelling at the leading edge and negatively regulates cell migration. *FEBS Lett* 581(22):4279-87.
- Elfgang C, Eckert R, Lichtenberg-Fraté H, Butterweck A, Traub O, Klein RA, Hülser DF, Willecke K (1995) Specific permeability and selective formation of gap junction channels in connexin-transfected HeLa cells. *J Cell Biol* 129(3):805-17.

References

- Eliasson P, Jönsson JI (2010) The hematopoietic stem cell niche: low in oxygen but a nice place to be. *J Cell Physiol* 222(1):17-22.
- Elliott PM, Anastasakis A, Borger MA, Borggrefe M, Cecchi F, Charron P, Hagege AA, Lafont A, Limongelli G, Mahrholdt H, McKenna WJ, Mogensen J, Nihoyannopoulos P, Nistri S, Pieper PG, Pieske B, Rapezzi C, Rutten FH, Tillmanns C, Watkins H (2014) 2014 ESC Guidelines on diagnosis and management of hypertrophic cardiomyopathy: the Task Force for the Diagnosis and Management of Hypertrophic Cardiomyopathy of the European Society of Cardiology (ESC). *Eur Heart J* 35(39):2733-79.
- Epifantseva I, Shaw RM (2018) Intracellular trafficking pathways of Cx43 gap junction channels. *Biochim Biophys Acta Biomembr* 1860(1):40-47.
- Fabiato A, Fabiato F (1978) Myofilament-generated tension oscillations during partial calcium activation and activation dependence of the sarcomere length-tension relation of skinned cardiac cells. *J Gen Physiol* 72(5):667-99.
- Ferreira-Cornwell MC, Luo Y, Narula N, Lenox JM, Lieberman M, Radice GL (2002) Remodeling the intercalated disc leads to cardiomyopathy in mice misexpressing cadherins in the heart. *J Cell Sci* 115(Pt 8):1623-34.
- Feuerstein R, Wang X, Song D, Cooke NE, Liebhaber SA (1994) The LIM/double zinc-finger motif functions as a protein dimerization domain. *Proc Natl Acad Sci USA* 91(22):10655-9.
- Fielitz J, Kim MS, Shelton JM, Qi X, Hill JA, Richardson JA, Bassel-Duby R, Olson EN (2008) Requirement of protein kinase D1 for pathological cardiac remodeling. *Proc Natl Acad Sci USA* 105(8):3059-63.
- Firket H (1967) Ultrastructural aspects of myofibrils formation in cultured skeletal muscle. *Zeitschrift für Zellforschung und Mikroskopische Anatomie* 78(3):313-327.
- Flenner F, Jungen C, Kúpker N, Ibel A, Kruse M, Koivumäki JT, Rinas A, Zech ATL, Rhoden A, Wijnker PJM, Lemoine MD, Steenpass A, Girdeuskas E, Eschenhagen T, Meyer C, van der Velden J, Patten-Hamel M, Christ T, Carrier L (2021) Translational investigation of electrophysiology in hypertrophic cardiomyopathy. *J Mol Cell Cardiol* 157:77-89.
- Forsyth NR, Musio A, Vezzone P, Simpson AH, Noble BS, McWhir J (2006) Physiologic oxygen enhances human embryonic stem cell clonal recovery and reduces chromosomal abnormalities. *Cloning Stem Cells* 8(1):16-23.
- Frank D, Frey N (2011) Cardiac Z-disc signaling network. *J Biol Chem* 286(12):9897-904.
- Fusaki N, Ban H, Nishiyama A, Saeki K, Hasegawa M (2009) Efficient induction of transgene-free human pluripotent stem cells using a vector based on Sendai virus, an RNA virus that does not integrate into the host genome. *Proc Jpn Acad Ser B Phys Biol Sci* 85(8):348-62.
- Gaj T, Guo J, Kato Y, Sirk SJ, Barbas CF (2012) Targeted gene knockout by direct delivery of zinc-finger nuclease proteins. *Nat Methods* 9(8):805-7.
- Galloway CA, Lee H, Yoon Y (2012) Mitochondrial morphology-emerging role in bioenergetics. *Free Radic Biol Med* 53(12):2218-28.
- Gamerding M, Hajieva P, Kaya AM, Wolfrum U, Hartl FU, Behl C (2009) Protein quality control during aging involves recruitment of the macroautophagy pathway by BAG3. *Embo J* 28(7):889-901.
- Gasiunas G, Barrangou R, Horvath P, Siksnyš V (2012) Cas9-crRNA ribonucleoprotein complex mediates specific DNA cleavage for adaptive immunity in bacteria. *Proc Natl Acad Sci USA* 109(39):E2579-86.

References

- Gehmlich K, Asimaki A, Cahill TJ, Ehler E, Syrris P, Zachara E, Re F, Avella A, Monserrat L, Saffitz JE, McKenna WJ (2010) Novel missense mutations in exon 15 of desmoglein-2: role of the intracellular cadherin segment in arrhythmogenic right ventricular cardiomyopathy? *Heart Rhythm* 7(10):1446-53.
- Gehmlich K, Geier C, Osterziel KJ, Van der Ven PF, Furst DO (2004) Decreased interactions of mutant muscle LIM protein (MLP) with N-RAP and alpha-actinin and their implication for hypertrophic cardiomyopathy. *Cell Tissue Res* 317(2):129-36.
- Gehmlich K, Syrris P, Reimann M, Asimaki A, Ehler E, Evans A, Quarta G, Pantazis A, Saffitz JE, McKenna WJ (2012) Molecular changes in the heart of a severe case of arrhythmogenic right ventricular cardiomyopathy caused by a desmoglein-2 null allele. *Cardiovasc Pathol* 21(4):275-82.
- Gokhin DS, Tierney MT, Sui Z, Sacco A, Fowler VM (2014) Calpain-mediated proteolysis of tropomodulin isoforms leads to thin filament elongation in dystrophic skeletal muscle. *Mol Biol Cell* 25(6):852-65.
- Granzier HL, Labeit S (2004) The giant protein titin: a major player in myocardial mechanics, signaling, and disease. *Circ Res* 94(3):284-95.
- Green KJ, Jaiganesh A, Broussard JA (2019) Desmosomes: Essential contributors to an integrated intercellular junction network. *F1000Res* 8.
- Guenther MG, Frampton GM, Soldner F, Hockemeyer D, Mitalipova M, Jaenisch R, Young RA (2010) Chromatin structure and gene expression programs of human embryonic and induced pluripotent stem cells. *Cell Stem Cell* 7(2):249-57.
- Guo Q, Mintier G, Ma-Edmonds M, Storton D, Wang X, Xiao X, Kienzle B, Zhao D, Feder JN (2018) 'Cold shock' increases the frequency of homology directed repair gene editing in induced pluripotent stem cells. *Sci. Rep.* 8(1):2080.
- Guo Y, Pu WT (2020) Cardiomyocyte Maturation. *Circ Res* 126(8):1086-1106.
- Hansen A, Eder A, Bonstrup M, Flato M, Mewe M, Schaaf S, Aksehirlioglu B, Schwoerer AP, Uebeler J, Eschenhagen T (2010) Development of a drug screening platform based on engineered heart tissue. *Circ Res* 107(1):35-44.
- Hausser A, Storz P, Märtens S, Link G, Toker A, Pfizenmaier K (2005) Protein kinase D regulates vesicular transport by phosphorylating and activating phosphatidylinositol-4 kinase III β at the Golgi complex. *Nat. Cell Biol* 7(9):880-886.
- Haworth RS, Cuello F, Herron TJ, Franzen G, Kentish JC, Gautel M, Avkiran M (2004) Protein kinase D is a novel mediator of cardiac troponin I phosphorylation and regulates myofilament function. *Circ Res* 95(11):1091-9.
- Heidler J, Strecker V, Csintalan F, Bleier L, Wittig I (2013) Quantification of protein complexes by blue native electrophoresis. *Methods Mol Biol* 1033:363-79.
- Henning RH, Brundel B (2017) Proteostasis in cardiac health and disease. *Nat Rev Cardiol* 14(11):637-653.
- Herman DS, Lam L, Taylor MR, Wang L, Teekakirikul P, Christodoulou D, Conner L, DePalma SR, McDonough B, Sparks E, Teodorescu DL, Cirino AL, Banner NR, Pennell DJ, Graw S, Merlo M, Di Lenarda A, Sinagra G, Bos JM, Ackerman MJ, Mitchell RN, Murry CE, Lakdawala NK, Ho CY, Barton PJ, Cook SA, Mestroni L, Seidman JG, Seidman CE (2012) Truncations of titin causing dilated cardiomyopathy. *N Engl J Med* 366(7):619-28.
- Hernandez-Segura A, Nehme J, Demaria M (2018) Hallmarks of Cellular Senescence. *Trends Cell Biol* 28(6):436-453.

References

- Herwig M, Kolijn D, Lódi M, Hölper S, Kovács Á, Papp Z, Jaquet K, Haldenwang P, Dos Remedios C, Reusch PH, Mügge A, Krüger M, Fielitz J, Linke WA, Hamdani N (2020) Modulation of Titin-Based Stiffness in Hypertrophic Cardiomyopathy via Protein Kinase D. *Front Physiol* 11:240.
- Hirschy A, Croquelois A, Perriard E, Schoenauer R, Agarkova I, Hoerstrup SP, Taketo MM, Pedrazzini T, Perriard JC, Ehler E (2010) Stabilised beta-catenin in postnatal ventricular myocardium leads to dilated cardiomyopathy and premature death. *Basic Res Cardiol* 105(5):597-608.
- Hirschy A, Schatzmann F, Ehler E, Perriard JC (2006) Establishment of cardiac cytoarchitecture in the developing mouse heart. *Dev Biol* 289(2):430-41.
- Horvath P, Barrangou R (2010) CRISPR/Cas, the immune system of bacteria and archaea. *Science* 327(5962):167-70.
- Houser SR, Margulies KB, Murphy AM, Spinale FG, Francis GS, Prabhu SD, Rockman HA, Kass DA, Molkentin JD, Sussman MA, Koch WJ (2012) Animal Models of Heart Failure. *Circ Res* 111(1):131-150.
- Hug N, Longman D, Cáceres JF (2016) Mechanism and regulation of the nonsense-mediated decay pathway. *Nucleic Acids Res* 44(4):1483-95.
- Humphries JD, Wang P, Streuli C, Geiger B, Humphries MJ, Ballestrem C (2007) Vinculin controls focal adhesion formation by direct interactions with talin and actin. *J Cell Biol* 179(5):1043-57.
- Hunkeler NM, Kullman J, Murphy AM (1991) Troponin I isoform expression in human heart. *Circ Res* 69(5):1409-14.
- Huo J, Kamalakar A, Yang X, Word B, Stockbridge N, Lyn-Cook B, Pang L (2016) Evaluation of Batch Variations in Induced Pluripotent Stem Cell-Derived Human Cardiomyocytes from 2 Major Suppliers. *Toxicol. Sci.* 156(1):25-38.
- Huxley AF, Niedergerke R (1954) Structural changes in muscle during contraction; interference microscopy of living muscle fibres. *Nature* 173(4412):971-3.
- Huxley H, Hanson J (1954) Changes in the Cross-Striations of Muscle during Contraction and Stretch and their Structural Interpretation. *Nature* 173(4412):973-976.
- Iglesias T, Waldron RT, Rozengurt E (1998) Identification of in Vivo Phosphorylation Sites Required for Protein Kinase D Activation*. *Journal of Biological Chemistry* 273(42):27662-27667.
- Ismaili D, Schulz C, Horváth A, Koivumäki JT, Mika D, Hansen A, Eschenhagen T, Christ T (2023) Human induced pluripotent stem cell-derived cardiomyocytes as an electrophysiological model: Opportunities and challenges-The Hamburg perspective. *Front Physiol* 14:1132165.
- Ito Y, Yoshida M, Masuda H, Maeda D, Kudo-Asabe Y, Umakoshi M, Nanjo H, Goto A (2021) Disorganization of intercalated discs in dilated cardiomyopathy. *Sci. Rep.* 11(1):11852.
- Jani K, Schöck F (2007) Zasp is required for the assembly of functional integrin adhesion sites. *J Cell Biol* 179(7):1583-97.
- Jhun BS, J OU, Adaniya SM, Mancini TJ, Cao JL, King ME, Landi AK, Ma H, Shin M, Yang D, Xu X, Yoon Y, Choudhary G, Clements RT, Mende U, Sheu SS (2018) Protein kinase D activation induces mitochondrial fragmentation and dysfunction in cardiomyocytes. *J Physiol* 596(5):827-855.
- Jinek M, Chylinski K, Fonfara I, Hauer M, Doudna JA, Charpentier E (2012) A programmable dual-RNA-guided DNA endonuclease in adaptive bacterial immunity. *Science* 337(6096):816-21.

References

- Jirka C, Pak JH, Grosogeat CA, Marchetii MM, Gupta VA (2019) Dysregulation of NRAP degradation by KLHL41 contributes to pathophysiology in nemaline myopathy. *Hum Mol Genet* 28(15):2549-2560.
- Johansen T, Lamark T (2011) Selective autophagy mediated by autophagic adapter proteins. *Autophagy* 7(3):279-96.
- Kadmas JL, Beckerle MC (2004) The LIM domain: from the cytoskeleton to the nucleus. *Nat Rev Mol Cell Biol* 5(11):920-31.
- Kaplan SR, Gard JJ, Protonotarios N, Tsatsopoulou A, Spiliopoulou C, Anastasakis A, Squarcioni CP, McKenna WJ, Thiene G, Basso C, Brousse N, Fontaine G, Saffitz JE (2004) Remodeling of myocyte gap junctions in arrhythmogenic right ventricular cardiomyopathy due to a deletion in plakoglobin (Naxos disease). *Heart Rhythm* 1(1):3-11.
- Kattman SJ, Witty AD, Gagliardi M, Dubois NC, Niapour M, Hotta A, Ellis J, Keller G (2011) Stage-specific optimization of activin/nodal and BMP signaling promotes cardiac differentiation of mouse and human pluripotent stem cell lines. *Cell Stem Cell* 8(2):228-40.
- Kharrazian D, Herbert M, Vojdani A (2020) Cross-Reactivity between Chemical Antibodies Formed to Serum Proteins and Thyroid Axis Target Sites. *Int J Mol Sci* 21(19).
- Kilpinen H, Goncalves A, Leha A, Afzal V, Alasoo K, Ashford S, Bala S, Bensaddek D, Casale FP, Culley OJ, Danecek P, Faulconbridge A, Harrison PW, Kathuria A, McCarthy D, McCarthy SA, Meleckyte R, Memari Y, Moens N, Soares F, Mann A, Streeter I, Agu CA, Alderton A, Nelson R, Harper S, Patel M, White A, Patel SR, Clarke L, Halai R, Kirton CM, Kolb-Kokocinski A, Beales P, Birney E, Danovi D, Lamond AI, Ouwehand WH, Vallier L, Watt FM, Durbin R, Stegle O, Gaffney DJ (2017) Common genetic variation drives molecular heterogeneity in human iPSCs. *Nature* 546(7658):370-375.
- Kim S, Kim D, Cho SW, Kim J, Kim JS (2014) Highly efficient RNA-guided genome editing in human cells via delivery of purified Cas9 ribonucleoproteins. *Genome Res* 24(6):1012-9.
- Kirchner F, Schuetz A, Boldt LH, Martens K, Dittmar G, Haverkamp W, Thierfelder L, Heinemann U, Gerull B (2012) Molecular insights into arrhythmogenic right ventricular cardiomyopathy caused by plakophilin-2 missense mutations. *Circ Cardiovasc Genet* 5(4):400-11.
- Kley RA, Maerkens A, Leber Y, Theis V, Schreiner A, van der Ven PF, Uszkoreit J, Stephan C, Eulitz S, Euler N, Kirschner J, Muller K, Meyer HE, Tegenthoff M, Furst DO, Vorgerd M, Muller T, Marcus K (2013) A combined laser microdissection and mass spectrometry approach reveals new disease relevant proteins accumulating in aggregates of filaminopathy patients. *Mol Cell Proteomics* 12(1):215-27.
- Kolwicz SC, Jr., Odom GL, Nowakowski SG, Moussavi-Harami F, Chen X, Reinecke H, Hauschka SD, Murry CE, Mahairas GG, Regnier M (2016) AAV6-mediated Cardiac-specific Overexpression of Ribonucleotide Reductase Enhances Myocardial Contractility. *Mol Ther* 24(2):240-250.
- Kosicki M, Tomberg K, Bradley A (2018) Repair of double-strand breaks induced by CRISPR-Cas9 leads to large deletions and complex rearrangements. *Nat Biotechnol* 36(8):765-771.
- Koskenvuo JW, Saarinen I, Ahonen S, Tommiska J, Weckstrom S, Seppala EH, Tuupanen S, Kangas-Kontio T, Schleit J, Helio K, Hathaway J, Gummesson A, Dahlberg P, Ojala TH, Vepsalainen V, Kytola V, Muona M, Sistonen J, Salmenpera P, Gentile M, Paananen J, Myllykangas S, Alastalo TP, Helio T (2021) Biallelic loss-of-function in NRAP is a cause of recessive dilated cardiomyopathy. *PLoS One* 16(2):e0245681.
- Kotin RM, Linden RM, Berns KI (1992) Characterization of a preferred site on human chromosome 19q for integration of adeno-associated virus DNA by non-homologous recombination. *Embo j* 11(13):5071-8.

References

- Kuo IY, Ehrlich BE (2015) Signaling in muscle contraction. *Cold Spring Harb Perspect Biol* 7(2):a006023.
- Kuzmanov U, Guo H, Buchsbaum D, Cosme J, Abbasi C, Isserlin R, Sharma P, Gramolini AO, Emili A (2016) Global phosphoproteomic profiling reveals perturbed signaling in a mouse model of dilated cardiomyopathy. *Proc Natl Acad Sci USA* 113(44):12592-12597.
- Kwon SY, Chun SY, Ha YS, Kim DH, Kim J, Song PH, Kim HT, Yoo ES, Kim BS, Kwon TG (2017) Hypoxia Enhances Cell Properties of Human Mesenchymal Stem Cells. *Tissue Eng Regen Med* 14(5):595-604.
- Lahmers S, Wu Y, Call DR, Labeit S, Granzier H (2004) Developmental control of titin isoform expression and passive stiffness in fetal and neonatal myocardium. *Circ Res* 94(4):505-13.
- Lange S, Gehmlich K, Lun AS, Blondelle J, Hooper C, Dalton ND, Alvarez EA, Zhang X, Bang ML, Abassi YA, Dos Remedios CG, Peterson KL, Chen J, Ehler E (2016) MLP and CARP are linked to chronic PKC α signalling in dilated cardiomyopathy. *Nat Commun* 7:12120.
- Lange S, Pinotsis N, Agarkova I, Ehler E (2020) The M-band: The underestimated part of the sarcomere. *Biochim Biophys Acta Mol Cell Res* 1867(3):118440.
- Lee JH, Protze SI, Laksman Z, Backx PH, Keller GM (2017) Human Pluripotent Stem Cell-Derived Atrial and Ventricular Cardiomyocytes Develop from Distinct Mesoderm Populations. *Cell Stem Cell* 21(2):179-194.e4.
- Lee JW, Bae SH, Jeong JW, Kim SH, Kim KW (2004) Hypoxia-inducible factor (HIF-1) α : its protein stability and biological functions. *Exp Mol Med* 36(1):1-12.
- Li H, Handsaker B, Wysoker A, Fennell T, Ruan J, Homer N, Marth G, Abecasis G, Durbin R (2009) The Sequence Alignment/Map format and SAMtools. *Bioinformatics* 25(16):2078-9.
- Lian X, Hsiao C, Wilson G, Zhu K, Hazeltine LB, Azarin SM, Raval KK, Zhang J, Kamp TJ, Palecek SP (2012) Robust cardiomyocyte differentiation from human pluripotent stem cells via temporal modulation of canonical Wnt signaling. *Proc Natl Acad Sci USA* 109(27):E1848-57.
- Linke WA (2008) Sense and stretchability: the role of titin and titin-associated proteins in myocardial stress-sensing and mechanical dysfunction. *Cardiovasc Res* 77(4):637-48.
- Liu Y, Bai F, Tang Z, Liu N, Liu Q (2021a) Integrative transcriptomic, proteomic, and machine learning approach to identifying feature genes of atrial fibrillation using atrial samples from patients with valvular heart disease. *BMC Cardiovasc Disord* 21(1):52.
- Liu Y, Ma G, Gao Z, Li J, Wang J, Zhu X, Ma R, Yang J, Zhou Y, Hu K, Zhang Y, Guo Y (2022) Global chromosome rearrangement induced by CRISPR-Cas9 reshapes the genome and transcriptome of human cells. *Nucleic Acids Res* 50(6):3456-3474.
- Liu Z, Chaillou T, Santos Alves E, Mader T, Jude B, Ferreira DMS, Hynynen H, Cheng AJ, Jonsson WO, Pironti G, Andersson DC, Kenne E, Ruas JL, Tavi P, Lanner JT (2021b) Mitochondrial NDUFA4L2 is a novel regulator of skeletal muscle mass and force. *Faseb J* 35(12):e22010.
- Liu Z, Hui Y, Shi L, Chen Z, Xu X, Chi L, Fan B, Fang Y, Liu Y, Ma L, Wang Y, Xiao L, Zhang Q, Jin G, Liu L, Zhang X (2016) Efficient CRISPR/Cas9-Mediated Versatile, Predictable, and Donor-Free Gene Knockout in Human Pluripotent Stem Cells. *Stem Cell Rep.* 7(3):496-507.
- Livak KJ, Schmittgen TD (2001) Analysis of relative gene expression data using real-time quantitative PCR and the 2^{(-Delta Delta C(T))} Method. *Methods* 25(4):402-8.
- Loh YH, Agarwal S, Park IH, Urbach A, Huo H, Heffner GC, Kim K, Miller JD, Ng K, Daley GQ (2009) Generation of induced pluripotent stem cells from human blood. *Blood* 113(22):5476-9.

References

- Love MI, Huber W, Anders S (2014) Moderated estimation of fold change and dispersion for RNA-seq data with DESeq2. *Genome Biol* 15(12):550.
- Lu J, McKinsey TA, Nicol RL, Olson EN (2000) Signal-dependent activation of the MEF2 transcription factor by dissociation from histone deacetylases. *Proc Natl Acad Sci USA* 97(8):4070-5.
- Lu S, Borst DE, Horowitz R (2005) N-RAP expression during mouse heart development. *Dev Dyn* 233(1):201-12.
- Lu S, Borst DE, Horowitz R (2008) Expression and alternative splicing of N-RAP during mouse skeletal muscle development. *Cell Motil Cytoskeleton* 65(12):945-54.
- Lu S, Carroll SL, Herrera AH, Ozanne B, Horowitz R (2003) New N-RAP-binding partners alpha-actinin, filamin and Krp1 detected by yeast two-hybrid screening: implications for myofibril assembly. *J Cell Sci* 116(Pt 11):2169-78.
- Lu S, Crawford GL, Dore J, Anderson SA, Despres D, Horowitz R (2011) Cardiac-specific NRAP overexpression causes right ventricular dysfunction in mice. *Exp Cell Res* 317(8):1226-37.
- Lu S, Horowitz R (2008) Role of nonmuscle myosin IIB and N-RAP in cell spreading and myofibril assembly in primary mouse cardiomyocytes. *Cell Motil Cytoskeleton* 65(9):747-61.
- Luo G, Herrera AH, Horowitz R (1999) Molecular interactions of N-RAP, a nebulin-related protein of striated muscle myotendon junctions and intercalated disks. *Biochem*. 38(19):6135-43.
- Luo G, Zhang JQ, Nguyen TP, Herrera AH, Paterson B, Horowitz R (1997) Complete cDNA sequence and tissue localization of N-RAP, a novel nebulin-related protein of striated muscle. *Cell Motil Cytoskeleton* 38(1):75-90.
- Luo Y, Liu C, Cerbini T, San H, Lin Y, Chen G, Rao MS, Zou J (2014) Stable Enhanced Green Fluorescent Protein Expression After Differentiation and Transplantation of Reporter Human Induced Pluripotent Stem Cells Generated by AAVS1 Transcription Activator-Like Effector Nucleases. *Stem Cells Translational Medicine* 3(7):821-835.
- Luther PK (2009) The vertebrate muscle Z-disc: sarcomere anchor for structure and signalling. *J Muscle Res Cell Motil* 30(5-6):171-85.
- Lyon RC, Zanella F, Omens JH, Sheikh F (2015) Mechanotransduction in cardiac hypertrophy and failure. *Circ Res* 116(8):1462-1476.
- Lyu C, Shen J, Wang R, Gu H, Zhang J, Xue F, Liu X, Liu W, Fu R, Zhang L, Li H, Zhang X, Cheng T, Yang R, Zhang L (2018) Targeted genome engineering in human induced pluripotent stem cells from patients with hemophilia B using the CRISPR-Cas9 system. *Stem Cell Res Ther* 9(1):92.
- Ma J, Guo L, Fiene SJ, Anson BD, Thomson JA, Kamp TJ, Kolaja KL, Swanson BJ, January CT (2011) High purity human-induced pluripotent stem cell-derived cardiomyocytes: electrophysiological properties of action potentials and ionic currents. *Am J Physiol Heart Circ Physiol* 301(5):H2006-17.
- Mackrill JJ (2022) Evolution of the cardiac dyad. *Philos Trans R Soc Lond B Biol Sci* 377(1864):20210329.
- Maier SK, Westenbroek RE, McCormick KA, Curtis R, Scheuer T, Catterall WA (2004) Distinct subcellular localization of different sodium channel alpha and beta subunits in single ventricular myocytes from mouse heart. *Circ. J.* 109(11):1421-7.
- Makowski L, Caspar DL, Phillips WC, Goodenough DA (1977) Gap junction structures. II. Analysis of the x-ray diffraction data. *J Cell Biol* 74(2):629-45.

References

- Mali P, Yang L, Esvelt KM, Aach J, Guell M, DiCarlo JE, Norville JE, Church GM (2013) RNA-guided human genome engineering via Cas9. *Science* 339(6121):823-6.
- Manisastry SM, Zaal KJ, Horowitz R (2009) Myofibril assembly visualized by imaging N-RAP, alpha-actinin, and actin in living cardiomyocytes. *Exp Cell Res* 315(12):2126-39.
- Mannhardt I, Breckwoldt K, Letuffe-Brenière D, Schaaf S, Schulz H, Neuber C, Benzin A, Werner T, Eder A, Schulze T, Klampe B, Christ T, Hirt MN, Huebner N, Moretti A, Eschenhagen T, Hansen A (2016) Human Engineered Heart Tissue: Analysis of Contractile Force. *Stem Cell Rep.* 7(1):29-42.
- Mannhardt I, Saleem U, Benzin A, Schulze T, Klampe B, Eschenhagen T, Hansen A (2017) Automated Contraction Analysis of Human Engineered Heart Tissue for Cardiac Drug Safety Screening. *J Vis Exp*(122).
- Mannhardt I, Saleem U, Mosqueira D, Loos MF, Ulmer BM, Lemoine MD, Larsson C, Améen C, de Korte T, Vlaming MLH, Harris K, Clements P, Denning C, Hansen A, Eschenhagen T (2020) Comparison of 10 Control hPSC Lines for Drug Screening in an Engineered Heart Tissue Format. *Stem Cell Rep.* 15(4):983-998.
- Marcus FI, Edson S, Towbin JA (2013) Genetics of arrhythmogenic right ventricular cardiomyopathy: a practical guide for physicians. *J Am Coll Cardiol* 61(19):1945-8.
- Marian AJ, Braunwald E (2017) Hypertrophic Cardiomyopathy: Genetics, Pathogenesis, Clinical Manifestations, Diagnosis, and Therapy. *Circ Res* 121(7):749-770.
- Marks AR (2003) A Guide for the Perplexed. *Circ. J* 107(11):1456-1459.
- Maron BA, Wang RS, Carnethon MR, Rowin EJ, Loscalzo J, Maron BJ, Maron MS (2022) What Causes Hypertrophic Cardiomyopathy? *Am J Cardiol* 179:74-82.
- Maron BJ (2018) Clinical Course and Management of Hypertrophic Cardiomyopathy. *N Engl J Med* 379(7):655-668.
- Maron BJ, Towbin JA, Thiene G, Antzelevitch C, Corrado D, Arnett D, Moss AJ, Seidman CE, Young JB (2006) Contemporary Definitions and Classification of the Cardiomyopathies. *Circ. J* 113(14):1807-1816.
- Marrone D, Zampieri F, Basso C, Zanatta A, Thiene G (2019) History of the discovery of Arrhythmogenic Cardiomyopathy. *Eur Heart J* 40(14):1100-1104.
- Martin TG, Kirk JA (2020) Under construction: The dynamic assembly, maintenance, and degradation of the cardiac sarcomere. *J Mol Cell Cardiol* 148:89-102.
- Mathers CD, Boerma T, Ma Fat D (2009) Global and regional causes of death. *Br. Med. Bull.* 92(1):7-32.
- Maurer C, Boleti O, Najarzadeh Torbati P, Norouzi F, Fowler ANR, Minaee S, Salih KH, Taherpour M, Birjandi H, Alizadeh B, Salih AF, Bijari M, Houlden H, Pittman AM, Maroofian R, Almashham YH, Karimiani EG, Kaski JP, Faqeih EA, Vakilian F, Jamshidi Y (2023) Genetic Insights from Consanguineous Cardiomyopathy Families. *Genes* 14(1).
- McKinsey TA, Zhang CL, Olson EN (2002) MEF2: a calcium-dependent regulator of cell division, differentiation and death. *Trends Biochem. Sci.* 27(1):40-47.
- McNally EM, Barefield DY, Puckelwartz MJ (2015) The genetic landscape of cardiomyopathy and its role in heart failure. *Cell Metab* 21(2):174-182.
- Milner DJ, Mavroidis M, Weisleder N, Capetanaki Y (2000) Desmin cytoskeleton linked to muscle mitochondrial distribution and respiratory function. *J Cell Biol* 150(6):1283-98.

References

- Mohiddin SA, Lu S, Cardoso JP, Carroll S, Jha S, Horowitz R, Fananapazir L (2003) Genomic organization, alternative splicing, and expression of human and mouse N-RAP, a nebulin-related LIM protein of striated muscle. *Cell Motil Cytoskeleton* 55(3):200-12.
- Moncman CL, Wang K (1996) Assembly of nebulin into the sarcomeres of avian skeletal muscle. *Cell Motil Cytoskeleton* 34(3):167-84.
- Moncman CL, Wang K (1999) Functional dissection of nebulin demonstrates actin binding of nebulin-like repeats and Z-line targeting of SH3 and linker domains. *Cell Motil Cytoskeleton* 44(1):1-22.
- Monovich L, Vega RB, Meredith E, Miranda K, Rao C, Capparelli M, Lemon DD, Phan D, Koch KA, Chao JA, Hood DB, McKinsey TA (2010) A novel kinase inhibitor establishes a predominant role for protein kinase D as a cardiac class IIa histone deacetylase kinase. *FEBS Letters* 584(3):631-637.
- Muchtar E, Blauwet LA, Gertz MA (2017) Restrictive Cardiomyopathy. *Circ Res* 121(7):819-837.
- Mummery CL (2018) Perspectives on the Use of Human Induced Pluripotent Stem Cell-Derived Cardiomyocytes in Biomedical Research. *Stem Cell Rep.* 11(6):1306-1311.
- Murray JI, Spivey AC, Woscholski R (2013) Alternative synthetic tools to phospho-specific antibodies for phosphoproteome analysis: progress and prospects. *J Chem Biol* 6(4):175-84.
- Musunuru K, Sheikh F, Gupta RM, Houser SR, Maher KO, Milan DJ, Terzic A, Wu JC (2018) Induced Pluripotent Stem Cells for Cardiovascular Disease Modeling and Precision Medicine: A Scientific Statement From the American Heart Association. *Circ. Genom. precis. Med.* 11(1):e000043.
- Nag AC (1980) Study of non-muscle cells of the adult mammalian heart: a fine structural analysis and distribution. *Cytobios* 28(109):41-61.
- Nagueh SF, Shah G, Wu Y, Torre-Amione G, King NM, Lahmers S, Witt CC, Becker K, Labeit S, Granzier HL (2004) Altered titin expression, myocardial stiffness, and left ventricular function in patients with dilated cardiomyopathy. *Circ. J* 110(2):155-62.
- Nakatani Y, Kudo I Regulatory mechanisms for cytosolic prostaglandin E synthase, cPGES/p23. In: Miyazaki A., Imawari M. (eds) *New Frontiers in Lifestyle-Related Diseases*, Tokyo, 2008// 2008. Springer Japan, p 77-80.
- Nielsen MS, Opbergen CJMv, Veen TABv, Delmar M (2023) The intercalated disc: a unique organelle for electromechanical synchrony in cardiomyocytes. *Physio. Rev.* 103(3):2271-2319.
- Oceguera-Yanez F, Kim SI, Matsumoto T, Tan GW, Xiang L, Hatani T, Kondo T, Ikeya M, Yoshida Y, Inoue H, Woltjen K (2016) Engineering the AAVS1 locus for consistent and scalable transgene expression in human iPSCs and their differentiated derivatives. *Methods* 101:43-55.
- Ogata T, Kozuka T, Kanda T (2003) Identification of an insulator in AAVS1, a preferred region for integration of adeno-associated virus DNA. *J Virol* 77(16):9000-7.
- Ommen SR, Mital S, Burke MA, Day SM, Deswal A, Elliott P, Evanovich LL, Hung J, Joglar JA, Kantor P, Kimmelstiel C, Kittleson M, Link MS, Maron MS, Martinez MW, Miyake CY, Schaff HV, Semsarian C, Sorajja P (2020) 2020 AHA/ACC Guideline for the Diagnosis and Treatment of Patients With Hypertrophic Cardiomyopathy: Executive Summary: A Report of the American College of Cardiology/American Heart Association Joint Committee on Clinical Practice Guidelines. *J Am Coll Cardiol* 76(25):3022-3055.

References

- Ono Y, Sorimachi H (2012) Calpains — An elaborate proteolytic system. *Biochim. Biophys. Acta - Proteins and Proteomics* 1824(1):224-236.
- Opitz CA, Leake MC, Makarenko I, Benes V, Linke WA (2004) Developmentally regulated switching of titin size alters myofibrillar stiffness in the perinatal heart. *Circ. Res* 94(7):967-75.
- Orlando SJ, Santiago Y, DeKelver RC, Freyvert Y, Boydston EA, Moehle EA, Choi VM, Gopalan SM, Lou JF, Li J, Miller JC, Holmes MC, Gregory PD, Urnov FD, Cost GJ (2010) Zinc-finger nuclease-driven targeted integration into mammalian genomes using donors with limited chromosomal homology. *Nucleic Acids Res* 38(15):e152.
- Ortega A, Tarazón E, Gil-Cayuela C, García-Manzanares M, Martínez-Dolz L, Lago F, González-Juanatey JR, Cinca J, Jorge E, Portolés M, Roselló-Lletí E, Rivera M (2017) Intercalated disc in failing hearts from patients with dilated cardiomyopathy: Its role in the depressed left ventricular function. *PLOS ONE* 12(9):e0185062.
- Pablo Tortola C, Fielitz B, Li Y, Rüdibusch J, Luft FC, Fielitz J (2020) Activation of Tripartite Motif Containing 63 Expression by Transcription Factor EB and Transcription Factor Binding to Immunoglobulin Heavy Chain Enhancer 3 Is Regulated by Protein Kinase D and Class IIa Histone Deacetylases. *Front Physiol* 11:550506.
- Pacesa M, Lin CH, Cléry A, Saha A, Arantes PR, Bargsten K, Irby MJ, Allain FH, Palermo G, Cameron P, Donohoue PD, Jinek M (2022) Structural basis for Cas9 off-target activity. *Cell* 185(22):4067-4081.e21.
- Palpant NJ, Pabon L, Friedman CE, Roberts M, Hadland B, Zaunbrecher RJ, Bernstein I, Zheng Y, Murry CE (2017) Generating high-purity cardiac and endothelial derivatives from patterned mesoderm using human pluripotent stem cells. *Nat Protoc* 12(1):15-31.
- Pappas CT, Bliss KT, Zieseniss A, Gregorio CC (2011) The Nebulin family: an actin support group. *Trends Cell Biol* 21(1):29-37.
- Pappas CT, Krieg PA, Gregorio CC (2010) Nebulin regulates actin filament lengths by a stabilization mechanism. *J Cell Biol* 189(5):859-70.
- Paulin D, Li Z (2004) Desmin: a major intermediate filament protein essential for the structural integrity and function of muscle. *Exp Cell Res* 301(1):1-7.
- Perez-Riverol Y, Csordas A, Bai J, Bernal-Llinares M, Hewapathirana S, Kundu DJ, Inuganti A, Griss J, Mayer G, Eisenacher M, Pérez E, Uszkoreit J, Pfeuffer J, Sachsenberg T, Yilmaz S, Tiwary S, Cox J, Audain E, Walzer M, Jarnuczak AF, Ternent T, Brazma A, Vizcaíno JA (2019) The PRIDE database and related tools and resources in 2019: improving support for quantification data. *Nucleic Acids Res* 47(D1):D442-d450.
- Perriard J-C, Hirschy A, Ehler E (2003) Dilated Cardiomyopathy: A Disease of the Intercalated Disc? *Trends Cardiovasc. Med.* 13(1):30-38.
- Pervolaraki E, Dachtler J, Anderson RA, Holden AV (2018) The developmental transcriptome of the human heart. *Sci Rep* 8(1):15362.
- Pieperhoff S, Franke WW (2007) The area composita of adhering junctions connecting heart muscle cells of vertebrates - IV: coalescence and amalgamation of desmosomal and adhaerens junction components - late processes in mammalian heart development. *Eur J Cell Biol* 86(7):377-91.
- Pinto AR, Ilinykh A, Ivey MJ, Kuwabara JT, D'Antoni ML, Debuque R, Chandran A, Wang L, Arora K, Rosenthal NA, Tallquist MD (2016a) Revisiting Cardiac Cellular Composition. *Circ. Res* 118(3):400-9.

References

- Pinto YM, Elliott PM, Arbustini E, Adler Y, Anastasakis A, Böhm M, Duboc D, Gimeno J, de Groote P, Imazio M, Heymans S, Klingel K, Komajda M, Limongelli G, Linhart A, Mogensen J, Moon J, Pieper PG, Seferovic PM, Schueler S, Zamorano JL, Caforio ALP, Charron P (2016b) Proposal for a revised definition of dilated cardiomyopathy, hypokinetic non-dilated cardiomyopathy, and its implications for clinical practice: a position statement of the ESC working group on myocardial and pericardial diseases. *European Heart Journal* 37(23):1850-1858.
- Pioner JM, Guan X, Klaiman JM, Racca AW, Pabon L, Muskheli V, Macadangdang J, Ferrantini C, Hoopmann MR, Moritz RL, Kim DH, Tesi C, Poggesi C, Murry CE, Childers MK, Mack DL, Regnier M (2020) Absence of full-length dystrophin impairs normal maturation and contraction of cardiomyocytes derived from human-induced pluripotent stem cells. *Cardiovasc Res* 116(2):368-382.
- Pluess M, Daeubler G, Dos Remedios CG, Ehler E (2015) Adaptations of cytoarchitecture in human dilated cardiomyopathy. *Biophys Rev* 7(1):25-32.
- Ponikowski P, Anker SD, AlHabib KF, Cowie MR, Force TL, Hu S, Jaarsma T, Krum H, Rastogi V, Rohde LE, Samal UC, Shimokawa H, Budi Siswanto B, Sliwa K, Filippatos G (2014) Heart failure: preventing disease and death worldwide. *ESC Heart Failure* 1(1):4-25.
- Portbury AL, Willis MS, Patterson C (2011) Tearin' up my heart: proteolysis in the cardiac sarcomere. *J Biol Chem* 286(12):9929-34.
- Pourcel C, Salvignol G, Vergnaud G (2005) CRISPR elements in *Yersinia pestis* acquire new repeats by preferential uptake of bacteriophage DNA, and provide additional tools for evolutionary studies. *J. Microbiol.* 151(3):653-663.
- Prill K, Dawson JF (2020) Assembly and Maintenance of Sarcomere Thin Filaments and Associated Diseases. *Int J Mol Sci* 21(2)
- Radice GL, Rayburn H, Matsunami H, Knudsen KA, Takeichi M, Hynes RO (1997) Developmental defects in mouse embryos lacking N-cadherin. *Dev Biol* 181(1):64-78.
- Rampazzo A, Calore M, Hengel Jv, Roy Fv (2014) Intercalated Discs and Arrhythmogenic Cardiomyopathy. *Circulation: Cardiovascular Genetics* 7(6):930-940.
- Ran FA, Hsu PD, Wright J, Agarwala V, Scott DA, Zhang F (2013) Genome engineering using the CRISPR-Cas9 system. *Nat Protoc* 8(11):2281-2308.
- Rana JS, Khan SS, Lloyd-Jones DM, Sidney S (2021) Changes in Mortality in Top 10 Causes of Death from 2011 to 2018. *J Gen Intern Med* 36(8):2517-2518.
- Rappsilber J, Mann M, Ishihama Y (2007) Protocol for micro-purification, enrichment, pre-fractionation and storage of peptides for proteomics using StageTips. *Nat Protoc* 2(8):1896-906.
- Rasmussen TB, Nissen PH, Palmfeldt J, Gehmlich K, Dalager S, Jensen UB, Kim WY, Heickendorff L, Mølgaard H, Jensen HK, Baandrup UT, Bross P, Mogensen J (2014) Truncating plakophilin-2 mutations in arrhythmogenic cardiomyopathy are associated with protein haploinsufficiency in both myocardium and epidermis. *Circ Cardiovasc Genet* 7(3):230-40.
- Rath D, Amlinger L, Rath A, Lundgren M (2015) The CRISPR-Cas immune system: Biology, mechanisms and applications. *Biochimie* 117:119-128.
- Reiss K, Cheng W, Ferber A, Kajstura J, Li P, Li B, Olivetti G, Homcy CJ, Baserga R, Anversa P (1996) Overexpression of insulin-like growth factor-1 in the heart is coupled with myocyte proliferation in transgenic mice. *Proc Natl Acad Sci USA* 93(16):8630-5.

References

- Rey O, Sinnett-Smith J, Zhukova E, Rozengurt E (2001a) Regulated nucleocytoplasmic transport of protein kinase D in response to G protein-coupled receptor activation. *J Biol Chem* 276(52):49228-35.
- Rey O, Young SH, Cantrell D, Rozengurt E (2001b) Rapid protein kinase D translocation in response to G protein-coupled receptor activation. Dependence on protein kinase C. *J Biol Chem* 276(35):32616-26.
- Rhee D, Sanger JM, Sanger JW (1994) The premyofibril: Evidence for its role in myofibrillogenesis. *Cell Motility* 28(1):1-24.
- Rhett JM, Jourdan J, Gourdie RG (2011) Connexin 43 connexon to gap junction transition is regulated by zonula occludens-1. *Mol Biol Cell* 22(9):1516-28.
- Ribeiro AJ, Ang YS, Fu JD, Rivas RN, Mohamed TM, Higgs GC, Srivastava D, Pruitt BL (2015) Contractility of single cardiomyocytes differentiated from pluripotent stem cells depends on physiological shape and substrate stiffness. *Proc Natl Acad Sci USA* 112(41):12705-10.
- Risebro CA, Searles RG, Melville AA, Ehler E, Jina N, Shah S, Pallas J, Hubank M, Dillard M, Harvey NL, Schwartz RJ, Chien KR, Oliver G, Riley PR (2009) Prox1 maintains muscle structure and growth in the developing heart. *Development* 136(3):495-505.
- Roberts B, Haupt A, Tucker A, Grancharova T, Arakaki J, Fuqua MA, Nelson A, Hookway C, Ludmann SA, Mueller IA, Yang R, Horwitz R, Rafelski SM, Gunawardane RN (2017) Systematic gene tagging using CRISPR/Cas9 in human stem cells to illuminate cell organization. *Mol. Biol. Cell* 28(21):2854-2874.
- Rozengurt E (2011) Protein kinase D signaling: multiple biological functions in health and disease. *Physiology (Bethesda)* 26(1):23-33.
- Rybin VO, Guo J, Steinberg SF (2009) Protein kinase D1 autophosphorylation via distinct mechanisms at Ser744/Ser748 and Ser916. *J Biol Chem* 284(4):2332-43.
- Saleem U, van Meer BJ, Katili PA, Mohd Yusof NAN, Mannhardt I, Garcia AK, Tertoolen L, de Korte T, Vlaming MLH, McGlynn K, Nebel J, Bahinski A, Harris K, Rossman E, Xu X, Burton FL, Smith GL, Clements P, Mummery CL, Eschenhagen T, Hansen A, Denning C (2020) Blinded, Multicenter Evaluation of Drug-induced Changes in Contractility Using Human-induced Pluripotent Stem Cell-derived Cardiomyocytes. *Toxicol. Sci.* 176(1):103-123.
- Sanger JW, Wang J, Fan Y, White J, Mi-Mi L, Dube DK, Sanger JM, Pruyne D (2017) Assembly and Maintenance of Myofibrils in Striated Muscle. *Handb Exp Pharmacol* 235:39-75.
- Saphir O, Karsner HT (1924) An Anatomical and Experimental Study of Segmentation of the Myocardium and its Relation to the Intercalated Discs. *J Med Res* 44(5):539-556.5.
- Sasse S, Brand NJ, Kyprianou P, Dhoot GK, Wade R, Arai M, Periasamy M, Yacoub MH, Barton PJ (1993) Troponin I gene expression during human cardiac development and in end-stage heart failure. *Circ. Res* 72(5):932-8.
- Sato PY, Coombs W, Lin X, Nekrasova O, Green KJ, Isom LL, Taffet SM, Delmar M (2011) Interactions between ankyrin-G, Plakophilin-2, and Connexin43 at the cardiac intercalated disc. *Circ. Res* 109(2):193-201.
- Schaaf S, Shibamiya A, Mewe M, Eder A, Stöhr A, Hirt MN, Rau T, Zimmermann WH, Conradi L, Eschenhagen T, Hansen A (2011) Human engineered heart tissue as a versatile tool in basic research and preclinical toxicology. *PLoS One* 6(10):e26397.
- Schafer DA, Hug C, Cooper JA (1995) Inhibition of CapZ during myofibrillogenesis alters assembly of actin filaments. *J Cell Biol* 128(1-2):61-70.

References

- Schlaeger TM, Daheron L, Brickler TR, Entwisle S, Chan K, Cianci A, DeVine A, Ettenger A, Fitzgerald K, Godfrey M, Gupta D, McPherson J, Malwadkar P, Gupta M, Bell B, Doi A, Jung N, Li X, Lynes MS, Brookes E, Cherry AB, Demirbas D, Tsankov AM, Zon LI, Rubin LL, Feinberg AP, Meissner A, Cowan CA, Daley GQ (2015) A comparison of non-integrating reprogramming methods. *Nat Biotechnol* 33(1):58-63.
- Schmeichel KL, Beckerle MC (1994) The LIM domain is a modular protein-binding interface. *Cell* 79(2):211-9.
- Shaw RM, Fay AJ, Puthenveedu MA, von Zastrow M, Jan YN, Jan LY (2007) Microtubule plus-end-tracking proteins target gap junctions directly from the cell interior to adherens junctions. *Cell* 128(3):547-60.
- Sheikh F, Chen Y, Liang X, Hirschy A, Stenbit AE, Gu Y, Dalton ND, Yajima T, Lu Y, Knowlton KU, Peterson KL, Perriard JC, Chen J (2006) alpha-E-catenin inactivation disrupts the cardiomyocyte adherens junction, resulting in cardiomyopathy and susceptibility to wall rupture. *Circ. J* 114(10):1046-55.
- Shima H, Takubo K, Tago N, Iwasaki H, Arai F, Takahashi T, Suda T (2010) Acquisition of G₀ state by CD34-positive cord blood cells after bone marrow transplantation. *Exp Hematol* 38(12):1231-40.
- Shooter RA, Gey GO (1952) Studies of the mineral requirements of mammalian cells. *Br J Exp Pathol* 33(1):98-103.
- Siedner S, Krüger M, Schroeter M, Metzler D, Roell W, Fleischmann BK, Hescheler J, Pfister G, Stehle R (2003) Developmental changes in contractility and sarcomeric proteins from the early embryonic to the adult stage in the mouse heart. *J Physiol* 548(Pt 2):493-505.
- Simkin D, Papakis V, Bustos BI, Ambrosi CM, Ryan SJ, Baru V, Williams LA, Dempsey GT, McManus OB, Landers JE, Lubbe SJ, George AL, Jr., Kiskinis E (2022) Homozygous might be hemizygous: CRISPR/Cas9 editing in iPSCs results in detrimental on-target defects that escape standard quality controls. *Stem Cell Rep.* 17(4):993-1008.
- Simsek Papur O, Sun A, Glatz JFC, Luiken JJFP, Nabben M (2018) Acute and Chronic Effects of Protein Kinase-D Signaling on Cardiac Energy Metabolism. *Frontiers Cardiovasc Med.* 5
- Smith JR, Maguire S, Davis LA, Alexander M, Yang F, Chandran S, French-Constant C, Pedersen RA (2007) Robust, Persistent Transgene Expression in Human Embryonic Stem Cells Is Achieved with AAVS1-Targeted Integration. *Stem Cells* 26(2):496-504.
- Smith MA, Hoffman LM, Beckerle MC (2014) LIM proteins in actin cytoskeleton mechanoresponse. *Trends Cell Biol* 24(10):575-83.
- Soonpaa MH, Kim KK, Pajak L, Franklin M, Field LJ (1996) Cardiomyocyte DNA synthesis and binucleation during murine development. *Am. J. Physiol. - Heart Circ. Physiol.* 271(5):H2183-H2189.
- Squire J (2019) Special Issue: The Actin-Myosin Interaction in Muscle: Background and Overview. *Int J Mol Sci* 20(22).
- Stathopoulou K, Cuello F, Candasamy AJ, Kemp EM, Ehler E, Haworth RS, Avkiran M (2014) Four-and-a-half LIM domains proteins are novel regulators of the protein kinase D pathway in cardiac myocytes. *Biochem J* 457(3):451-61.
- Stöhr A, Friedrich FW, Flenner F, Geertz B, Eder A, Schaaf S, Hirt MN, Uebeler J, Schlossarek S, Carrier L, Hansen A, Eschenhagen T (2013) Contractile abnormalities and altered drug response in engineered heart tissue from Mybpc3-targeted knock-in mice. *J Mol Cell Cardiol* 63:189-98.

References

- Taegtmeyer H, Sen S, Vela D (2010) Return to the fetal gene program: a suggested metabolic link to gene expression in the heart. *Ann N Y Acad Sci* 1188:191-8.
- Takahashi K, Hattori A (1989) α -Actinin Is a Component of the Z-Filament, a Structural Backbone of Skeletal Muscle Z-Disks. *J. Biochem. J BIOCHEM* 105(4):529-536.
- Takahashi K, Tanabe K, Ohnuki M, Narita M, Ichisaka T, Tomoda K, Yamanaka S (2007) Induction of pluripotent stem cells from adult human fibroblasts by defined factors. *Cell* 131(5):861-72.
- Takahashi K, Yamanaka S (2006) Induction of pluripotent stem cells from mouse embryonic and adult fibroblast cultures by defined factors. *Cell* 126(4):663-76.
- Takahashi M, Tajika Y, Khairani AF, Ueno H, Murakami T, Yorifuji H (2013) The localization of VAMP5 in skeletal and cardiac muscle. *Histochem Cell Biol* 139(4):573-82.
- Tello D, Balsa E, Acosta-Iborra B, Fuertes-Yebra E, Elorza A, Ordóñez Á, Corral-Escariz M, Soro I, López-Bernardo E, Perales-Clemente E, Martínez-Ruiz A, Enríquez JA, Aragonés J, Cadenas S, Landázuri MO (2011) Induction of the mitochondrial NDUFA4L2 protein by HIF-1 α decreases oxygen consumption by inhibiting Complex I activity. *Cell Metab* 14(6):768-79.
- Thomas D, Cunningham NJ, Shenoy S, Wu JC (2022) Human-induced pluripotent stem cells in cardiovascular research: current approaches in cardiac differentiation, maturation strategies, and scalable production. *Cardiovasc Res* 118(1):20-36.
- Tokuyasu KT (1989) Immunocytochemical studies of cardiac myofibrillogenesis in early chick embryos. III. Generation of fasciae adherentes and costameres. *J Cell Biol* 108(1):43-53.
- Tóth AD, Schell R, Lévy M, Vettel C, Theis P, Haslinger C, Alban F, Werhahn S, Frischbier L, Krebs-Haupenthal J, Thomas D, Gröne HJ, Avkiran M, Katus HA, Wieland T, Backs J (2018) Inflammation leads through PGE/EP(3) signaling to HDAC5/MEF2-dependent transcription in cardiac myocytes. *EMBO Mol Med* 10(7).
- Trinick J, Knight P, Whiting A (1984) Purification and properties of native titin. *J Mol Biol* 180(2):331-56.
- Truszkowska GT, Bilinska ZT, Muchowicz A, Pollak A, Biernacka A, Kozar-Kaminska K, Stawinski P, Gasperowicz P, Kosinska J, Zielinski T, Ploski R (2017) Homozygous truncating mutation in NRAP gene identified by whole exome sequencing in a patient with dilated cardiomyopathy. *Sci Rep* 7(1):3362.
- Tu M, Tan VP, Yu JD, Tripathi R, Bigham Z, Barlow M, Smith JM, Brown JH, Miyamoto S (2022) RhoA signaling increases mitophagy and protects cardiomyocytes against ischemia by stabilizing PINK1 protein and recruiting Parkin to mitochondria. *Cell Death and Differ.* 29(12):2472-2486.
- Ulmer BM, Eschenhagen T (2020) Human pluripotent stem cell-derived cardiomyocytes for studying energy metabolism. *Biochim Biophys Acta Mol Cell Res* 1867(3):118471.
- Ulmer BM, Stoehr A, Schulze ML, Patel S, Gucek M, Mannhardt I, Funcke S, Murphy E, Eschenhagen T, Hansen A (2018) Contractile Work Contributes to Maturation of Energy Metabolism in hiPSC-Derived Cardiomyocytes. *Stem Cell Rep.* 10(3):834-847.
- Vasilescu C, Ojala TH, Brilhante V, Ojanen S, Hinterding HM, Palin E, Alastalo TP, Koskenvuo J, Hiiippala A, Jokinen E, Jahnukainen T, Lohi J, Pihkala J, Tyni TA, Carroll CJ, Suomalainen A (2018) Genetic Basis of Severe Childhood-Onset Cardiomyopathies. *J Am Coll Cardiol* 72(19):2324-2338.
- Veeraraghavan R, Lin J, Hoeker GS, Keener JP, Gourdie RG, Poelzing S (2015) Sodium channels in the Cx43 gap junction perinexus may constitute a cardiac ephapse: an experimental and modeling study. *Pflugers Arch* 467(10):2093-105.

References

- Vega RB, Harrison BC, Meadows E, Roberts CR, Papst PJ, Olson EN, McKinsey TA (2004) Protein kinases C and D mediate agonist-dependent cardiac hypertrophy through nuclear export of histone deacetylase 5. *Mol Cell Biol* 24(19):8374-85.
- Veres A, Gosis BS, Ding Q, Collins R, Ragavendran A, Brand H, Erdin S, Cowan CA, Talkowski ME, Musunuru K (2014) Low incidence of off-target mutations in individual CRISPR-Cas9 and TALEN targeted human stem cell clones detected by whole-genome sequencing. *Stem Cell* 15(1):27-30.
- Vermij SH, Abriel H, van Veen TA (2017) Refining the molecular organization of the cardiac intercalated disc. *Cardiovasc Res* 113(3):259-275.
- Vignier N, Schlossarek S, Fraysse B, Mearini G, Kramer E, Pointu H, Mougnot N, Guiard J, Reimer R, Hohenberg H, Schwartz K, Vernet M, Eschenhagen T, Carrier L (2009) Nonsense-mediated mRNA decay and ubiquitin-proteasome system regulate cardiac myosin-binding protein C mutant levels in cardiomyopathic mice. *Circ. Res* 105(3):239-48.
- Volk T, Fessler LI, Fessler JH (1990) A role for integrin in the formation of sarcomeric cytoarchitecture. *Cell* 63(3):525-36.
- Volk T, Geiger B (1984) A 135-kd membrane protein of intercellular adherens junctions. *Embo J* 3(10):2249-60.
- Vozzi C, Dupont E, Coppens SR, Yeh HI, Severs NJ (1999) Chamber-related differences in connexin expression in the human heart. *J Mol Cell Cardiol* 31(5):991-1003.
- Wakana Y, Campelo F (2021) The PKD-Dependent Biogenesis of TGN-to-Plasma Membrane Transport Carriers. *Cells* 10(7):1618.
- Waldron RT, Rey O, Iglesias T, Tugal T, Cantrell D, Rozengurt E (2001) Activation loop Ser744 and Ser748 in protein kinase D are transphosphorylated in vivo. *J Biol Chem* 276(35):32606-15.
- Wang H, La Russa M, Qi LS (2016) CRISPR/Cas9 in Genome Editing and Beyond. *Annu Rev Biochem* 85:227-64.
- Wang J, Fan Y, Dube S, Agassy NW, Dube DK, Sanger JM, Sanger JW (2020) Myofibril assembly and the roles of the ubiquitin proteasome system. *Cytoskeleton (Hoboken)* 77(10):456-479.
- Wang J, Fan Y, Sanger JM, Sanger JW (2022) STED analysis reveals the organization of nonmuscle muscle II, muscle myosin II, and F-actin in nascent myofibrils. *Cytoskeleton (Hoboken)* 79(12):122-132.
- Wang K, Williamson CL (1980) Identification of an N2 line protein of striated muscle. *Proc Natl Acad Sci U S A* 77(6):3254-8.
- Wang N, Tytell JD, Ingber DE (2009) Mechanotransduction at a distance: mechanically coupling the extracellular matrix with the nucleus. *Nat Rev Mol Cell Biol* 10(1):75-82.
- Wang Z, Raunser S (2023) Structural Biochemistry of Muscle Contraction. *Annu Rev Biochem.* 92, 411–433.
- Watanabe T, Kimura A, Kuroyanagi H (2018) Alternative Splicing Regulator RBM20 and Cardiomyopathy. *Front Mol Biosci* 5:105.
- Weinberger F, Mannhardt I, Eschenhagen T (2017) Engineering Cardiac Muscle Tissue: A Maturing Field of Research. *Circ. Res* 120(9):1487-1500.
- Weintraub RG, Semsarian C, Macdonald P (2017) Dilated cardiomyopathy. *The Lancet* 390 (10092):400-414.

References

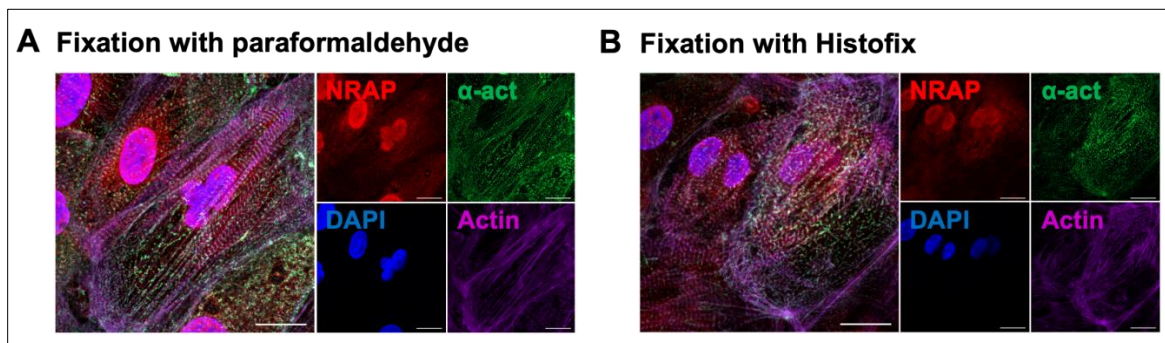
- Weterings E, Chen DJ (2008) The endless tale of non-homologous end-joining. *Cell Res* 18(1):114-24.
- Wettwer E, Christ T, Endig S, Rozmaritsa N, Matschke K, Lynch JJ, Pourrier M, Gibson JK, Fedida D, Knaut M, Ravens U (2013) The new antiarrhythmic drug vernakalant: ex vivo study of human atrial tissue from sinus rhythm and chronic atrial fibrillation. *Cardiovas Res* 98(1):145-154.
- Wigle ED, Heimbecker RO, Gunton RW (1962) Idiopathic ventricular septal hypertrophy causing muscular subaortic stenosis. *Circ. J* 26:325-40.
- Willems E, Spiering S, Davidovics H, Lanier M, Xia Z, Dawson M, Cashman J, Mercola M (2011) Small-molecule inhibitors of the Wnt pathway potently promote cardiomyocytes from human embryonic stem cell-derived mesoderm. *Circ. Res* 109(4):360-4.
- Willis MS, Townley-Tilson WH, Kang EY, Homeister JW, Patterson C (2010) Sent to destroy: the ubiquitin proteasome system regulates cell signaling and protein quality control in cardiovascular development and disease. *Circ. Res* 106(3):463-78.
- Wilson AJ, Schoenauer R, Ehler E, Agarkova I, Bennett PM (2014) Cardiomyocyte growth and sarcomerogenesis at the intercalated disc. *Cell Mol Life Sci* 71(1):165-81.
- Witt SH, Granzier H, Witt CC, Labeit S (2005) MURF-1 and MURF-2 target a specific subset of myofibrillar proteins redundantly: towards understanding MURF-dependent muscle ubiquitination. *J Mol Biol* 350(4):713-22.
- Xue R-Q, Zhao M, Wu Q, Yang S, Cui Y-L, Yu X-J, Liu J, Zang W-J (2019) Regulation of mitochondrial cristae remodelling by acetylcholine alleviates palmitate-induced cardiomyocyte hypertrophy. *Free Radic. Biol. Med. FREE RADICAL BIO MED* 145:103-117.
- Yang D, Liu H-Q, Liu F-Y, Guo Z, An P, Wang M-Y, Yang Z, Fan D, Tang Q-Z (2022) Mitochondria in Pathological Cardiac Hypertrophy Research and Therapy. *Frontiers Cardiovasc Med.* 8:822969.
- Yu T, Sheu SS, Robotham JL, Yoon Y (2008) Mitochondrial fission mediates high glucose-induced cell death through elevated production of reactive oxygen species. *Cardiovasc Res* 79(2):341-51.
- Zaman R, Hamidzada H, Epelman S (2021) Exploring cardiac macrophage heterogeneity in the healthy and diseased myocardium. *Curr Opin Immunol* 68:54-63.
- Zemljic-Harpe AE, Miller JC, Henderson SA, Wright AT, Manso AM, Elsherif L, Dalton ND, Thor AK, Perkins GA, McCulloch AD, Ross RS (2007) Cardiac-myocyte-specific excision of the vinculin gene disrupts cellular junctions, causing sudden death or dilated cardiomyopathy. *Mol Cell Biol* 27(21):7522-37.
- Zhang CL, McKinsey TA, Chang S, Antos CL, Hill JA, Olson EN (2002) Class II histone deacetylases act as signal-responsive repressors of cardiac hypertrophy. *Cell* 110(4):479-88.
- Zhang J, Klos M, Wilson GF, Herman AM, Lian X, Raval KK, Barron MR, Hou L, Soerens AG, Yu J, Palecek SP, Lyons GE, Thomson JA, Herron TJ, Jalife J, Kamp TJ (2012) Extracellular matrix promotes highly efficient cardiac differentiation of human pluripotent stem cells: the matrix sandwich method. *Circ. Res* 111(9):1125-36.
- Zhang JQ, Elzey B, Williams G, Lu S, Law DJ, Horowitz R (2001) Ultrastructural and biochemical localization of N-RAP at the interface between myofibrils and intercalated disks in the mouse heart. *Biochem.* 40(49):14898-906.

References

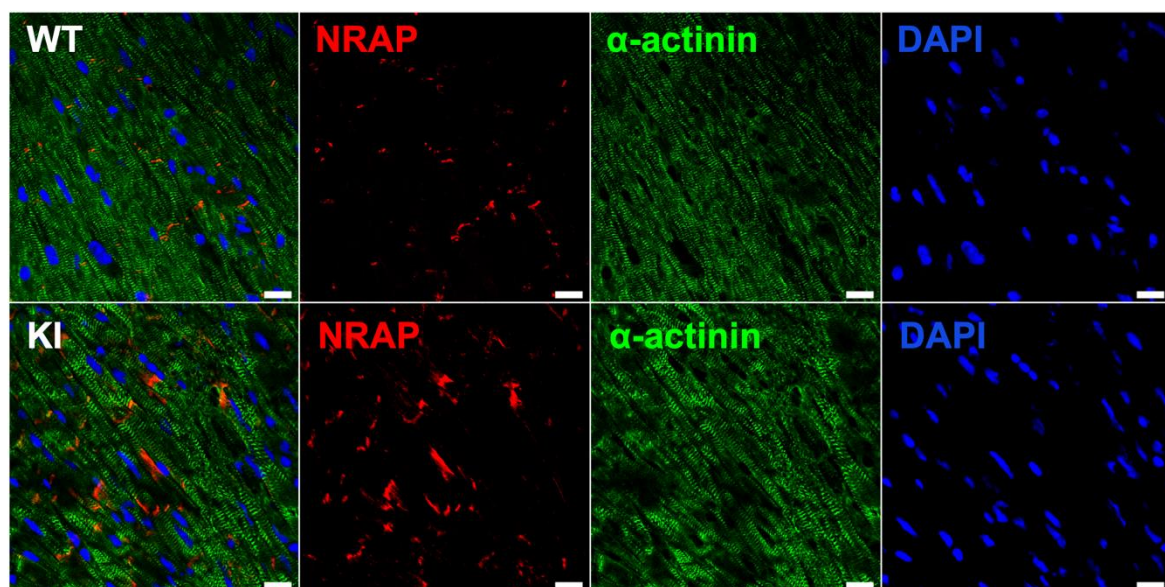
- Zhang Z, Xu K, Ji L, Zhang H, Yin J, Zhou M, Wang C, Yang S (2023) A novel loss-of-function mutation in NRAP is associated with left ventricular non-compaction cardiomyopathy. *Front Cardiovasc Med* 10:1097957.
- Zhao D, Wang W, Wang H, Peng H, Liu X, Guo W, Su G, Zhao Z (2017) PKD knockdown inhibits pressure overload-induced cardiac hypertrophy by promoting autophagy via AKT/mTOR pathway. *Int J Biol Sci* 13(3):276-285.
- Zhao G, Qiu Y, Zhang HM, Yang D (2019) Intercalated discs: cellular adhesion and signaling in heart health and diseases. *Heart Fail Rev* 24(1):115-132.
- Zhou P, Pu WT (2016) Recounting Cardiac Cellular Composition. *Circ. Res* 118(3):368-70.
- Zhu L, Choudhary K, Gonzalez-Teran B, Ang YS, Thomas R, Stone NR, Liu L, Zhou P, Zhu C, Ruan H, Huang Y, Jin S, Pelonero A, Koback F, Padmanabhan A, Sadagopan N, Hsu A, Costa MW, Gifford CA, van Bommel JG, Hüttenhain R, Vedantham V, Conklin BR, Black BL, Bruneau BG, Steinmetz L, Krogan NJ, Pollard KS, Srivastava D (2022) Transcription Factor GATA4 Regulates Cell Type-Specific Splicing Through Direct Interaction With RNA in Human Induced Pluripotent Stem Cell-Derived Cardiac Progenitors. *Circ. J* 146(10):770-787.
- Zimmer A, Zimmer AM, Reynolds K (1994) Tissue specific expression of the retinoic acid receptor-beta 2: regulation by short open reading frames in the 5'-noncoding region. *J Cell Biol* 127(4):1111-9.
- Zimmermann WH, Fink C, Kralisch D, Remmers U, Weil J, Eschenhagen T (2000) Three-dimensional engineered heart tissue from neonatal rat cardiac myocytes. *Biotechn. Bioeng.* 68(1):106-114.
- Zong L, Zhu Y, Liang R, Zhao H-B (2016) Gap junction mediated miRNA intercellular transfer and gene regulation: A novel mechanism for intercellular genetic communication. *Sci. Rep.* 6(1):19884.
- Zugaza JL, Sinnott-Smith J, Van Lint J, Rozengurt E (1996) Protein kinase D (PKD) activation in intact cells through a protein kinase C-dependent signal transduction pathway. *Embo J* 15(22):6220-30.

11. Supplements

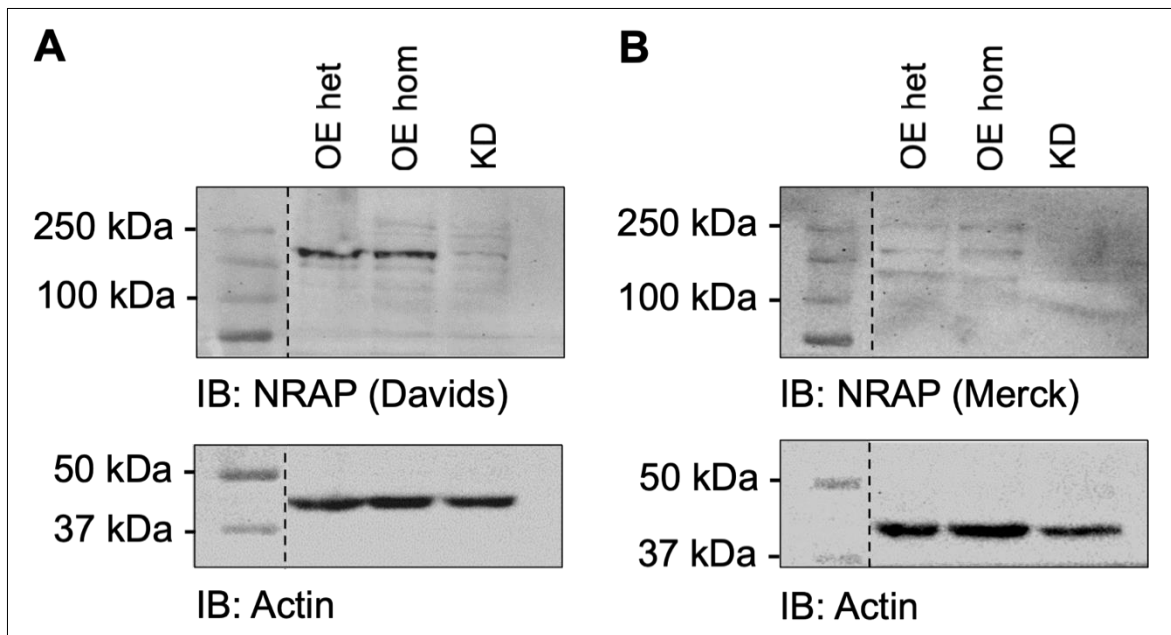
11.1 Figures and tables



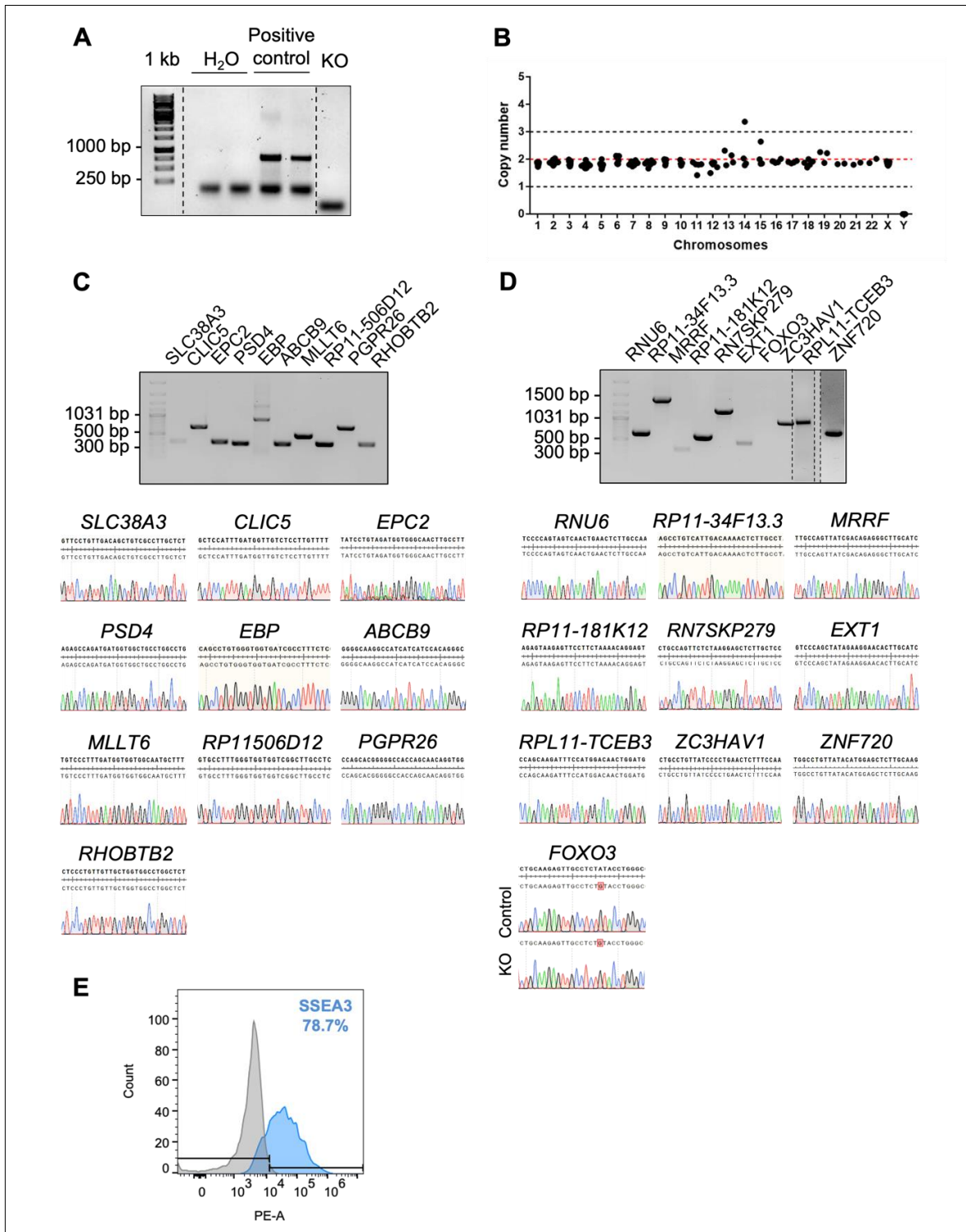
Supplementary figure 1: Investigation of different fixation methods of cardiac myocytes for immunofluorescence with anti-NRAP. Human induced pluripotent stem cell (hiPSC) derived cardiac myocytes were fixed with **A**) 4% paraformaldehyde or **B**) histofix. Cardiac myocytes were stained for NRAP (1:500; red), Z-discs with α -actinin (green), F-actin with phalloidin (purple) and nuclei with DAPI (blue). Scale bar are equal to 20 μ m (n = 1).



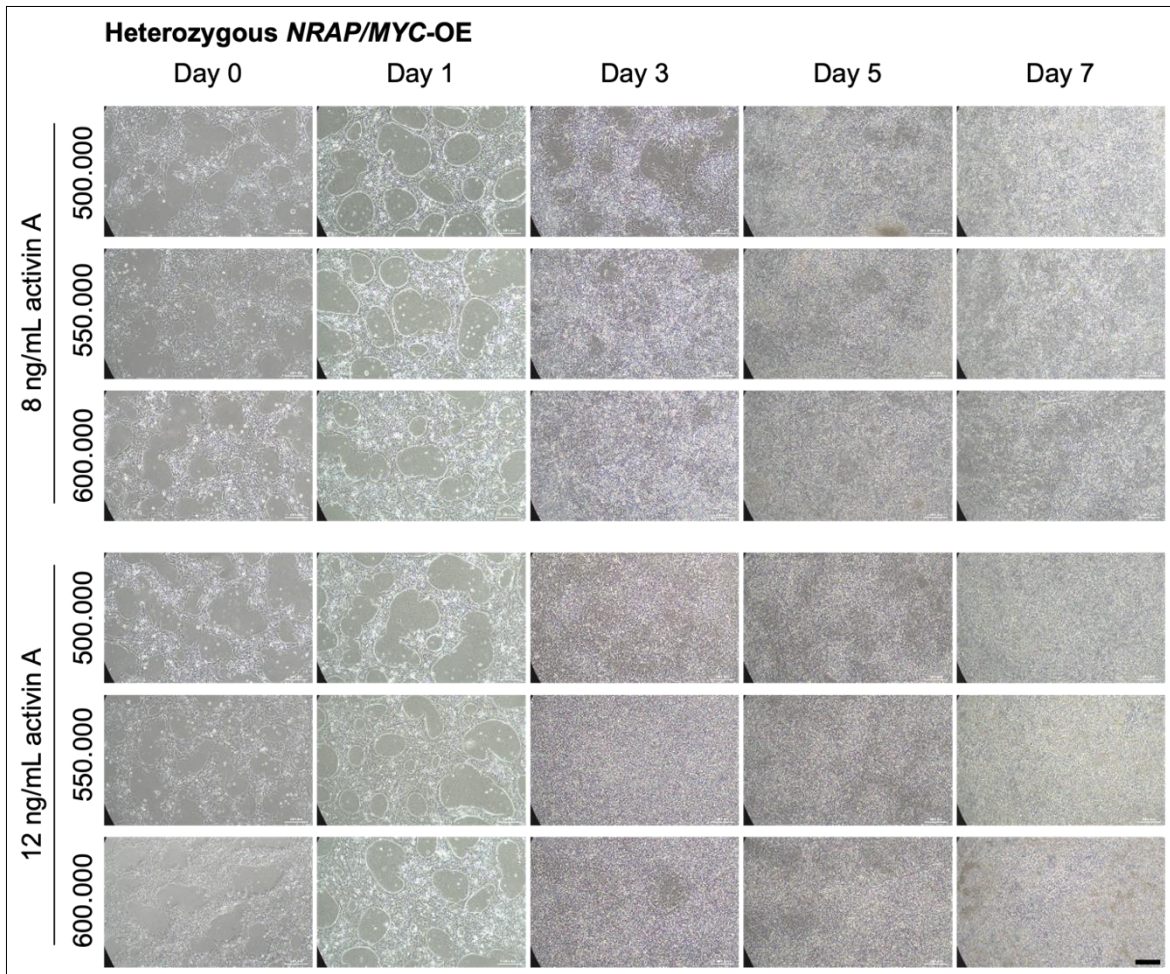
Supplementary figure 2: Localisation of NRAP in hypertrophic cardiomyopathy. Immunofluorescence in heart sections of wildtype and *Mybpc3*-knock-In (KI) mice stained for α -actinin (green), DAPI (blue), NRAP (red). Images were captured using the Leica TCS SP5II confocal laser scanning microscope. Images of the heart sections are representative and experiments were repeated twice using independently prepared heart sections of different mice. Scale bars are equal to 10 μ m. This figure was adopted from my master thesis in 2020.



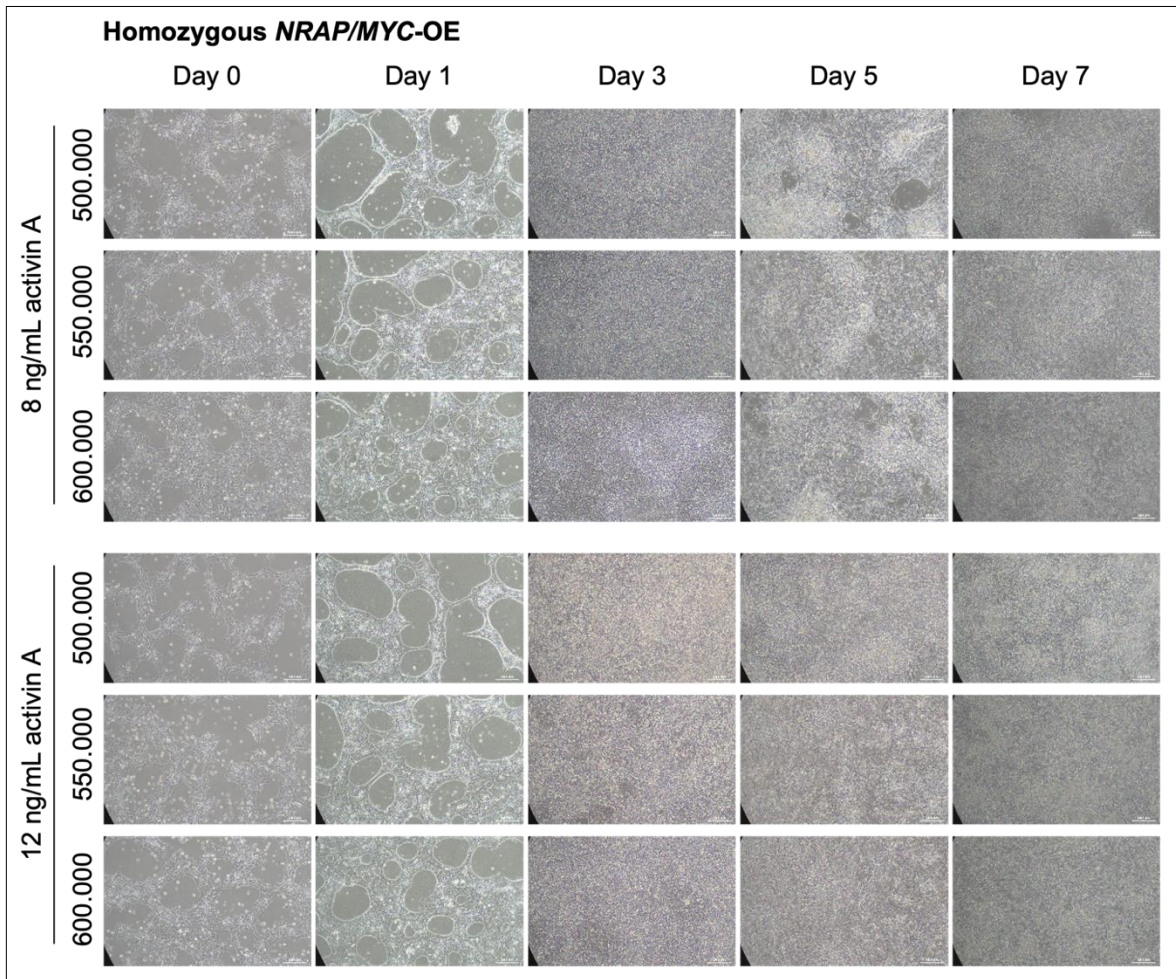
Supplementary figure 3: NRAP protein levels in *NRAP*-overexpressing (OE) and knock-down (KD) hiPSC-derived cardiac myocytes. Western immunoblot for NRAP and cardiac actin loading control from heterozygous (het) and homozygous (hom) *NRAP/MYC*-OE or *NRAP*-KD cardiac myocytes after 7 days of culture with **A**) the human NRAP antibody from Davids Biotechnology and **B**) a commercial human NRAP antibody from Merck. Cardiac actin was used as a loading control. Data are representative from two independent cardiac differentiations.



Supplementary figure 4: Quality controls for the *NRAP*-knock-down (KD) human-induced pluripotent stem cell (hiPSC) line. **A) Agarose gel representing the result of mycoplasma testing with water as negative control and previously positive-revealed samples as positive control. **B**) For investigation of genetic abnormalities, karyotypes were analysed to exclude alterations in the number of chromosomes. **C, D**) Off-target analysis of the top ten predicted off-targets sites for each gRNA that were identified by the CRISPOR website and investigated by polymerase chain reaction and subsequent Sanger sequencing. **E**) Measurement of the stage specific embryonic antigen 3 (SSEA3) by flow cytometry to determine pluripotency.**

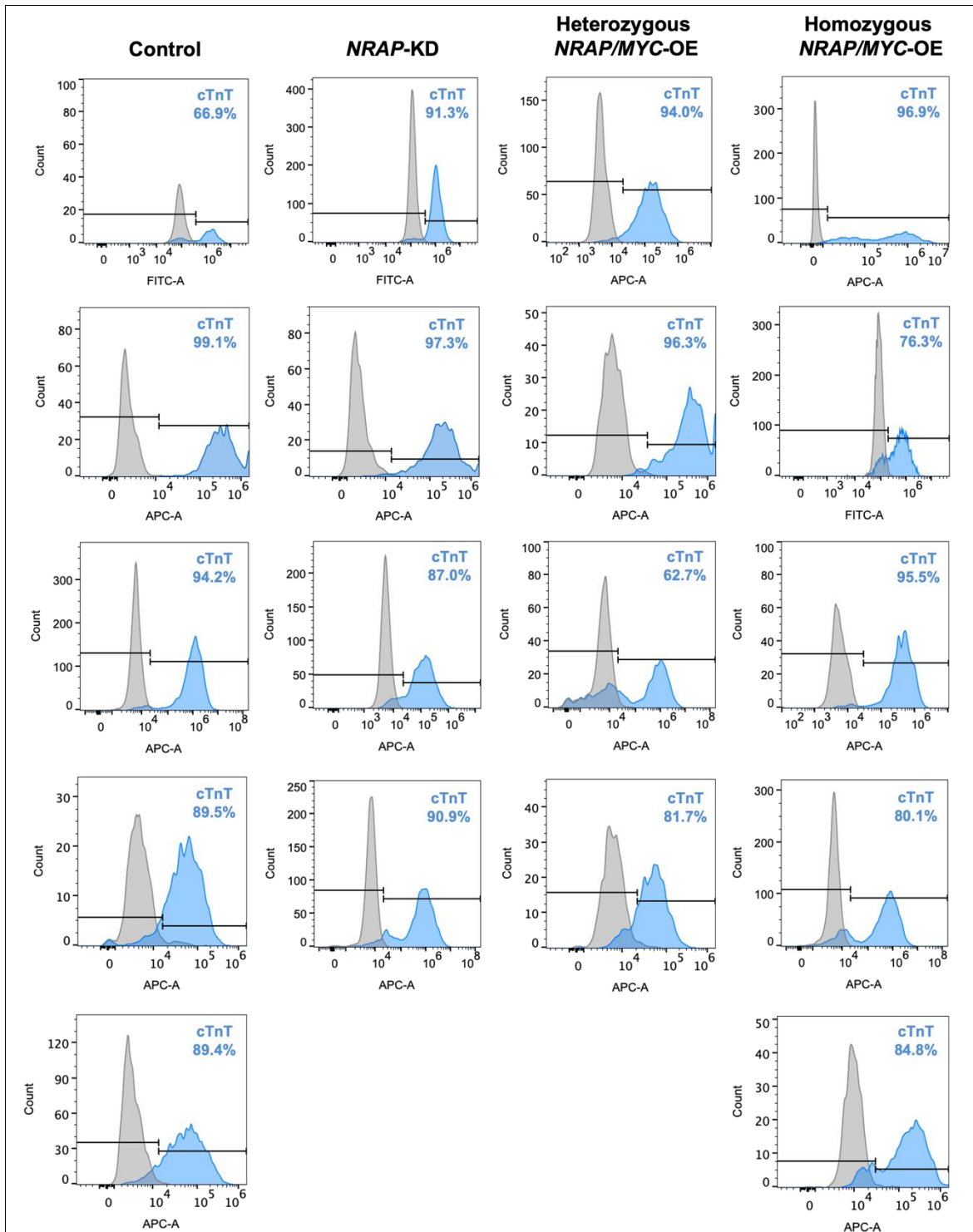


Supplementary figure 5: Testing of different conditions for cardiac monolayer differentiation for the heterozygous *NRAP/MYC-OE* cell line. Different amounts of activin A (8 ng/mL or 12 ng/mL) were used and cell densities of 500.000, 550.000 or 600.000 cells for each 35 mm dish were used. Images were taken after every medium change. These images are representative. The scale bars are equal to 200 μ m.

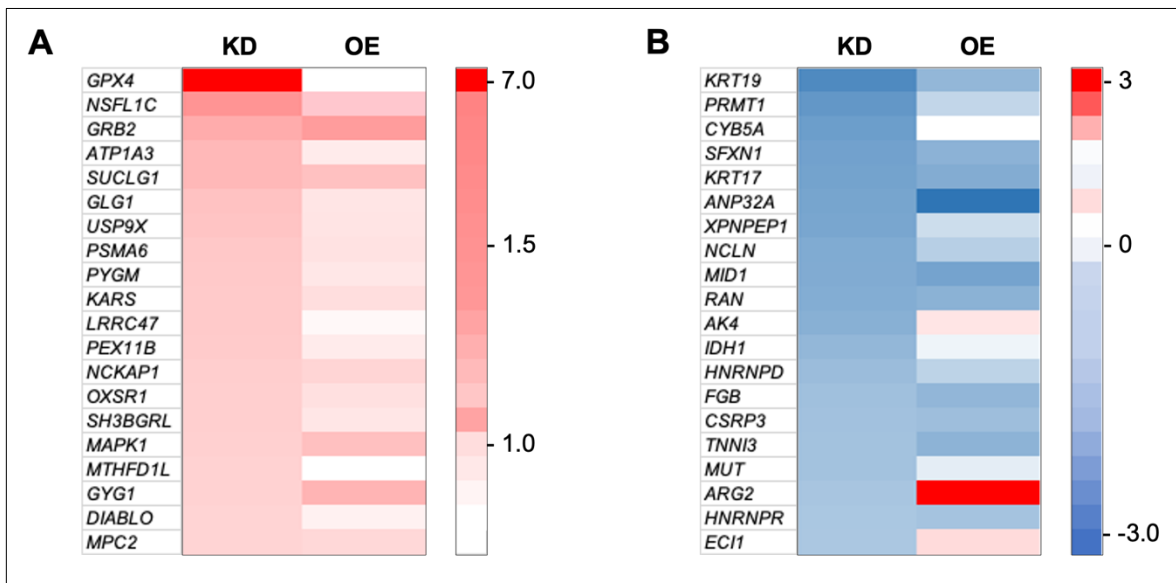


Supplementary figure 6: Testing of different conditions for cardiac monolayer differentiation for the homozygous *NRAP/MYC-OE* cell line. Different amounts of activin A (8 ng/mL or 12 ng/mL) were used and cell densities of 500.000, 550.000 or 600.000 cells for each 35 mm dish were used. Images were taken after every medium change. These images are representative. The scale bars are equal to 200 μm.

Supplements



Supplementary figure 7: Cardiac troponin T values of investigated batches of control, heterozygous and homozygous *NRAP/MYC*-overexpressing (OE) and *NRAP*-knock-down (KD) EHTs. The cardiac-specific marker troponin T (cTnT) was measured by flow cytometry from 4 batches for *NRAP*-KD and heterozygous *NRAP/MYC*-OE or 5 batches for control and homozygous *NRAP/MYC*-OE. Data were analysed and represented with FlowJo.

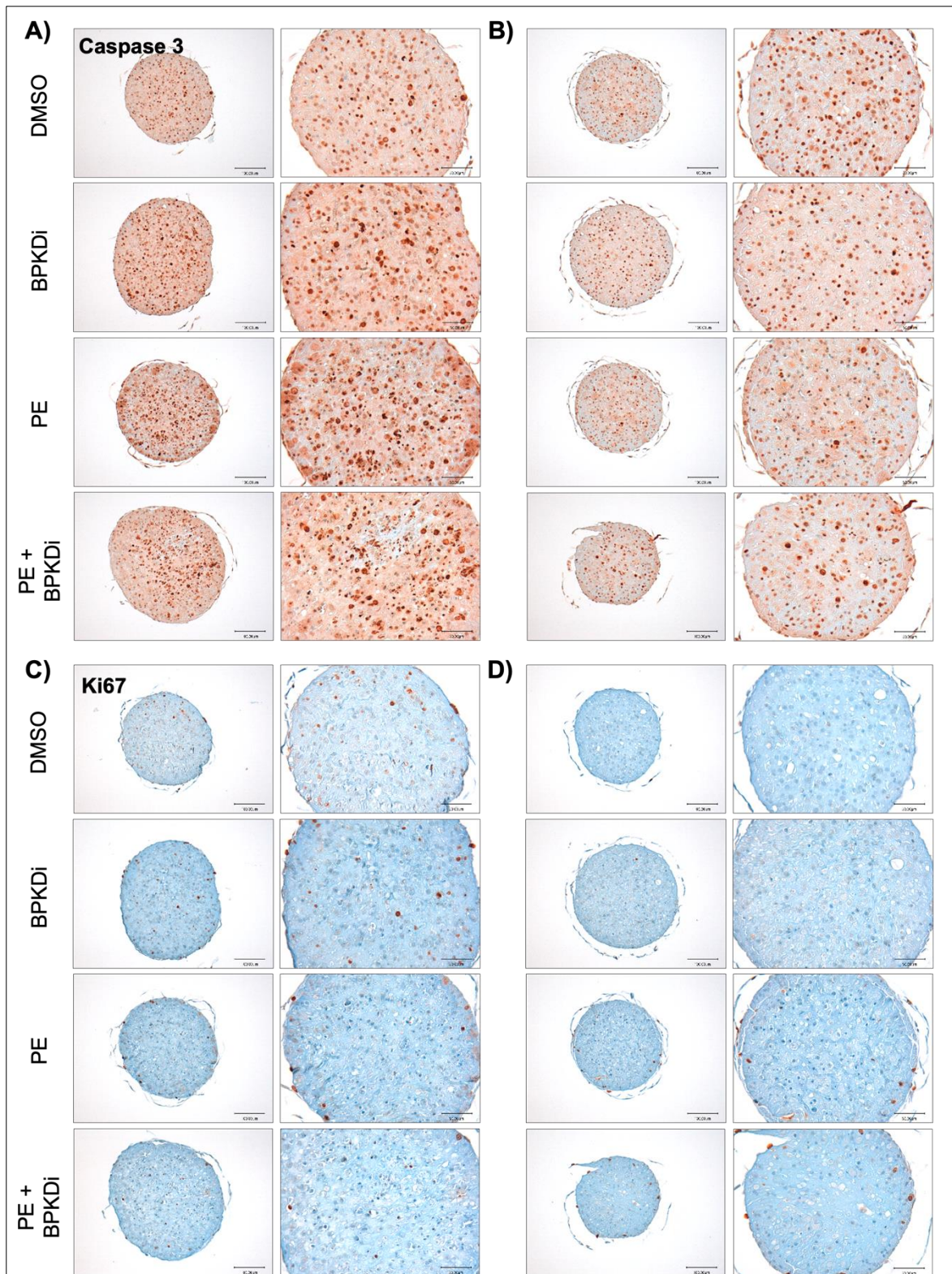


Supplementary figure 8: Clustering analysis of top higher and lower abundant proteins in NRAP-knock-down (KD) EHTs. Heatmaps represent the relative abundance as indicated by log₂ fold changes of highest (red) to lowest (blue) abundant proteins of NRAP/MYC-overexpressing (OE) and NRAP-Knock-down (KD) proteins. **A)** Top 20 higher abundant proteins in NRAP-KD EHTs and comparison to NRAP/MYC-OE EHTs, and **B)** top 20 lower abundant proteins in NRAP-KD EHTs. Mean of four samples from four independent differentiations (n = 4) with three combined EHTs each. Only values with p<0.05 were included into analysis.

NRAP antibody immunisation sequence:
AKKAHELASDIKYRQDFNK

Rattus norvegicus				Mus musculus			
Score	Expect	Identities	Positives	Score	Expect	Identities	Positives
24.8 bits(51)	5.2	7/10(70%)	8/10(80%)	25.7 bits(53)	3.0	8/18(44%)	12/18(66%)
Query	7	LASDIKYRQD	16	Query	2	KKAHELASDIKYRQDFNK	19
		LASD+KY D				K +E S++KY +DF K	
Sbjct	263	LASDVKYKDD	272	Sbjct	111	KRTQEIQISNVKYHEDFEK	128

Supplementary figure 9: Sequenz alignment of the NRAP immunisation peptide sequence with rat and mouse nebullette. The NRAP peptide sequence was aligned to nebullette of *rattus norvegicus* and *mus musculus*.



Supplementary figure 10: Impact of protein kinase D (PKD) inhibition on proliferation and apoptosis. Neonatal rat ventricular myocyte (NRVMs)- derived engineered heart tissue (EHT) were treated daily with DMSO or 3 μ M of the pharmacological PKD inhibitor BPKDi, in presence or absence of 20 μ M of the pro-hypertrophic stimulus phenylephrine (PE). The treatment was performed as an **A, C**) early treatment from day 2-9 after the generation of EHTs or **B, D**) as a late treatment from day 14-21 after the generation of EHTs when EHTs reached their force plateau. The EHTs were used for immunohistochemical staining of **A, B**) caspase 3 and **C, D**) Ki67 (n = 1). Scale bars are equal to 100 μ m.

11.2 Materials

11.2.1 Buffer and cell culture medium compositions

Table 2: Buffer compositions for SDS-PAGE and western immunoblot analysis.

3 x Reducing sample buffer

187.5 mM Tris-HCl pH 6.8
6% SDS (w/v)
30% Glycerol (v/v)
15% β -mercaptoethanol (v/v)
0.015% Bromophenol blue (w/v)

4 x Running gel buffer

1.5 M Tris base
0.4% SDS (w/v)
Adjust to pH 8.7

9% SDS running gel

2.5 mL 4x running gel buffer
3 mL 30% acrylamid (v/v)
4.39 mL ddH₂O
100 μ L TEMED
10 μ L 10% ammonium persulfate

SDS stacking gel

2.5 mL 4x stacking gel buffer
1.16 mL 30% acrylamid (v/v)
6.23 mL ddH₂O
100 μ L TEMED
10 μ L 10% ammonium persulfate

Transfer buffer

47.9 mM Tris base
38.6 mM Glycine
1.3 mM SDS (w/v)
20% Methanol (v/v)

4 x Stacking gel buffer

0.5 M Tris base
0.4% SDS (w/v)
Adjust to pH 6.8

5% SDS running gel

2.5 mL 4x running gel buffer
1.66 mL 30% acrylamid (v/v)
5.73 mL ddH₂O
100 μ L TEMED
10 μ L 10% ammonium persulfate

10.5% SDS running gel

2.5 mL 4x running gel buffer
3.5 mL 30% acrylamid (v/v)
3.89 mL ddH₂O
100 μ L TEMED
10 μ L 10% ammonium persulfate

10 x Electrophoresis buffer

0.25 M Tris base
1.92 M Glycine
0.4% SDS (w/v)

10 x TBS

199.8 mM Tris base
368.9 mM NaCl
adjust to pH 7.6 with HCl

TBS-T

10% 10 x TBS (v/v)
0.1% Tween® 20 (v/v)

Supplements

Table 3: Buffer compositions used for immunofluorescence.

<p>Immunofluorescence buffer pH 7.5 10 mM Tris 155 mM NaCl 2 mM EGTA 2 mM MgCl₂ 1% BSA (w/v) adjust to pH 7.2 with HCl</p>	<p>Mounting medium 30 mM Tris-HCl 70% Glycerol (v/v) 5% N-Propyl gallate (w/v)</p>
--	--

Table 4: Buffer and medium compositions for NRVMs isolation and culture.

<p>CBFHH buffer 0.14 M NaCl 5.4 mM KCl 0.81 mM MgSO₄*7H₂O 0.44 mM KH₂HPO₄ 0.34 mM Na₂HPO₄*H₂O 0.56 mM Glucose 100 ml Hepes stock solution</p>	<p>Hepes stock 47.66g/l Hepes adjust to pH 7.4</p>
<p>Non-cardiac myocyte medium (NCM) 500 mL DMEM (1 g glucose) 57 mL Heat-inactivated FCS 5.7 mL Pen/Strep 5.7 mL Glutamine (200 mM)</p>	<p>DNase stock solution 0.1 g DNase II, Type V 50 mL PBS</p>
<p>RIPA buffer 50 mM Tris-HCl pH 7.4 150 mM NaCl 1% (v/v) Triton-X 100 0.1% (w/v) SDS cOmplete protease inhibitor</p>	<p>Trypsin stock solution 0.9 g Trypsin 9 mL CBFHH</p>
<p>Plating medium (PM) 335 mL DMEM + Glutamax 85 mL M199 50 mL Horse serum 25 mL FCS 5 mL Pen/Strep</p>	<p>Trypsin-working solution 0.5 mL P/S 100-X 0.6 mL DNase stock 1.3 mL Trypsin stock 47.6 mL CBFHH</p>
<p>Pre-plating medium (PPM) 32 mL Plating medium 16 mL FCS</p>	<p>DNase-working solution 0.5 mL P/S 100-X 0.6 mL DNase stock 1.7 mL FCS 47.2 mL CBFHH</p>
	<p>Maintenance medium (MM) 197.5 mL DMEM + Glutamax 50 mL M199 2.5 mL Pen/Strep</p>

Supplements

Table 5: Buffer and medium compositions for hiPSC culture, cardiac myocyte differentiation, cardiac myocyte culture, dissociation of cardiac myocytes and flow cytometry.

FTDA

DMEM/F-12 without glutamine
2 mM L-glutamine
0.1% Lipid mix (v/v)
5 mg/L Transferrin
5 µg/L Selenium
0.1% (v/v) Human serum albumin
5 µg/mL Human recombinant insulin
2.5 ng/mL Activin-A
30 ng/mL FGF
50 nM Dorsomorphin
0.5 ng/mL TGFβ1

Stage 0

StemPro-34™ SFM + Supplement
1 µg/L BMP4
2 mM GlutaMAX
1% Matrigel high growth factor (v/v)

Stage 1

StemPro-34™ SFM + Supplement
10 µg/L BMP-4
2 mM GlutaMAX
8 or 12 ng/L Activin A

Stage 2.1

RPMI 1640
2% B27 (without Insulin)(v/v)
10 µM XAV939
10 µM KY021111

Stage 2.2

RPMI 1640
2% B27 (v/v)
10 µM KY021111
10 µM XAV939
25 µM Insulin

Cardiac myocyte medium

RPMI 1640
2% B27 (v/v)
25 µM Insulin

mTESR+

400 mL mTESR+ basal medium
100 mL mTESR 1 5x Supplement

FGF stock

0.1 µg/mL FGF
10% Human serum albumin
PBS

LB medium

10 g Tryptone
5 g Yeast extract
10 g NaCl
Add to 1 L aqua destillata
100 mg ampicillin/mL

Washing buffer

HBSS (without calcium/magnesium)
10 µM Y-27632

Dissociation buffer (cardiac myocytes)

HBSS (without calcium/magnesium)
200 U/mL collagenase II
1 mM HEPES
10 µM Y-27632
30 µM BTS

Dnase solution

100 mg Dnase II, type V
50 mL PBS

Flow cytometry buffer

PBS
5% FBS (v/v)
0.05% sodium azide (v/v)
0.5% saponin (w/v)

Cardiac myocyte thawing medium

RPMI 1640
10% B27 + Insulin

TAE buffer

0.4 M Tris acetate
0.01 M EDTA
ddH₂O, pH 8.3

Supplements

Table 6: Buffer and medium composition for generation, culture and dissociation of EHTs.

<p>Agarose for EHT casting 2% Agarose (w/v) PBS Sterilised by autoclaving before use</p>	<p>Dissociation buffer (EHTs) 10 U/mL Papain 1 mM EDTA 5.5 mM L-Cysteine-HCl EBSS</p>
<p>EHT medium DMEM 1% Penicillin/streptomycin (v/v) 33 mg/L Aprotinin 10% Horse serum inactivated (v/v) 10 mg/L Insulin</p>	<p>Thrombin 1000 U Thrombin 4 mL Aqua ad injectabilia 6 mL PBS</p>
<p>Tyrodes solution 120 mM NaCl 5.4 mM KCl 1 mM MgCl₂ x 6H₂O 0.4 mM NaH₂PO₄ 22.6 mM NaHCO₃ 5 mM glucose 0 mM CaCl₂ for wash 0.6 mM CaCl₂ for submaximal 1.8 mM CaCl₂ for baseline Aqua ad injectabilia</p>	<p>2 x DMEM 536 mg DMEM powder 4.8 mL Horse serum 0.4 mL Pen/Strep Add to 20 mL aqua ad injectabilia Filter sterile (0.22 µm)</p>
	<p>Fibrinogen 200 mg/mL fibrinogen 100 µg/mL aprotinin 0.9% NaCl solution</p>

Table 7: Media and sera.

Compound	Company (Catalogue number)
Bovine serum albumin	Sigma, A9647
DMEM	Biochrom, F0415
DMEM/F-12 without glutamine	Gibco, 11530566
DMEM + Glutamax	Gibco, 31966047
Fetal bovine serum superior	Biochrom, S0615
Horse serum	Life Technologies, 26050-088
Human serum albumin	Biological Industries, 05-720-1B
M199	Gibco, 11825015
mTeSR plus	StemCell Technologies, 05825
Normal goat serum	Sigma, NS02L
OptiMEM reduced serum medium	Thermo Fisher, 11058021
RPMI 1640	Life Technologies, 21875-034
SILAC medium	Silantes, 282926433
StemPro™-34 SFM	Life Technologies, 10639011

11.2.2 Antibodies, kits and enzymes

Table 8: Antibodies for immunofluorescence, western immunoblotting and flow cytometry.

Antibodies used for immunofluorescence	Species	Dilution	Catalogue number	Company
Sarcomeric α -actinin	mouse	1:500	A7811	Sigma
Golgi 58K Protein	mouse	1:100	G2404	Sigma
NRAP	rabbit	1:500	-	Dauids Biotechnology
NRAP	rabbit	1:50	HPA037954	Merck
AlexaFluor 488 (F(ab') ₂ fragment)	goat anti-mouse	1:100	A-11001	Invitrogen
AlexaFluor 488	goat anti-rabbit	1:100	A-11008	Invitrogen
DyLight-547	goat anti-rabbit	1:100	ab96884	Abcam
AlexaFluor 647	goat anti-mouse	1:100	A-21235	Invitrogen
Dyes				
4',6-diamidino-2-phenylindole (DAPI)	-	1:100	D9542/32670	Sigma
Phalloidin/ DY-633	-	1:100	A22284	Invitrogen
Wheat germ agglutinin	-	1:100	29022-1	Biotium
MitoSPY	-	1:100	424803	BioLegend
Antibodies used for western blotting				
Cardiac actin	mouse	1:2000	AC1-20.4.2	Progen
Sarcomeric α -actinin	mouse	1:500	A7811	Sigma
Sarcomeric myosin heavy chain	mouse	1:1000	A4.1025	DSHB
c-MYC	mouse	1:1000	AC1-20.4.2	Merck
NRAP	rabbit	1:500	-	Dauids Biotechnology
NRAP	rabbit	1:500	HPA037954	Merck
HRP-conjugated anti-rabbit	donkey-anti-rabbit	1:1000	NA9340V	Amersham
HRP-conjugated anti-mouse	sheep-anti-mouse	1:1000	NA9310+D33: D35V	Amersham
Flow cytometry				
REA control - PE		1:50	557714	BD Biosciences
Anti-SSEA-3 - PE		1:50	561145	BD Biosciences
REA Control - APC		1:50	130- 120-709	Miltenyi Biotec
Anti-cardiac Troponin T - APC		1:50	130- 120-403	Miltenyi Biotec
REA Control - FITC		1:50	130- 120-709	Miltenyi Biotec
Anti-cardiac troponin T- FITC		1:50	130-119-674	Miltenyi Biotec

Supplements

Table 9: Kits and enzymes.

	Company	Catalogue number
DNeasy blood & tissue kit	Qiagen	69504
Amaxa™ P3 Primary Cell 4D-Nucleofector Kit	Lonza	V4XP-3024
Clarity™ western ECL substrate kit	Bio-Rad	1705060
High capacity cDNA reverse transcription kit	Applied Biosystems	4368814
Maxima SYBR Green/Rox qPCR master mix	Thermo Fisher	K0221
High pure PCR purification kit	Roche	11732676001
SuperScript™ III Reverse Transcriptase Kit	Invitrogen	18080093
DreamTaq DNA polymerase	Thermo Fisher	EP0705
Q5® High-Fidelity DNA Polymerase	NEB	M0492S
LongAmp Taq PCR Kit	NEB	E5200S
FastDigest BamHI	Thermo Fisher	FD0054
FastDigest BglII	Thermo Fisher	FD0083
TRIzol Reagent	Life Technologies	15596026
CytoTune-iPS Sendai Reprogramming Kit	Life Technologies	A1377801
β-galactosidase staining kit	Cell signaling technology	9860

11.2.3 Primer

Table 10: Primer sequences used in this thesis for sequencing, validation and qPCRs.

Name	Forward primer	Reverse primer
NRAP sequencing 1	GTTGTGCTTTCTCTGACCAG	
NRAP sequencing 2	CACCGAGCTGCAAGAAC	
NRAP sequencing 3		GGCTGCACATTCATGGTG
NRAP sequencing 4	GTGTTGCATTCTCTCTGG	
NRAP sequencing 5	GGAATGTGCAGACCAATATGG	
NRAP sequencing 6	GAGTAAGACCCGGTTTCACC	
NRAP sequencing 7	GGTCATTAATGTGGAGCAGG	
NRAP sequencing 8	GCGTAATCTTCGTGCTCAAG	
NRAP sequencing 9	CCAGTGATGTGCACTACAGG	
NRAP sequencing 10		CTAGGACGCACCATTCTCAC
NRAP sequencing 11	CAGAATAAGTTGGTCCTGAG	
NRAP sequencing 12	CCACTGGTAACAGGATTAGC	
NRAP sequencing 13	GAATAGTGTATGCGGCGAC	
NRAP sequencing 14	AGAGGGCATGATGAACGCAT	
NRAP sequencing 15		ATCACTTGCCAGCTCATTGG
NRAP sequencing 16		GTGTCCTGTAGTCGTGGTCCG
HA-L Insert 1	CTTCGACCTACTCTCTCCGC	GTA CTCCGGTCATCTCGAGC
HA-R insert 2	CCTGGCTTTAGCCACCTCTC	ACAGTGACCAACCATCCCTG
OE validation 1	GCAGGCTCCAGAGTGACAAT	GCATTCTAGTTGTGGTTTGTCCA
OE validation 2	CAGTGTCGACGATGACCCAA	GGGTCATATGTCACAGATCCTCT
NDUFA4L2 qPCR	CGCTTTACTTGCTGCGACTC	GGTCGGTACAGTCGAAGGTG
NDUFA4 qPCR	AAGCCACATCCGCACAATTT	AGTTCAG AGCATACTTTCAGCAT
HIF1A qPCR	GAGCACCTT GTGCAGTTTGG	CTAAACCCTGAGCCGTGACA
KD Validation 1	GTCAGCAGCTGTCCCTTGATTTAC	GATTACAGCAGGCCGTCCAAG
KD Validation 2	CTGCATGTGAACCTGCCATTTC	GCAGCATGTGTAGAGGCCACACAG
Human NRAP qPCR	GTA CTGTACGCCCATAACC	CCAGTGGCTGCCTGTTAG
Human GusB qPCR	ACGATTGCAGGGTTTCACCA	CACTCTCGTCGGTGACTGTT

Table 11: Off-target primer.

Off-target gene	Forward primer	Reverse primer
<i>TTN</i>	GTTGGGCGTCCCTTGATGA	ACTCAAGTGCTATGTGGAGCAT
<i>APPL2</i>	AGCTTCCGGCCTTACAGATG	TGGGGGAATATGGAATGTCCAAG
<i>CDK8</i>	TAGTGCCTTCCAAAATGCCTG	GGGGAAGAAACCCACAAAACAT
<i>RP11-556E13.1</i>	GCATCTTGCTTGAAGGTGTAGG	TCTGTCTGACCACAAACTGCAT
<i>QRFRP</i>	GGCTCATCACTCCTAAAGGCA	ACCACATCCAAACCAGGACT
<i>RP11-40A13.1</i>	AAGGCACTGCAGTCGTTAC	CAGTTCTGCCCCGCTCTTAG
<i>MLIP-IT1</i>	AGGGCAAGGGGCTTTATCTT	AGATAGTGCTAGGCCATTTGGG
<i>SLC8A1-AS1</i>	ACCCTAGTAGTGGTCTCCAG	GCCTAGCTTCACCTCTCATCT
<i>RHOT2</i>	CATCCTGTTACTGGGCGAGG	CGCTACCTGAGTAGTCCACG
<i>NAB1</i>	ATTAAAGCCTGGGAATGGGTGA	AGAAAGCCCTCTGCATGGGTA
<i>SLC38A3</i>	TCAAAGGGGGTGGTGTTCATC	AGAAGTCAGGAGCTTGTCCC
<i>CLIC5</i>	TGCACATCTAGTGCAGGAGC	GCATAAAGCACGGCAAACCA
<i>EPC2</i>	AGGTTGGACTGCTTCAGATGAG	ACGTCTTCAGTGAAATCTGACCA
<i>PSD4</i>	GTGTGTGACACTTTGATGCTCC	GTTGAAGGTCTGGTTCCGGT
<i>EBP</i>	AGTATGCCAAGGGAGACAGCC	CTGGAAGGGCACCGTTGAG
<i>ABCB9</i>	CACTCATGAAGGCCAAAGTCACC	GCAGTGGGCACTCAGTAAGTATCC
<i>MLLT6</i>	CCTGTAACCGCCATGGATGTCGAC	CTTGGGCAGGGACTGGGTTTTTTT
<i>RP11-506D12</i>	GGACTCATGGGACACCTTTCC	GTGTTGGGGCTCTAAGAACTGG
<i>PGPR26</i>	GAGCACCTTTTCTGTGGAGC	CACGGGTGTCACCTGAAATGTTT
<i>RHOBTB2</i>	CACTGCATGGAGACCTCGTT	TTTAGCAGCCCGGAGTCATC
<i>RNU6</i>	CGTGCCAGCCTACAATAACAC	GCACATCTCCTTGCCCTTAGA
<i>RP11-34F13.3</i>	AAAGCACCTTGTTGCAGTTGAT	CTAAACCTGTCTGTTATAGGCTTGA
<i>MRRF</i>	AGTGGTACCAGGAGTGGACAT	GGACAACCACCCCGTTTCAT
<i>RP11-181K12</i>	GCCTGCCCTTTACAAACGAAA	CCCGGCATGATATGGTGTTT
<i>RN7SKP279</i>	CCTCCATAGTACTGGTGTGACC	GTGGTAAGAGATGAGTTTGGCTGC
<i>EXT1</i>	GCCTCTGTGCTAAGAGTGTAAAGAC	CATCTTTGTGGACCTGGAGGATC
<i>FOXO3</i>	GACTTTCCAGCTCAGTAGCTGG	GACTTACTGTAAGCGCCGAGG
<i>ZC3HAV1</i>	CCTCAGCAGAGGTATAGATCCTGG	ACTCCTCAGTCCAGCATTGTTAG
<i>RPL11-TCEB3</i>	CTCAGTGCTCTTGTGCAACTGTAG	CCTATGCTGAAGACCTCCAAACAG
<i>ZNF720</i>	CACCAACTCGCAATCTTTCTGCTC	CCCCTGGTCTTGAGATCTTGAGA

11.2.4 Devices, consumables and programmes

Table 12: Devices and respective manufacturer.

Device	Manufacturer
4D-Nucleofector™ Core Unit	Lonza
4D-Nucleofector™ X Unit	Lonza
7900HT Fast Real-Time PCR system	Applied Biosystems
Accu-jet Pro	BRAND
Analytic Scale Genius	Sartorius AG
Avanti JXN-26 centrifuge	Beckman Coulter
Axiovert 25	Zeiss
Benchtop centrifuge	Sarstedt AG & Co.
Cell culture incubator CB 220	Binder
Cell culture incubators MCO-19M & MCO-20AIC	Sanyo
Cell culture incubators S2020 1.8, HERAcell 240 & 150i	Thermo Fisher Scientific
Centrifuge 5415 R/5415R/5810R	Eppendorf
Centrifuge universal 30RF	Hettich
ChemiDoc™ touch imaging system	Bio-Rad Laboratories
Cryopreservation system Asymptote EF600M	Grant Instruments
Cryopreservation system asymptote EF600M	Grant Instruments
Cryostar Nx70	Thermo Scientific
Cryostat Leica CM 300	Leica
Ice machine	Scotsman Ice Systems
Incubator shaker (C25 classic)	New Brunswick Scientific
J2-21 centrifuge	Beckmann
LSM 800 airyscan confocal microscope	Carl Zeiss
Magnetic stirrer	Janke & Kunkel
Magnetic stirrer/heating plate	Gerhardt
Mastercycler pro 384	Eppendorf
Mastercycler pro PCR system	Eppendorf
Microscope Axioskop 2 with AxioCam colour	Zeiss
Microscope EVOS FL cell imaging system	Thermo Fisher scientific
Microwave	Bosch
Milli-Q Reference C79625	Merck Millipore
Mini centrifuge Combi-spin FVL-2400N	peQLab Biotechnologie GmbH
Mini Protean 3 cell and Trans-Blot cell	Bio-Rad Laboratories
Mini Protean tetra handcast system	Bio-Rad Laboratories
Mini Protean tetra vertical electrophoresis cell	Bio-Rad Laboratories
Mr. Frosty freezing container	Sigma
Multiplate reader	Tecan GmbH
Nanodrop 1000 spectrophotometer	Thermo Fisher Scientific
nCounter® SPRINT	Nanostring
Neubauer counting chamber	BRAND GmbH
Neubauer counting chamber	Karl-Hecht KG
NovoCyte Quanteon flow cytometer system	Agilent
PCR cycler (2720 Thermal cycler)	Applied Biosystems
PCR cycler (GeneAmp® PCR System 9700)	Applied Biosystems
pH meter	Mettler-Toledo
Pipettes (2, 10, 20, 100 and 1000 µL)	Eppendorf
Power supply EV243	peQLab Biotechnologie GmbH

Supplements

PowerPac basic power supply	Bio-Rad Laboratories
Precision Advanced Scale	Ohaus
qPCR plate, 384-well	Thermo Fisher
Quant studio qPCR (ABI Prism 7900HT)	Thermo Fisher
Sterile work bench HS-12	Heraeus Instruments
Stirrer Variomag/ Cimarec Biosystem 4	Thermo Fisher scientific
Sub-cell GT electrophoresis cell	Bio-Rad Laboratories
TE77 semi-dry transfer unit	GE Healthcare
Thermoblock Techne Ori-Block DB-1	Techne
Thermomixer comfort	Eppendorf
Tissue lyser	Qiagen
Tissue lyser II	QIAGEN
TubeRoller R3005	Benchmark Scientific
Varioklav	MediTech
Video-optical EHT analysis system	EHT Technologies GmbH
Vortex Reax 200	Heidolph
Vortexer	Heidolph
Warming cabinet Kelvitron	Heraeus Instruments
Water bath	Medax

Table 13: Consumables and manufacturer.

Consumable items	Manufacturer
250 mL and 500 mL vacuum filter unit	TPP
Cell culture plates (48 well, 24 well, 12 well, 6 well)	Nunc, Thermo Fisher
Aspiration pipette 2 mL	Sarstedt
Blotting membrane (nitrocellulose, PDVF)	GE Healthcare
Blotting-System (Mini Trans-Blot® cell)	Bio-Rad
Cell culture flask T75, T175	Sarstedt
Cellulose paper	GE Healthcare
Cell scraper	Sarstedt
Comb 10 well/15 well (1.0 mm, 1.5 mm)	Bio-Rad Laboratories
Cryovials 2mL	Sarstedt
Eppendorf tubes (1.5 mL, 2.0 mL)	Eppendorf
Falcon tubes (15 mL and 50 mL)	Sarstedt AG & Co.
Glass cover slip	VWR
Glassware	Schott Duran
Hamilton syringe (25µl, 100µl)	Hamilton
Nitril powder-free gloves	Ansell
Parafilm	Bemis
PCR tube strips	Sarstedt
Petri dishes	Sarstedt
Pipette tips with filter Biosphere	Sarstedt
Pipette filter tip (10 µL, 200 µL, 1000 µL)	Sarstedt
Pipette tip (10 µL, 200 µL, 1000 µL)	Sarstedt
Pipettes 10 µL, 100 µL, 1000 µL	Eppendorf
Serological pipette (1 mL, 2 mL, 5 mL, 10 mL, 25 mL, wide-mouth)	Sarstedt
Steel beads, 5 mm	QIAGEN

Supplements

SuperFrost Plus microscope slides	R. Langenbrinck GmbH
Cell culture microplate 96 well µClear® black CELLSTAR	Greiner
Cell culture plate 6 / 12 / 24-well	Nunc
Cell scraper	Sarstedt
Cell strainer 100 µm (Sysmex,)	Sysmex
Cryovial CryoPure 1.6 mL	Sarstedt
Flow cytometry tubes	Sarstedt
Pacing adapter/cables	EHT Technologies GmbH
Pacing electrode carbon	EHT Technologies GmbH
Reaction tubes conical 15 / 50 mL	Sarstedt
Reaction tubes safe lock 0.2 – 2 mL	Eppendorf
Round bottom tube 12 mL	Greiner
Silicone rack	EHT Technologies GmbH
Syringe filtration unit Filtropur S 0.2 µm	Sarstedt
Teflon Spacer	EHT Technologies GmbH
TissueLyser Steel Beads	QIAGEN
EHT PDMS rack	EHT Technologies GmbH
EHT PTFE spacer	EHT Technologies GmbH
Flow cytometry tubes	Sarstedt

Table 14: Programmes and corresponding companies that were used in this thesis.

Programme	Company
AxioVision Rel. 4.8.2	Zeiss
BioRender	BioRender
CRISPOR 4.99	(Concordet JP, Haeussler M)
Endnote X6	Clarivate
Excel	Microsoft
FACSDiva	BD Biosciences
FlowJo V10	BD Biosciences
Image Lab	Bio-Rad Laboratories
ImageJ	NIH
Labchart	ADInstruments
nCounter	Nanostring
Prism 8.0	GraphPad Software
Sequence Detection Systems 2.4	Applied Biosystems
SnapGene® 3.3.4	GSL Biotech LLC
ZEN 2012	Zeiss

11.2.5 Chemical compounds including H- and P-statements

Table 15: Substances and chemicals with corresponding company names and H- and P-statements.

Substance/ Chemical	Company	Catalogue number	H-statement	P-statement
1-Thioglycerol	Sigma	M6145	H: 302, 311, 331, 315, 317	P: 261, 264, 280, 301, 312, 302, 352, 312, 304, 340, 311
1,4-Dithiothreitol (DTT)	Roth	6908.2	H: 302, 315, 319, 412	P: 264, 270, 273, 280, 337, 313, 501
2-Mercaptoethanol	Sigma	M6250	H: 301, 331, 310, 315, 317, 318, 373, 410	P: 270, 280, 302+352, 330, 304, 340, 305, 351, 338, 310
2-Propanol	Roth	9866.6	H: 225, 319, 336	P: 210, 261, 305, 351, 338
2x DMEM	Gibco	52100-021	-	-
6x DNA loading dye	Thermo Fisher	R0611	H: 315-319- 335360	P:201-261,305+351+ 338308+313
Accutase® Cell Dissociation Reagent	Sigma	A6964	-	-
Acetic acid	Roth	6755.1	H: 226, 290, 314	P: 210, 280, 301, 330, 331, 305, 351, 338, 308, 310
Acetone	Merck	67-64-1	H225, H319, H336	P: 210, 240, 305, 351, 338, 403, 233
Activin A	R&D Systems	338-AC	-	-
Acrylamide/bis solution (30%)	Bio-Rad		H: 302, 312, 315, 317, 319, 340, 350, 361, 372	P: 260, 280, 281, 305, 351, 338, 405, 501
Agar	BD Biosciences	214010	-	-
Agarose	Invitrogen™	15510-027	-	-
Alt-R® Cas9 Electroporation Enhancer	IDT	1075916	-	-
Alt-R® CRISPR- Cas9 crRNA	IDT	self- designed	-	-
Alt-R® CRISPR- Cas9 tracrRNA, 5 nmol	IDT	1072532	-	-
Alt-R™ S.p. Cas9 Nuclease V33	IDT	1081058	-	-
Ammonium acetate	Merck		-	-
Ammonium persulphate (APS)	Bio-Rad	1610700	H: 272, 302, 315, 317, 319, 334, 335	P: 210, 221, 285, 305, 351, 338, 405, 501
Aprotinin	Sigma/Merck	A1153	-	-
Aqua ad iniectabilia	Baxter	1428	-	-
B27	Gibco	17504-044	-	-
bFGF	Peptrotech	233-FB	-	-
BMP4	R&D systems	314-BP	-	-

Supplements

Bovine serum albumin (BSA)	Sigma		-	-
Bromophenol blue	Sigma	115-39-9	-	-
BTS (N-Benzyl-p-Toluenesulfonamide)	TCI	B3082-25G	H: 301	P: 264, 270, 301+310, 321, 330, 405, 501
Calcium chloride (CaCl ₂)	Roth	10043-52-4	H: 319	P: 280, 305, 351, 338, 337, 313
Carbon dioxide (CO ₂) gas	SOL		H: 280	P: 403
CloneR 10x Cloning Supplement	StemCell Technologies	0588	-	-
Collagenase II	Worthington	LS004176	H: 334	P: 261, 284, 304+340, 342+311
cOmplete protease inhibitor cocktail tablets	Merck	11697498001	-	-
Coomassie Blue G250	Bio-Rad	1610406	-	-
Dimethyl sulfoxide (DMSO)	Sigma	D4540	-	-
Dithiothreitol (DTT)	Roth	3483-12-3	H: 302, 315, 319, 412	P: 302, 350, 260, 270, 305, 351, 338, 337, 313
DNase II, type V	Sigma/Merck	D8764	-	-
Dorsomorphin dihydrochloride	Tocris	3093	-	-
Ethanol, absolute	Chemsolute®	22461000	H: 225, 319	P: 210, 240, 305, 351, 338, 403, 233
Ethylene diamine tetraacetic acid (EDTA)	Roth	8043.2	H: 319	P305+351+338
Ethylene glycerol tetraacetic acid (EGTA)	Roth	67-42-5	H: 319	P: 305+351+338
Fetal calf serum (FCS)	Gibco™	A4766801	-	-
Fibrinogen	Sigma	F8630	-	-
Geltrex	Gibco™	A1413302	-	-
GeneRuler 1 kb DNA Ladder	Thermo Fisher	SM0313	-	-
GeneRuler 100 bp DNA Ladder	Thermo Fisher	SM0243	-	-
Glucose	Merck	110187-42-3	-	-
Glutamine	Gibco™	25030-081	-	-
Glutaraldehyde	Science Services	E16222	H: 302, 314, 317, 331, 334, 400,411	P: 285, 310, 303, 361, 353, 305, 351, 338, 405, 501
Glycerol	Merck		-	-
Glycine	Roth		-	-
HBSS (-) Ca ²⁺ /Mg ²⁺	Gibco	14175-053	-	-
HEPES	Roth	9105.4	-	-
Horse serum	Gibco		-	-

Supplements

Hydrochloric acid, 37% fuming	Emsure®	7647-01-0	H: 290, 314, 335	P: 280, 301, 330, 331, 305, 351+338, 308, 310
Insulin	Sigma	I9278	-	-
Isoprenaline	Sigma	I6504	H: 315, 319, 335	P: 261, 264, 271, 280, 302, 352, 305, 351, 338
KY02111	Tocris	4731	H: 302, 400	P: 273
Lipidmix	Sigma	L5146	H: 225, 319	P: 210, 233, 240, 241, 242, 305, 351, 338
Loading dye, 6x	Thermo scientific	R0611	H: 315, 319, 335, 360	P: 201, 261, 305, 351, 338, 308, 313
Magnesium chloride (MgCl ₂)	Invitrogen	R0971	-	-
Matrigel®	Corning	354234, 354230	-	-
Methanol	J T Baker	10241061	H: 225, 331, 311, 301, 370	P: 210, 233, 280, 302, 352
Midori Green	Biozym	617004	H: 319, 335, 315	P: 261, 280
Milk powder	Carl-Roth	T145.2	-	-
N,N,N',N'-Tetramethylethylenediamine (TEMED)	Biorad	161-0801	H: 225, 332, 302, 314	P: 210, 233, 280, 301, 330, 331, 305, 351, 338, 308, 310
Nitrogen, liquid	TMG	-	-	-
Normal goat serum (NGS)	Sigma	G9023	-	-
OCT (tissue freezing medium)	Sakura	6200	-	-
Paraformaldehyde 16% solution (PFA)	Agar Scientific	AGR1026	H: 331, 341, 350, 302, 312, 315, 319, 317, 335	P: 101, 102, 103, 261, 280, 301, 312, 305, 351, 338, 405, 501
Penicillin/Streptomycin (Penstrep)	Gibco	15140	H: 315, 317, 334, 335	P: 280, 261, 264, 284, 271, 302, 352, 304, 340, 333, 313
Phenylephrine	Sigma	P6126	H:302, 315, 319-335	P:261, 305, 351, 338
Phorbol 12-myristate 13-acetate (PMA)	TOCRIS Bioscience	1201	H: 315	P: 264, 280, 302, 352, 333, 313
Phosphate buffered saline (PBS)	Gibco	14190250	-	-
Ponceau S staining solution	Sigma	A40000279	H: 315, 319, 335	P: 261, 305, 351, 338
Potassium chloride	Merck	-	-	-
Precision Plus Protein™ Dual Color Standard	Bio-Rad	1610374	-	-
Proteinase K	Qiagen	19133	H: 334	P: 304+340, 261, 342+311, 284
Puromycin	Invivogen	QLL-38-04B	H:302	
Pursept	Schülke	-	H: 226, 319	P: 210, 280, 305, 351, 338, 337, 313, 403, 235
Roti®-Histofix 4%	Carl-Roth	P087.3	H: 302, 317, 341, 350	P: 261, 280,

Supplements

Saponin	Sigma	8047-15-2	H: 319, 335	P 261, 305+351+338
Sodium azide	Sigma	71290	H: 300-400-410	P: 273–309-310
Sodium chloride	B. Braun	3570210	-	-
Sodium dodecyl sulphate (SDS)	Carl-Roth	151-21-3	H: 228, 302, 332, 315, 318, 335, 412	P: 210, 261, 280, 302, 352, 305, 351, 338, 312
SYBR Green/Rox qPCR Master Mix (2x)	Thermo Fisher	K0222	-	-
TBS	Sigma	T6664	-	-
TGF beta 1	Peprro Tech	100-21	-	-
Thrombin	Sigma	T7513	H: 315, 319, 334, 335	P: 261, 305+351+338, 342+311
Transferrin human	Sigma Aldrich	S5261	-	-
Tris-base	Sigma/Merck	T1503	H: 315, 319, 335	P: 261, 305, 351, 338
Tris-HCl	Sigma/Merck	1185-53-1	H: 315, 319, 335	P: 280, 302, 352, 305, 351, 338
Triton X-100	Roth	3051.3	H: 302, 315, 318, 410	P: 273, 301, 312, 330, 302, 352, 305, 351, 338, 310
TRizol reagent	Life Technologies	15596026	H: 301, 311, 331, 314, 335, 341, 373, 412	P: 260, 264, 273, 280
Trypan blue stain (0.4%)	Biochrom	L 6323	H: 350	P: 201, 308, 313
Tryptone	BD Biosciences	211705	-	-
Tween 20	Sigma/Merck	P1379	-	-
XAV939	Tocris	3748	H: 301, 319	P: 301+310, 305+351+338
Y-27632	Biorbyt	PKI-Y27632-010	H: 302-312-332	P: 280
Yeast extract	BD Biosciences	212750	-	-
N-Propyl gallate	Sigma	121-79-9	-	-
MgSO ₄ *7H ₂ O	Sigma		-	-
KH ₂ PO ₄	Sigma	P0662	-	-
Na ₂ HPO ₄ *H ₂ O	Sigma	7782-85-6	-	-
Selenium	Sigma	214485-5G	H: 300+330, 315, 317, 319, 411	P: 273, 280, 301+310+330, 302+352, 304+340+310, 305+351+338
MgCl ₂ x 6H ₂ O	Merck	1374248	-	-
NaH ₂ PO ₄	Merck	7558-80-7	-	-
NaHCO ₃	Sigma	144-55-8	-	-
Papain	Sigma	P4762	H: 315, 319, 334, 335	P: 302, 352, 305, 351, 338
Gelantine	Sigma	G1393	-	-
Bipyridyl PKD inhibitor (BPKDi)	Axon Medchem	1201673-28-0	-	-

Supplements

Bafilomycin A1	Sigma	1914819-148	-	-
MG132	Sigma	M7449	-	-

11.3 Financial support

This thesis was supported by a stipend of the Studienstiftung des Deutschen Volkes and the German centre for cardiovascular research (DZHK). In addition, laboratory materials were funded by the DZHK, the German Heart Foundation and the University-Medical Centre Hamburg-Eppendorf.

11.4 Declaration of contribution

The results of this thesis are currently unpublished. The first part containing the testing of appropriate hiPSC culture conditions will be submitted for publishing. This part of the thesis includes the participation of other people that are mentioned in the publication list.

I hereby declare that all procedures such as samples preparations, experiments, data analysis, visualisation and data interpretation were conducted by me if not stated otherwise in the respective method section. The development of a *NRAP*-KD hiPSC line and basal characterisation in EHTs were part of the masterthesis of the student Vanessa Lewandowski that I supervised. I planned the project and design, performed the nucleofection and initial selection of clones, performed the measurement of the SSEA3 value and some of the off-target analysis. Moreover, I produced the master and working cell bank and helped with the differentiation, dissociation, generation and culture of EHTs. The analysis of cardiac myocytes was completely performed by me.

12. Acknowledgements

In this final part of my thesis, I would like to emphasise my gratitude towards everyone who has contributed professionally or personally to this thesis. First and foremost, I am extremely grateful to my supervisors, Prof. Dr. Friederike Cuello and Prof. Dr. Wolfram Brune for the opportunity to work on this interesting project, their invaluable advice, motivation and continuous support. In addition, I would like to thank Prof. Dr. Thomas Eschenhagen and Prof. Dr. Ralph Holl for their interest in my work and accepting to be a part of my thesis committee. This endeavor would not have been possible without the financial support of the German Academic Scholarship Foundation and the German Heart Foundation.

I would also like to express my deepest appreciation to Prof. Dr. Elisabeth Ehler who functioned as a mentor for me during this journey with her immense knowledge in the field and I would also like to thank her for taking the time to give me a valuable scientific feedback to this thesis. Moreover, I would like to thank everyone from my laboratory group for technical and personal support through all the challenges and also for an exceptional and awesome work environment. In this context, I would like to highlight Dr. Konstantina Stathopoulou who kindly proofread parts of this thesis and always offered help and tried to solve problems. I would also like to thank Angelika Piasecki for her help and encouraging words. In addition, I am extremely grateful that I had the opportunity to work with Vanessa Lewandowski and Hannah Münch. I would like to thank them not only for their great work and help within the project but also for their enthusiasm and motivation during the last year. Lastly, I would like to mention and thank Julia Pflaumenbaum for her emotional support and motivation.

Moreover, I would like to acknowledge PD Dr. Thorsten Christ, Anna Steenpaß, Dr. Bärbel Ulmer, Dr. Michaela Schweizer, Julie Lange, Dr. Patrick Laurette, Dr. Ilka Wittig, Dr. Sigrid Fuchs, Niels Pietsch, Elisabeth Krämer, Dr. Aya Schibaya, Birgit Klampe, Ellen Oertey, Kristin Hartmann for their contribution to parts of this work.

I would also like to take this opportunity to thank the qualified translator Christine Wilhelm-Peters for proofreading this thesis concerning English accuracy.

Furthermore, I am extremely grateful to my family and my friends for their support and encouragement through out my studies. I would like to extend my sincere thanks to Nell Gryschka, Patrick Watermann and Florian Raabe for always inspiring and motivating me.

Acknowledgements

Finally, I would like to express my deepest gratitude to my parents Christine and Matthias Raabe for doing everything in their power to provide me with the best opportunities for my future. I could have not undertaken this journey without their tremendous understanding, love and unconditional support. Last but not least, I also owe deepest gratitude to Mike Zander for always supporting me and being by my side for many years through all ups and downs over the last years.

13. Declaration of academic honesty - Eidesstaatliche Erklärung

I hereby declare that the present thesis entitled “Role of the nebulin related anchoring protein – NRAP in the development of heart disease” was written independently by myself. No other sources or aid than indicated were used. The submitted bound copy of the dissertation is identical with the electronical form and was not evaluated elsewhere in an examination procedure.

Hiermit versichere ich an Eides statt, die vorliegende Dissertation mit dem Titel „Role of the nebulin related anchoring protein – NRAP in the development of heart disease” selbst verfasst wurde und keine anderen Hilfsmittel als die angegebenen verwendet wurden. Ich versichere, dass die im Studienbüro Chemie eingereichte gedruckte und gebundene Fassung mit der elektronischen Version der Dissertation übereinstimmt und in keinem vorherigen Promotionsverfahren eingereicht wurde.

Hamburg, den 06.07.2023

Janice Raabe